

FINAL DEGREE THESIS

**Double Bachelor's Degree in Biomedical Engineering, Industrial
Electronics and Automatic Control Engineering**

**DETECTION SYSTEM FOR PREVENTING TISSUE DAMAGE IN
CRYOTHERAPY THROUGH TEMPERATURE AND CAPACITANCE
MONITORING**



Report and Annex

Author: Nicolau Solé Coves
Supervisor: Noelia Vaquero Gallardo
Department: Department of Electronic Engineering
Co-supervisor: Herminio Martínez García
Call: 2025, July

Abstract

This Bachelor's Thesis, which integrates concepts from biomedical engineering and industrial electronics, addresses the prevention of tissue damage in cryolipolysis by identifying pre-freezing conditions, such as the phase change of water. Cryolipolysis relies on controlled cooling, but unintended freezing can lead to adverse effects. Temperature monitoring is commonly used to detect freezing via the exothermic peak; however, it presents limitations in responsiveness and in its ability to effectively monitor the entire treated area.

As an alternative, this work explores capacitance as a proxy for tissular water crystallization detection. A capacitive sensing system was designed, built, and experimentally tested alongside a temperature sensor for validation. Signal characterization and algorithmic analysis, notably employing a standard deviation threshold method, enabled real-time detection of the onset of freezing in water-saturated paper samples simulating the dermis. Experimental work also optimized thermal conditions, sample geometry, electrode configuration, and signal processing strategies for the proposed platform.

As a result, the developed laboratory-scale detection system achieved a sensitivity and precision of 93.33 %, and an overall accuracy above 91.11 %, often detecting freezing before the thermal reference.



Resum

Aquest Treball de Fi de Grau, que integra conceptes de l'enginyeria biomèdica i l'electrònica industrial, es centra en la prevenció del dany tissular en la criolipòlisi mitjançant la identificació de condicions prèvies a la congelació, com ara el canvi de fase de l'aigua. La criolipòlisi es basa en un refredament controlat, però la congelació no desitjada pot provocar efectes adversos. El monitoratge de la temperatura s'utilitza habitualment per detectar la congelació a través del pic exotèrmic; tanmateix, presenta limitacions tant en la rapidesa de resposta com en la seva capacitat de monitorizar eficaçment tota l'àrea tractada.

Com a alternativa, aquest treball explora la capacitatància com a indicador de la detecció de la cristal·lització de l'aigua en el teixit. S'ha dissenyat, construït i provat experimentalment un sistema de detecció capacitiva, que s'ha validat juntament amb un sensor de temperatura. La caracterització dels senyals i l'anàlisi algorítmica, incloent-hi un mètode basat en llindars de desviació estàndard, han permès la detecció en temps real de l'inici de la congelació en mostres de paper saturades d'aigua que simulen la dermis. A més, el treball experimental ha optimitzat les condicions tèrmiques, la geometria de les mostres, la configuració dels elèctrodes i les estratègies de processament de senyals per a la plataforma proposada.

Com a resultat, el sistema desenvolupat de detecció a escala de laboratori ha aconseguit una sensibilitat i una precisió del 93,33 %, així com una exactitud global superior al 91,11 %, detectant sovint la congelació abans de la referència tèrmica.

Resumen

Este Trabajo Fin de Grado, que integra conceptos de ingeniería biomédica y electrónica industrial, se ha centrado en la prevención del daño tisular en la criolipólisis mediante la identificación de condiciones previas a la congelación, como el cambio de fase del agua. La criolipólisis se basa en un enfriamiento controlado, pero la congelación no deseada puede provocar efectos adversos. La monitorización de la temperatura se utiliza habitualmente para detectar la congelación a través del pico exotérmico; sin embargo, presenta limitaciones tanto en la rapidez de respuesta como en su capacidad para monitorizar de forma eficaz toda el área tratada.

Como alternativa, se ha explorado el uso de la capacitancia como indicador para la detección de la cristalización del agua en el tejido. Se ha diseñado, construido y probado experimentalmente un sistema de detección capacitivo, que ha sido validado mediante un sensor de temperatura. La caracterización de las señales y el análisis algorítmico, incluyendo un método basado en umbrales de desviación estándar, han permitido la detección en tiempo real del inicio de la congelación en muestras de papel saturadas de agua que simulan la dermis. Además, se han optimizado las condiciones térmicas, la geometría de las muestras, la configuración de los electrodos y las estrategias de procesamiento de señales de la plataforma propuesta.

Como resultado, el sistema de detección desarrollado a escala de laboratorio ha alcanzado una sensibilidad y precisión del 93,33 %, así como una exactitud global superior al 91,11 %, detectando a menudo la congelación antes que la referencia térmica.



Acknowledgments

I would like to express my sincere gratitude to my supervisor, Noelia Vaquero Gallardo, for her constant support, guidance, and expertise throughout this project. I also thank Professor Herminio Martínez García for his valuable insights, particularly regarding the A/D conversion module.

To my family, for their unconditional support and trust in every step of this journey.

To Mònica Laplana, for being by my side through the entire degree and especially during the final months, and to Albert Brustenga, for always being there when I needed him.

To all the friends I've met during the degree, for expanding my support network and bringing critical thought into engineering discussions, and to my lifelong friends, for their patience and understanding over the last few months.

Thank you all.



Glossary

Glossary of Terms

Acronyms, abbreviations formed from the initial letters of a phrase and pronounced as a word.

Acronym	Explanation
ASDS	American Society for Dermatologic Surgery.
ECTS	European Credit Transfer and Accumulation System.
EEBE	<i>Escola d'Enginyeria de Barcelona Est.</i>
EVM	Evaluation Module.
FDA	Food and Drug Administration.
GUI	Graphical User Interface.
IDE	Integrated Development Environment.
ISO	International Organization for Standardization.
NHANES	National Health and Nutrition Examination Survey.
RoHS	Restriction of Hazardous Substances Directive.
SI	International System of Units.
SIG	<i>Sistemes Integrats de Gestió.</i>
TI	Texas Instruments.
UNE-EN	<i>Una Norma Española</i> (Spanish standard harmonized with European Norm).
UPC	<i>Universitat Politècnica de Catalunya.</i>
WEEE	Waste Electrical and Electronic Equipment Directive.

Abbreviations, shortened forms of words or phrases.

Abbreviation	Origin	Meaning
ca.	<i>circa</i>	Approximately.
e.g.	<i>exempli gratia</i>	For example.
eq.	Equation	Mathematical expression.
et al.	<i>et alii</i>	And others (used in citations).
i.e.	<i>id est</i>	That is (used to clarify).
L	Left	Direction.
R	Right	Direction.
in vitro	Latin phrase	In glass; outside a living organism.



Initialisms, abbreviations consisting of initial letters pronounced separately, not as a word.

Initialism	Explanation
AC	Alternating Current.
BF	Body Floating (electrical safety term).
CE	<i>Conformité Européenne</i> (European Conformity).
CT	X-ray Computed Tomography.
DC	Direct Current.
EMC	Electromagnetic Compatibility.
EU	European Union.
ICD	Implantable Cardioverter Defibrillator.
I2C	Inter-Integrated Circuit (communication protocol).
I/O	Inputs / Outputs.
IC	Integrated Circuit.
IVA	<i>Impuesto sobre el Valor Añadido</i> (Value-Added Tax, in Spanish).
MRI	Magnetic Resonance Imaging.
NIR	Near Infrared.
PCB	Printed Circuit Board.
PWM	Pulse Width Modulation.
RoHS	Restriction of Hazardous Substances, EU directive.
ROS	Reactive Oxygen Species.
SPS	Samples Per Second.
SRAM	Static Random-Access Memory.
UART	Universal Asynchronous Receiver-Transmitter (communication protocol).
USB	Universal Serial Bus.
UV	Ultraviolet.
™	Trademark: brand names, logos, slogans (not registered).
®	Registered Trademark: officially registered trademark.
©	Copyright: protects original works (text, music, art, software).

Symbols and Units used in scientific and technical contexts.

Symbol	Explanation
CO ₂	Carbon dioxide.
H ₂ O	Water.
LN ₂	Liquid nitrogen.
V _{pp}	Peak-to-peak voltage.
j	Imaginary unit, $j \triangleq \sqrt{-1}$.
π	Number Pi, $\pi \approx 3.14$.
kB	Kilobyte (1 kB = 1024 bytes).
mmHg	Millimeters of mercury (1 mmHg = 133.322 Pa).
X̄	Mean of variable X; the arithmetic average of a data set.
σ(X)	Standard deviation of variable X; measures the dispersion of the data around the mean.
n	Number of statistical samples.
CV	Coefficient of Variation; it expresses the relative variability as a ratio or percentage.



Glossary of SI Symbols

Non-SI units accepted for use with the SI units [1].

Quantity	Name of unit	Symbol for unit	Value in SI units
time	minute	min	1 min = 60 s
	hour	h	1 h = 60 min = 3600 s
	day	d	1 d = 24 h = 86 400 s
length plane and phase angle	astronomical unit	au	1 au = 149 597 870 700 m
	degree	°	1° = $(\pi / 180)$ rad
	minute	'	1' = $(1 / 60)^\circ = (\pi / 10 800)$ rad
	second	"	1" = $(1 / 60)'$ = $(\pi / 648 000)$ rad
area	hectare	ha	1 ha = 1 hm ² = 10^4 m ²
volume	litre	L	1 L = 1 dm ³ = 10^3 cm ³ = 10^{-3} m ³
mass	metric ton	t	1 t = 10^3 kg
mass	dalton	Da	1 Da = 1.660 539 040 (20) × 10^{-27} kg
energy	electronvolt	eV	1 eV = 1.602 176 634 × 10^{-19} J
logarithmic	neper	Np	see text [1]
ratio	bel	B	see text [1]
quantities	decibel	dB	see text [1]

SI prefixes [1].

Factor	Name	Symbol	Factor	Name	Symbol
10^1	deka	da	10^{-1}	deci	d
10^2	hecto	h	10^{-2}	centi	c
10^3	kilo	k	10^{-3}	milli	m
10^6	mega	M	10^{-6}	micro	μ
10^9	giga	G	10^{-9}	nano	n
10^{12}	tera	T	10^{-12}	pico	p
10^{15}	peta	P	10^{-15}	femto	f
10^{18}	exa	E	10^{-18}	atto	a
10^{21}	zetta	Z	10^{-21}	zepto	z
10^{24}	yotta	Y	10^{-24}	yocto	y

SI base units [1].

Base quantity Name	Symbol	Base unit Name	Symbol
time	t	second	s
length	l	meter	m
mass	m	kilogram	kg
electric current	I, i	ampere	A
thermodynamic temperature	T	K	
amount of substance	n	mole	mol
luminous intensity	I _v	candela	cd



Derived SI units with special names and symbols used in this thesis, reworked from [1].

Derived quantity	Symbol	Name of unit	In base units	In other SI units
frequency	f	hertz	$\text{Hz} = \text{s}^{-1}$	
pressure, stress	P	pascal	$\text{Pa} = \text{kg m}^{-1} \text{s}^{-2}$	
power, radiant flux	P	watt	$\text{W} = \text{kg m}^2 \text{s}^{-3}$	J/s
electric charge	Q	coulomb	$\text{C} = \text{A s}$	
electric potential difference	V	volt	$\text{V} = \text{kg m}^2 \text{s}^{-3} \text{A}^{-1}$	W/A
capacitance	C	farad	$\text{F} = \text{kg}^{-1} \text{m}^{-2} \text{s}^4 \text{A}^2$	C/V
electric resistance	R	ohm	$\Omega = \text{kg m}^2 \text{s}^{-3} \text{A}^{-2}$	V/A
inductance	L	henry	$\text{H} = \text{kg m}^2 \text{s}^{-2} \text{A}^{-2}$	Wb/A
Celsius temperature	T	degree Celsius	${}^\circ\text{C} = \text{K}$	

Coherent derived units in the SI expressed in terms of base units used in this thesis [1]¹.

Name	Symbol	Units
capacitance difference	ΔC	F
charge density distribution	ρ	C/m^3
dielectric constant	ϵ_r'	
dielectric displacement ²	\mathbf{D}	C/m^2
dielectric loss factor	ϵ_r''	
distance between plates	d	m
electric field	\mathbf{E}	$\text{V/m} = \text{N/C}$
electric susceptibility	χ_e	
electric impedance	X	Ω
electric reactance	Z	Ω
magnetic field strength	\mathbf{H}	A/m
polarization density	\mathbf{P}	C/m^2
relative permittivity	ϵ_r	
speed of light	c	299,792,458 m/s
thermal resistance	R_{th}	W/K
time	t	s
vacuum permeability	μ_0	$4\pi \times 10^{-7} \text{ N/A}^2$
vacuum permittivity	ϵ_0	$8.8542 \times 10^{-12} \text{ F/m}$

¹ This document does not fully follow the SI (International System of Units) conventions for formatting large numbers. While a point is correctly used as the decimal separator, commas are incorrectly used to group digits in the integer part (e.g., 1,234,567.123456789). According to the SI standard, spaces (not commas) should be used to group digits in sets of three for the integer part, and no grouping should be applied to the decimal part.

² Scientific symbols in bold represent vector quantities, whereas italic symbols indicate scalar values.

List of Equations

(Eq. 3.1)	16
(Eq. 3.2)	16
(Eq. 3.3)	16
(Eq. 3.4)	16
(Eq. 4.1)	27
(Eq. 4.2)	27
(Eq. 4.3)	27
(Eq. 4.4)	27
(Eq. 4.5)	27
(Eq. 4.6)	27
(Eq. 4.7)	29
(Eq. 4.8)	29
(Eq. 4.9)	29
(Eq. 4.10)	29
(Eq. 5.1)	41
(Eq. 5.2)	47
(Eq. 5.3)	47
(Eq. 5.4)	55

(Eq. 5.5)	55
(Eq. 5.6)	55
(Eq. 5.7)	55
(Eq. 5.8)	64
(Eq. 5.9)	65
(Eq. 5.10)	65
(Eq. 5.11)	65
(Eq. 5.12)	66
(Eq. 6.1)	85
(Eq. 6.2)	86
(Eq. 6.3)	87

List of Figures

Figure 3.1.a) A man self-administering hydrotherapy, sitting outside in a barrel [6].b) Carbon dioxide snow collector and compressor, by Hall-Edwards 1913 [7]. c) Modern cryosurgery device, CryoPro® by Cortex™. _____ 5

Figure 3.2. Representative clinical result before (L) and after (R) cryolipolysis. The patient underwent one treatment cycle to the right flank following the manufacturer's standard protocol. Results are shown two months post-treatment [30]. _____ 7

Figure 3.3. Survey data made by ASDS members, who performed over 1 million body sculpting in 2019 [32]. _____ 8

Figure 3.4. One week after localized cooling of porcine skin. Note the lobular panniculitis affecting the adipose tissue (A, 5X magnification). At higher magnification (B, 20X magnification), individual adipocytes are surrounded by a predominantly mononuclear cell infiltrate [30]. _____ 9

Figure 3.5. Number of patients affected by specific side effects after cryolipolysis treatment [48].10

Figure 3.6. Skin erythema and blistering after cold treatment, resembling frostbite [53]. _____ 10

Figure 3.7. Schematic of freezing tissue with simultaneous temperature monitoring of the evolving ice front by means of two thermocouple needles [59]. _____ 12

Figure 3.8. Temperature profile (°C) with respect to time (min) from an ambient temperature value and freezing the area. It is observed that freezing occurs above -22 °C [60]. _____ 12

Figure 3.9.a) Time-dependent (s) freezing curves (°C) for fish muscle pre-frozen in LN₂ slowly thawed in air and for fresh fish muscle. b) Rate of temperature (°C/s) change for the freezing curves. Adapted from [62]. _____ 12

Figure 3.10. Impedance profile (upper, Ω) and temperature (lower, °C) as a function of time (min). Measurements are recorded from ambient temperature down to the freezing temperature of the area. It is observed that freezing occurs at temperatures above -22 °C [60]. _____ 14

Figure 3.11. a) Typical plots showing the impedance (Ω) as a function of f (Hz) of meat throughout the thawing process for different temperatures. b) Typical plots of impedance (Ω) as a function of

temperature (°C) for six selected frequencies. The impedance was taken during the rapid thawing process of pork muscle [68]. _____ 14

Figure 3.12. a) Impedance components resistance (R) and reactance (X) of pork meat tissue at 4 °C after freezing and thawing, and the b) $R(f)$ and $X(f)$ curves of slow thawed and fast thawed pork meat tissue. Each line in both figures represent the mean impedance of ten meat samples [68]. _____ 14

Figure 3.13. Freeze Depth Indicator®, an impedance-based method for controlled cryosurgery of malignant tumors developed by M. Savic and S. A. Zacarian [70]. a) Schematic representation of current flow using a single-needle electrode configuration. b) Illustration of the dual-needle electrode setup: electrode (a) is inserted centrally and beneath the tumor, while electrode (b) is positioned at the tumor margin. Each electrode independently monitors tissue impedance at its respective location to assess freezing depth. Both electrodes are millimeter-calibrated to allow precise determination of frozen tissue depth [70]. _____ 15

Figure 3.14. Frequency response (Hz) of polarization mechanisms of water [78]. _____ 17

Figure 3.15. Dielectric spectra (Hz) of ice (dark grey) and water (light grey) at 0 °C [79]. _____ 17

Figure 3.16. Comparison between $\varepsilon r'$ of water (a) and ice (b) as a function of f (Hz) and T (°C) [80].
_____ 18

Figure 3.17. Frequency (Hz) dispersion of water and ice real dielectric constants at different temperatures [81]. _____ 18

Figure 3.18. Statistical analysis of the laboratory data. a) Values of capacitance (raw data) obtained for each sensor during the first experiment. b) Internal temperature of the climatic chamber during the first experiment with the indication of the state condition detected by a sensor. c) Time (min) instants of state transitions estimated for each sensor during three different experiments. d) Standard deviations of time instants (s) of wet-icy and icy-wet state transitions estimated for each sensor during three different experiments [80]. _____ 19

Figure 4.1. Block diagram of the freezing platform. Author's own work. _____ 21

Figure 4.2. Schema of how a Peltier cell or TEC (Thermoelectric Cooler) works [86]. _____ 22

Figure 4.3. TEC1-12706 cells used in this thesis. Author's own photograph.	22
Figure 4.4. FAN478 fan and heat sink used in this thesis [88].	23
Figure 4.5. Block diagram of the experimental platform used for real-time acquisition of data in freezing events. Author's own work.	24
Figure 4.6. MATLAB GUI for real time (s) temperature (upper graph, °C) and capacitance (lower graph, pF) monitoring. Author's own work.	25
Figure 4.7. Full data representation in a MATLAB plot, given at the end of the procedure by the MATLAB GUI. Author's own work.	25
Figure 4.8. Temperature AHT10 module used in this thesis [90].	26
Figure 4.9. Parallel plate capacitor made of copper tapes glued on methacrylate. Author's own work.	26
Figure 4.10. Underlap/overlap two and three-plate bridge configurations, extracted and modified from [77].	28
Figure 4.11. Electric fields of a parallel plate capacitor and its fringing effect [91].	29
Figure 4.12. Input capacitance signal of the system under different shielding conditions. From 0 s to 12 s: no shielding; from 15 s to 55 s: shielded, but with the laptop connected to the power stage; from 55 s onward: shielded and electrically isolated from the power stage. The x-axis represents time (s), and the y-axis represents capacitance (pF). Source: Author.	30
Figure 4.13. Ground shield electrode configuration (L) and its equipotential lines (R). Reworked from [77].	31
Figure 4.14. FDC1004EVM and its sections, modified from [103].	35
Figure 5.1. Performance curves of the TEC1-12706, adapted from [85].	37

Figure 5.2. Experimental setup for freezing point detection. The AHT10 sensor is placed on the cold side of the TEC. The capacitance measurement system was not used in this configuration. Author's own diagram. _____ 38

Figure 5.3. Photograph of the five water-saturated absorbent paper samples, each wrapped in plastic film and varying in the number of layers, used in the experiment. Author's own image. ___ 39

Figure 5.4. Experimental platform column marked with increasing distances of 1 cm from the *CGND*. Author's own picture. _____ 42

Figure 5.5. Experimental setup for freezing point detection. The sample (blue object) is placed on the cold side of the TEC, over the ground plate, and below the *Cin*. Author's own diagram. ___ 42

Figure 5.6. Experimental setup for freezing point detection via *Cint* with $T(t)$ as a reference. The sample (blue object) is placed on the cold side of the TEC, over the ground plate, and below the *Cin*. Author's own diagram. _____ 45

Figure 5.7. Temperature profile (right y-axis, garnet, °C) and raw (non-filtered) capacitance signal (left y-axis, black, pF) plotted against time (x-axis, seconds). Author's own work. _____ 48

Figure 5.8. Effect of extreme window sizes W on filtering the capacitance signal within the Region of Interest (ROI). Each subplot compares the filtered signals using moving average (solid red line) and local linear polynomial fit (solid magenta line) against the raw capacitance data (black dots). Increasing window size smooths noise but may distort important signal transitions. The x-axis is time (s). Author's own work. _____ 49

Figure 5.9. Zoomed-in view of the Region of Interest (ROI) showing temperature (right y-axis, garnet, °C) and unfiltered capacitance (left y-axis, black, pF) versus time (s) for different window sizes (samples). This highlights the critical signal features relevant to detection algorithm performance within the (90 s, 180 s) and (9.6 pF, 10.4 pF) range. Author's own work. _____ 49

Figure 5.10. Temperature curves for experiments conducted at 11 V (solid line) and 12 V (dashed line), used to determine the optimal Peltier cell voltage, and assess the AHT10 sensor's ability to detect freezing. The red ellipse marks the exothermic curves. The x-axis represents time (s); the y-axis shows temperature (°C). Author's own work. _____ 50

Figure 5.11. Statistical summary of Experiment 1, showing individual data points, mean values, and standard deviations for both voltage conditions. The x-axis indicates the experimental group (11 V or 12 V); the y-axis refers to the type of data analyzed. Author's own work. _____ 51

Figure 5.12. Temperature profile of a water droplet cooled by a TEC device powered at 12 V. The final stabilized temperature is marked with a blue data tip at -12.78 °C after 200 s. The x-axis represents time (s); the y-axis shows temperature (°C). Author's own work. _____ 51

Figure 5.13. Statistical summary of Experiment 2, showing individual data points, mean values, and standard deviations for each sample type. The x-axis indicates the experimental group (1, 2, 4, 8 and 16 layers); the y-axis refers to the type of data analyzed. Author's own work. _____ 54

Figure 5.14. Temperature curves of water-saturated absorbent paper samples with varying numbers of layers; the x-axis represents time (s), and the y-axis represents temperature (°C). Author's own work. _____ 54

Figure 5.15. Temperature curves from 30 trials using 8-layer absorbent paper samples. The x-axis represents time (s), and the y-axis represents temperature (°C). Author's own work. _____ 56

Figure 5.16. Capacitance curves for five different electrode separation distances using a sensing area of $AC = 3 \text{ cm}^2$. Each subplot shows one of five trials per distance. The x-axis represents time in seconds (s); the y-axis shows $C_{in}(\text{pF})$. Distance between electrodes, d , is given in centimetres (cm). Author's own work. _____ 58

Figure 5.17. Capacitance variation (ΔC) as a function of electrode separation distance for a $AC = 3 \text{ cm}^2$. Data points (hollow points) represent the mean change across five trials per distance. The mean (solid points) and its standard deviation (error bars) are also shown. Both linear (solid line) and exponential (dashed line) fits are shown to evaluate the trend. The x-axis represents distance (cm), and the y-axis represents change in capacitance (pF). Author's own work. _____ 58

Figure 5.18. Capacitance curves for five different electrode separation distances using a sensing area of $AC = 16 \text{ cm}^2$. Each subplot shows one of five trials per distance. The x-axis represents time in seconds (s); the y-axis shows $C_{in}(\text{pF})$. Distance between electrodes, d , is given in centimetres (cm). Author's own work. _____ 60

Figure 5.19. Capacitance variation (ΔC) as a function of electrode separation distance for a $AC = 16 \text{ cm}^2$. Data points (hollow points) represent the mean change across five trials per distance.

The mean (solid points) and its standard deviation (error bars) are also shown. Both linear (solid line) and exponential (dashed line) fits are shown to evaluate the trend. The x-axis represents distance (cm), and the y-axis represents change in capacitance (pF). Author's own work. _____ 61

Figure 5.20. Representative output from Experiment 5, sample 1, illustrating the temperature profile $T(t)$ (solid garnet line) and the filtered capacitance input signal $Cin(t)$ (dotted magenta line), obtained using a moving average filter with a window size of $W = 25$ samples. The x-axis denotes time (s); the left y-axis corresponds to capacitance (pF), and the right y-axis corresponds to temperature ($^{\circ}$ C). Author's own work. _____ 63

Figure 5.21. Data overview of sample 7, illustrating the temperature profile $T(t)$ (solid garnet line) and the filtered capacitance input signal $Cin(t)$ (dotted magenta line), obtained using a moving average filter with a window size of $W = 25$ samples. The x-axis denotes time (s); the left y-axis corresponds to capacitance (pF), and the right y-axis corresponds to temperature ($^{\circ}$ C). Author's own work. _____ 64

Figure 5.22. Photograph of water droplets being formed by condensation on top of the input electrode. Own author's photograph. _____ 65

Figure 5.23. Analysed Interest Points: Ci (green point), Cf (purple point), Cf' (magenta point), $dC dt \in t1, t2$ (red line), $t1, t2$ (black points), $dC dt \in t *= 0$, with $d2C dt2t = t * > 0$ (orange point). Author's own work. _____ 66

Figure 5.24. Representative output from Experiment 5, sample 1, showing the temperature profile $T(t)$ (solid garnet line) and the filtered input capacitance signal $Cin(t)$ (dotted magenta line, window size $W = 25$). Peaks (red) and valleys (green) were identified using the non-averaged derivative (solid black line). The x-axis denotes time (s); the left y-axis corresponds to capacitance (pF) in the upper graph and to the derivative of capacitance over time (pF/s) in the lower graph; the right y-axis corresponds to temperature ($^{\circ}$ C). Author's own work. _____ 67

Figure 5.25. Representative output from Experiment 5, sample 1, showing the temperature profile $T(t)$ (solid garnet line) and the filtered input capacitance signal $Cin(t)$ (dotted magenta line, window size $W = 25$). Peaks (red) and valleys (green) were identified using the averaged derivative (solid black line, $W = 25$). The x-axis denotes time (s); in the upper graph the left y-axis corresponds to capacitance (pF) and in the lower graph the derivative of capacitance over time (pF/s); the right y-axis corresponds to temperature ($^{\circ}$ C). Author's own work. _____ 68

Figure 5.26. Output from Experiment 5, sample 11, showing the temperature profile $T(t)$ (solid garnet line) and the filtered input capacitance signal $Cin(t)$ (dotted magenta line, window size $W = 25$). Peaks (red) and valleys (green) were identified using the averaged derivative (solid black line, $W = 99$). The x-axis denotes time (s); in the upper graph the left y-axis corresponds to capacitance (pF) and in the lower graph the derivative of capacitance over time (pF/s); the right y-axis corresponds to temperature ($^{\circ}$ C). Author's own work. _____ 68

Figure 5.27. Output from Experiment 5, sample 1, showing the temperature profile $T(t)$ (solid garnet line) and the filtered input capacitance signal $Cin(t)$ (dotted magenta line, $W = 25$). A change in the trend of $Cin(t)$ was identified (solid black marker) using the standard deviation $\sigma(Cint)$ (solid blue line), along with an upper threshold (solid gray line) and a lower threshold (solid black line). The x-axis denotes time (s); the left y-axis corresponds to capacitance (pF) in the upper graph and to the standard deviation of capacitance (pF) in the lower graph; the right y-axis corresponds to temperature ($^{\circ}$ C). Author's own work. _____ 69

Figure 5.28. Schematic of the first-valley detection algorithm based on MATLAB's "gradient()". Developed by the author. _____ 70

Figure 5.29. Standard deviation threshold detection algorithm schema. Author's own work. _____ 71

Figure 5.30. Comparison of the two proposed detection algorithms against the gold standard, based on Experiment 5 results. Each subplot presents the distribution of detection delays with mean values (solid black lines), 95 % CI (dark shaded areas), and standard deviation (light shaded areas). Scatter points represent the individual trial value. Top subplot: Temperature delay ΔT ($^{\circ}$ C), defined as the difference between $T_{detected}$ and the exothermic peak temperature T_{peak} . Bottom subplot: Time delay Δt (s), defined as the temporal offset between the detected point and the time of the exothermic peak t_{peak} . Relative uncertainty εr is also provided as a percentage of the mean value for each method. Visualization and analysis performed by the author. _____ 72

Figure 6.1. Representation of the Experimental Platform. Author's own work. _____ 75

Figure 6.2. Block diagram of the proposed detection system platform, including the freezing (in blue) and the data collection (in green) platforms. Author's own work. _____ 75

Figure 6.3. Top view of the proposed detection system platform, indicating where each element is. Author's own photograph. _____ 76



Figure 6.4. Isometric view of the proposed detection system platform built. Author's own photograph.

76

Figure 6.5. Data overview of sample 6. The temperature profile $T(t)$ (solid garnet line) and the filtered input capacitance signal $Cin(t)$ (dotted magenta line, $W = 25$) are shown in the upper graph. No significant change in $Cin(t)$ was detected, as the standard deviation $\sigma(Cint)$ (solid blue line) (solid blue line) remained below the upper threshold (solid gray line); the lower threshold (solid black line) is also shown. The x-axis indicates time (s); the left y-axis shows capacitance (pF) in the upper graph and its standard deviation (pF) in the lower graph; the right y-axis shows temperature ($^{\circ}$ C). Author's own work.

78

Figure 6.6. Results of the iterative parameter search. The upper plot shows the mean temperature difference ΔT ($^{\circ}$ C), and the lower plot shows the mean time delay Δt (s), both represented by black markers with 95 % confidence intervals (grey error bars). Individual trial values are shown as light grey points. A vertical black line indicates the selected optimal window size for a threshold $th2 = 0.002$ pF. Author's own work.

79

Figure 6.7. Results of the iterative parameter search. The upper plot shows the mean temperature difference ΔT ($^{\circ}$ C), and the lower plot shows the mean time delay Δt (s), both represented by black markers with 95 % confidence intervals (grey error bars). Individual trial values are shown as light grey points. A vertical black line indicates the selected optimal threshold $th2$ for a window size of $W = 25$ samples. Author's own work.

79

Figure 6.8. Results of the iterative parameter search. The upper plot shows the mean temperature difference ΔT ($^{\circ}$ C), and the lower plot shows the mean time delay Δt (s), both represented by black markers with 95 % confidence intervals (grey error bars). Individual trial values are shown as light grey points. A vertical black line indicates the selected optimal window size for a threshold $th2 = 0.0024$ pF. Author's own work.

80

Figure 6.9. Results of the iterative parameter search. The upper plot shows the mean temperature difference ΔT ($^{\circ}$ C), and the lower plot shows the mean time delay Δt (s), both represented by black markers with 95 % confidence intervals (grey error bars). Individual trial values are shown as light grey points. A vertical black line indicates the selected optimal threshold $th2$ for a window size of $W = 23$ samples. Author's own work.

80

Figure 6.10. Results of the iterative parameter search. The upper plot shows the mean temperature difference ΔT ($^{\circ}$ C), and the lower plot shows the mean time delay Δt (s), both represented by

black markers with 95 % confidence intervals (grey error bars). Individual trial values are shown as light grey points. A vertical black line indicates the selected optimal window size for a threshold $th2 = 0.0021$ pF. Author's own work. _____ 81

Figure 6.11. Detection delay results for different $(W, th2)$ parameter pairs from the optimization process, compared to the temperature-based gold standard. Each subplot shows trial delays as scatter points, with mean (black line), 95 % confidence interval (dark shade), and standard deviation (light shade). ΔT ($^{\circ}$ C), is shown above, Δt (s). below. Each pair includes relative uncertainty εr and the number of successful detections n . Analysis by the author. _____ 81

Figure 6.12. Data overview of TP sample 1: Temperature $T(t)$ (dashed garnet line, $^{\circ}$ C) and filtered capacitance signal $Cin(t)$ (dotted magenta line, pF; window size $W = 25$ samples). Detected points $T_{detected}$ and $C_{detected}$ and exothermic peak $Tpeak$ are marked. The lower graph shows standard deviation $\sigma(Cint)$ crossing upper $th1$ (gray) and lower $th2$ (black) thresholds. Author's own work. _____ 88

Figure 6.13. Data overview of TP sample 1: Temperature $T(t)$ (dashed garnet line, $^{\circ}$ C) and filtered capacitance signal $Cin(t)$, with no detection triggered. Author's own work. _____ 88

Figure 6.14. Box-and-whisker plots for TP detection parameters: ΔT (upper left, $^{\circ}$ C), Δt (upper right, s), $T_{detected}$ (lower left, $^{\circ}$ C), $t_{detected}$ (lower left, s). Each plot shows the individual sample values (grey dots), the mean (black solid line), the standard deviation (dark grey shaded area), and the 95 % CI (light grey shaded area). Author's own work. _____ 89

Figure 6.15. Box plots comparing freezing detection parameters for true positives between the threshold algorithm (gray) and the gold standard (yellow). Top left: ΔT ($^{\circ}$ C); Top right: Δt (s); Bottom left: $Tchange$ ($^{\circ}$ C); Bottom right: $tchange$ (s). Each plot shows individual samples (dots), mean (solid line), standard deviation (dark band), and 95 % confidence interval (light band). The algorithm detects events earlier (lower $tchange$, higher $Tchange$) with consistent uncertainty. Author's own work. _____ 90

Figure 10.1. Thesis Cost Breakdown Pie Chart. Author's own work. _____ 103

Figure 0.1. Screenshot of the GitHub repository containing the materials generated during the development of this thesis. Author's own work. _____ 119

List of Tables

Table 4.1 Two plate electrode configurations and its applications, extracted and later modified from [77].	28
Table 4.2. Comparison of potential capacitance sensor interfaces.	34
Table 5.1. Confusion matrix summarizing the classification outcomes for the 30 trials conducted using the 8-layer absorbent paper configuration in Experiment 2.	55
Table 5.2. Statistics summary of Experiment 3 results.	57
Table 5.3. Statistics summary of Experiment 4 results.	61
Table 6.1 Confusion matrix summarizing classification results for 45 trials.	85
Table 6.2. Confidence intervals for classification metrics (Wilson score method).	86
Table 7.1. Maximum permissible current values under normal and single-fault conditions according to UNE-EN 60601-1:2008 [115].	94
Table 10.1. Experimental Platform Building Costs.	101
Table 10.2. Experimental Consumable Costs.	102
Table 0.1. Bill of Materials in order to build this TFE.	122
Table 0.2. Results of Experiment 1, where $V = 11$ V.	143
Table 0.3. Results of exerperiment 1, where $V = 12$ V.	143
Table 0.4. Summary of measurements from Experiment 2 with 1 layer.	144
Table 0.5. Summary of measurements from Experiment 2 with 2 layers.	144
Table 0.6. Summary of measurements from Experiment 2 with 4 layers.	144

Table 0.7. Summary of measurements from Experiment 2 with 8 layers. _____ 144

Table 0.8. Summary of measurements from Experiment 2 with 16 layers. _____ 144

Table 0.9. Summary of measurements from Experiment 2, validation of measurements with 8-layer samples. _____ 145

Table 0.10. Summary of measurements from Experiment 3 with 1 cm of separation between plates.
_____ 146

Table 0.11. Summary of measurements from Experiment 3 with 2 cm of separation between plates.
_____ 146

Table 0.12. Summary of measurements from Experiment 3 with 3 cm of separation between plates.
_____ 146

Table 0.13. Summary of measurements from Experiment 3 with 4 cm of separation between plates.
_____ 146

Table 0.14. Summary of measurements from Experiment 3 with 5 cm of separation between plates.
_____ 146

Table 0.15. Statistics of Experiment 3 results. _____ 146

Table 0.16. Summary of measurements from Experiment 3 with 1 cm of separation between plates.
_____ 147

Table 0.17. Summary of measurements from Experiment 3 with 2 cm of separation between plates.
_____ 147

Table 0.18. Summary of measurements from Experiment 3 with 3 cm of separation between plates.
_____ 147

Table 0.19. Summary of measurements from Experiment 3 with 4 cm of separation between plates.
_____ 147

Table 0.20. Summary of measurements from Experiment 3 with 5 cm of separation between plates.

147

Table 0.21. Statistics of Experiment 4 results. 147

Table 0.22. Different tried Correlation Parameters Statistics Results. 148

Table 0.23. Results of the Threshold Algorithm Validation. 150



Index

ABSTRACT	I
RESUM	III
RESUMEN	V
ACKNOWLEDGMENTS	VII
GLOSSARY	IX
Glossary of Terms	ix
Glossary of SI Symbols	xi
LIST OF EQUATIONS	XIII
LIST OF FIGURES	XV
LIST OF TABLES	XXV
INDEX	XXIX
1. PREFACE	1
1.1. Background	1
1.2. Motivation.....	1
1.3. Previous Requirements.....	1
2. INTRODUCTION	3
2.1. Objective	3
2.2. Scope	3
3. STATE OF THE ART	5
3.1. Introduction to Cryogenics	5
3.1.1. Early Cryotherapy Innovations.....	5
3.1.2. Advancements in Cryosurgery	6
3.1.3. Biological Effects and Clinical Applications	6
3.2. Introduction to Cryolipolysis.....	7
3.2.1. Cryolipolysis Development.....	8
3.2.2. Side Effects of Cryolipolysis	9
3.3. Freezing Events Monitoring.....	11
3.3.1. Direct Freezing Monitoring - Temperature Sensors	11
3.3.2. Indirect Freezing Monitoring - Bioimpedance Sensors.....	13



3.4. A Novel Approach for Tissue Freezing Detection – Capacitive Sensor.....	16
4. MATERIALS	21
4.1. Freezing Platform.....	21
4.1.1. Microcontroller.....	21
4.1.2. Power supply.....	21
4.1.3. Peltier Cells.....	22
4.1.4. Relay module	23
4.1.5. Heat sink.....	23
4.1.6. Thermal Paste	23
4.2. Data Collection Framework.....	24
4.2.1. The Temperature Sensor – Gold Standard.....	26
4.2.2. The Capacitive Sensor – Custom Design.....	26
4.2.3. The Evaluation Module.....	31
4.2.4. The Software	36
5. METHODS	37
5.1. Data Collection.....	37
5.1.1. Experiment 1: Freezing Point Detection.....	37
5.1.2. Experiment 2: Optimal Sample Height	39
5.1.3. Experiment 3: Plate Separation Distance Optimization	41
5.1.4. Experiment 4: Effect of Increasing Electrode Area.....	44
5.1.5. Experiment 5: Input Capacitance Behavior Correlated to Freeze.....	45
5.2. Analysis and Results.....	50
5.2.1. Experiment 1: Freezing Point Detection.....	50
5.2.2. Experiment 2: Optimal Sample Size.....	53
5.2.3. Experiment 3: Plate Separation Distance Optimization	57
5.2.4. Experiment 4: Effect of Increasing Electrode Area.....	60
5.2.5. Experiment 5: Input Capacitance Behavior Correlated to Freeze.....	63
6. DETECTION SYSTEM PROPOSAL	75
6.1. Freeze Detection Algorithm	77
6.1.1. Optimization of Algorithm Parameters	77
6.2. Validation of the Detection System	83
6.2.1. Design of the Validation Experiment.....	83
6.2.2. Results	85
6.2.3. Conclusions	91
7. APPLICABLE STANDARDS	93



7.1.	Scope of Standards Application	93
7.2.	Applicable Standards and Electrical Safety Requirements	93
7.2.1.	Device Classification and Risk Category	93
7.2.2.	Permissible Current Limits.....	94
7.3.	Patient Safety and Exclusion Criteria.....	95
7.4.	Additional Relevant Standards	95
7.4.1.	Electromagnetic Compatibility (EMC)	95
7.4.2.	Usability Engineering.....	95
7.4.3.	Risk Management.....	96
7.5.	Summary	96
8.	FUTURE WORK _____	97
9.	SUSTAINABILITY ANALYSIS _____	99
10.	ECONOMIC ANALYSIS _____	101
10.1.	Materials and Software.....	101
10.1.1.	Experimental Platform	101
10.1.2.	Experimental Procedures and Consumables	102
10.2.	Software and Licensing Costs	102
10.3.	Engineering Costs and Labour	102
10.3.1.	Student Research and Development Time	102
10.3.2.	Supervision and Collaboration Costs.....	102
10.3.3.	Final Summup.....	103
CONCLUSIONS _____	105	
BIBLIOGRAPHY _____	107	
ANNEX _____	119	
ANNEX A: TECHNICAL DOCUMENTATION _____	121	
A1.	Experimental Platform Electric Schematic	121
A2.	Bill of Materials (BOM).....	122
ANNEX B: CODE _____	123	
B1.	Arduino Data Collection: “PELTIER_TEMP_HUM_TIMESTAMP.ino”	123
B2.	MATLAB GUI Data Collection: “GUI_T_C_Time.m”	124
B3.	Ploting and saving the samples from Experiment 5, were the C curve was filtered.	127

B4.	Plotting the derivative of the C sample, and detecting valleys and peaks with an average filter to the gradient.....	129
B5.	Auxiliar Function: “ <i>exopeak_choose.m</i> ”	131
B6.	Data processing Algorithm with GUI.....	132
B7.	Data Validation and Figures Code	136
ANNEX C: ADQUIRED DATA		143
C1.	Experiment 1: Freezing Point Detection	143
C2.	Experiment 2: Optimal Sample Size	144
C3.	Experiment 3: Plate Separation Distance Optimization	146
C4.	Experiment 4: Effect of Increasing Electrode Area	147
C5.	Experiemnt 5: Input Capcaitance Behaviour Correlated to Freeze	148
C6.	Statistic Analysis of the Proposed Algorithm	150
ANNEX D: PROJECT MANAGEMENT		153
D1.	GANTT Diagram	153
D2.	Thesis Economic Study	154
D3.	Thesis Economic Study – Price Links	155

1. Preface

1.1. Background

This project has been developed as part of a collaborative effort with the PhD research of Noelia Vaquero Gallardo, funded by the *Pla de Doctorats Industrials of the Secretaria d'Universitats i Recerca del Departament d'Empresa i Coneixement de la Generalitat de Catalunya* (grant 2022 DI 037), and the Spanish *Ministerio de Ciencia, Innovación y Universidades* (MICINN) – *Agencia Estatal de Investigación* (AEI) through project PID2022-138631OB-I00, under the supervision of Professor Herminio Martínez García. As a student at *Escola d'Enginyeria Barcelona Est – Universitat Politècnica de Catalunya* (EEBE-UPC) pursuing a double degree in Biomedical Engineering and Industrial Electronics and Automatic Control Engineering, this Bachelor's Thesis (TFE) represents the culmination of my academic training in both fields. While rooted in an academic and research-oriented context, the project also emphasizes practical experimentation and applied engineering, allowing me to bridge theoretical knowledge with real-world implementation.

1.2. Motivation

Driven by a strong interest in medical electronics cultivated during my Biomedical Engineering studies, I pursued a second degree in Industrial Electronics and Automatic Control Engineering. This thesis bridges both disciplines, offering a unique opportunity to deepen and apply my knowledge in the field of electromedical devices. In collaboration with doctoral candidate Noelia Vaquero Gallardo, who is developing a cryolipolysis module designed to circumvent patented temperature-based methods, and under the joint supervision of Professor Herminio Martínez García, I undertook the development of a system to detect tissue freezing via capacitance measurements, complementing her research on bioimpedance. This project not only contributes to an ongoing research initiative but also provides me with valuable experience in applied scientific research, a path I am eager to continue exploring.

1.3. Previous Requirements

The development of this project required foundational knowledge in both biomedical sciences and electronics. A biomedical background was essential to understand scientific literature related to cryolipolysis and the biological principles underlying the technique. Simultaneously, knowledge of electronics was necessary to design and implement the measurement system, understand its operation, and evaluate its expected performance and limitations.



2. Introduction

2.1. Objective

The objective of this project is to design and validate a real-time laboratory prototype capable of detecting pre-freezing conditions in tissue through changes in capacitance. This includes the development of a detection algorithm that identifies the onset of freezing events using real-time capacitive sensor data. The system is validated against temperature measurements, often considered the gold standard due to their simplicity and well-established use. Nonetheless, their spatial limitations highlight the need for complementary detection methods. This work aims to contribute a more spatially inclusive and responsive monitoring approach for cryotherapy applications, with the goal of improving tissue protection.

2.2. Scope

The scope of this project encompasses the design, implementation, and optimization of a laboratory-scale prototype for capacitive sensing of tissue freezing. The work includes the development of a real-time detection algorithm, based on the parameterization of capacitance signal curves, to identify the onset of freezing events. Additionally, the project includes a review of cryotherapy procedures, their underlying mechanisms, and an analysis of current sensing technologies used in the field. Framed within the doctoral research of Noelia Vaquero Gallardo, who investigates non-temperature-based detection methods such as bioimpedance, this thesis explores capacitance as a novel and complementary strategy for detecting freezing, with the aim of enhancing tissue protection during cryotherapeutic applications.



3. State of the Art

3.1. Introduction to Cryogenics

Cryogenics is the branch of engineering concerned with the study of materials and their properties at extremely low temperatures. These ultra-low temperatures can significantly alter the chemical attributes of materials, leading to new applications and technologies. Cryogenics has become crucial in modern medicine, paving the way for advancements such as the preservation of biological tissues, organ storage, and the treatment of diseases using controlled freezing, namely cryosurgery [2].

The medical use of cryogenic cooling dates back to Ancient Egypt and Hippocrates, who applied cold treatments for injuries and inflammation [3], [4]. Over the past two centuries, cryogenic applications have evolved from generalized cold therapies, like hydrotherapy, Figure 3.1.a), to the targeted tissue destruction that forms the foundation of modern cryosurgery [3], [5].

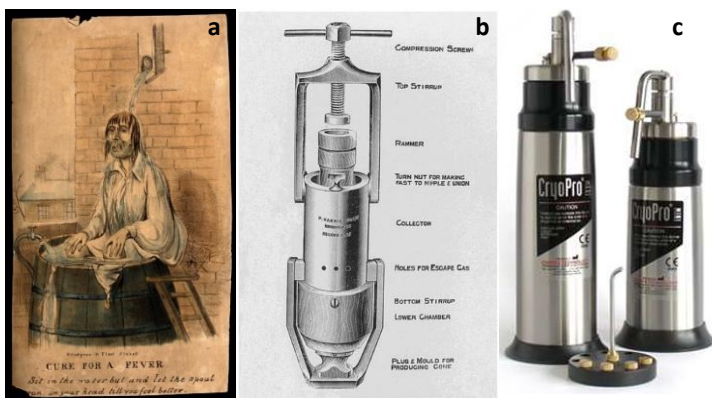


Figure 3.1.a) A man self-administering hydrotherapy, sitting outside in a barrel [6].**b)** Carbon dioxide snow collector and compressor, by Hall-Edwards 1913 [7]. **c)** Modern cryosurgery device, CryoPro® by Cortex™.

3.1.1. Early Cryotherapy Innovations

James Arnott (1819-1879) pioneered cryotherapy using a salt-ice mixture for tumors, later replaced by Benjamin Richardson's ether spray in 1866 for its simplicity [8]. In 1891, ethyl chloride superseded ether for analgesia [8].

Advances in gas liquefaction in the late 19th century facilitated medical refrigeration. In 1877, Cailletet and Pictet developed systems for oxygen and nitrogen liquefaction [9]. Dewar's 1892 vacuum flask improved cryogen storage, and von Linde commercialized liquefied air in 1895 [9]. Dr. Campbell White introduced liquid air for dermatological treatments in 1899 via spray, swabs, or rollers [10]. However, due to its hazards, liquid air was replaced by carbon dioxide snow, first used by Dr. William Pusey in

1907 [11]. Stored in pressurized cylinders, CO₂ snow became widely used for skin and gynecological conditions until the 1940s, Figure 3.1.b), [9].

3.1.2. Advancements in Cryosurgery

The increasing complexity of cryosurgical tools led to a separation between physicians and engineers. In 1938, Temple Fay and George Henny developed the first closed cryosurgical system using ice-saline instruments [12]. Fay's observation that tumors rarely formed in cooler body regions inspired further research into cryotherapy for malignancies [12].

After World War II, liquid nitrogen became commercially available. Allington introduced it for dermatology in 1950, achieving superficial freezing with cotton swabs [13]. Rowbotham pioneered its use for brain tumor treatment in 1959 with a vacuum flask system [14]. Tytus and Ries later experimented with Freon and Boeing-developed liquid nitrogen probes, reaching -190 °C [15].

In 1961, Cooper and Lee introduced the first closed liquid nitrogen system for Parkinson's treatment. Their insulated cooling cannula remains the basis for modern cryoprobes [9]. Since then, cryosurgery has expanded to treat cervical, oral, rectal, bronchial, and bone cancers, among other conditions [3], [4], [5], [9].

3.1.3. Biological Effects and Clinical Applications

Over the past 50 years, research has focused on liquid nitrogen's biological effects. Temperature probes have enabled precise tissue temperature measurement during freezing [3]. Cell sensitivity studies show that melanocytes are highly susceptible, leading to post-cryosurgery depigmentation, while collagen remains intact even after deep freezing, minimizing scarring [16]. Cartilage necrosis is rare, making cryosurgery ideal for preserving function in sensitive areas like the ears, eyes, and nose [17].

Cryosurgery is a mainstay in dermatology, effectively treating benign lesions such as warts, seborrheic keratoses, *molluscum contagiosum*, spider angiomas, and digital myxoid cysts, as well as premalignant solar keratoses and Bowen's disease. It is also used for squamous cell carcinomas and *lentigo maligna* [18].

Beyond dermatology, ophthalmologists use cryosurgery for eyelash ablation in trichiasis [19], retinopathy of prematurity [20], and retinal detachment. Retinal tear cryotherapy was first reported by Bietti in 1933, and by 1966, Bellowes had documented its use in cataract extraction, glaucoma, and tumor treatments [21].

Cryosurgery continues to expand into other fields, such as nephron-sparing kidney cancer treatment [22] and prostate cancer therapy [23]. This newer technique to kill the cancerous cells is being called cryoablation [24], which involves the use of extreme cold to destroy malignant tissue, and has shown promising results in the treatment of various cancers, including those of the liver, prostate, and kidney [25].

3.2. Introduction to Cryolipolysis

Cryolipolysis, commonly known as fat freezing, is a noninvasive procedure designed for targeted fat reduction. By exposing adipose tissue to controlled cooling, cryolipolysis triggers apoptosis in fat cells while preserving surrounding tissues. This selective fat cell breakdown leads to their gradual removal by macrophages, resulting in a noticeable reduction of the fat layer. As a nonsurgical alternative to liposuction, cryolipolysis offers an effective and accessible cosmetic solution [26].

This technique involves placing an applicator over an area containing unwanted subcutaneous fat. The applicator ranges in temperatures from 7 °C to -15 °C for 25 min to 60 min [27], as adipocytes are susceptible to these temperatures, whereas the surrounding tissues remain unaffected [28]. At these temperatures, a combination of fat apoptosis and necrosis occurs [29]. Apoptosis begins after 2 to 3 days, peaks at 2 weeks, and is completed approximately 3 months post-treatment with replacement of adipose tissue by fibrosis [30], [31].

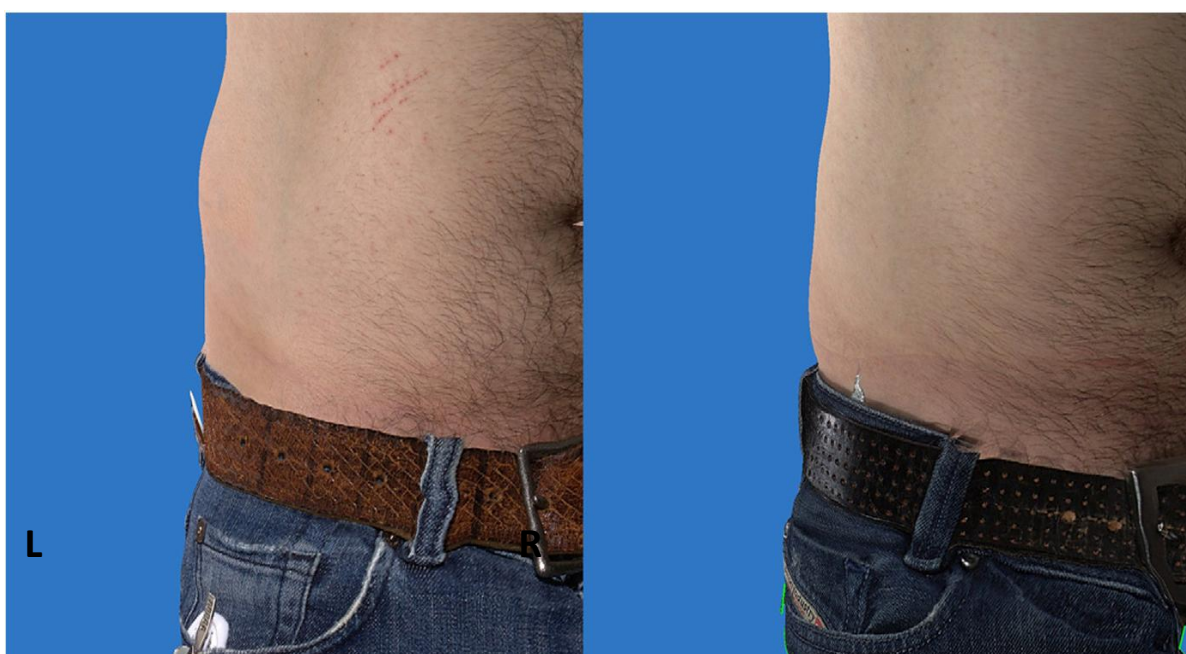


Figure 3.2. Representative clinical result before (L) and after (R) cryolipolysis. The patient underwent one treatment cycle to the right flank following the manufacturer's standard protocol. Results are shown two months post-treatment [30].

The most recent comprehensive survey data available is from 2019, which indicated that American Society for Dermatologic Surgery (ASDS) members performed over 1 million body sculpting procedures with a 60 % of growth, with cryolipolysis accounting for more than a quarter of these treatments with more than a 100 % increase. This indicates that cryolipolysis was the most popular non-invasive body contouring method at that time [32].

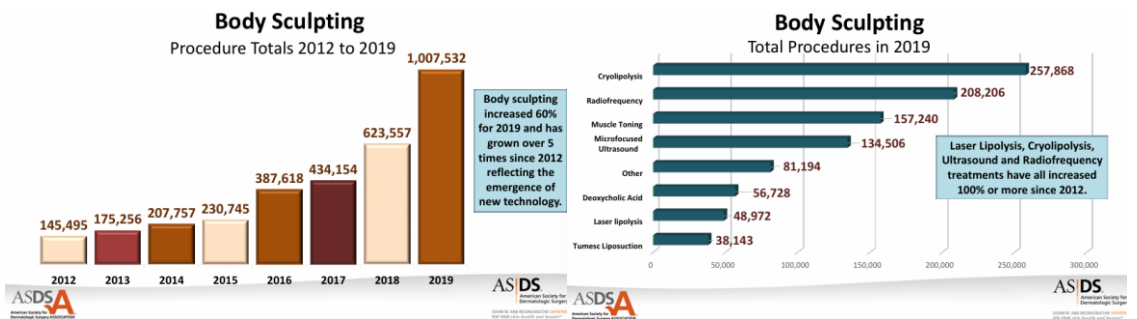


Figure 3.3. Survey data made by ASDS members, who performed over 1 million body sculpting in 2019 [32].

Furthermore, experts predict a 14.02 % compound annual growth rate by the year 2030 to meet the needs of millions of people seeking treatment [26]. This growth reflects the increasing popularity of nonsurgical options for fat reduction and body sculpting, as patients seek alternatives to traditional invasive surgeries. Cryolipolysis, with its ability to target and reduce localized adipose tissue, has emerged as a promising nonsurgical technique in the field of body contouring. It offers patients a valuable option for achieving their desired body shape without the need for a lengthy recovery period or major surgery. This is particularly appealing to individuals who may have concerns about the risks and complications associated with invasive procedures.

3.2.1. Cryolipolysis Development

Cold-induced adipose tissue damage has been documented since 1902, when Hochsinger reported firm subcutaneous nodules in children [33]. Later, in 1941, Haxthausen named the term “*adiponecrosis e frigore*,” establishing a link between cold exposure and fat necrosis [34]. Between 1940 and 1970, similar cases were described, including “popsicle panniculitis” by Epstein and Oren, which occurred in infants sucking on popsicles. These findings reinforced that lipid-rich tissues are more susceptible to cold than water-rich tissues [35], [36], [37], [38].

This susceptibility aligns with fundamental biochemistry: saturated fats solidify at room temperature, while unsaturated fats remain liquid. Young children's fat, which contains higher levels of palmitic and stearic acid, appears particularly prone to cold-induced lipotrophy, a phenomenon also confirmed in animal studies [39], [40].

Early investigations into cold-induced fat reduction were conducted using Yucatán pigs. In these studies, exposure to a 7 °C copper plate resulted in a measurable reduction of the fat layer within three

months. Ultrasound analysis confirmed a 30 % reduction, with minimal adverse effects [41], [42]. *In vitro* studies suggested that apoptosis is a key mechanism in fat loss, alongside reperfusion injury, inflammation, reactive oxygen species (ROS) production, and cell death [43]. Unlike heat-based treatments, which cause immediate necrosis, cryolipolysis triggers a delayed inflammatory response. By day 2 post-treatment, inflammatory infiltrates appear, progressing to lobular *panniculitis* within 2 to 4 weeks, Figure 3.4. This inflammatory process can persist for up to three months, during which macrophages remove apoptotic adipocytes, coinciding with clinical fat reduction.

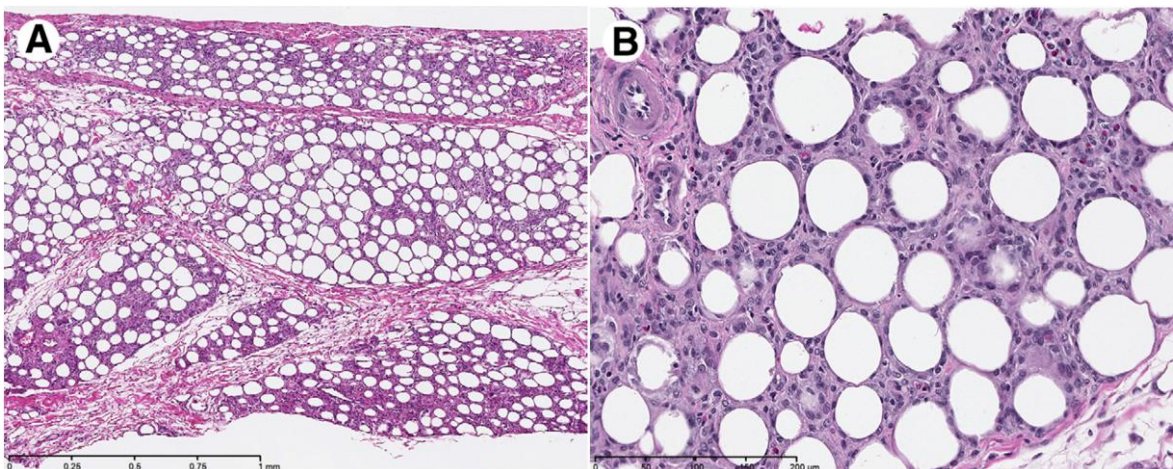


Figure 3.4. One week after localized cooling of porcine skin. Note the lobular panniculitis affecting the adipose tissue (A, 5X magnification). At higher magnification (B, 20X magnification), individual adipocytes are surrounded by a predominantly mononuclear cell infiltrate [30].

Afterward, in 2007, Manstein *et al.* introduced cryolipolysis, as method specifically designed to target fat cells at warmer temperatures [44].

Finally, on 2010 the first cryolipolysis device, ZELTIQ™ Dermal Cooling Device, received FDA clearance for treating the area of the flanks being classified as a class II medical device, (2010, K080521). In the following years, the use of the device on for the abdomen (K120023), thighs (K133212) and later for flexible treatment parameters (K142491) were FDA cleared [45]. Other devices like CoolSculpting® and CoolContour®, from Allergan Aesthetics™ were also cleared by the FDA for fat reduction in the following years [26], [46].

3.2.2. Side Effects of Cryolipolysis

Cryolipolysis is widely considered a safe procedure, with side effects generally mild and transient. The most frequently reported reactions include erythema (typically resolving within 72 hours), edema, bruising (ecchymosis), numbness, and minor skin changes. These are particularly common in patients on anticoagulant therapy. A temporary reduction in skin sensitivity occurs in most patients, usually resolving within one week, although mild residual effects may persist for up to two months. Notably,

no cases of permanent sensory loss have been reported. Furthermore, cryolipolysis has shown no impact on triglyceride levels or liver function [47], [48].

These observations are supported by a review of 53 studies involving 3,312 patients, which confirms erythema, numbness, bruising, and skin changes as the most prevalent side effects [49].

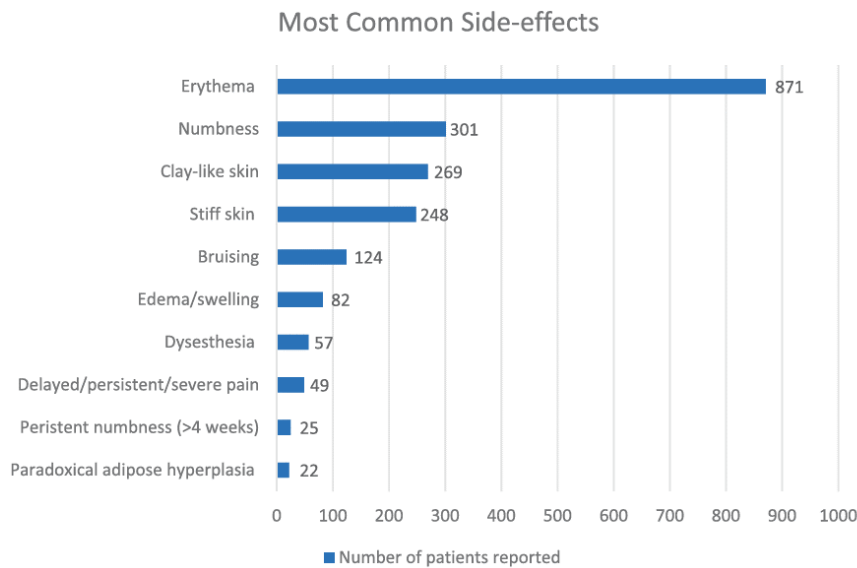


Figure 3.5. Number of patients affected by specific side effects after cryolipolysis treatment [48].

However, cold burns, previously considered an unlikely risk of cryolipolysis, have been reported [50], [51], [52]. Improper application of cryolipolysis, such as prolonged exposure, can lead to tissue freezing and crystallization, potentially resulting in adipocyte apoptosis in severe cases.



Figure 3.6. Skin erythema and blistering after cold treatment, resembling frostbite [53].

To improve safety, new techniques are being developed to minimize adverse effects. One such approach involves a system that integrates temperature and bioimpedance monitoring, allowing real-time detection of tissue freezing and enhancing patient protection against cold-induced burns [53].

Establishing a real-time sensing system capable of detecting potential clinical complications is crucial for ensuring safe cryolipolysis treatments. Such a system could automatically adjust the medical device's response to prevent tissue damage and improve patient outcomes.

3.3. Freezing Events Monitoring

Historically, tissue freezing detection has been classified into local and global monitoring approaches. Local monitoring relies on direct invasive measurements using thermometry or impedancemetry, where sensors such as thermocouples, thermistors, or voltage-measuring electrodes are placed within or around the treated tissue. These sensors assess the extent of freezing by measuring temperature or electrical resistance. However, local monitoring presents limitations, including the need for additional sensors beyond the cryosurgery probe and the restriction of data collection to the immediate vicinity of the measurement site, potentially leading to inadequate or excessive freezing [54].

In contrast, global monitoring has significantly advanced with the development of tomographic imaging modalities, such as X-ray computed tomography (CT), ultrasound (US), and magnetic resonance imaging (MRI) [55]. These imaging techniques offer notable advantages over local monitoring by providing high spatial resolution and capturing comprehensive information across the entire affected region. This enables more precise and real-time assessment of the freezing process, improving procedural outcomes [54].

Freezing can also be detected through direct or indirect methods. Direct detection involves measuring physical parameters such as mass, reflective properties, electrical or thermal conductivity, dielectric constant, and inductance. Indirect detection, on the other hand, relies on identifying conditions favorable to freezing, such as temperature and humidity, or observing its effects [56]. Models used for freezing detection can be either empirical or deterministic. While numerous frost detection techniques exist, this application primarily focuses on methods based on temperature variations, capacitive sensing, and impedance measurements, which are effective in assessing tissue freezing with high sensitivity [57].

3.3.1. Direct Freezing Monitoring - Temperature Sensors

Thermometry is based on direct measurements of temperature at discrete points in tissue with thermocouples or thermistors placed inside (i.e. needles, Figure 3.7) or around the undesirable tissue that is being frozen. This type of local monitoring has been used since 1970, where the use of thermometry during cryosurgery had become routine [58].



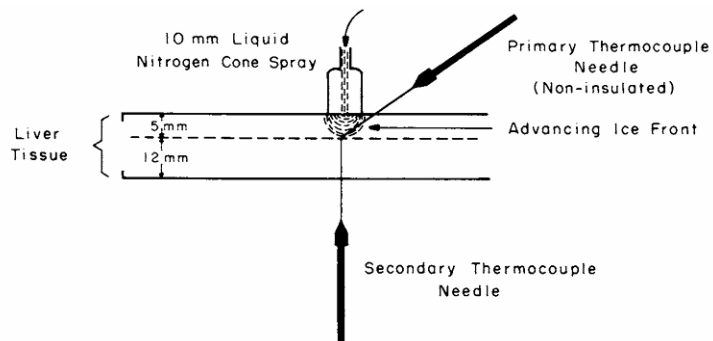


Figure 3.7. Schematic of freezing tissue with simultaneous temperature monitoring of the evolving ice front by means of two thermocouple needles [59].

Figure 3.8 illustrates the skin temperature profile and its behavior during these treatments, which demonstrates that the initial temperature is at room temperature before cold is applied to the skin. Over time, the temperature decreases, and after 2 minutes of cold application, the skin reaches a freezing point of approximately -22°C . Subsequently, 4 minutes after freezing, the temperature is observed to rise slightly above 0°C [60].

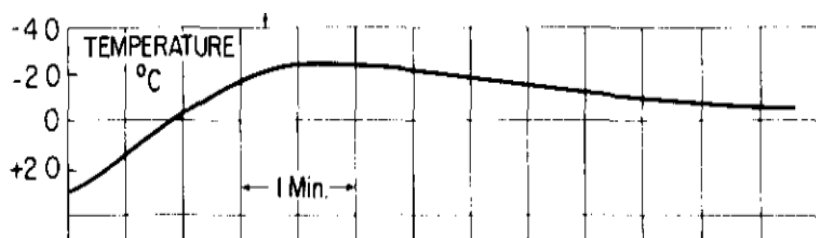


Figure 3.8. Temperature profile ($^{\circ}\text{C}$) with respect to time (min) from an ambient temperature value and freezing the area. It is observed that freezing occurs above -22°C [60].

At the beginning of the century, freezing temperature curve-based monitoring was proposed as a way to rapidly characterize the properties of a material, and this technique it has been since implemented as an important tool in bioanalytical fields [61]. However, additional effort is still needed to reduce the noise inherent in the measurement in order to improve the repeatability of the freezing curve [62].

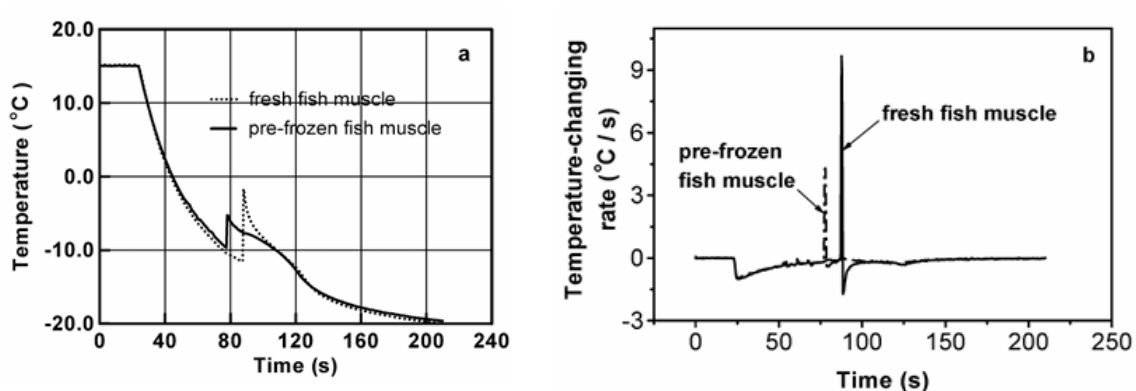


Figure 3.9.a) Time-dependent (s) freezing curves ($^{\circ}\text{C}$) for fish muscle pre-frozen in LN_2 slowly thawed in air and for fresh fish muscle. **b)** Rate of temperature ($^{\circ}\text{C}/\text{s}$) change for the freezing curves. Adapted from [62].

Due to advancements in freezing detection through temperature measurement, companies like Allergan, which absorbed ZELTIQ™, have developed patented systems approved by the FDA [63], establishing themselves as pioneers and market leaders in the field of cryolipolysis. However, systems using this approach still exhibit a common limitation. Despite the use of thermocouple matrices, these do not cover the entire area of interest for freezing, leading to the possibility of undetected or delayed detection of tissue freezing in regions farther from the thermocouples [59]. This means that excessive freezing can still occur elsewhere in the treated area.

Furthermore, new research is being conducted to improve sensor materials, enhancing their speed and sensitivity. Additionally, innovative imaging processing techniques, materials and sensors using NIR, UV, and US technologies are being explored [64], [65], [66]. Although these methods are still costly and not real-time, they open new possibilities for more precise and efficient freezing detection and monitoring, especially focused on solving the issue of localizing the area where the ice formation occurs.

3.3.2. Indirect Freezing Monitoring - Bioimpedance Sensors

Traditional monitoring of malignant tumors using thermocouple needles remains valuable but has significant limitations, mainly delay and undetected freezing opportunities due to the position of the sensor, as already explained in Section 3.3.1.

To address this, alternative methods have been developed that detect electrical current flow or its cessation (resistance) to indicate effective cryonecrosis in real time.

Damage to biological material due to freezing or heating can cause significant deviations in its electrical impedance compared to that of undamaged tissue. Monitoring changes in impedance ratios under various freezing and heating conditions offers a valuable strategy for assessing the extent of damage sustained by biomaterials during procedures such as cryosurgery, cryopreservation, and hyperthermia [62]. Numerous studies have demonstrated that skin impedance varies with temperature, as illustrated in Figure 3.10. Furthermore, it can be seen that the impedance increases as the temperature approaches the freezing point. Upon reaching the freezing temperature, the impedance, which had risen more than $10 \text{ M}\Omega$, drops sharply to $0.1 \text{ M}\Omega$. This observation suggests that, as a potential future enhancement, freezing events could be detected based on impedance changes rather than temperature alone [67].

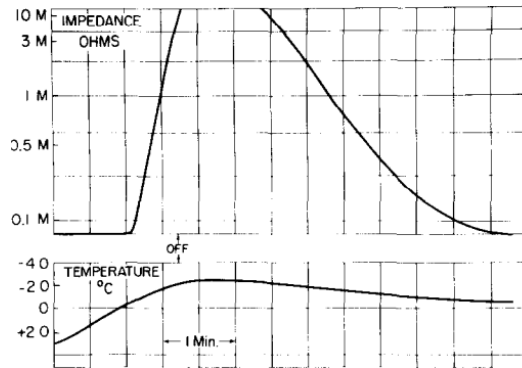


Figure 3.10. Impedance profile (upper, Ω) and temperature (lower, $^{\circ}\text{C}$) as a function of time (min). Measurements are recorded from ambient temperature down to the freezing temperature of the area. It is observed that freezing occurs at temperatures above $-22\text{ }^{\circ}\text{C}$ [60].

According to [68], impedance decreases from the onset of freezing through to the end of thawing. The results show that during the thawing process, impedance decreases rapidly with increasing temperature, both during thawing and once above the freezing point. The rate of impedance change as the temperature approaches the freezing point is illustrated in Figure 3.11 and Figure 3.12.

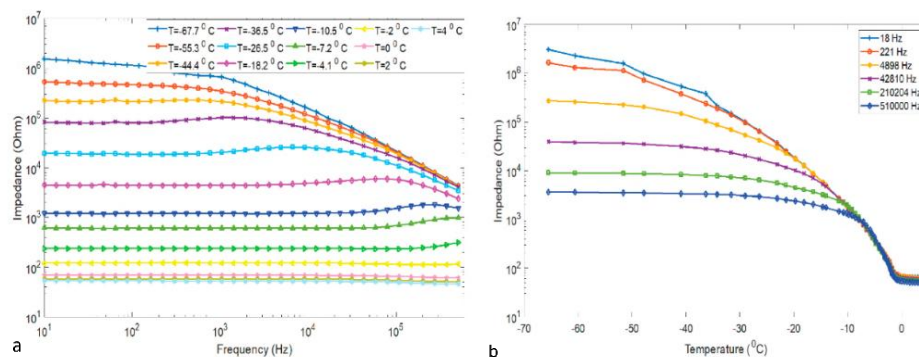


Figure 3.11. a) Typical plots showing the impedance (Ω) as a function of f (Hz) of meat throughout the thawing process for different temperatures. b) Typical plots of impedance (Ω) as a function of temperature ($^{\circ}\text{C}$) for six selected frequencies. The impedance was taken during the rapid thawing process of pork muscle [68].

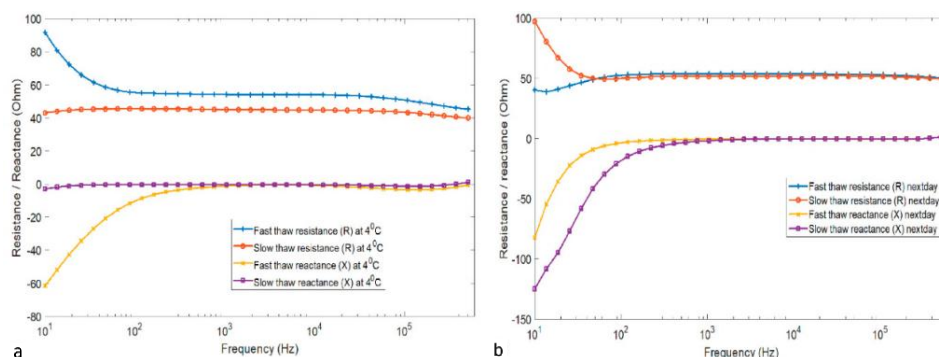


Figure 3.12. a) Impedance components resistance (R) and reactance (X) of pork meat tissue at $4\text{ }^{\circ}\text{C}$ after freezing and thawing, and the b) $R(f)$ and $X(f)$ curves of slow thawed and fast thawed pork meat tissue. Each line in both figures represent the mean impedance of ten meat samples [68].

These techniques not only improve accuracy but also allow simultaneous monitoring of up to five focal areas within a lesion, overcoming the single-point measurement constraint of thermocouples [59].

In 1977, electrical current measurement devices such as Savic-Zacarian's Freeze Depth Indicator® and Torre's EZEE Cryometer® were introduced for experimental use. These devices used pre-marked vertical or curved needles to measure temperature at multiple tissue points. However, they only allowed the operator to correlate specific resistance values with fixed temperature ranges (e.g., 1 MΩ, 2 MΩ, and 5 MΩ corresponding to -3 °C, -4 °C, and -50 °C, respectively) [69].

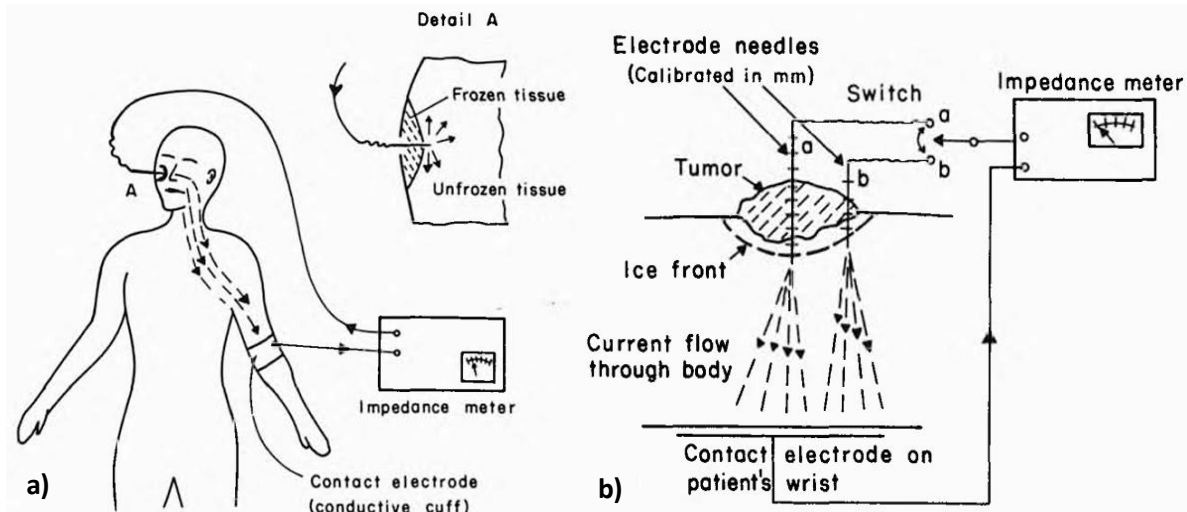


Figure 3.13. Freeze Depth Indicator®, an impedance-based method for controlled cryosurgery of malignant tumors developed by M. Savic and S. A. Zacarian [70]. **a)** Schematic representation of current flow using a single-needle electrode configuration. **b)** Illustration of the dual-needle electrode setup: electrode (a) is inserted centrally and beneath the tumor, while electrode (b) is positioned at the tumor margin. Each electrode independently monitors tissue impedance at its respective location to assess freezing depth. Both electrodes are millimeter-calibrated to allow precise determination of frozen tissue depth [70].

Although significant progress has been made in cryosurgical monitoring through bioimpedance techniques, current cryolipolysis systems do not implement real-time bioimpedance monitoring to assess tissue changes during treatment. For example, devices such as the CRISTAL® system by DELEO™ launched in 2014 [71] and the Cooltech Define® by Sinclair™ [72] focus primarily on precise temperature control and applicator ergonomics, without integrating bioimpedance sensors for intra-procedural feedback. This presents a clear opportunity for future technological developments in cryolipolysis, where incorporating bioimpedance-based monitoring could enhance treatment accuracy, safety, and efficacy.

3.4. A Novel Approach for Tissue Freezing Detection – Capacitive Sensor

Capacitive sensors provide a reliable, non-invasive method for frost and freezing detection, demonstrating high sensitivity to even minimal frost accumulation during the early stages of icing [73], [74]. These sensors are renowned for their simplicity and reliability, even in extreme environments [75], [76].

Capacitive sensing relies on the modulation of the electric field established between two electrodes by the presence of a dielectric medium. The resulting dielectric displacement alters the charge storage between the electrodes, thereby modifying the overall capacitance of the system. This variation enables characterization of material properties such as permittivity, conductivity, and their spatial distribution [77].

When a dielectric material is subjected to an electric field, polarization occurs through mechanisms that depend on the nature of the material and the frequency of excitation. These mechanisms include electronic, atomic, dipolar, and space charge polarization, each contributing an individual susceptibility component [78]. The total electric susceptibility χ_e is the sum of the individual susceptibilities of the various polarization mechanisms:

$$\chi_e = \chi_{el} + \chi_{atom} + \chi_{dip} + \chi_{sc} \quad (\text{Eq. 3.1})$$

A material's dielectric behavior is characterized by its relative permittivity ε_r , which depends on external factors such as pressure, temperature, and excitation frequency. The dielectric displacement \mathbf{D} is expressed as:

$$\mathbf{D} = \varepsilon_0 \varepsilon_r \mathbf{E} = \varepsilon_0 \mathbf{E} + \mathbf{P} \quad (\text{Eq. 3.2})$$

Where ε_0 is the vacuum permittivity, \mathbf{E} is the electric field, and \mathbf{P} is the polarization vector. The relative permittivity ε_r can also be related to the electric susceptibility:

$$\varepsilon_r = 1 + \frac{\mathbf{P}}{\varepsilon_0 \mathbf{E}} = 1 + \chi_e \quad (\text{Eq. 3.3})$$

Hence relative permittivity can be understood as a complex quantity, where the real part, ε_r' , is the dielectric constant, and the imaginary part, ε_r'' , corresponds to the dielectric losses.

$$\varepsilon_r = \varepsilon_r' + j\varepsilon_r'' \quad (\text{Eq. 3.4})$$

As seen in Figure 3.14, each polarization mechanism exhibits a characteristic frequency response [78]. Electronic and atomic polarizations typically exhibit resonant behavior with distinct overshoot at resonance frequencies. In contrast, dipolar and space charge polarizations are governed by relaxation dynamics involving the physical reorientation of dipoles.

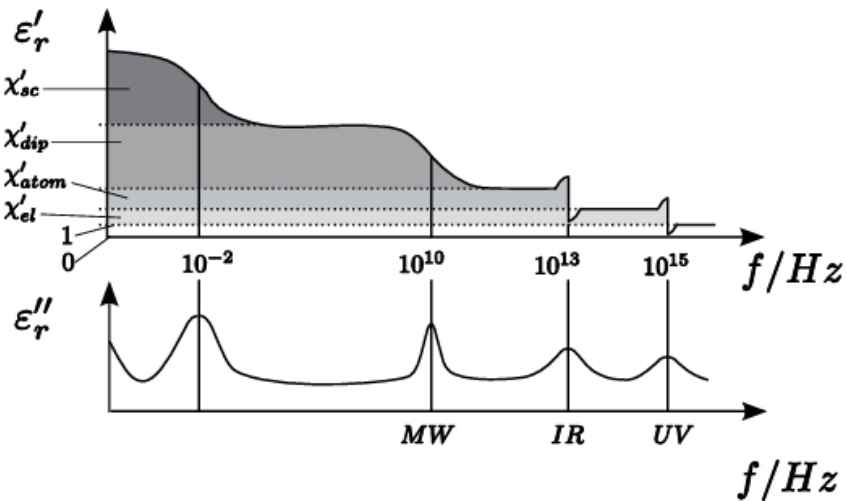


Figure 3.14. Frequency response (Hz) of polarization mechanisms of water [78].

Dipolar polarization is particularly significant in water due to its strong permanent dipole moment. Alignment of water molecules with the applied electric field is opposed by thermal (i.e. Brownian) motion, and their dynamic balance determines the net polarization. As seen in Figure 3.14 characteristic cutoff frequency for dipolar relaxation in water is on the order of 10^9 Hz.

Notably, as seen in Figure 3.15, water and ice show different dielectric behaviors in the 10 kHz to 100 kHz frequency range. At 0 °C, the dipolar relaxation frequency f_D of unfrozen water is approximately 10 GHz, while for ice, it decreases significantly to ca. 3 kHz [14]. This shift is a result of the Debye relaxation process, where the real part of permittivity $\epsilon_r'(f)$ decreases and the imaginary part $\epsilon_r''(f)$ has a peak near f_D .

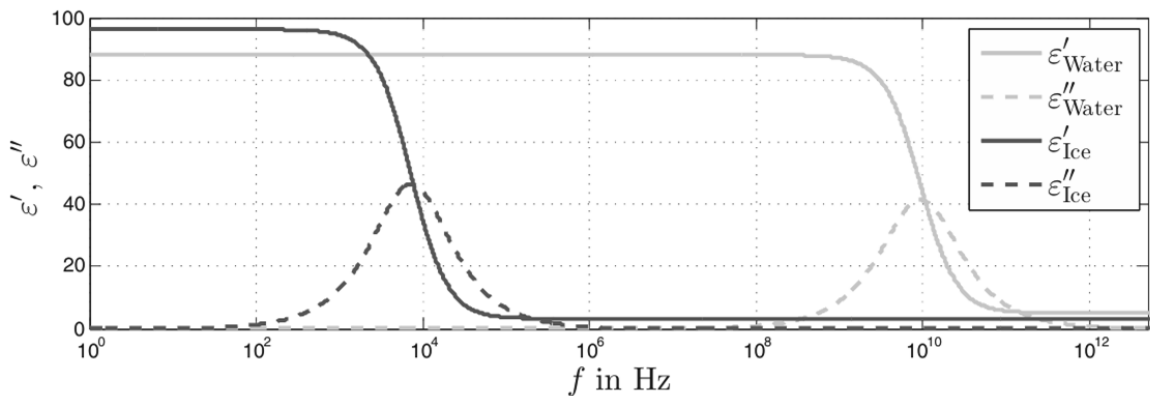


Figure 3.15. Dielectric spectra (Hz) of ice (dark grey) and water (light grey) at 0 °C [79].

Furthermore, the dielectric constant of water is primarily governed by its dipolar polarization. The strong polarity of H₂O molecules, resulting from the high electronegativity of oxygen, leads to the formation of distinct positive and negative charge centers, although the molecule remains electrically neutral overall.

Upon freezing, water crystallizes into a hexagonal lattice structure that restricts molecular rotation, effectively immobilizing dipoles and suppressing their ability to respond to external fields [80]. Consequently, the relative permittivity of ice is significantly reduced. At 0 °C and a measurement frequency of 10⁵ Hz, the relative permittivity of liquid water is $\epsilon'_r \approx 80$, whereas for ice at -10 °C, it is $\epsilon'_r \approx 4.2$, Figure 3.16 [80]. This significant contrast in dielectric properties enables the capacitive detection of ice formation by monitoring frequency-dependent changes in sensor capacitance.

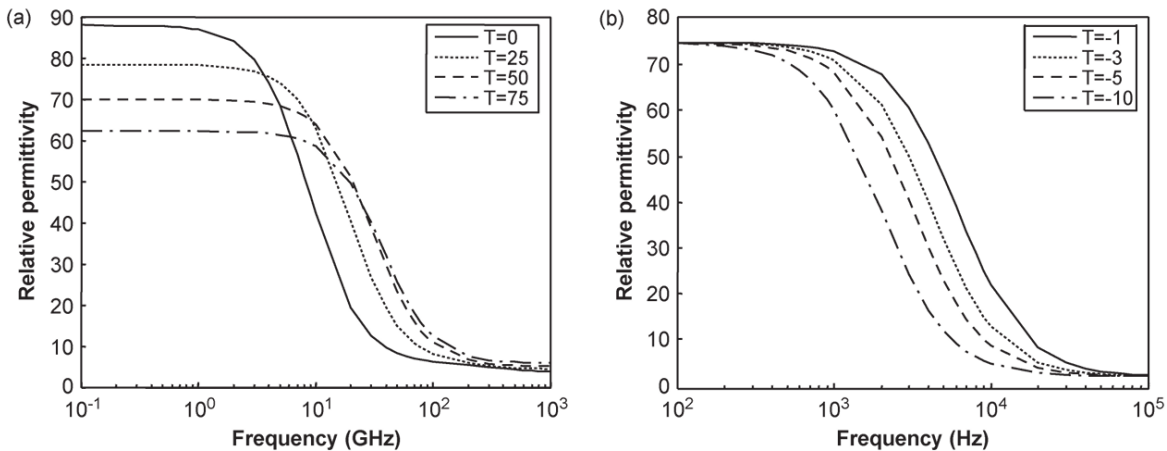


Figure 3.16. Comparison between ϵ'_r of water (a) and ice (b) as a function of f (Hz) and T (°C) [80].

The dielectric properties of ice are also temperature dependent. As the temperature decreases the dielectric trends of ice shift towards lower frequencies. Additionally, lower temperatures lead to an increase in permittivity and a decrease in conductivity [79]. Moreover, as illustrated by the trends Figure 3.17, a distinct change in the dielectric properties of the material is evident in the frequency range around 1 kHz to 10 kHz, especially during the transition from water to ice. This observation suggests that utilizing this frequency range could enhance ice detection via temperature changes [79].

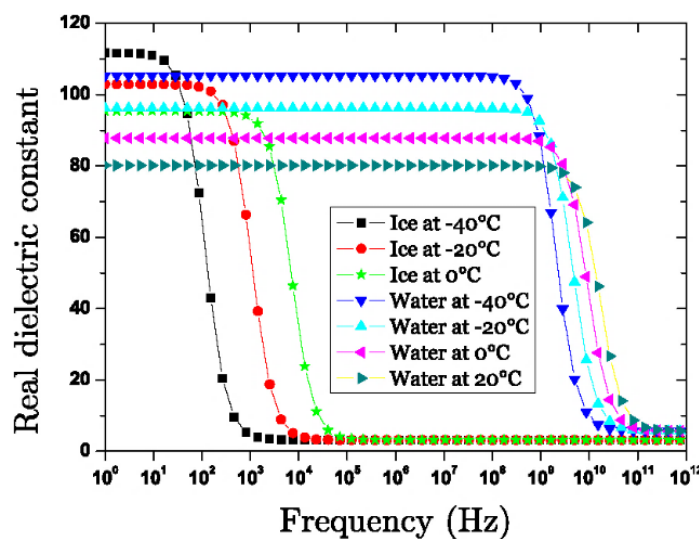


Figure 3.17. Frequency (Hz) dispersion of water and ice real dielectric constants at different temperatures [81].

Furthermore, researchers at *Politecnico di Torino* developed a concentric conductive electrode capacitive sensor specifically designed to differentiate between liquid water and ice by leveraging their distinct dielectric properties. As illustrated in Figure 3.1 [80], measurements performed at higher excitation frequencies, *ca.* 10⁷ Hz, demonstrated a significantly greater contrast in capacitance between the two phases, accompanied by a notably smaller standard deviation. This indicates not only improved sensitivity but also enhanced measurement stability at higher frequencies. Nevertheless, even at lower frequencies, such as 200 Hz, the sensor still exhibited a measurable difference in capacitance between the water and ice states, confirming the viability of capacitive detection across a broad frequency spectrum.

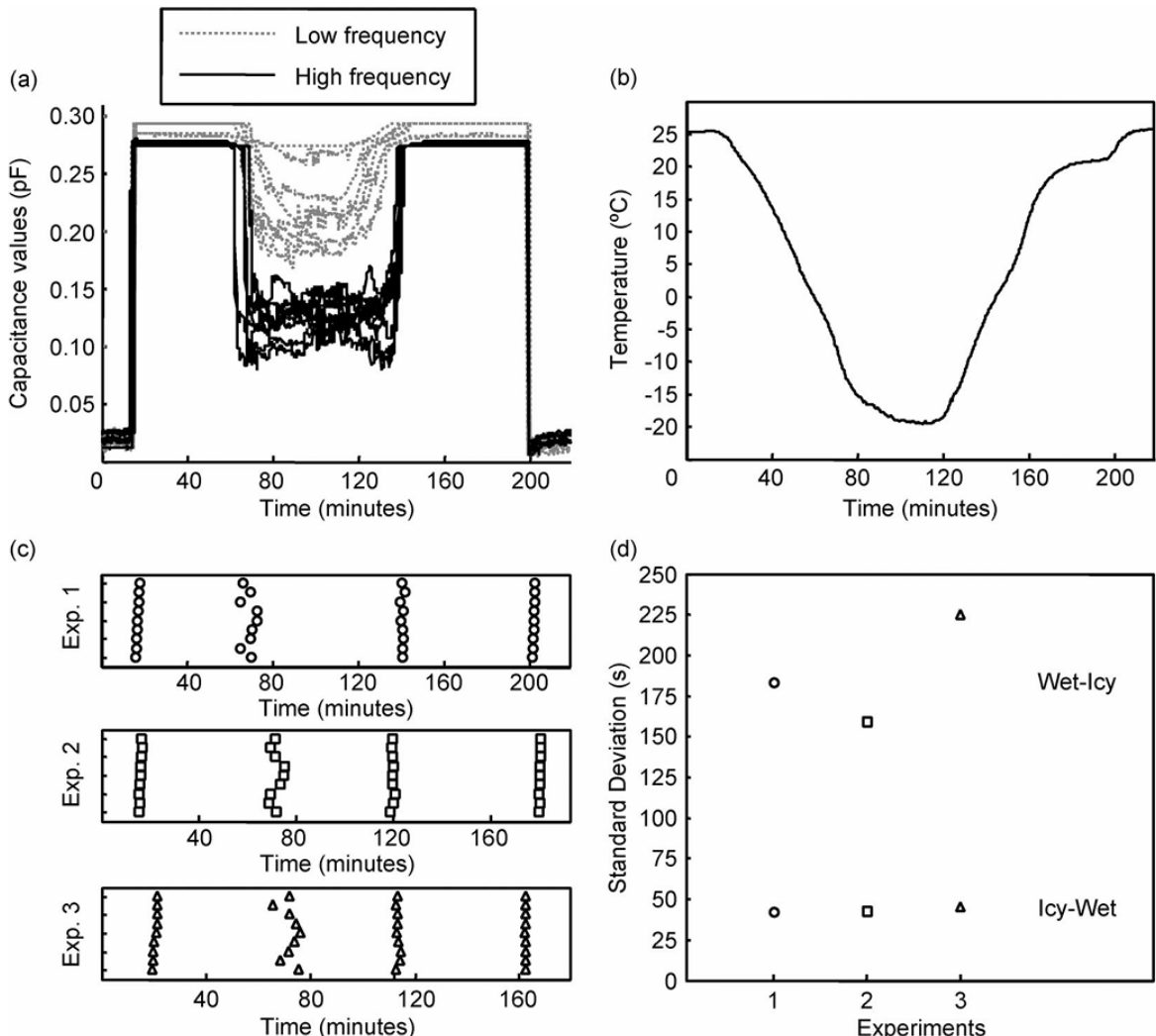


Figure 3.18. Statistical analysis of the laboratory data. **a)** Values of capacitance (raw data) obtained for each sensor during the first experiment. **b)** Internal temperature of the climatic chamber during the first experiment with the indication of the state condition detected by a sensor. **c)** Time (min) instants of state transitions estimated for each sensor during three different experiments. **d)** Standard deviations of time instants (s) of wet-icy and icy-wet state transitions estimated for each sensor during three different experiments [80].

Other successful implementations include the capacitive sensor designed by Zhi *et al.*[82], for detecting ice formation on fuel pipe surfaces, as well as Texas Instruments' (TI) solution for monitoring ice buildup, which demonstrates the practical application of capacitive sensing in safety-critical environments [83].

4. Materials

This section details the materials and methods employed in the research, providing a comprehensive description to ensure that the study can be precisely replicated.

4.1. Freezing Platform

In order to induce freezing in the samples a personalized freezing platform was designed, Figure 4.1. This platform allowed us to freeze samples up to -10 °C using TEC, a heat sink, and a microcontroller.

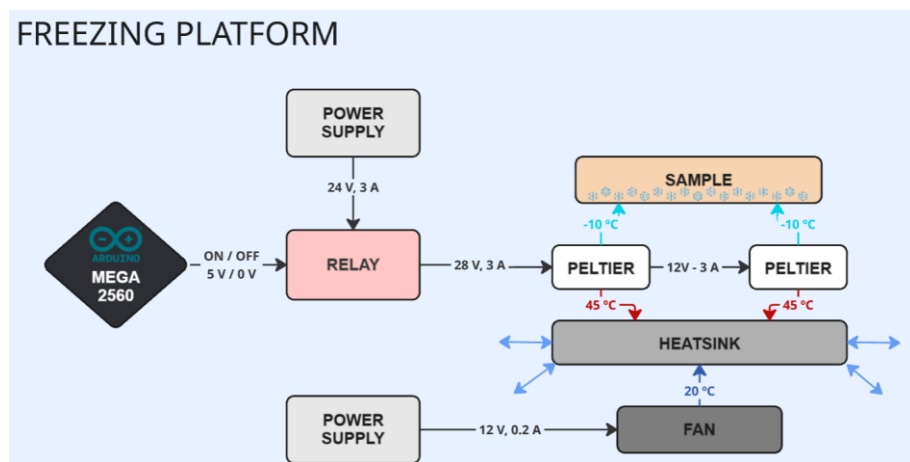


Figure 4.1. Block diagram of the freezing platform. Author's own work.

4.1.1. Microcontroller

To control the freezing process, a microcontroller was required. While alternative, more simple microcontrollers could have been selected for this specific task, the Arduino MEGA 2560 was chosen due to its availability. It is designed around the ATmega2560 microcontroller, featuring 256 KB of flash memory, 8 KB of SRAM, and 54 digital I/O pins (15 of which support PWM). Its compatibility with numerous sensor libraries and its robust serial communication capabilities further justified its use.

4.1.2. Power supply

To power both the heat sink and the Peltier cells, dedicated power supplies were required for each component, as detailed in Annex 0. Given that the TEC is working at a voltage of 28 V and a current of 3 A, the Promax FA-665 power supply was employed for this purpose. This unit, provided by the EEBE-UPC, features two independent and floating outputs configurable from 0 to 30 V and up to 5 A each, as well as an auxiliary fixed output of 5 V at 1 A. The device also includes current and thermal protection systems, and a 3½-digit digital display for precise monitoring [84].

4.1.3. Peltier Cells

To achieve controlled freezing and thawing of the samples, Peltier cells were selected for their capacity to generate temperature gradients via the Peltier effect. Specifically, TEC1-12706 thermoelectric modules were chosen due to their reliable performance and suitability for this application. These modules operate at a maximum voltage of 15.4 V and a maximum current of 6 A, delivering a rated cooling power of approximately 60 W [85].

In this design¹, two TEC1-12706 modules are connected in series and powered by a 28 V, 3 A source, in accordance with manufacturer recommendations. A Thermoelectric Cooler (TEC) is a solid-state device that functions based on the Peltier effect, discovered by Jean Charles Athanase Peltier in 1834, which describes the heating or cooling generated when an electric current flows through the junction of two different conductors. TECs typically use bismuth telluride semiconductors arranged in alternating N-type and P-type pairs, as illustrated in Figure 4.2.

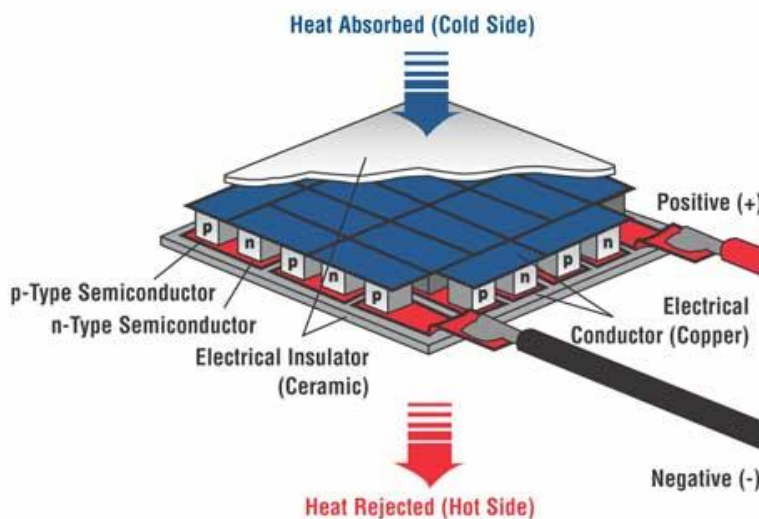


Figure 4.2. Schema of how a Peltier cell or TEC (Thermoelectric Cooler) works [86].

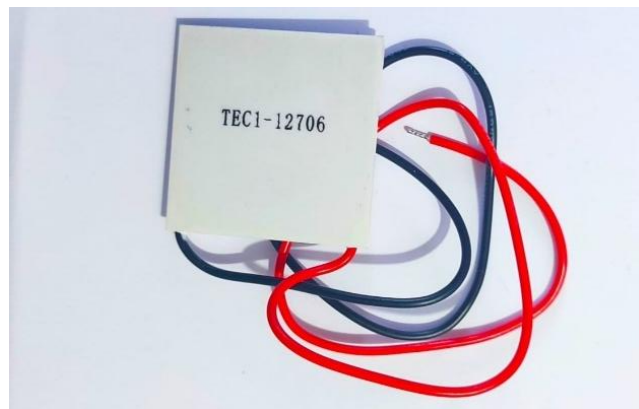


Figure 4.3. TEC1-12706 cells used in this thesis. Author's own photograph.

4.1.4. Relay module

To regulate the power delivered to the Peltier cells, a relay module capable of switching high-current and high-voltage DC loads was necessary. The module selected for this application was required to support at least 30 V and 6 A in DC operation. The chosen module integrates a PC814 optocoupler and a 2TY transistor driver, enabling secure and reliable switching through galvanic isolation between the low-voltage control circuit and the high-power load. The relay itself, a JQC-3FF-S-Z, is actuated by a 5 V DC control signal and features contact ratings of 10 A at 250 V AC, 15 A at 125 V AC, and 10 A at 30 V DC. These characteristics ensure a sufficient safety margin relative to the operational requirements of the Peltier modules, making this relay configuration a robust and suitable choice for the system's thermal management circuitry, [87].

4.1.5. Heat sink

To ensure proper operation of the TEC1-12706 Peltier modules, a heat sink is required to dissipate the heat generated on the hot side of the cells. Without sufficient heat dissipation, the temperature gradient necessary for freezing cannot be maintained. For this purpose, the FAN478 heat sink from StarTech was selected [88]. This component offers an efficient thermal pathway, allowing heat to be transferred away from the Peltier modules and into the surrounding environment, especially when used in combination with forced convection from a fan.



Figure 4.4. FAN478 fan and heat sink used in this thesis [88].

4.1.6. Thermal Paste

In order to accomplish a good thermal contact between the heatsink and the Peltier cells, the SYY-157 silicon based thermal paste was used. This thermal paste has a thermal conductivity of $R_{th} = 15.7 \text{ W/mK}$ with an operating temperature range from -50 °C to 200 °C.

4.2. Data Collection Framework

Once the freezing platform is built, a data acquisition system must be developed to enable effective monitoring. It is therefore essential to clearly define the function of each component within the detection system and to establish suitable communication protocols. Figure 4.5 illustrates a block diagram of the experimental platform, highlighting the interaction between the capacitive sensor, signal conditioning unit, data acquisition module, and software interface. This structured architecture ensures consistent data collection and supports thorough analysis.

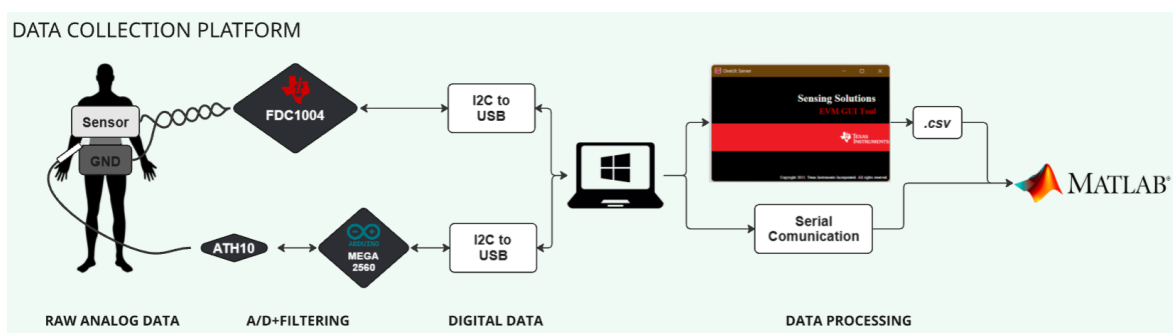


Figure 4.5. Block diagram of the experimental platform used for real-time acquisition of data in freezing events.
Author's own work.

As depicted in Figure 4.5, temperature and capacitance measurements are acquired and processed in parallel:

- The Arduino Mega 2560 captures data from the ATH10 sensor¹, which is directly transmitted to the MATLAB GUI² via serial communication.
- The FDC1004EVM processes capacitance measurements but requires an additional step:
 - o The raw data is first processed by the Sensing Solutions EVM GUI.
 - o It is then exported as a .csv file before being imported into the MATLAB GUI for further analysis.

This workflow enables real-time visualization of temperature and capacitive values, as illustrated in Figure 4.6. Additionally, at the end of the process, a comprehensive dataset of all recorded values is displayed in Figure 4.7, facilitating in-depth analysis of freezing events.

¹ To see the Arduino code, visit Anex B1.

² To see the MATLAB code of the GUI, visit Anex B2.

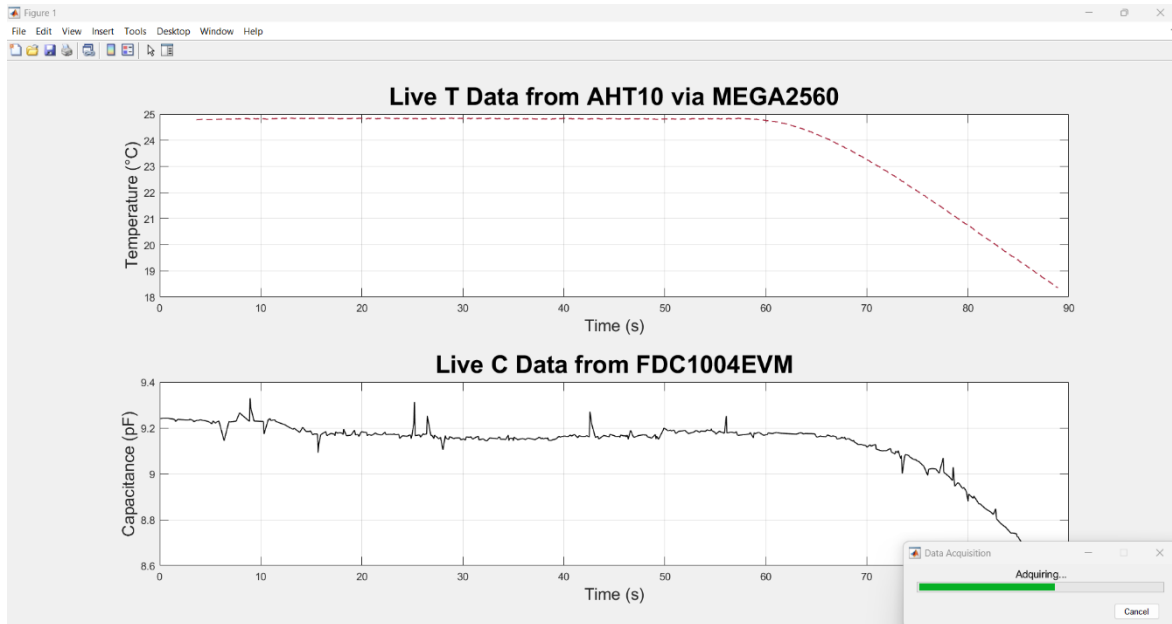


Figure 4.6. MATLAB GUI for real time (s) temperature (upper graph, °C) and capacitance (lower graph, pF) monitoring. Author's own work.

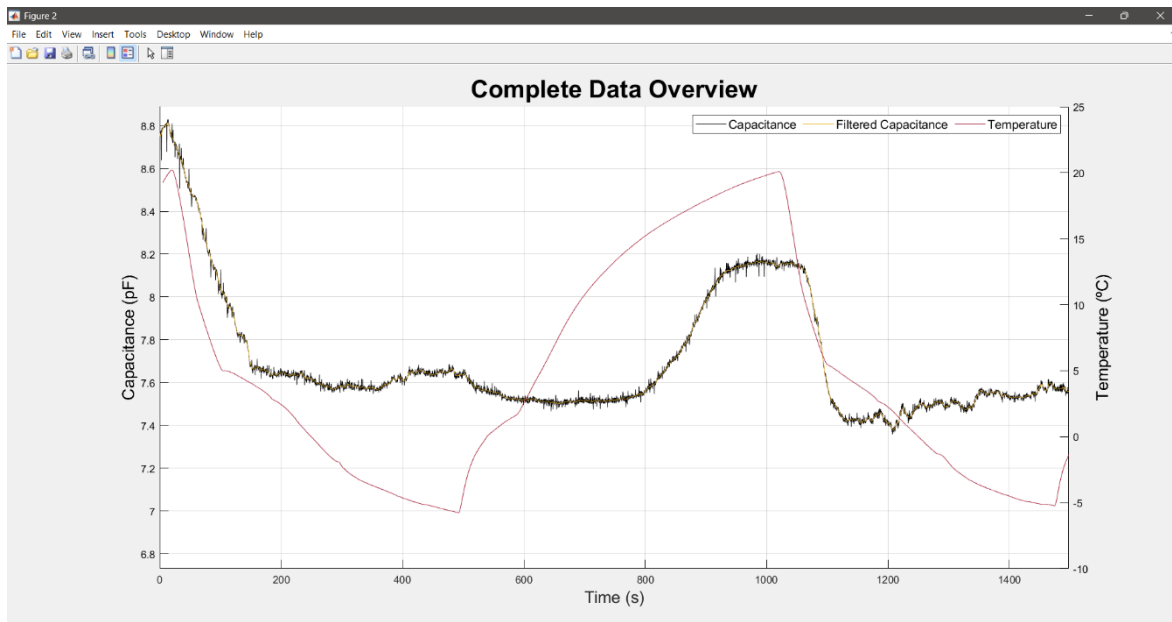


Figure 4.7. Full data representation in a MATLAB plot, given at the end of the procedure by the MATLAB GUI. Author's own work.

4.2.1. The Temperature Sensor – Gold Standard

To reliably monitor the temperature cycles in the experiment and have a reference for freezing and thawing events, a temperature sensor was required with a minimum resolution of 0.5 °C, an accuracy of ± 0.3 °C, and the ability to withstand repeated temperatures as low as -10 °C and high humidity conditions. Additionally, it needed to support real-time data transmission via a compatible communication interface. The AHT10 module was selected for fulfilling all these criteria [89], [90]. It operates with a supply voltage of 3.3 V to 5 V, communicates via the I2C protocol, and withstands temperatures up to -40 °C with an accuracy of ± 0.3 °C.



Figure 4.8. Temperature AHT10 module used in this thesis [90].

4.2.2. The Capacitive Sensor – Custom Design

To measure the capacitance of the samples, a capacitive sensor was designed using two parallel copper plates separated by 1 cm, as it can be seen Figure 4.9. This configuration enables capacitance measurement over a large surface area, avoiding the drawbacks of quantization of electron noise, current noise and ensuring a stable and uniform electric field distribution, improving the accuracy of capacitance measurements.

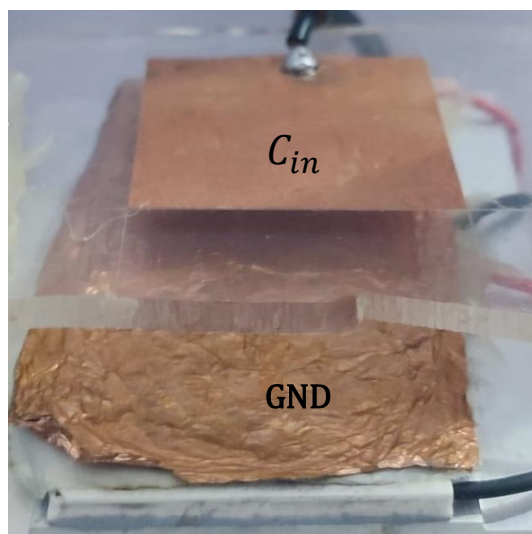


Figure 4.9. Parallel plate capacitor made of copper tapes glued on methacrylate. Author's own work.

4.2.2.1. Design of the Capacitive Sensing

Capacitive sensing relies on the principle of capacitive coupling. Fundamentally, a capacitive sensor comprises any metallic or conductive element capable of detecting objects whose conductivity or dielectric constant differs from that of air. In practical implementations, sensor designs typically involve charge displacement across partially conductive surfaces under the influence of an AC potential source.

For an accurate analysis of the electric fields and currents within a capacitive sensor, Maxwell-Heaviside equations should ideally be applied. However, when the system's time constants are much shorter than the circuit's overall response time, magnetic field effects become negligible. In such cases, a simplified electroquasistatic approximation can be employed without significant loss of accuracy. This approximation reduces Maxwell's equations to a form where only the electric field \mathbf{E} is considered, assuming that the magnetic field strength \mathbf{H} is negligible [77]. The simplified governing equations are Gauss' law (Eq. 4.1), Gaus' law for magnetism (Eq. 4.2), Faraday's law (Eq. 4.3) and Ampère-Maxwell law (Eq. 4.4).

$$\nabla \cdot \mathbf{E} = \frac{\rho}{\epsilon_0} \quad (\text{Eq. 4.1})$$

$$\nabla \cdot \mathbf{B} = 0 \quad (\text{Eq. 4.2})$$

$$\nabla \times \mathbf{E} = -\frac{\partial \mathbf{B}}{\partial t} = -\mu_0 \frac{\partial \mathbf{H}}{\partial t} \approx 0 \quad (\text{Eq. 4.3})$$

$$\nabla \times \mathbf{B} = \mu_0 (\mathbf{J} + \frac{\partial}{\partial t} \epsilon_0 \mathbf{E}) \approx 0 \quad (\text{Eq. 4.4})$$

where the magnetic flux definition in the vacuum was applied, (Eq. 4.5).

$$\mathbf{B} = \mu_0 \mathbf{H} \quad (\text{Eq. 4.5})$$

Within this framework, a given charge density distribution ρ generates an electric field \mathbf{E} , while variations in \mathbf{H} are negligible for the analysis. The physical constants in these expressions include the vacuum permeability, μ_0 (defined in SI units as $4\pi \times 10^{-7}$ N/A²), and the vacuum permittivity, ϵ_0 , which is related to μ_0 and the speed of light c by:

$$\epsilon_0 = \frac{1}{\mu_0 c^2} \quad (\text{Eq. 4.6})$$

Given that c is defined as 299,792,458 m/s, the resulting value of ϵ_0 is approximately 8.8542×10^{-12} F/m. The dielectric material inserted between the sensor electrodes has a permittivity greater than that of vacuum, expressed by the relative dielectric constant ϵ_r . For many dry solid materials, ϵ_r typically ranges between 2 and 10, while liquids often exhibit significantly higher values.

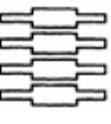
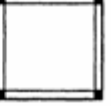
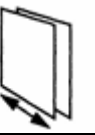
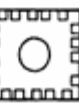


With these simplifications, the problem of capacitive sensing reduces to determining the electric field arising from specific charge distributions in materials with varying dielectric properties. Many capacitive sensors implement plate geometries for which common applications include:

- Material property detection: Measuring dielectric properties.
- Displacement sensing: Detecting change by varying plate separation or overlapping area.
- Proximity detection: Identifying conductive or dielectric objects nearby.

The classic parallel-plate configuration is particularly useful for material characterization and motion measurement, Table 4.1, where changes in d or overlapping area alter capacitance.

Table 4.1 Two plate electrode configurations and its applications, extracted and later modified from [77].

Application	Plate geometry	Application	Plate geometry
Material properties		Motion detect analog/digital	
Micrometer high sensitivity		Motion detect 2-axis	
Micrometer small movement		Proximity detector	
Motion detect large movement		Silicon sensors	

More complex electrode geometries are designed to optimize linearity and range in motion sensing applications as shown in Figure 4.10. Underlap/overlap two and three-plate bridge configurations, extracted and modified from [77].

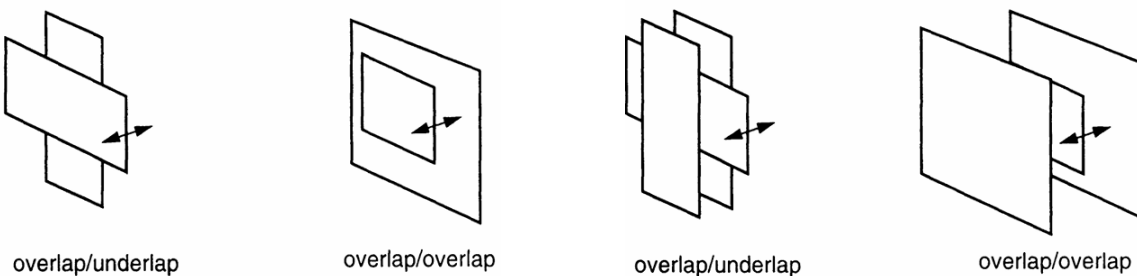


Figure 4.10. Underlap/overlap two and three-plate bridge configurations, extracted and modified from [77].

For the intended application, analyzing the permittivity of water as a function of temperature, the most suitable configuration is a parallel-plate capacitor.

In an ideal charged parallel-plate capacitor, each plate carries an equal but opposite charge uniformly distributed over its surface. As a result, the electric field is established from the plate at the higher potential to the plate at the lower potential. This analysis assumes a uniform electric field and neglects fringing effects, a simplification that is valid when d is small relative to the plate dimensions, ensuring a nearly uniform field over most of the area, see Figure 4.11.

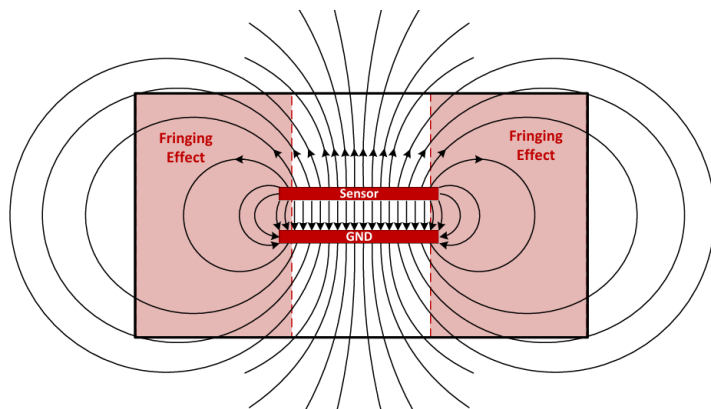


Figure 4.11. Electric fields of a parallel plate capacitor and its fringing effect [91].

For the parallel plate geometry like Figure 4.11, applying a voltage V between the plates, a total charge Q accumulates according to the relation:

$$Q = CV \quad (\text{Eq. 4.7})$$

Where C is the capacitance, which quantifies the capacitor's ability to store charge per unit voltage [77]. In the ideal case of a uniform electric field along the integration path (i.e. perpendicular to the plates), the voltage between the plates is simplified by:

$$V = \int_0^d \mathbf{E} \cdot d\mathbf{l} = Ed \quad (\text{Eq. 4.8})$$

Furthermore Gauss' law, (Eq. 4.1), for a parallel plate can also be rewritten as

$$EA_C = \frac{Q}{\epsilon_0 \epsilon_r} \quad (\text{Eq. 4.9})$$

Hence, capacitance can be determined substituting (Eq. 4.8) and (Eq. 4.9) into (Eq. 4.7):

$$C = \frac{\epsilon_0 \epsilon_r(T) A_C}{d} \quad (\text{Eq. 4.10})$$

where:

- C is the capacitance, in farads (F),
- ϵ_0 is the electric permittivity in the vacuum,
- $\epsilon_r(T)$ is the relative electric T dependant permittivity of the material between the plates,
- A_C is the plate area, in square meters (m^2),
- d is the spacing between plates, in meters (m).

This derivation holds for a two-electrode system where all electric field lines emanating from one plate terminate on the opposite plate, thereby simplifying the analysis. In more complex, multi-electrode configurations, these assumptions may no longer apply. Furthermore, if both d and A are held constant, the capacitance C will vary only with T due to the temperature dependence of ϵ_r .

This temperature variation in capacitance is the basis of the sensing mechanism explored in this thesis.

4.2.2.2. Considerations for Measurement Precision and its Limits

4.2.2.2.1 Noise

In capacitive measurement systems like the one used in this project, the main limitation to precision arises from electronic noise rather than fundamental physical limits such as charge quantization, which is negligible in practical setups. Given the high impedance of capacitive sensors, current noise tends to dominate over voltage noise, but modern amplifiers, such as those integrated in the FDC1004EVM module, offer femtoampere-level noise performance and include built-in filtering, effectively minimizing this impact. Remaining sources of noise, such as thermal and excess noise in passive components, may still influence measurements but are generally secondary to the high-quality signal conditioning provided by the module [77].

Given these considerations, the capacitance sensor must be carefully shielded and electrically isolated from any switching power components, as these can introduce interference, transients, or even saturate the sensor, as demonstrated in Figure 5.30 using the experimental platform.

Noise effect in input capacitance signal of the system under different shielding conditions.

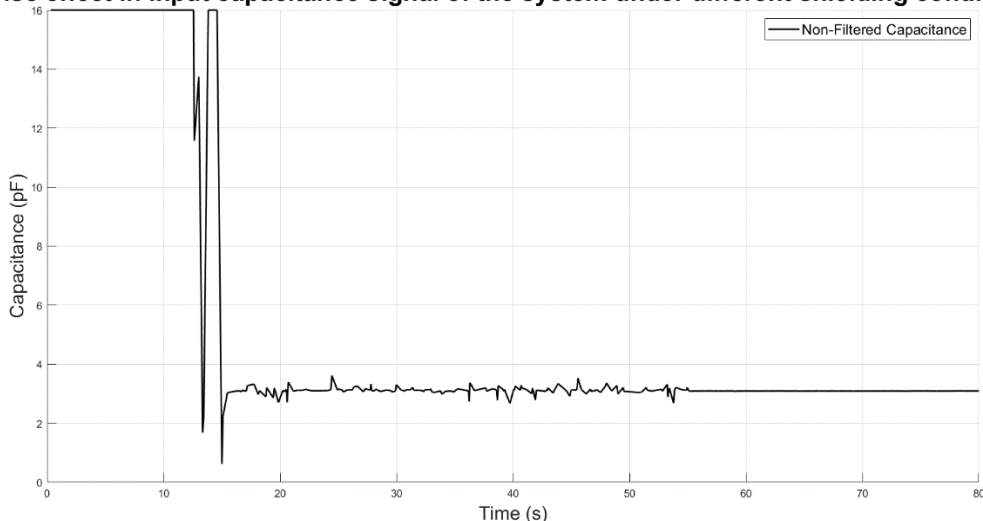


Figure 4.12. Input capacitance signal of the system under different shielding conditions. From 0 s to 12 s: no shielding; from 15 s to 55 s: shielded, but with the laptop connected to the power stage; from 55 s onward: shielded and electrically isolated from the power stage. The x-axis represents time (s), and the y-axis represents capacitance (pF). Source: Author.

4.2.2.2.2 Fringing Effects

Fringing effects occur at the edges of capacitor plates, where the electric field lines spread out, reducing field density and consequently lowering the contribution to total capacitance. These effects can introduce measurement inaccuracies depending on the application. To minimize fringing effects, beveling the plate edges or using thinner plates can help. Additionally, for applications requiring large gaps, surrounding the plates with a grounded shield reduces fringing flux, as illustrated in Figure 4.13.

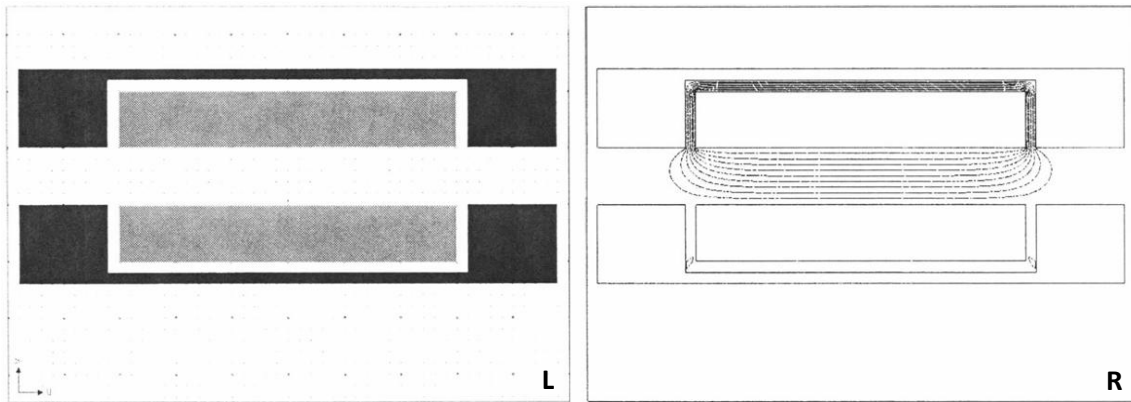


Figure 4.13. Ground shield electrode configuration (L) and its equipotential lines (R). Reworked from [77].

4.2.2.2.3 Sensor Stability

Mechanical stability is a critical concern, as variations in plate separation directly affect capacitance, leading to deviations in permittivity measurements. Ensuring mechanical rigidity is essential for maintaining measurement accuracy.

4.2.3. The Evaluation Module

Once the capacitive sensor structure was defined, a dedicated electronic system was required to excite the sensor, amplify, and filter the signal, and digitize the measured capacitance. Various hardware solutions were considered, including both custom PCB designs and commercial evaluation modules. The following options were evaluated based on key performance metrics such as resolution, operating temperature, maximum input capacitance, technology, and availability.

4.2.3.1. Custom PCB Design Approach¹

A fully customized system allows for greater flexibility in experimental design. CAP1298 (Microchip Technology) is a capacitive microchip design for touch sensors featuring up to eight channels. It is priced at approximately €1.1 [92], with an ordering delay of around 3 days. The operating temperature range extends from -40 °C to 125 °C, and it supports a maximum input capacitance of 50 pF. It employs switched-capacitor technology but lacks an existing GUI or simulation model. While this approach provides design flexibility, it requires developing the entire system from the ground up, including sensor excitation, data acquisition, and software interface development, which would increase the price, building time and complexity of the system.

¹ All prices, timings, and availability are based on market conditions including national taxes (IVA) and at the time the platform was built (March 2025, Barcelona, Spain).

4.2.3.2. Commercial Evaluation Modules

Although the custom PCB is a promising solution, many suitable commercial evaluation module boards are already available on the market, such as:

- TIDA-01465 (TI) is an evaluation module platform designed to be built by the customer and modified according to specific requirements. It is priced at approximately €600 [93], with an estimated ordering and assembly delay of 3 weeks. The system provides a 28-bit resolution with 4 channels for capacitive sensing, utilizing an LC tank circuit architecture with a maximum input capacitance of 250 nF. TI has developed a dedicated GUI for data processing and analysis, and the system has previously been used for ice formation measurements (Richard Wang, TI) [94].
- FDC1004 (TI) is a high-resolution (0.5 fF) capacitive sensing IC with a price of €382.87 [95], and an ordering delay of about 3 days. It operates in a temperature range of -40 °C to 125 °C, offering a resolution of 24 bits and 4 sensing channels. The technology is based on switched-capacitor circuits, with a maximum input capacitance of 15 nF and a sampling rate of 400 SPS. This module includes a pre-developed GUI and a simulation model and has been used for ice detection applications (Jarrod Krebs, TI) [96].
- FDC2214 (TI) is an advanced capacitive sensing IC with a price of €654.25 [97], and an ordering delay of 4 days. It supports an operating temperature range of -40 °C to 125 °C and provides a 28-bit resolution with 4 sensing channels. The architecture is based on an LC tank circuit, allowing a maximum input capacitance of 250 nF and a sampling rate of 4.08 kSPS. TI provides a GUI and a simulation model, and the module has been validated for ice detection applications (Richard Wang, TI) [98].
- FDC2114 (TI) is a low-power, lower-resolution capacitive sensing IC priced at €521.53 [99], with an ordering delay of 18 weeks. It operates within a temperature range of -40 °C to 125 °C, offering a 28-bit resolution across 4 sensing channels. The system uses an LC tank circuit architecture, supports a maximum input capacitance of 250 nF, and achieves a sampling rate of 13.3 kSPS. It includes a GUI and a simulation model but has not been used for ice measurement applications [100].
- AD7746 (Analog Devices) is a high-resolution capacitive-to-digital converter designed for precision measurements. It is priced at €80.17 [101], with an ordering delay of 4 days. The module functions within a temperature range of -40 °C to 125 °C, providing a resolution of 24 bits across 2 sensing channels. The maximum input capacitance is 4 aF, with a sampling rate of 90 SPS. It does include an existing GUI but no a simulation model. It has not been utilized for ice measurements [102].

4.2.3.3. Considerations for System Selection

Several key aspects were analyzed to determine the most suitable solution. Some evaluation modules include a pre-developed GUI, streamlining the experimental process by eliminating the need for custom firmware development, I2C-to-UART communication programming, and raw data processing.

Regarding sensing technology, LC tank circuit architectures generally offer greater robustness against noise, making them preferable in high-interference environments. However, if broadband noise is not a significant concern, switched-capacitor circuit technology may provide a more cost-effective alternative. Additionally, switched-capacitor circuits allow for a more direct connection to the sensors, requiring no extra components beyond the sensor itself, whereas LC tank circuits necessitate a specific resonance circuit tailored to each application. This not only reduces costs but also simplifies mounting and debugging.

Finally, given that the experimental setup may be exposed to low temperatures, the selected system must withstand at least -20 °C to prevent performance degradation or operational failure.

To facilitate decision-making Table 4.2 was compiled to highlight critical limitations (marked in red) and advantageous features (marked in green) for each evaluated option. The final selection will be based on a trade-off between resolution, environmental robustness, ease of integration, and cost-effectiveness for experimental use in cryolipolysis skin capacitance measurement.

Table 4.2. Comparison of potential capacitance sensor interfaces.

Model	Price (€)	Ordering Time	T Range (°C)	Res. (bits)	Channels	Used for Ice Detection?	Tech.	GUI	Sim. Model	Max C _{in} (nF)	Sampling Rate (SPS)
FDC1004	382.87	3 days	-40 to 125	24	4	YES (Jarrod Krebs, TI) YES (Richard Wang, TI)	Switched-Capacitor	YES	YES	15	400
FDC2214	654.25	4 days	-40 to 125	28	4	NO	LC Tank Circuit	YES	YES	250	4080
FDC2114	521.53	18 weeks	-40 to 125	28	4	NO	LC Tank Circuit	YES	YES	250	13300
CAP1298¹	1.1	3 days	-40 to 125	-	8	NO	Switched-Capacitor	NO	NO	50	-
AD7746	80.17	4 days	-40 to 125	24	2	NO	-	YES	NO	4	90
TIDA-01465²	-	3 weeks	-40 to 125	28	4	YES (Richard Wang, TI)	LC Tank Circuit	YES	NO	250	-

¹ Since it is solely a microcontroller, it would require designing the excitation signal module, implementing I2C-to-UART communication, programming the microcontroller, and processing the data in *Python* or *MATLAB*. Therefore, the cost and other parameters are yet to be determined.

² Obsolete and replaced by FDC2XX family.

Based on Table 4.2, the FDC1004EVM was selected as the most suitable option for the experimental measurement platform. A sampling rate of 400 SPS and a maximum input capacitance (C_{in}) of 15 nF are sufficient for our application. Compared to the FDC2214, which offers higher SPS and C_{in} values that are not necessary for this setup, the FDC1004EVM provides a more cost-effective solution at half the price. Additionally, its switched-capacitor architecture simplifies the setup by allowing direct sensor connection, eliminating the need for external resonance circuits. The FDC1004EVM, Figure 4.14, provides high resolution (0.5 fF) at a resonance frequency of 25 kHz, making it well-suited for ice detection. It also integrates seamlessly with TI's Sensing Solutions EVM GUI, enabling easy register access and user-friendly configuration [103].

The evaluation module (EVM) has pre-cut lines on the borders of each section that allow for a flexible and specific system design, in our case changing the sensor for a parallel plate capacitor. These sections, shown in Figure 4.14, are:

1. USB-to-I2C section: interface the communication of FDC1004 to a USB port.
2. FDC1004 section: embeds FDC1004 capacitive to digital converter.
3. Sensor: contains a capacitive sensor for human proximity and gesture recognitions.

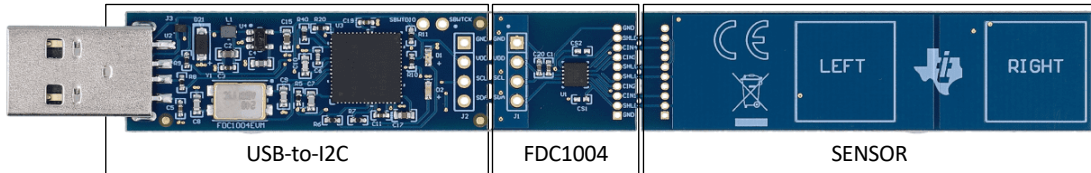


Figure 4.14. FDC1004EVM and its sections, modified from [103].

4.2.4. The Software

A combination of software tools was required to program some devices, acquire, and process signals, and visualize results.

4.2.4.1. Sensing Solutions EVM GUI

The host machine is required for device configuration and data streaming. The following steps are necessary to prepare the EVM for the GUI:

- The GUI and EVM driver must be installed on a host computer
- The EVM must be connected to a full speed USB port (USB 1.0 or above)

The Sensing Solutions EVM GUI supports the Windows operating systems, both 32-bit and 64-bit (i.e., Windows XP, Windows 7, Windows 8, Windows 8.1, Windows 10, and Windows 11). For more information about installation and configuration of the software, refer to [103].

4.2.4.2. MATLAB

To enable real-time visualization of T and C values, and to facilitate further data processing and analysis, MATLAB was used. MATLAB was chosen for its:

- Robust support for serial communication.
- Built-in tools for data plotting and analysis.
- Efficient automation of data extraction (e.g., from .csv files).
- Familiarity among the development team.

The version employed in this project was MATLAB R2023b.

4.2.4.3. Arduino IDE

The Arduino Integrated Development Environment (IDE) was used to program the Arduino MEGA2560 microcontroller, which manages the control of the Peltier cells via the relay module and acquires temperature data from the ATH10 sensor for transmission to the host computer. The Arduino IDE was selected due to its:

- Native compatibility with Arduino hardware, with built-in serial monitor for real-time debugging and basic data visualization.
- Extensive library support for the ATH10 sensor and peripheral integration.

This environment significantly streamlined firmware development integration during the project.

5. Methods

5.1. Data Collection

To investigate whether there is a correlation between the freezing of a sample and an increase in its capacitance, 5 different controlled experiments were designed, each one with own objectives.

5.1.1. Experiment 1: Freezing Point Detection

5.1.1.1. Objective

This experiment aimed to determine whether the exothermic temperature change during the freezing of water could be reliably detected using the AHT10 digital temperature sensor, and to assess the ability of the TEC device to achieve a target surface temperature of approximately $T_f \approx -10^\circ\text{C}$.

Two input voltages, 11 V and 12 V¹, were selected based on manufacturer performance data for the TEC1-12706, Figure 5.1. These voltages correspond to operating currents between 3.5 A and 4.5 A, and are expected to produce a temperature gradient (ΔT) of about 40 °C, assuming a hot-side temperature (T_h) between 25 °C and 40 °C. This range was anticipated under passive and forced-convection cooling conditions, allowing for sufficient cold-side cooling performance.

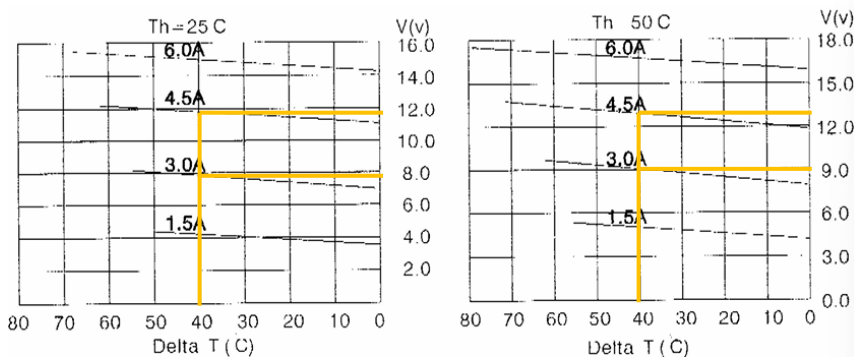


Figure 5.1. Performance curves of the TEC1-12706, adapted from [85].

Hence, the two primary objectives of Experiment 1 were:

- To compare the effectiveness of 11 V and 12 V in achieving a $T_f \approx -10^\circ\text{C}$.
- To evaluate the AHT10's capacity to resolve and reliably detect the thermal signature of the freezing transition.

¹ As there was two TEC devices, the final voltage given by the power supply is the double (22 V or 24 V).

5.1.1.2. Experimental Setup

As depicted in Figure 5.2, the setup consisted of the TEC1-12706 module mounted on the FAN478. The Promax FA-665 power supply was used to provide the input voltage (either 11 V or 12 V). The AHT10 sensor was positioned in direct contact with the TEC's cold surface to measure temperature in the region where water droplets would be placed.

Real-time data acquisition was performed using a MATLAB-based GUI. The FDC1004EVM capacitance measurement system was excluded from this configuration, as it was not relevant for this experiment.

EXPERIMENT 1: SETUP

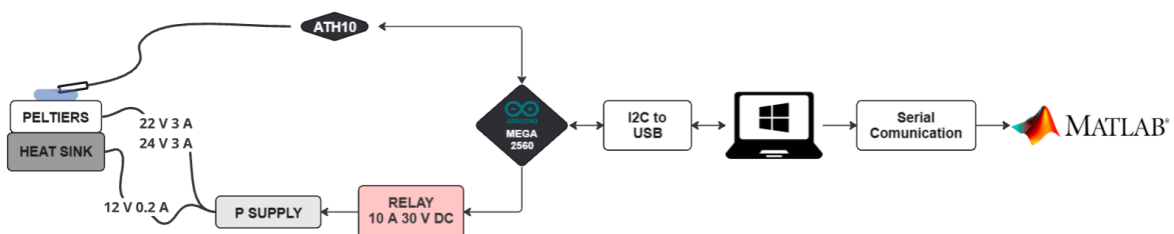


Figure 5.2. Experimental setup for freezing point detection. The AHT10 sensor is placed on the cold side of the TEC. The capacitance measurement system was not used in this configuration. Author's own diagram.

5.1.1.3. Procedure

1. Assemble the system as shown in Figure 5.2, excluding the FDC1004EVM and capacitance sensor.
2. Position the AHT10 sensor on the TEC's cold surface, ensuring good thermal contact.
3. Connect the Arduino to the USB port.
4. Apply the selected voltage (22 or 24 V) to the TECs using the DC power supply.
5. Use a pipette to place a water droplet onto the sensor, ensuring contact with both the sensor and TEC.
6. Start the data acquisition using the custom MATLAB GUI.
7. Allow the system to cool until temperature readings.
8. Save the recorded data using the “*save.m*” script.
9. Calculate and record the key parameters
 - a. The start and end time of the exothermic event, associated with ice formation, ($t_{i,exo}$ and $t_{f,exo}$).
 - b. The temperatures at the beginning and end of this event ($T_{i,exo}$ and $T_{f,exo}$).
 - c. The final temperature reached by the sample (T_f)
 - d. The duration (Δt_{exo}) and temperature span (ΔT_{exo}) of the exothermic peak
10. Repeat the entire process five times for each voltage condition.

5.1.2. Experiment 2: Optimal Sample Height

5.1.2.1. Objective

Biological tissues are typically modeled as distributed resistive-capacitive (RC) networks. Hydrated cellulose demonstrates temperature-dependent dielectric behavior reminiscent of biological tissues. Christie *et al.* measured the dielectric properties of humid cellulose over a wide frequency range (10^{-3} – 10^5 Hz) and found strong moisture dependence and phase-angle behavior akin to tissue-like impedance [104]. Similarly, Boutros *et al.* reported that the dielectric constant and loss of cellulose fibers increase with frequency, temperature, and humidity, echoing trends seen in living tissues [104].

In bioimpedance and dielectric spectroscopy studies, hydrated biological tissues exhibit dielectric dispersion primarily due to water dipole relaxation, an effect similarly observed in cellulose, water systems [105], [106]. Consequently, the cellulose-in-film combination closely approximates the RC behavior of skin: the plastic film acts as a mostly capacitive layer, while the moisture-laden cellulose provides resistive and dielectric characteristics. This setup offers a cost-effective, reproducible, and ethically sound alternative to biological samples during the prototype's development stage.

This experiment aimed to determine the optimal sample size for reliable freezing detection using the exothermic thermal response. To emulate the electrothermal behavior of biological tissue, without the complexity and cost associated with using meat, water-saturated cellulose absorbent paper was wrapped in plastic film to form the test samples. Five variants (1, 2, 4, 8, and 16 - layers) were tested to evaluate detection sensitivity, as illustrated in Figure 5.3.

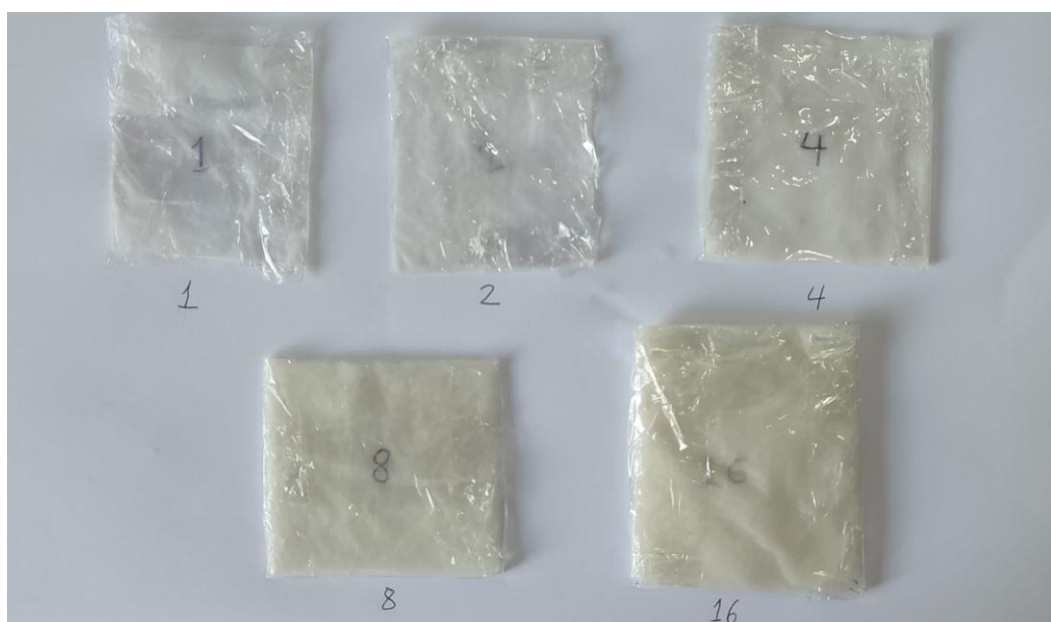


Figure 5.3. Photograph of the five water-saturated absorbent paper samples, each wrapped in plastic film and varying in the number of layers, used in the experiment. Author's own image.

To further evaluate the reliability of the selected sample configuration, previously identified as the optimal trade-off between detection speed and signal clarity, 30 additional trials were conducted and analyzed. Each trial involved cooling a hydrated sample to induce a freezing event, during which the temperature-time profile was recorded. The appearance of a distinct exothermic peak in the recorded curve was used as the detection criterion for latent heat release associated with the phase change of water.

Hence, the objectives of Experiment 2 were:

- Determine the ideal number of layers for the samples
- Determine the reliability to detect the exothermic curve using the optimal sample size

5.1.2.2. Experimental Setup

The experimental configuration followed the setup described in Subsection 5.1.1.2, with the only difference being the use of water-saturated absorbent paper instead of free water droplets. The AHT10 temperature sensor was placed in contact with the sample, and a 12 V supply was applied to the TEC.

5.1.2.3. Procedure

1. Assemble the system as shown in Figure 5.2, excluding the FDC1004EVM and capacitance sensor.
2. Place the sample on the cold surface of the TEC, ensuring good thermal contact.
3. Position the AHT10 sensor firmly on top of the sample.
4. Connect the Arduino to the USB port.
5. Apply 12 V to the TEC using a DC power supply.
6. Start the data acquisition using the custom MATLAB GUI.
7. Allow the system to cool until the temperature stabilizes.
8. Save the recorded data using the “*save.m*” script.
9. Calculate and record the key parameters
 - a. The start and end time of the exothermic event, associated with ice formation, ($t_{i,exo}$ and $t_{f,exo}$).
 - b. The temperatures at the beginning and end of this event ($T_{i,exo}$ and $T_{f,exo}$).
 - c. The duration (Δt_{exo}) and temperature span (ΔT_{exo}) of the exothermic peak
10. Repeat the entire process five times for each sample configuration.

5.1.2.4. Detection Classification Criteria

To enable quantitative evaluation if the sample was frozen (actual condition) and if it was detected (predicted), each trial outcome was classified according to the presence, timing, and amplitude of the exothermic peak. The following definitions were applied:

- True Positive (*TP*): A trial in which an exothermic event was detected with a peak initiation temperature $T_{i,exo} \leq 4^\circ\text{C}$, the temperature difference $\Delta T_{exo} \geq 0.2^\circ\text{C}$, and the sample was known to freeze.
- False Positive (*FP*): A trial in which an exothermic peak was detected with $T_{i,exo} > 4^\circ\text{C}$ or $\Delta T_{exo} < 0.2^\circ\text{C}$, considered too weak or inconsistent.
- False Negative (*FN*): A trial where the sample underwent freezing, but no exothermic peak was detected (missed detection).
- True Negative (*TN*): Not applicable in this dataset, as all samples were designed to undergo freezing. Thus, $TN = 0$.

5.1.3. Experiment 3: Plate Separation Distance Optimization

5.1.3.1. Objective

As discussed in Section 4.2.2.1, the system's capacitance can be modeled using (Eq. 4.10), which depends on three key parameters: the relative permittivity $\varepsilon_r'(T)$, the distance between plates d and the electrode area A_C . To ensure that variations in capacitance ΔC can be attributed solely to temperature-induced dielectric changes, the geometric parameters d and A_C must remain fixed or be systematically varied and controlled.

This experiment aims to investigate how the electrode separation d between the sensing electrode C_{in} and the ground plane C_{GND} influences the sensor's sensitivity, defined as the magnitude of measurable ΔC resulting from the introduction of the dielectric sample between the plates, compared to the baseline condition in air. The change in capacitance (ΔC), is defined as:

$$\Delta C = \overline{C_{peak}} - \overline{C_{base}} \quad (\text{Eq. 5.1})$$

where $\overline{C_{peak}}$ is the mean capacitance measured with the inserted sample from 25 s to 30 s), and $\overline{C_{base}}$ is the mean of the initial baseline capacitance from 0 s to 10 s.

Therefore, the objectives of Experiment 3 were:

- To determine, how the sensitivity of the system is affected by d .
- To determine the optimal plate separation d that maximizes the measurable change in capacitance ΔC in response to material-driven variations in dielectric properties, sensitiviy.



5.1.3.2. Experimental Setup

Five distinct separation distances were evaluated: 1 cm, 2 cm, 3 cm, 4 cm, and 5 cm. To eliminate confounding factors, electrode areas were fixed at:

- Ground plate area: $A_{GND} = 5 \text{ cm} \times 7.5 \text{ cm} = 37.5 \text{ cm}^2$
- Sensing plate area: $A_C = 1.5 \text{ cm} \times 2 \text{ cm} = 3 \text{ cm}^2$

The test platform was designed with a vertical mounting column marked at 1 cm increments to enable precise and repeatable positioning of C_{in} above C_{GND} , Figure 5.4. Furthermore, as shown in Figure 5.5, the sample, composed of 8-layers material used in Section 5.1.2, was positioned between the electrodes, placed on top of the cold surface of the thermoelectric cooler (TEC), directly above the ground electrode and beneath the sensing plate. The AHT10 digital temperature sensor was not used.

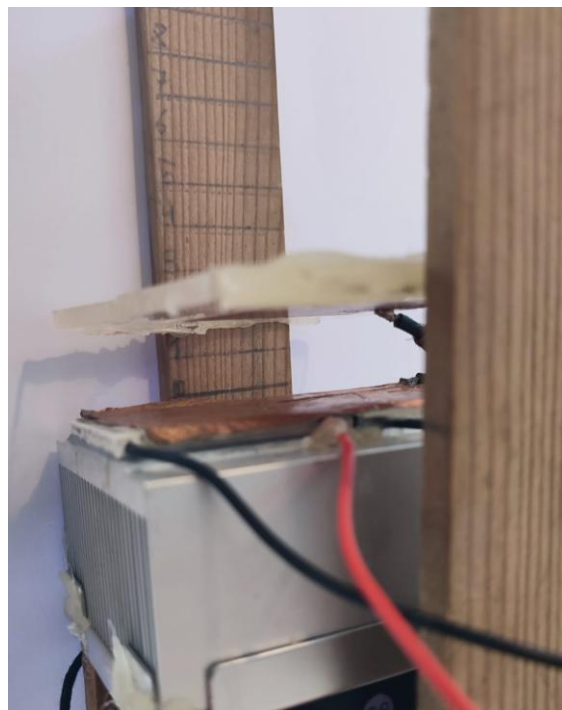


Figure 5.4. Experimental platform column marked with increasing distances of 1 cm from the C_{GND} . Author's own picture.

EXPERIMENT 3: SETUP

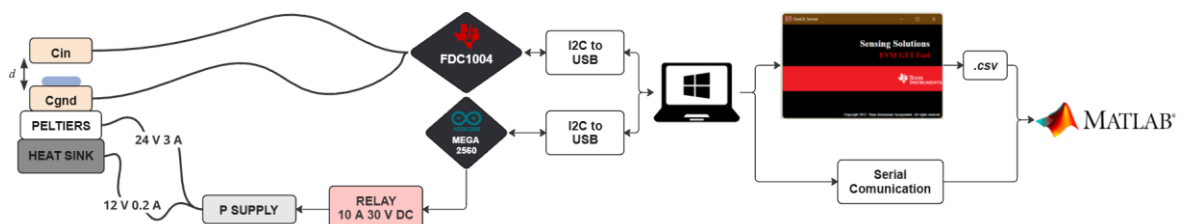


Figure 5.5. Experimental setup for freezing point detection. The sample (blue object) is placed on the cold side of the TEC, over the ground plate, and below the C_{in} . Author's own diagram.

5.1.3.3. Procedure

1. Assemble the system as illustrated in Figure 5.5, including the FDC1004EVM capacitance measurement module and the designated capacitor plates.
2. Prepare the dielectric sample externally: an 8-layer, water-saturated, cellulose-based paper stack sealed in plastic.
3. Position the top sensing electrode at the designated height mark on the column structure, corresponding to the target d .
4. Apply 12 V to each thermoelectric cooler (TEC) using a DC power supply, 24 V in total.
5. Connect the FDC1004EVM to the computer via USB.
6. Launch the “Sensing Solutions EVM GUI” software and wait for device recognition.
7. Navigate to the Data Streaming tab and specify the data saving location. The default path and format “.csv” are recommended.
8. Start the capacitance data acquisition.
9. Connect the Arduino to a separate USB port.
10. Open the MATLAB graphical interface and initialize the freezing detection platform.
11. Allow the system to stabilize and record the baseline capacitance (C_{base}) for approximately 20 seconds, in order that the transient time is passed and the capacitance is stable.
12. Insert the prepared dielectric sample between the capacitor plates.
13. Allow the transient capacitance increase, caused by the elevated permittivity of the hydrated material, to stabilize.
14. After approximately 10 seconds, remove the sample from the capacitor.
15. Continue recording for an additional 20 seconds to capture the return to baseline.
16. Terminate the MATLAB GUI and save the recorded data using the “*save.m*” script.
17. Repeat the complete procedure for each of the five plate separation distances ($d = 1 \text{ cm}, 2 \text{ cm}, 3 \text{ cm}, 4 \text{ cm}, 5 \text{ cm}$), performing 5 trials per configuration to ensure statistical robustness.

5.1.4. Experiment 4: Effect of Increasing Electrode Area

5.1.4.1. Objective

As discussed in Section 5.1.3.1, the core hypothesis of this thesis is that the freezing point of water can be detected via capacitance measurements. Knowing that the simplified proportionality $C(T) \propto \varepsilon_r'(T)$, derived from (Eq. 4.10), holds only under the condition that both d and A_C remain constant. Consequently, this experiment was designed to evaluate the effect of increasing the sensing electrode area on the system's sensitivity and robustness.

Specifically, the objectives for Experiment 4 were:

- To assess whether a larger sensing area improves the sensitivity of the system to dielectric changes during the freezing process.
- o assess whether a larger electrode reduces the impact of non-linear distance-capacitance effects by minimizing fringing field contributions.

5.1.4.2. Experimental Setup

This setup replicated the configuration used in Experiment 3, with the only modification being the replacement of the top sensing electrode with a larger square copper plate of dimensions $4\text{ cm} \times 4\text{ cm}$ ($A_C = 16\text{ cm}^2$). The bottom (ground) electrode remained unchanged, as platform constraints prevented the use of a larger one.

This choice was supported by recommendations in the Texas Instruments FDC1004 application notes [107], [108], [109], [110], [111], [112], [113], which suggest that larger electrodes improve immunity to environmental electrical noise. Conversely, smaller plates could reduce system robustness and increase susceptibility to capacitive noise artifacts.

5.1.4.3. Procedure

The procedure followed was identical to that of Experiment 3, with the only change being the use of the larger ($4\text{ cm} \times 4\text{ cm}$) top sensing electrode:

1. Replace the top electrode with the $4\text{ cm} \times 4\text{ cm}$ copper plate.
2. Repeat the experimental protocol outlined in Section 5.1.3.1 using the updated configuration.

5.1.5. Experiment 5: Input Capacitance Behavior Correlated to Freeze

5.1.5.1. Objective

This experiment aims to monitor and analyze the simultaneous evolution of temperature and input capacitance over time, $T(t)$ and $C_{in}(t)$, during the freezing process of water.

The primary objectives are:

- To identify characteristic features or trends in the $C_{in}(t)$, signal that correspond to the onset or progression of the phase change from liquid to solid, e.g. freezing.
- To evaluate whether a distinct and quantifiable pattern in $C_{in}(t)$, can serve as a predictive marker for freezing, enabling future blind detection without temperature measurements, see Chapter 6.

5.1.5.2. Experimental Setup

To measure both $T(t)$ and $C_{in}(t)$, and to freeze the samples, the full experimental platform was used, Figure 5.6. Moreover, the before optimized parameters were used ($V_{cells} = 24$ V, $d = 1$ cm, $A_C = 16$ cm² with 8 layers sample).

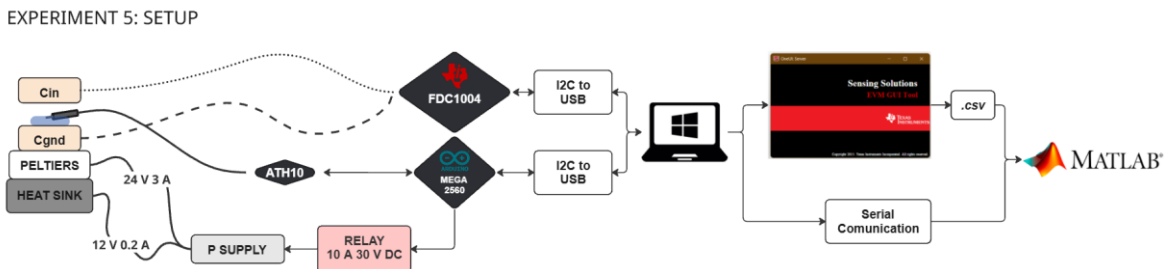


Figure 5.6. Experimental setup for freezing point detection via $C_{in}(t)$ with $T(t)$ as a reference. The sample (blue object) is placed on the cold side of the TEC, over the ground plate, and below the C_{in} . Author's own diagram.

5.1.5.3. Procedure

To have a reliable statistical population of samples to analyse, 30 trials were conducted.

1. Assemble the system as illustrated in Figure 5.6, including the FDC1004EVM capacitance measurement module and the designated capacitor plates.
2. Prepare the dielectric sample: an 8-layer, water-saturated, cellulose-based paper stack sealed in plastic.
3. Deposit the sample ontop of the ground electrode, ensuring that all the sample is in contact with it.
4. Position the top sensing electrode at the designated height mark on the column structure, corresponding to the target $d = 1$ cm.
5. Apply 12 V to each thermoelectric cooler (TEC) using the DC power supply, hence 24 V in total.
6. Connect the FDC1004EVM to the computer via USB.
7. Launch the “Sensing Solutions EVM GUI” software and wait for device recognition.
8. Navigate to the Data Streaming tab and specify the data saving location. The default path and format “.csv”are recommended.
9. Start the capacitance data acquisition.
10. Connect the Arduino to a separate USB port.
11. Open the MATLAB GUI and initialize the freezing detection platform.
12. Record the data until the exothermic peak in the $T(t)$ can be detected.
13. Terminate the MATLAB GUI and save the recorded data using the “*save.m*” script.
14. Repeat the complete procedure for each trial.

5.1.5.4. Pre-processes of Samples from Experiment 5: Filtering and Signal Processing

Before going to the Experiment 5, a filter for the capacitance was designed, as it would not have sense to try to analyze having noise in the data. To reduce high-frequency electrical noise in the capacitance signal $C_{in}(t)$, two filtering algorithms were studied: moving average and local polynomial fit.

5.1.5.4.1 Moving Average

This filtering process was performed using MATLAB' sbuilt-in “*movemean()*” function. This filter computes the unweighted average of a fixed number of samples within a symmetric window of width W centered at each time index t_i . It replaces each point with the average of its neighboring values, thereby smoothing short-term fluctuations while preserving longer-term trends.

Here, W is an odd integer that defines the number of samples in the window, and t_j spans the W time steps centered around t_i . This method is particularly effective for signals affected by stationary noise and is computationally efficient.

The filtered capacitance signal, $\overline{C_{in}(t_i)}$, is defined as:

$$\overline{C_{in}(t_i)} = \frac{1}{W} \sum_{j=i-\frac{W-1}{2}}^{i+\frac{W-1}{2}} C_{in}(t_j) \quad (\text{Eq. 5.2})$$

5.1.5.4.2 Local Linear Polynomial Fit

This technique involves fitting a first-degree (linear) polynomial within a moving window of size W , entered at each time index t_i . The fitted value $C_{poly}(t_i)$ is then evaluated at the central point t_i , producing a smoothed signal that is more responsive to local changes than standard averaging techniques.

$$C_{poly}(t_i) = p_1 t_i + p_0 \quad (\text{Eq. 5.3})$$

Where p_1 and p_0 are the coefficients of the linear polynomial obtained by solving the least squares fit of a polynomial of degree 1 to the W samples $\{(t_j, C_{in}(t_j))\}$, for $j \in [i - \frac{W-1}{2}, i + \frac{W-1}{2}]$.



5.1.5.4.3 Filter Effect Comparation

As shown in Figure 5.7, the change of slope in $C_{in}(t)$, which we could define as the Region of Interest (ROI), is between 90 s and 180 s and 9.6 pF and 10.4 pF. Within this range, the two filtering methods were compared against the raw signal. With *ca.* 2000 samples per experiment, a 29-sample window (*ca.* 1.5 % of the signal) balances smoothing with feature preservation.

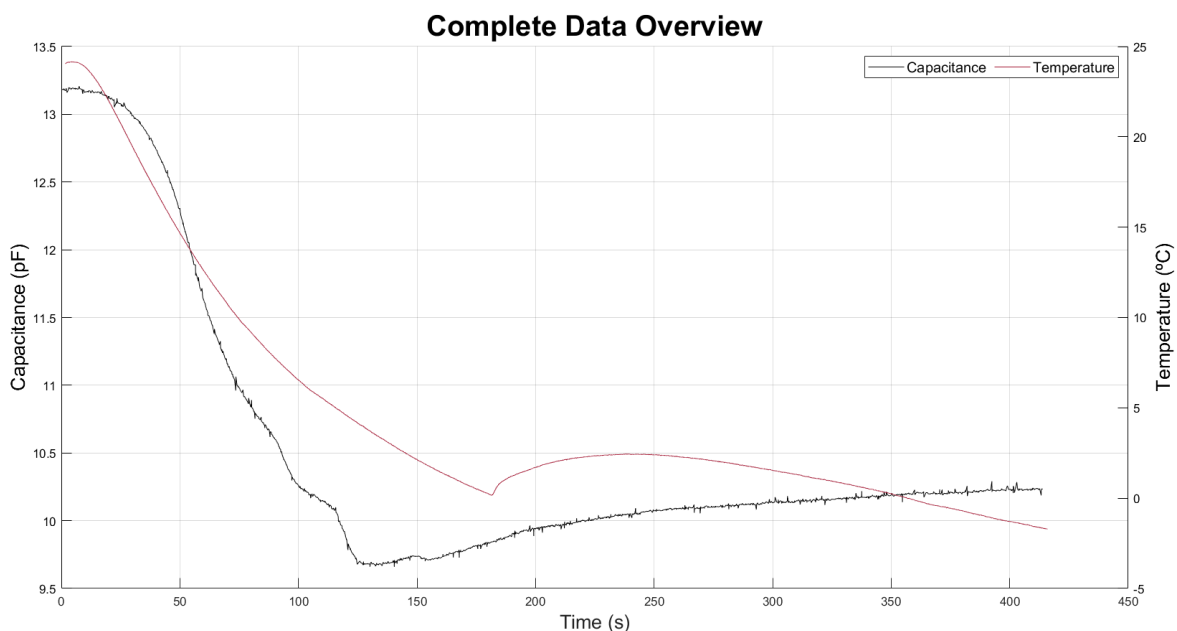


Figure 5.7. Temperature profile (right y-axis, garnet, °C) and raw (non-filtered) capacitance signal (left y-axis, black, pF) plotted against time (x-axis, seconds). Author's own work.

Although the optimal window size was selected empirically, care was taken to ensure that these windows do not result in a loss of relevant information. Given the sampling frequency of the capacitance signal (62.5 Hz), according to the Nyquist–Shannon sampling theorem, the sampling rate must be at least twice the highest frequency present in the signal to avoid aliasing and ensure that filtering does not distort the phenomena of interest. Therefore, the window size W should be chosen to preserve the signal's critical features without introducing excessive smoothing or distortion.

Furthermore Figure 5.8 illustrates the effect of extreme W values on the filtering process, highlighting how increasing the window size can distort critical transitions in the capacitance signal. Figure 5.9 further show that the optimal window size lies between 11 and 25 samples: smaller windows inadequately filter noise, while larger windows excessively smooth important features.

Additionally, the moving average filter slightly outperforms the local linear polynomial fit in preserving valleys and slopes, which are crucial for accurate detection. This observation is consistent with previous findings where relevant signal transitions typically span approximately 20 samples.

Based on these results, the ideal filter window should satisfy the following criteria:

- Be an odd number, to maintain symmetry around the center point.
- Be short enough to preserve temporal resolution, ideally fewer than 27 samples.
- Be long enough to effectively reduce noise, ideally more than 9 samples.

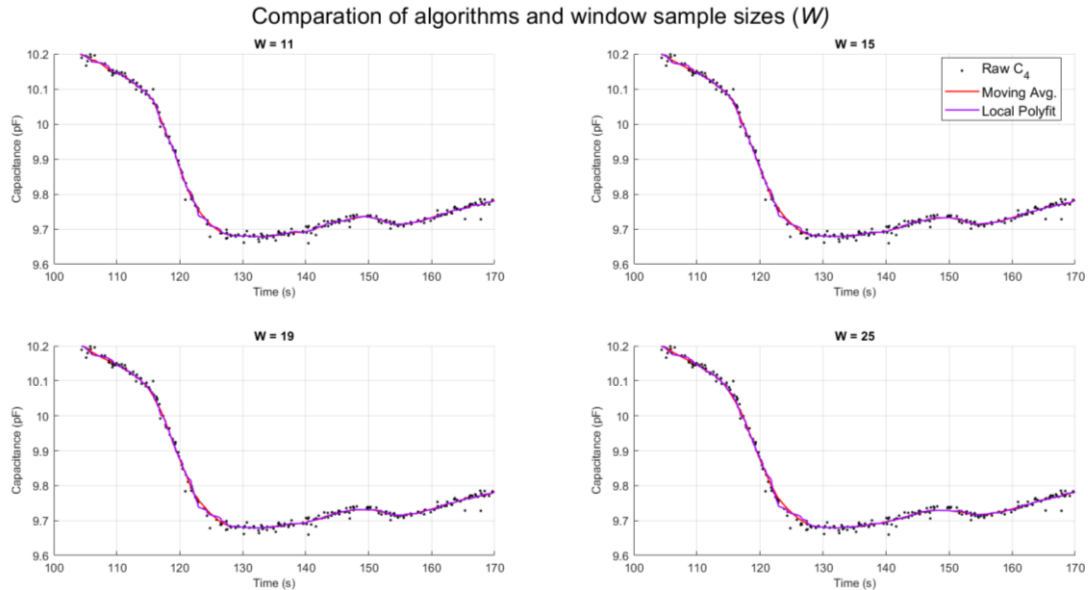


Figure 5.8. Effect of extreme window sizes W on filtering the capacitance signal within the Region of Interest (ROI). Each subplot compares the filtered signals using moving average (solid red line) and local linear polynomial fit (solid magenta line) against the raw capacitance data (black dots). Increasing window size smooths noise but may distort important signal transitions. The x-axis is time (s). Author's own work.

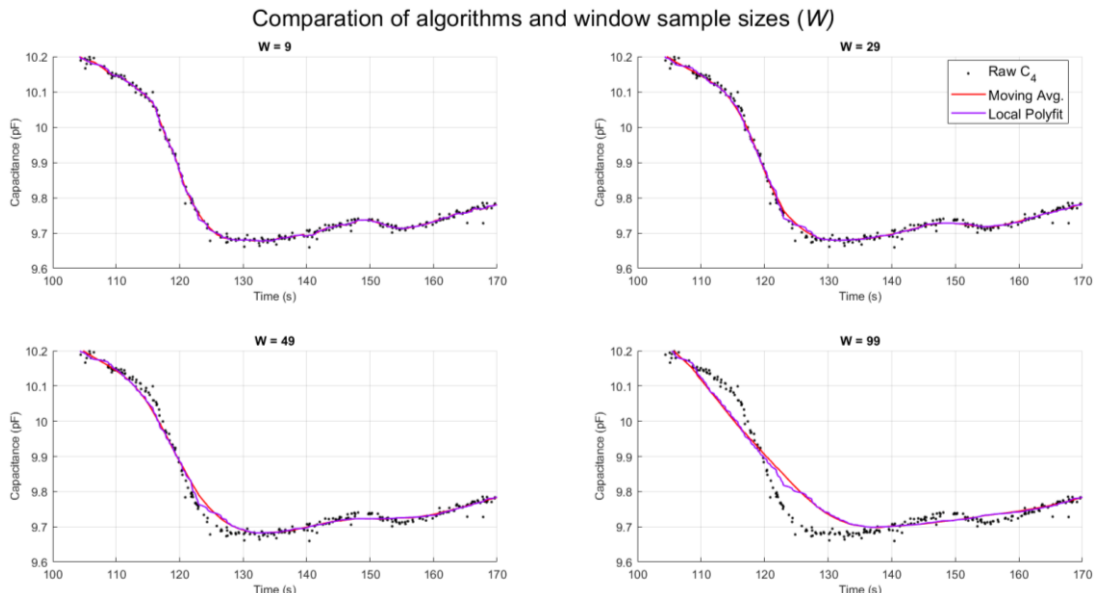


Figure 5.9. Zoomed-in view of the Region of Interest (ROI) showing temperature (right y-axis, garnet, °C) and unfiltered capacitance (left y-axis, black, pF) versus time (s) for different window sizes (samples). This highlights the critical signal features relevant to detection algorithm performance within the (90 s, 180 s) and (9.6 pF, 10.4 pF) range. Author's own work.

5.2. Analysis and Results

5.2.1. Experiment 1: Freezing Point Detection

5.2.1.1. Results

Figure 5.10. presents the temperature profiles from two experiments in which water droplets were frozen using thermoelectric (TEC) devices powered at 11 V and 12 V. In both cases, the AHT10 sensor successfully recorded the cooling process, showing a characteristic plateau followed by an exothermic peak, an indicator of the phase transition from liquid to solid. The red ellipse highlights the exothermic peak, which was more clearly visible at 12 V. This suggests that 12 V provides a more distinct and reliable detection of the freezing point.

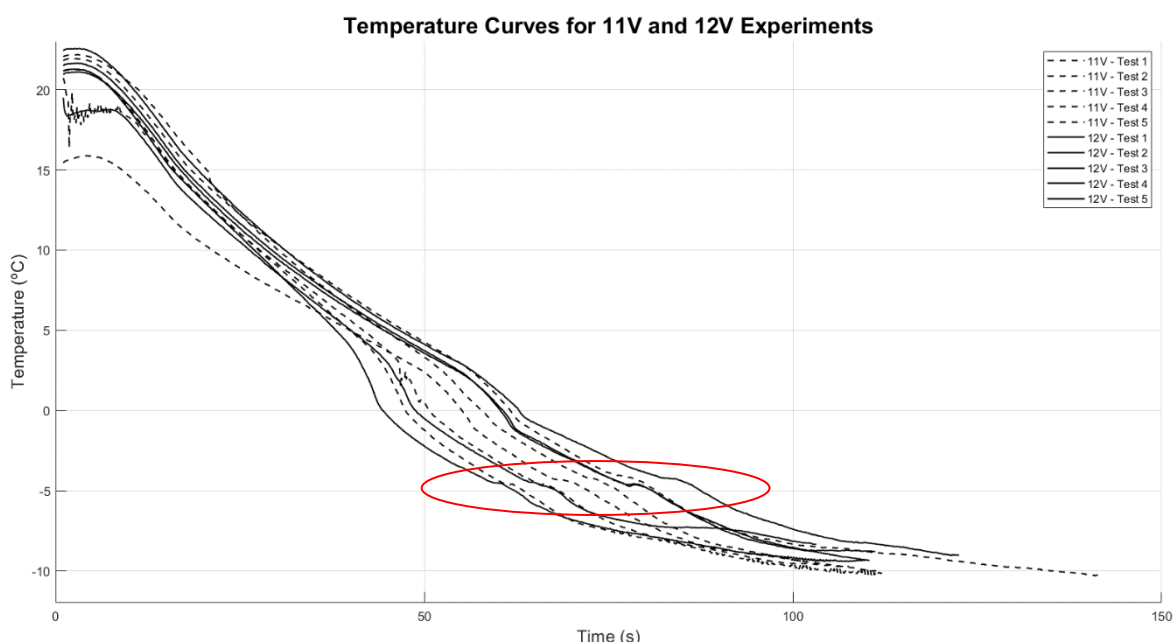


Figure 5.10. Temperature curves for experiments conducted at 11 V (solid line) and 12 V (dashed line), used to determine the optimal Peltier cell voltage, and assess the AHT10 sensor's ability to detect freezing. The red ellipse marks the exothermic curves. The x-axis represents time (s); the y-axis shows temperature (°C). Author's own work.

The average temperature rise during the exothermic event was slightly greater at 12 V ($0.056\text{ }^{\circ}\text{C}$) than at 11 V ($0.046\text{ }^{\circ}\text{C}$). However, the variability was significantly higher at 12 V, with a coefficient of variation (CV) of 56 %, compared to 35 % at 11 V. This indicates that while the thermal peak is more pronounced at 12 V, it is also less consistent, as illustrated in Figure 5.11.

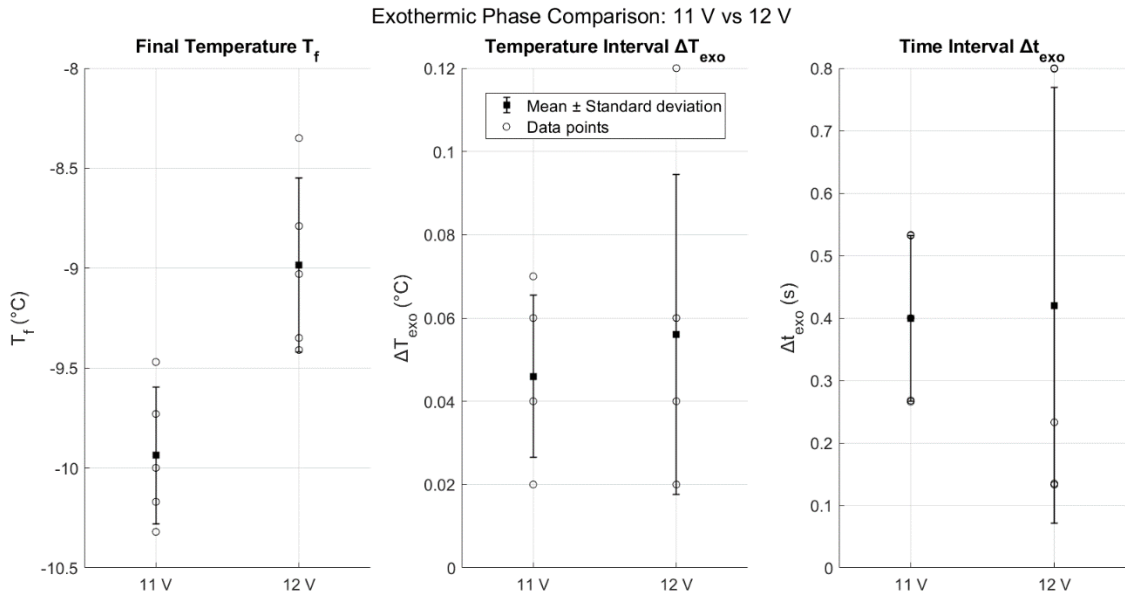


Figure 5.11. Statistical summary of Experiment 1, showing individual data points, mean values, and standard deviations for both voltage conditions. The x-axis indicates the experimental group (11 V or 12 V); the y-axis refers to the type of data analyzed. Author's own work.

The detailed results are presented in Table 0.2 and Table 0.3, in Annex C1. At 11 V, the final temperature averaged $-9.94\text{ }^{\circ}\text{C}$, compared to $-8.99\text{ }^{\circ}\text{C}$ at 12 V. However, it is worth noting that the 12 V temperature profiles had not fully stabilized within the recorded timeframe and continued to decline. Later experiments confirmed that they eventually reached temperatures below $-12\text{ }^{\circ}\text{C}$, as shown in Figure 5.5.

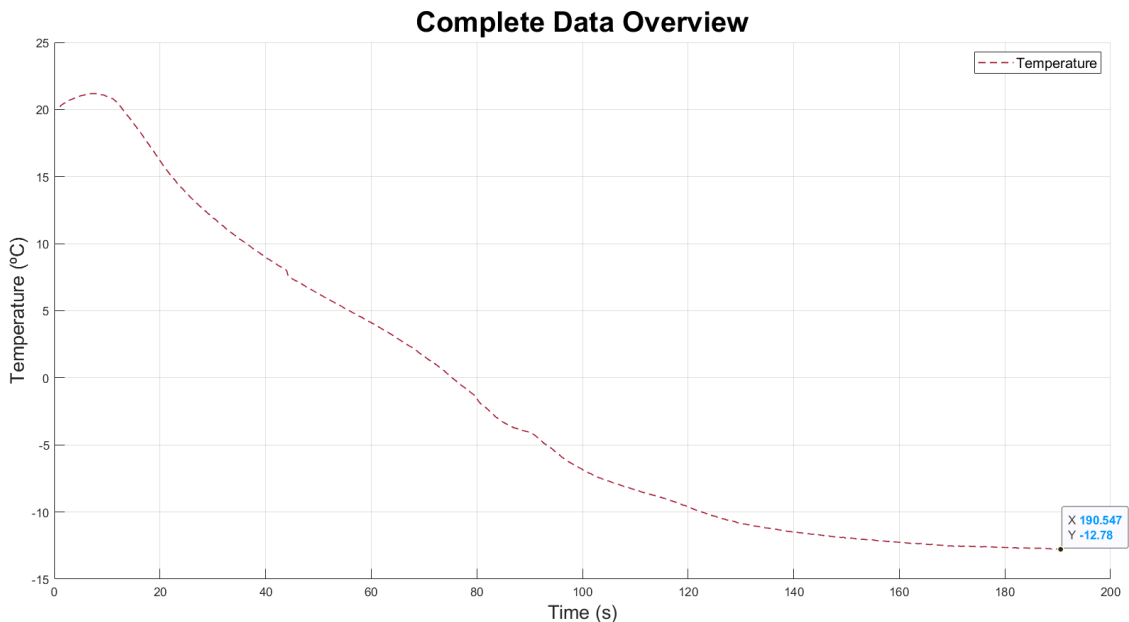


Figure 5.12. Temperature profile of a water droplet cooled by a TEC device powered at 12 V. The final stabilized temperature is marked with a blue data tip at $-12.78\text{ }^{\circ}\text{C}$ after 200 s. The x-axis represents time (s); the y-axis shows temperature ($^{\circ}\text{C}$). Author's own work.

5.2.1.2. Conclusions

- Both voltages achieved final temperatures close to -10 °C.
- Thermal peaks were clearer and more distinct at 12 V.
- The AHT10 sensor consistently detected the freezing event with similar onset temperatures at both voltages.
- 12 V offers a better trade-off for exothermic peak clarity, despite higher variability

Given the clearer exothermic signature at 12 V, this voltage was selected for subsequent experiments to ensure more reliable freezing point detection.

5.2.2. Experiment 2: Optimal Sample Size

5.2.2.1. Results

Figure 5.13 and Figure 5.14 show the thermal behavior of absorbent paper samples with increasing numbers of layers during the freezing process. A clear trend emerges: as the number of layers increases, the exothermic peaks become more distinguishable and easier to detect. This is attributed to the higher thermal mass and water content in thicker samples, which release greater amounts of latent heat upon freezing. However, this benefit comes at a cost: thicker samples introduce a delay in the onset of the exothermic signal.

In Figure 5.14, the displacement of the exothermic curve toward the right along the x-axis (time) indicates that freezing initiates in the lower layers, but the temperature sensor, positioned on the topmost layer, only detects the event once the upper portion of the sample freezes. This spatial mismatch introduces a measurable delay between the actual start of freezing and its detection. Furthermore, the physical placement of the sensor did not always guarantee optimal contact with the absorbent material, resulting in incomplete or underestimated ΔT values. In some trials, the exothermic curve was not detected at all, particularly in configurations with fewer layers, possibly due to insufficient thermal signal.

Among all tested configurations, the 8-layer sample emerged as the most balanced. It produced consistent and clearly detectable exothermic signals ($\overline{\Delta T} = 0.55 \text{ }^{\circ}\text{C}$)¹, while maintaining a moderate response time ($\overline{\Delta t} = 5.3 \text{ s}$). In contrast, the 16-layer samples, although producing the strongest thermal signatures ($\overline{\Delta T} = 0.95 \text{ }^{\circ}\text{C}$), required significantly longer times to freeze ($t_{i,exo} > 440 \text{ s}$). Such delays reduce their practicality for rapid detection systems. On the other end, the 1- and 2-layer configurations exhibited weaker thermal responses ($\overline{\Delta T} = 0.23 \text{ }^{\circ}\text{C}$ and $0.05 \text{ }^{\circ}\text{C}$, respectively) and lacked reliability, with several undetected events and high variability.

In summary, while increasing the number of layers enhances the detectability of the exothermic peak, it also slows down the freezing process. The 8-layer configuration represents the optimal trade-off, combining clear and reproducible thermal signals with a reasonably short detection time. This makes it the most suitable choice for future designs focused on timely and reliable identification of the phase change event.

¹ For detailed experimental data, shown in comprehensive results tables for Experiment 2, visit Annex C2.

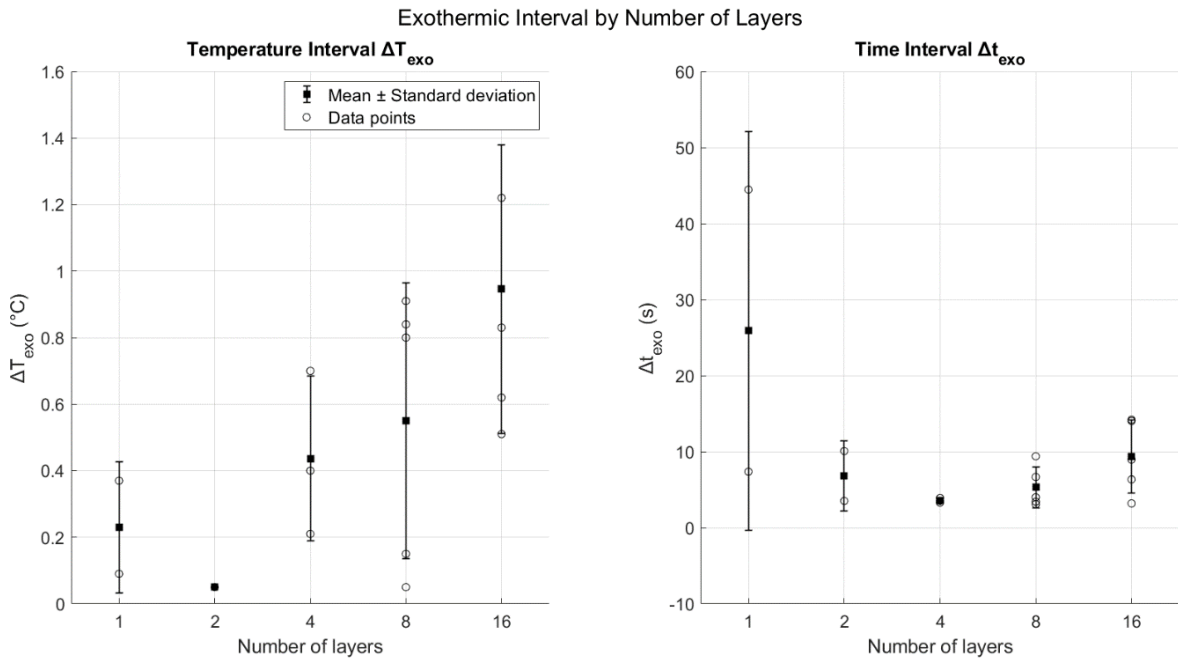


Figure 5.13. Statistical summary of Experiment 2, showing individual data points, mean values, and standard deviations for each sample type. The x-axis indicates the experimental group (1, 2, 4, 8 and 16 layers); the y-axis refers to the type of data analyzed. Author's own work.

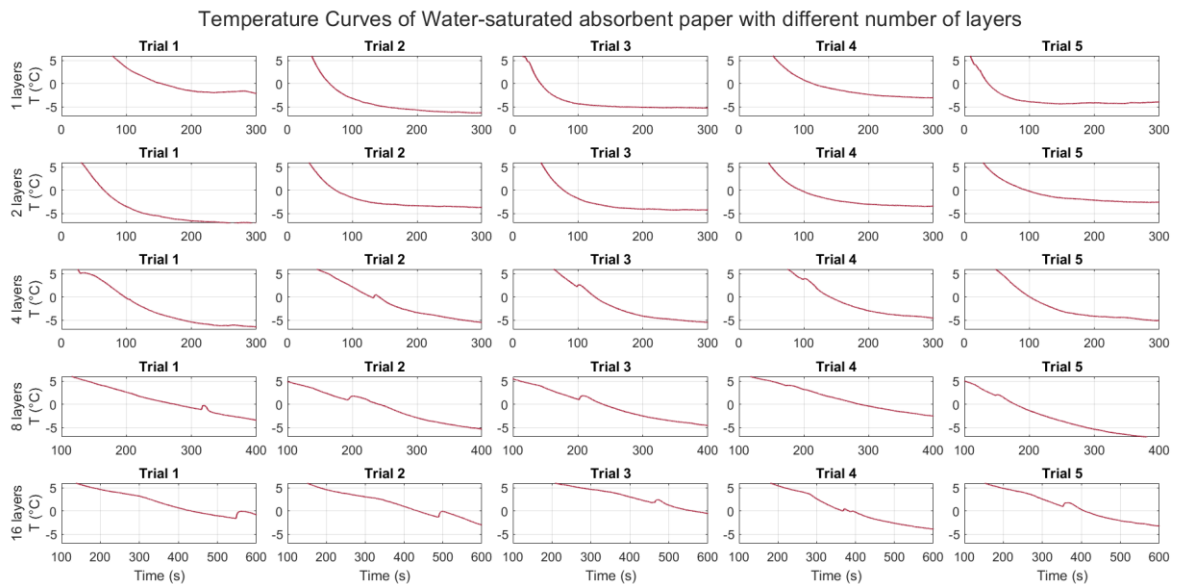


Figure 5.14. Temperature curves of water-saturated absorbent paper samples with varying numbers of layers; the x-axis represents time (s), and the y-axis represents temperature (°C). Author's own work.

To evaluate the performance of the 8-layer absorbent paper configuration, identified as the optimal compromise between detection speed and thermal signal clarity, a total of 30 independent trials were conducted. Following the analysis and classification of the data from Experiment 2¹, the resulting confusion matrix is presented in Table 5.1.

Table 5.1. Confusion matrix summarizing the classification outcomes for the 30 trials conducted using the 8-layer absorbent paper configuration in Experiment 2.

$n = 30 + 0 = 30$	<i>Predicted Positive (PP)</i>	<i>Predicted Negative (PN)</i>
<i>Actual Positive (AP)</i>	$TP = 23$	$FN = 1$
<i>Actual Negative (AN)</i>	$FP = 6$	$TN = -$

This table allowed to compute the performance metrics of the gold standard followed in this thesis:

- Precision (positive predictive value):

$$\text{Precision} = \frac{TP}{TP + FP} \quad (\text{Eq. 5.4})$$

Using (Eq. 5.4), it can be calculated that the precision is 0.793, which indicates that 79.3 % of detected events were true exothermic events associated with freezing.

- Recall / Sensitivity (true positive rate):

$$\text{Sensitivity} = \frac{TP}{TP + FN} \quad (\text{Eq. 5.5})$$

The system correctly identified 95.8 % of all actual freezing events.

- Accuracy:

$$\text{Accuracy} = \frac{TP + TN}{n} \quad (\text{Eq. 5.6})$$

As all samples underwent freezing, no true negatives were recorded, which slightly limits the interpretability of this metric.

- F1 Score (harmonic mean of precision and recall):

$$F1 = 2 \frac{\text{Precision} \cdot \text{Sensitivity}}{\text{Precision} + \text{Sensitivity}} \quad (\text{Eq. 5.7})$$

The F1 score provides a balanced measure of precision and sensitivity, yielding 85.2 %.

¹ For detailed experimental data, refer to Annex C2.

Exothermic peaks were successfully detected in 27 out of 30 trials, Figure 5.15., yielding a detection success rate of 90 %. Among the detected peaks:

- 23 trials (76.7 %) featured valid exothermic peaks consistent with physiological freezing, occurring below 4 °C with sufficient thermal amplitude and duration.
- 6 trials (20 %) showed false-positive signals, often attributed to minor thermal fluctuations, poor thermal contact, or delayed onset of freezing near or above 4 °C.
- 1 trial (3.3 %), failed to detect any peak despite freezing (false negative), possibly due to sensor misalignment or heterogeneous hydration.

These findings demonstrate that the 8-layer configuration provides high sensitivity (95.8 %) and strong detection fidelity ($F1 = 86.7\%$), making it well-suited for monitoring freezing events. The observed FP rate suggests further improvements in thresholding or noise rejection may enhance specificity.

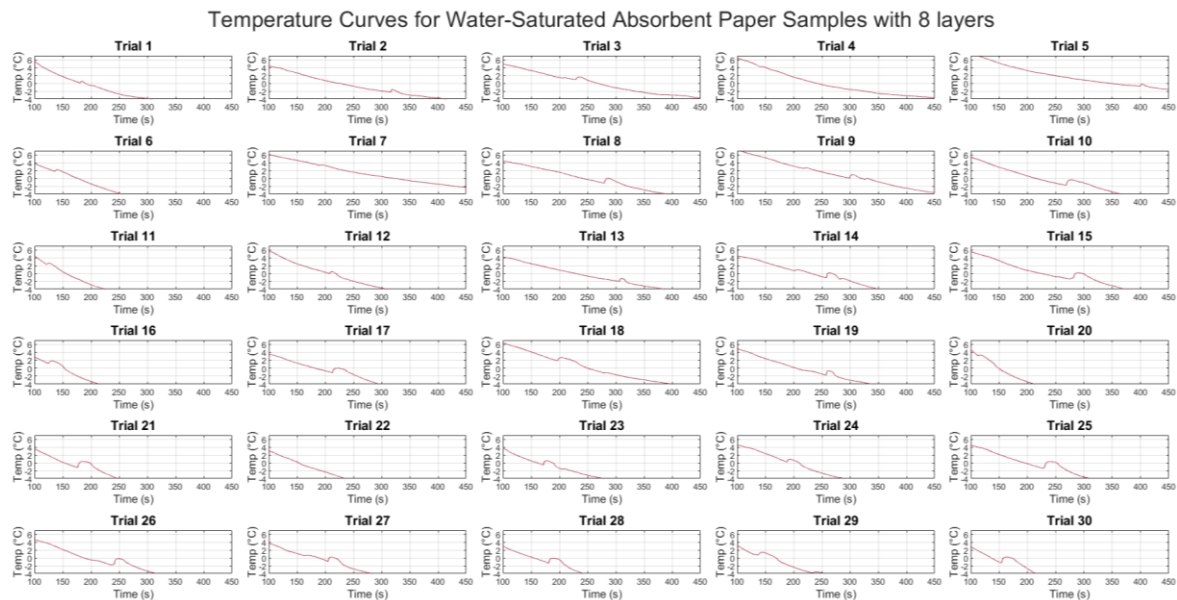


Figure 5.15. Temperature curves from 30 trials using 8-layer absorbent paper samples. The x-axis represents time (s), and the y-axis represents temperature (°C). Author's own work.

5.2.2.2. Conclusions

- Increasing the number of absorbent paper layers enhances the detectability of exothermic peaks during freezing, due to greater thermal mass and water content.
- Thicker samples delay the detection signal due to both thermal inertia and sensor placement.
- Among all configurations, the 8-layer sample offered the optimal compromise between detection speed and signal clarity, with a $\overline{\Delta T}$ of 0.55 °C and average detection delay Δt of 5.3 s.

Therefore, the 8-layer configuration was selected as the optimal design for future applications, as it ensures timely and reliable detection of freezing events in hydrated porous materials.

5.2.3. Experiment 3: Plate Separation Distance Optimization

5.2.3.1. Results

As shown in Figure 5.16, ΔC consistently decreased as d increased. The largest average change, $\Delta C = 0.5$ pF, occurred at 1 cm, while the lowest, $\Delta C = 0.02$ pF, was observed at 5 cm¹. This trend is further visualized in Figure 5.17, where both individual data points and means across five trials per distance are plotted. An exponential decay model clearly fits the data more accurately than a linear regression, with an $R^2 = 0.889$ compared to $R^2 = 0.516$, indicating that the relationship between distance and sensitivity is nonlinear and contradicting the theoretical inverse-linear model derived from ideal parallel-plate capacitor theory, (Eq. 4.10).

This deviation from the theoretically expected inverse-linear trend, derived from the parallel-plate capacitor model, can be attributed to fringing field effects. These effects become dominant when the separation distance d is comparable to or larger than the smallest electrode dimension. In such scenarios, electric field lines extend beyond the confined parallel-plate area, increasing the effective dielectric interaction and introducing nonlinear capacitance behavior. This is particularly relevant in this experiment, where the electrodes have small dimensions (1.5 cm × 2 cm); fringing becomes significant especially for $d > 2$ cm, distorting the ideal behavior.

The statistical analysis in Table 5.2 also reveals that the $CV(\Delta C)$ is highest at 1 cm (30.79 %), and progressively decreases with distance. This suggests that while smaller separations increase sensitivity, they also amplify measurement variability, primarily due to increased susceptibility to positioning errors. At very close distances, minor misalignments in plate placement can cause large deviations in the overlapping area and electric field uniformity, significantly affecting capacitance readings.

Table 5.2. Statistics summary of Experiment 3 results.

d (cm)	\bar{C}_{base} (pF)	$\sigma(C_{base})$ (pF)	$CV(C_{base})$ (%)	\bar{C}_{peak} (pF)	$\sigma(C_{peak})$ (pF)	$CV(C_{peak})$ (%)	$\bar{\Delta C}$ (pF)	$\sigma(\Delta C)$ (pF)	$CV(\Delta C)$ (%)
1	2.678	0.036	1.34	3.178	0.141	4.45	0.5	0.154	30.79
2	2.377	0.003	0.14	2.44	0.017	0.69	0.064	0.018	28.06
3	2.25	0.003	0.13	2.286	0.017	0.73	0.036	0.015	42.56
4	2.188	0.002	0.1	2.216	0.005	0.24	0.028	0.004	15.15
5	2.146	0.002	0.12	2.166	0.005	0.25	0.02	0.007	32.29

Linear fit equation: $y = -0.100x + 0.429$ $R^2 = 0.516$
Exponential fit equation: $y = 3.404e^{-1.919x}$ $R^2 = 0.889$

¹ To see the table with all the data of Experiment 3, visit Annex C3.

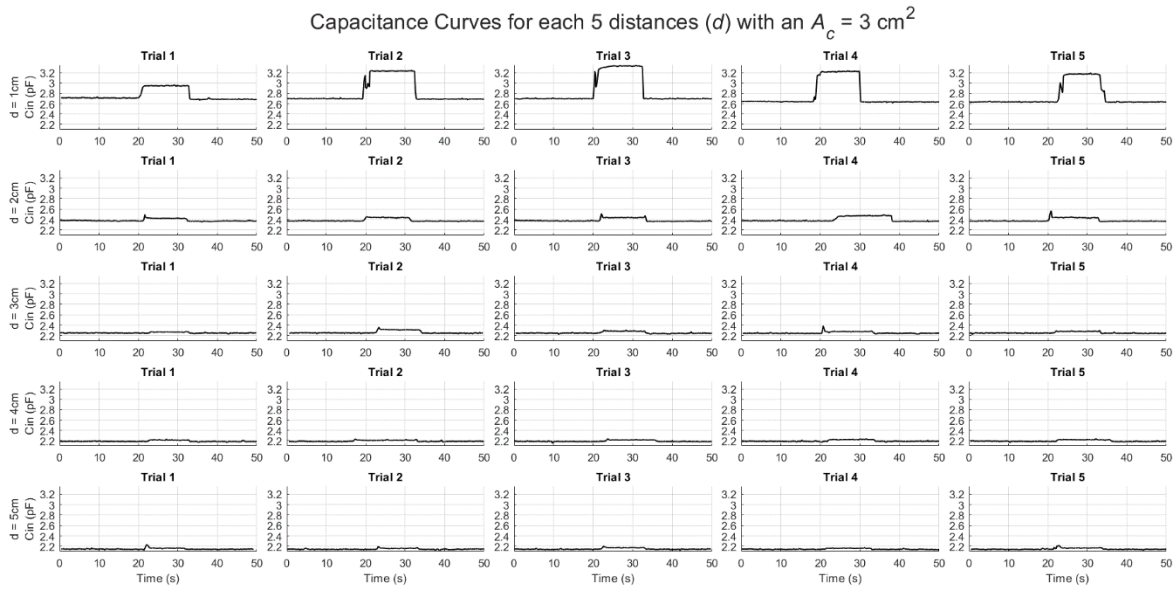


Figure 5.16. Capacitance curves for five different electrode separation distances using a sensing area of $A_C = 3 \text{ cm}^2$. Each subplot shows one of five trials per distance. The x-axis represents time in seconds (s); the y-axis shows C_{in} (pF). Distance between electrodes, d , is given in centimetres (cm). Author's own work.

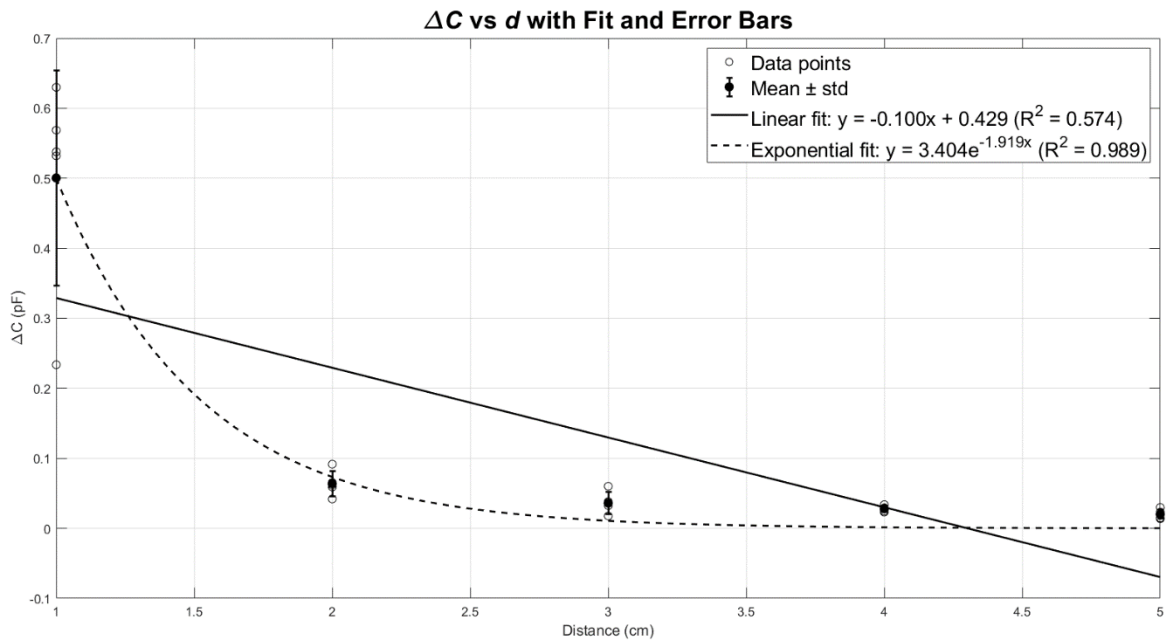


Figure 5.17. Capacitance variation (ΔC) as a function of electrode separation distance for a $A_C = 3 \text{ cm}^2$. Data points (hollow points) represent the mean change across five trials per distance. The mean (solid points) and its standard deviation (error bars) are also shown. Both linear (solid line) and exponential (dashed line) fits are shown to evaluate the trend. The x-axis represents distance (cm), and the y-axis represents change in capacitance (pF). Author's own work.

5.2.3.2. Conclusions

- ΔC decreases with distance, following an exponential decay trend ($R^2 = 0.889$).
- The expected inverse-linear relationship fails due to fringing field effects, especially pronounced for small electrodes and $d > 2$ cm
- Sensitivity is maximized at shorter distances (1 cm) but comes with significantly higher variability ($CV = 30.79\%$) due to amplified impact of positioning human errors.

Therefore, 1 cm was selected as the optimal plate distance for subsequent experiments to ensure that the system have the highest sensitivity.



5.2.4. Experiment 4: Effect of Increasing Electrode Area

5.2.4.1. Results

Figure 5.18 and Figure 5.19, illustrate the temporal and average ΔC responses, respectively. The larger electrode configuration consistently produced higher capacitance changes for all distances. The system exhibited consistently higher capacitance changes across all distances when compared to the smaller plate configuration used in Experiment 3. The larger electrode configuration consistently produced higher capacitance changes for all distances. Notably, at $d = 1\text{ cm}$, the response increased from approximately 0.5 pF to 1.45 pF , nearly tripling the sensitivity.

This confirms that increasing sensing area enhances the interaction with the dielectric medium and allegedly mitigates fringing field dominance, thereby improving the system's sensitivity to dielectric changes induced by freezing. Additionally, the improved fit of the exponential decay curve showed in Figure 5.19 has a way better R^2 value than Experiment 3 (0.987 versus 0.889), suggesting that the system's capacitance response behaves more consistently with increasing electrode area. However, the exact cause of the exponential trend remains unclear, and the influence of fringing fields on the measurements cannot be conclusively determined from the current data.

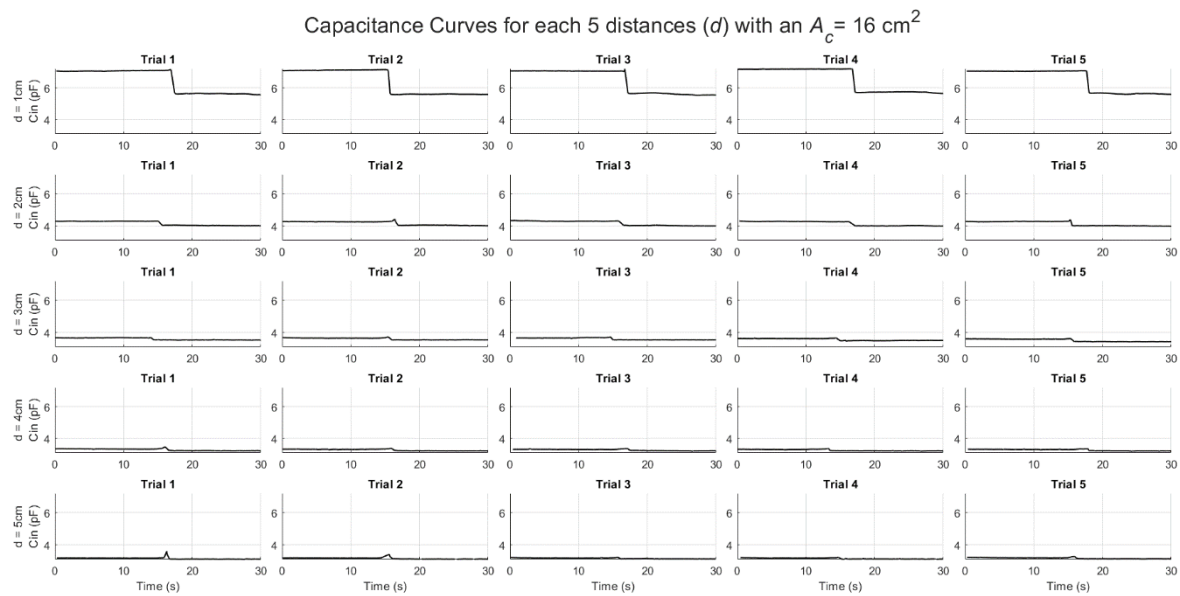


Figure 5.18. Capacitance curves for five different electrode separation distances using a sensing area of $A_c = 16\text{ cm}^2$. Each subplot shows one of five trials per distance. The x-axis represents time in seconds (s); the y-axis shows $C_{in}\text{(pF)}$. Distance between electrodes, d , is given in centimetres (cm). Author's own work.

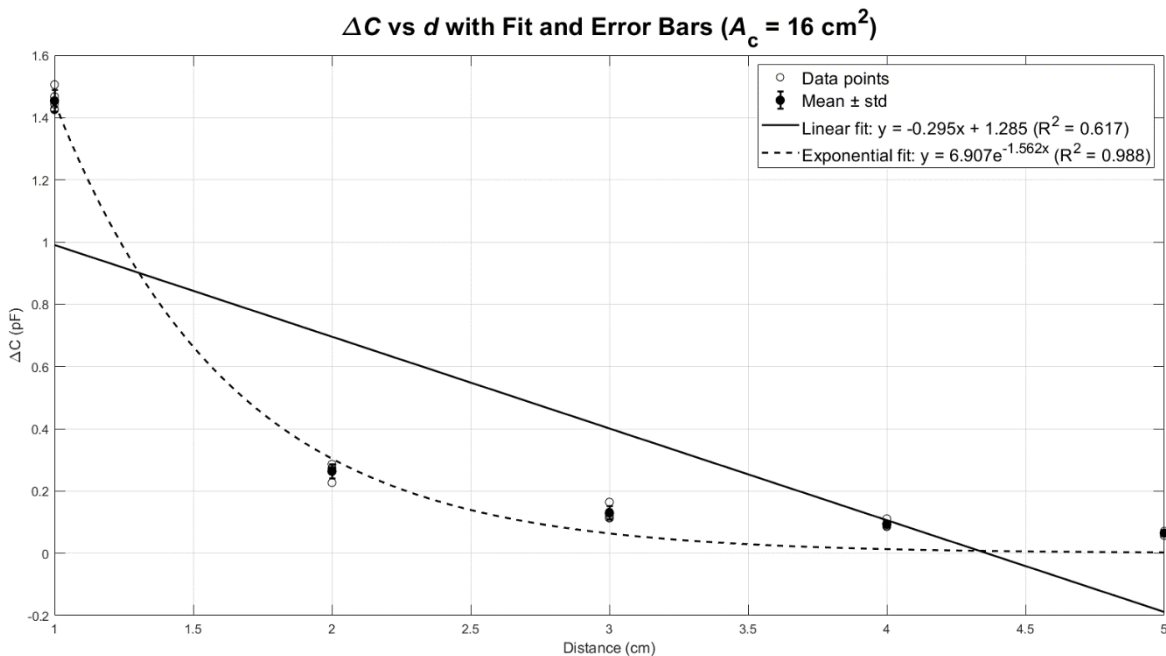


Figure 5.19. Capacitance variation (ΔC) as a function of electrode separation distance for a $A_C = 16 \text{ cm}^2$. Data points (hollow points) represent the mean change across five trials per distance. The mean (solid points) and its standard deviation (error bars) are also shown. Both linear (solid line) and exponential (dashed line) fits are shown to evaluate the trend. The x-axis represents distance (cm), and the y-axis represents change in capacitance (pF). Author's own work.

Moreover, Table 5.3 demonstrates a marked reduction in measurement variability. At $d = 1 \text{ cm}$, the standard deviation $\sigma(\Delta C)$ decreased from 0.154 pF (Experiment 3) to 0.034 pF, and the coefficient of variation (CV) from 30.79 % to 2.33 %, indicating a significant improvement in precision and reproducibility. Furthermore, the overall reduction in standard deviations across all distances¹ further indicates an enhanced signal-to-noise ratio and measurement robustness.

Table 5.3. Statistics summary of Experiment 4 results.

d (cm)	\bar{C}_{base} (pF)	$\sigma(C_{base})$ (pF)	$CV(C_{base})$ (%)	\bar{C}_{peak} (pF)	$\sigma(C_{peak})$ (pF)	$CV(C_{peak})$ (%)	$\bar{\Delta C}$ (pF)	$\sigma(\Delta C)$ (pF)	$CV(\Delta C)$ (%)
1	7.083	0.053	0.74	5.629	0.055	0.98	1.454	0.034	2.33
2	4.28	0.017	0.4	4.016	0.012	0.3	0.264	0.022	8.4
3	3.635	0.031	0.85	3.506	0.049	1.4	0.129	0.021	16.4
4	3.317	0.013	0.4	3.223	0.004	0.13	0.094	0.01	10.6
5	3.183	0.009	0.29	3.119	0.007	0.23	0.065	0.005	7.64

$$\text{Linear fit equation: } y = -0.295x + 1.285 \quad R^2 = 0.616$$

$$\text{Exponential fit equation: } y = 6.907e^{-1.562x} \quad R^2 = 0.988$$

¹ To see the full data of Experiment 3 and 4 visit Annex C3 and C4 respectively.

5.2.4.2. Conclusions

- The $A_C = 16 \text{ cm}^2$ produced substantially higher ΔC indicating an increase of sensitivity.
- Standard deviations and CVs decreased markedly, enhancing repeatability, reducing uncertainty and electrical noise.
- Capacitance response follows an exponential decay with distance.

Therefore, 16 cm^2 was selected as the optimal plate area for subsequent experiments.

5.2.5. Experiment 5: Input Capacitance Behavior Correlated to Freeze

5.2.5.1. Results

All samples demonstrated a decrease in capacitance as they were cooled.¹ For instance, in Figure 5.20, this trend occurs between 0 s and approximately 90 s, during which the temperature does not drop below 4 °C. After the initial decrease, the slope of the $C_{in}(t)$ curve tends to approach zero. This plateau behavior is interpreted as a possible indicator of the onset of phase transition, driven by the polarization of water dipoles within the sample [80]. Subsequently, the curve typically exhibits a positive slope, reflecting an increase in capacitance.

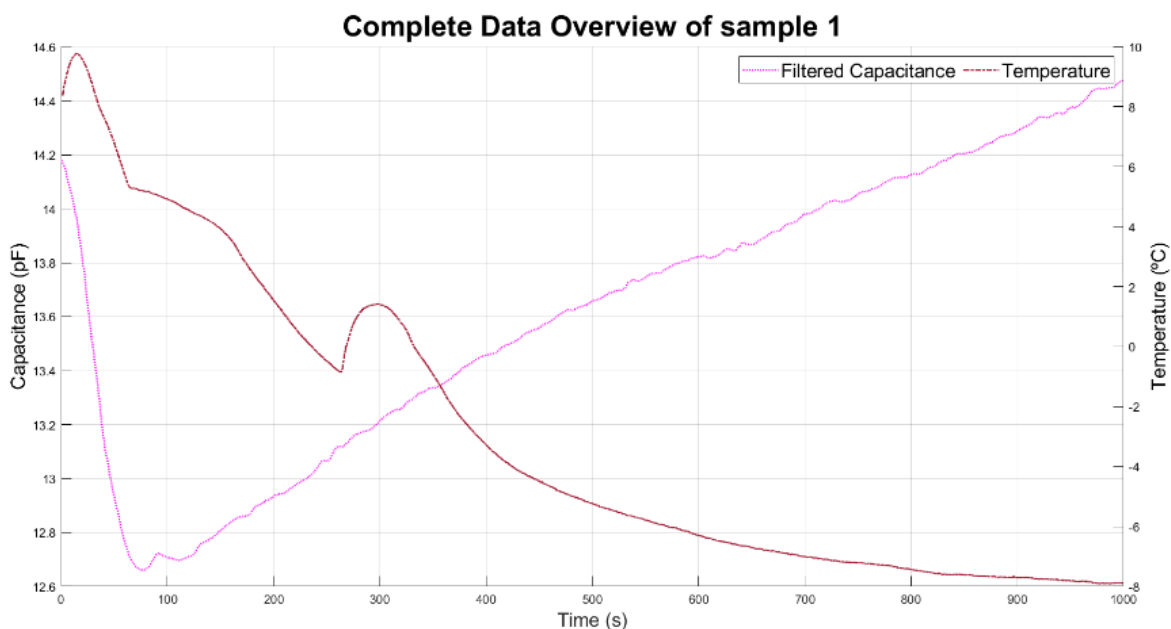


Figure 5.20. Representative output from Experiment 5, sample 1, illustrating the temperature profile $T(t)$ (solid garnet line) and the filtered capacitance input signal $\bar{C}_{in}(t)$ (dotted magenta line), obtained using a moving average filter with a window size of $W = 25$ samples. The x-axis denotes time (s); the left y-axis corresponds to capacitance (pF), and the right y-axis corresponds to temperature (°C). Author's own work.

However, this post-transition behavior is not consistent across all samples. In some cases, the capacitance slope remains near zero or even becomes negative, as seen in Figure 5.21. This variability suggests that while the general trend is observable, its exact manifestation is sample-dependent.

¹ To see the figure resultant of each trial, refer to the code of Annex B3 or the github repository of this thesis.

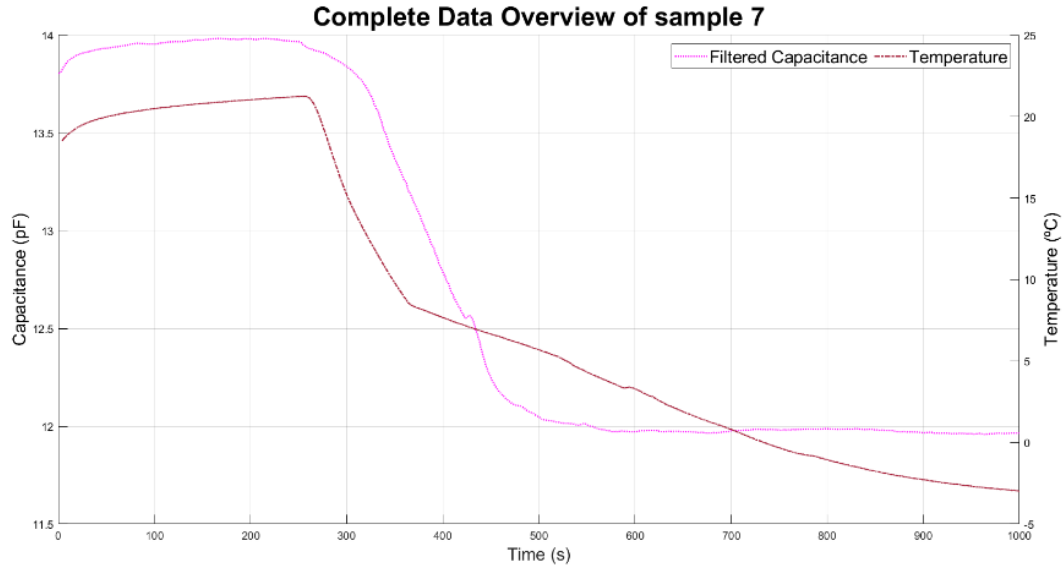


Figure 5.21. Data overview of sample 7, illustrating the temperature profile $T(t)$ (solid garnet line) and the filtered capacitance input signal $\bar{C}_{in}(t)$ (dotted magenta line), obtained using a moving average filter with a window size of $W = 25$ samples. The x-axis denotes time (s); the left y-axis corresponds to capacitance (pF), and the right y-axis corresponds to temperature (°C). Author's own work.

5.2.5.2. Detection Classification Criteria – Rationale Behind Metric Selection and Calculation

Based on the analysis of the capacitance signal $C_{in}(t)$, several characteristic points and derived metrics were identified with the objective of developing a reliable algorithm for detecting freezing events. These changes are presumed to reflect the polarization dynamics of water dipoles and the onset of freezing. Below is a detailed rationale behind each metric analysed and its computation:

5.2.5.2.1 Capacitance Difference Between Maximum and Final Value

$$\Delta C = C_i - C_f \quad (\text{Eq. 5.8})$$

Where:

- $C_i = \max(C_{in}(t))$ is the maximum observed capacitance,
- C_f is the final capacitance value at the end of the experiment.

This metric was initially considered to quantify the total change in dielectric response. However, it was found to be unreliable, as C_f did not stabilize consistently across trials. Environmental factors such as condensation on the electrodes (see Figure 5.22) caused $C_{in}(t)$ to continue increasing over time, leading to high variability and randomness in ΔC .



Figure 5.22. Photograph of water droplets being formed by condensation on top of the input electrode. Own author's photograph.

5.2.5.2.2 Capacitance Difference Between Maximum and Slope-Change Point

$$\Delta C' = C_i - C_f, \quad (\text{Eq. 5.9})$$

Where:

- $C_i = \max(C_{in}(t))$ is the maximum observed capacitance,
- C_f , is the capacitance at the point where a noticeable change in slope occurs (typically, just before freezing).

This metric was introduced to eliminate the influence of long-term drift and environmental noise. While $\Delta C'$, showed a closer relation to dipole polarization (as expected from the sharp decrease in ε_r), its reproducibility was still limited by variability between samples, yielding large confidence intervals and reducing its utility for consistent detection.

5.2.5.2.3 Slope of the Capacitance During the Exothermic Transition

$$\left. \frac{dC}{dt} \right|_{t \in [t_1, t_2]} \quad (\text{Eq. 5.10})$$

Where $[t_1, t_2]$ corresponds to the time window of the exothermic event identified from temperature data. The hypothesis was that the release of latent heat would correlate with a distinct change in $\frac{dC}{dt}$. However, across samples, the mean slope was only 0.00183 pF/s with a CV of 104 % (see Table 0.22 from Annex C5), indicating extremely poor repeatability. Likewise, the difference in capacitance between the start and end of the exothermic event had an average value of $\Delta C \approx 0.25$ pF, again with a CV of 104 %, rendering both metrics non-informative.

5.2.5.2.4 Capacitance-Temperature Ratio During the Exothermic Phase

$$\frac{\Delta C}{\Delta T} = \frac{C(t_2) - C(t_1)}{T(t_2) - T(t_1)} \quad (\text{Eq. 5.11})$$

This ratio was expected to reflect the dielectric sensitivity to temperature change during freezing. However, it showed extreme variability, with a coefficient of variation (*CV*) of 290 %, (see Table 0.22 from Annex C5), indicating that it is not suitable as a diagnostic metric in this experimental context.

5.2.5.2.5 Variance of the Capacitance Signal

By computing the standard deviation of $C_{in}(t)$ across a sliding window, W , temporal fluctuations in the signal were analyzed. In many samples, a sharp peak in $\sigma(t)$ appeared near the onset of freezing, followed by a rapid decrease and stabilization. This behavior supports the idea that microscopic changes (e.g., initial crystallization) cause increased dielectric noise, which later diminishes as the system transitions into a solid state.

5.2.5.2.6 Inflection Point in the Capacitance Curve (Slope Inversion)

This point was identified as the moment when the first derivative of $C_{in}(t)$ crosses zero from negative to positive, indicating a local minimum and potential polarization saturation:

$$\frac{dC}{dt} \Big|_{t=t^*} = 0, \text{ with } \frac{d^2C}{dt^2} \Big|_{t=t^*} > 0 \quad (\text{Eq. 5.12})$$

This point t^* proved to be consistent across most experiments and is interpreted as the end of dipolar alignment and the prelude to ice nucleation.

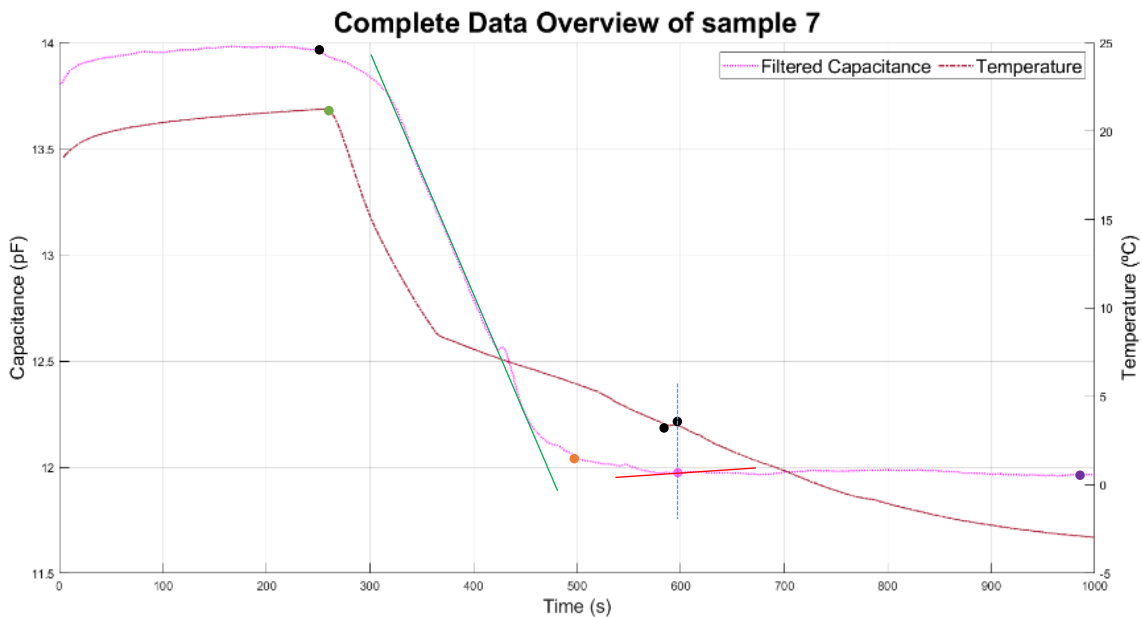


Figure 5.23. Analysed Interest Points: C_i (green point), C_f (purple point), C_f' (magenta point), $\frac{dC}{dt} \Big|_{t \in [t_1, t_2]}$ (red line), t_1, t_2 (black points), $\frac{dC}{dt} \Big|_{t=t^*} = 0$, with $\frac{d^2C}{dt^2} \Big|_{t=t^*} > 0$ (orange point). Author's own work.

5.2.5.3. Detection Classification Criteria – Relevant Characteristics

To further analyze this behavior, the derivative of the capacitance signal was computed using the gradient method, Figure 5.24. This revealed multiple peaks and valleys across the signal. However, due to the variability and noise in the raw derivative signal, a simple peak detection method based solely on zero-crossings proved insufficient and unreliable.

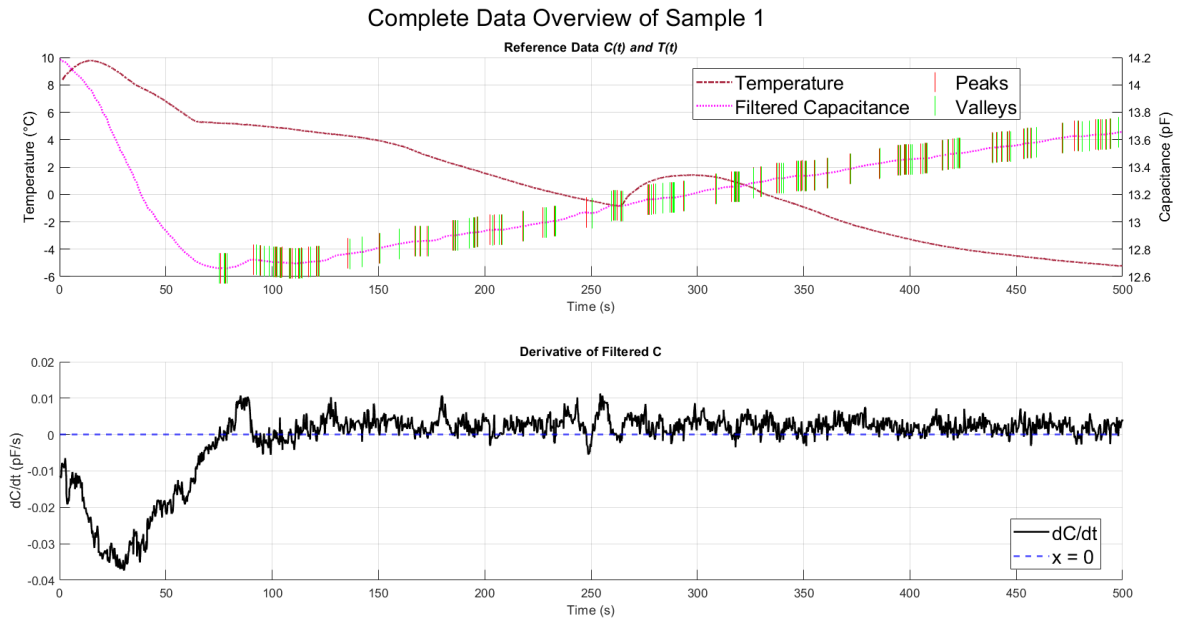


Figure 5.24. Representative output from Experiment 5, sample 1, showing the temperature profile $T(t)$ (solid garnet line) and the filtered input capacitance signal $\bar{C}_{in}(t)$ (dotted magenta line, window size $W = 25$). Peaks (red) and valleys (green) were identified using the non-averaged derivative (solid black line). The x-axis denotes time (s); the left y-axis corresponds to capacitance (pF) in the upper graph and to the derivative of capacitance over time (pF/s) in the lower graph; the right y-axis corresponds to temperature (°C). Author's own work.

To reduce noise and improve trend identification, the derivative signal was smoothed using a moving average. This smoothing reduced the number of false-positive peak/valley detections, highlighting only the most relevant changes in slope. Figure 5.25 illustrates this approach, which offers potential for algorithmic implementation based on slope change detection.¹

¹ The filter justification can be found at Section 5.1.5.4.

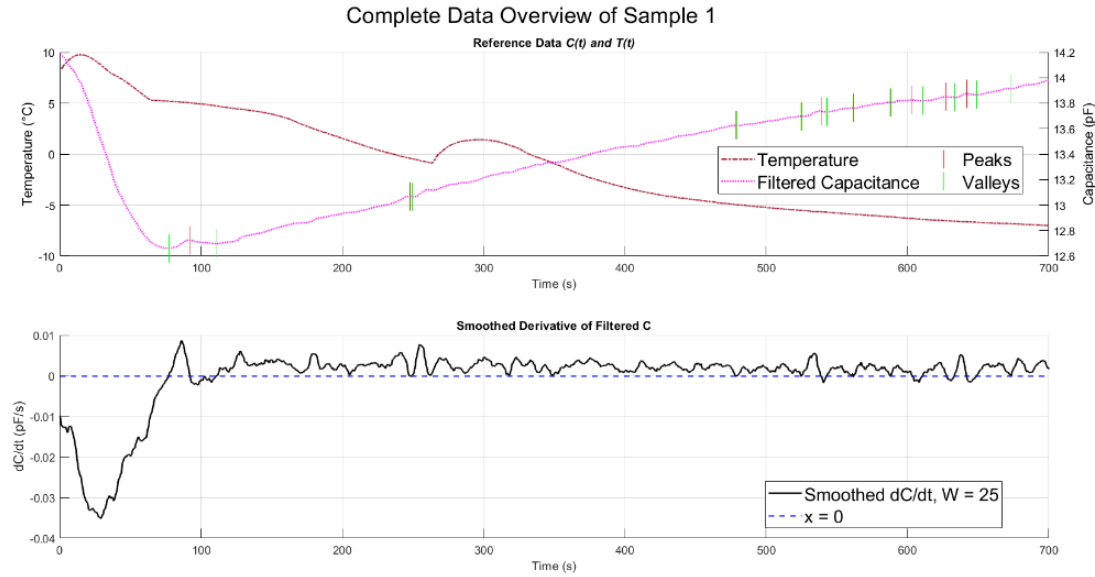


Figure 5.25. Representative output from Experiment 5, sample 1, showing the temperature profile $T(t)$ (solid garnet line) and the filtered input capacitance signal $\bar{C}_{in}(t)$ (dotted magenta line, window size $W = 25$). Peaks (red) and valleys (green) were identified using the averaged derivative (solid black line, $W = 25$). The x-axis denotes time (s); in the upper graph the left y-axis corresponds to capacitance (pF) and in the lower graph the derivative of capacitance over time (pF/s); the right y-axis corresponds to temperature ($^{\circ}$ C). Author's own work.

Further increasing the smoothing window (e.g., to $W = 99$) enabled generalization across a wider range of samples. However, this also led to detections of slope changes in regions with little analytical relevance, reducing the specificity of the approach. An example is shown in Figure 5.26.

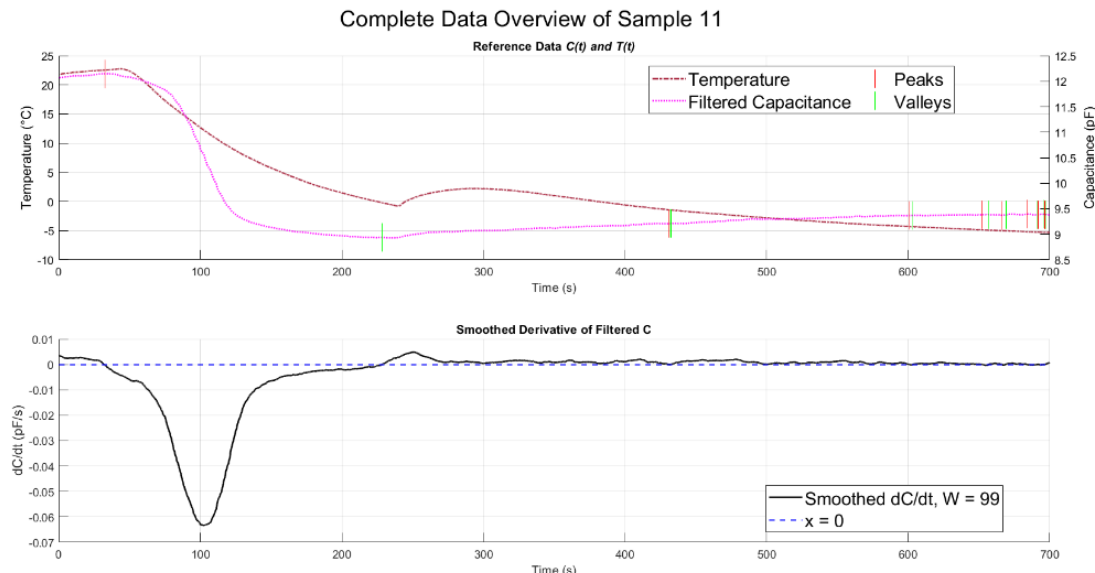


Figure 5.26. Output from Experiment 5, sample 11, showing the temperature profile $T(t)$ (solid garnet line) and the filtered input capacitance signal $\bar{C}_{in}(t)$ (dotted magenta line, window size $W = 25$). Peaks (red) and valleys (green) were identified using the averaged derivative (solid black line, $W = 99$). The x-axis denotes time (s); in the upper graph the left y-axis corresponds to capacitance (pF) and in the lower graph the derivative of capacitance over time (pF/s); the right y-axis corresponds to temperature ($^{\circ}$ C). Author's own work.

To further characterize signal behavior and improve trend detection, the standard deviation $\sigma(\bar{C}_{in}(t))$ was calculated for all samples in order to analyze the spreading of the sample. A common pattern was observed: a prominent peak in standard deviation during the initial decrease in $\bar{C}_{in}(t)$, followed by a sharp reduction to a low, stable value near the exothermic peak. This trend, shown in Figure 5.27 may indicate the start of dipole polarization and could serve as a repeatable feature for phase transition detection.

Based on this observation, an algorithm was developed to detect two key events: (1) when $\sigma(\bar{C}_{in}(t))$ exceeds an upper threshold (e.g., $th_1 = 0.02 \text{ pF}$) signaling the start of the capacitance drop, and (2) when it subsequently falls below a lower threshold (e.g., $th_2 = 0.0011 \text{ pF}$), indicating the stabilization of $\bar{C}_{in}(t)$. This approach allows for automated detection of transition points with minimal tuning across samples.

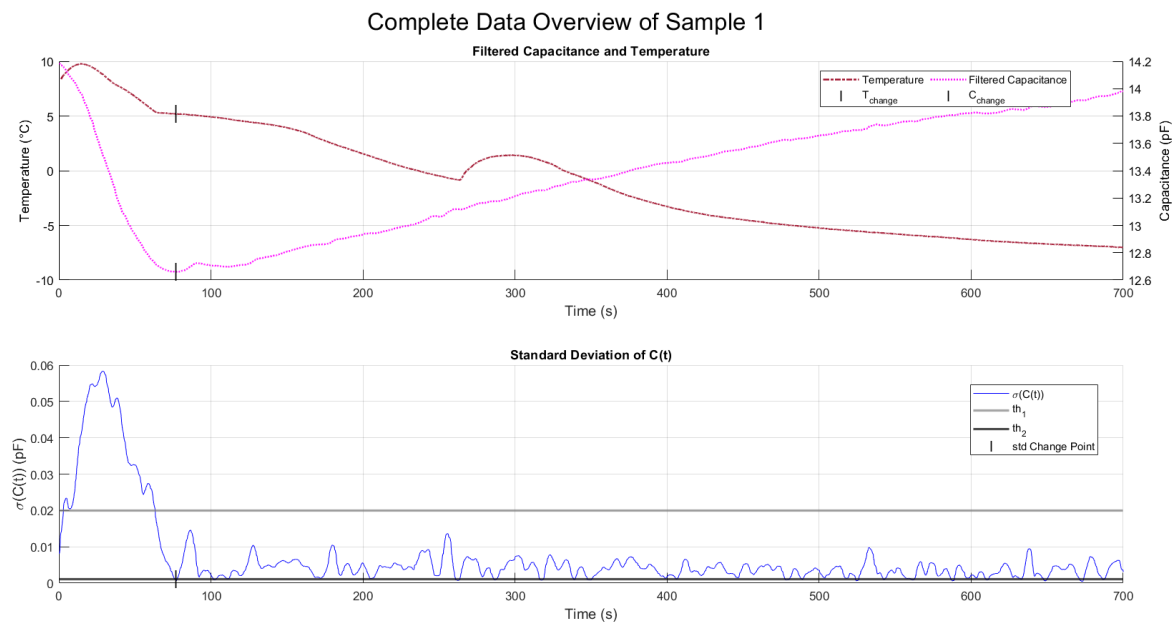


Figure 5.27. Output from Experiment 5, sample 1, showing the temperature profile $T(t)$ (solid garnet line) and the filtered input capacitance signal $\bar{C}_{in}(t)$ (dotted magenta line, $W = 25$). A change in the trend of $\bar{C}_{in}(t)$ was identified (solid black marker) using the standard deviation $\sigma(\bar{C}_{in}(t))$ (solid blue line), along with an upper threshold (solid gray line) and a lower threshold (solid black line). The x-axis denotes time (s); the left y-axis corresponds to capacitance (pF) in the upper graph and to the standard deviation of capacitance (pF) in the lower graph; the right y-axis corresponds to temperature (°C). Author's own work.

Despite these promising results, no other cross-sample features were consistently observed, such as oscillations, peak timing relative to the exothermic event, or other repeatable markers.

5.2.5.4. Proposal and Analysis of the Two Detection Algorithms

This section presents a comparative analysis of two algorithms developed for feature detection in the experimental signal.

5.2.5.4.1 Gradient-Based First-Minimum Detection

This method is designed to identify the first local minimum in the capacitance signal, which is often associated with the end of dipole alignment in water and the onset of freezing. To minimize the influence of noise and rapid fluctuations, the algorithm applies a series of averaging and gradient-based operations, as illustrated in Figure 5.28. First, the raw input signal ($C_{in}(t)$) is locally averaged ($\bar{C}_{in}(t)$) using a sliding window of defined width (W_C) to smooth out high-frequency variations. This smoothed signal is then processed with MATLAB's "*gradient()*" function to compute its numerical derivative ($\text{grad}(\bar{C}_{in}(t))$) over another window (W_G), capturing changes in the slope of the signal over time. The resulting gradient values are further averaged (\bar{G}_t) within the same windows (W_C and W_G) to provide a more stable estimate of the signal's slope behavior. The algorithm then continuously compares these averaged gradients at consecutive time points. The first instance where the gradient stops decreasing and starts increasing, i.e., when the difference between the previous and current averaged gradient becomes positive, is detected as a local minimum, referred to as the pre-freezing point.

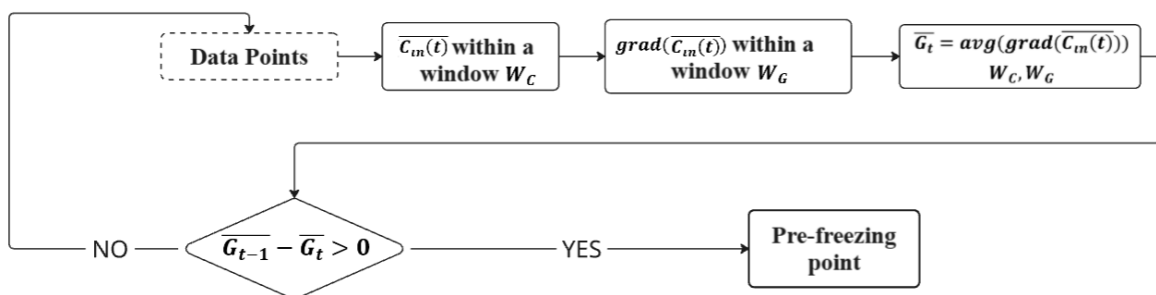


Figure 5.28. Schematic of the first-valley detection algorithm based on MATLAB's "*gradient()*". Developed by the author.

5.2.5.4.2 Standard Deviation Threshold Method

This method detects the onset of signal stabilization, believed to be associated with the transition into the freezing phase, by analyzing the local variability of the capacitance signal, Figure 5.29. The input signal ($C_{in}(t)$) is first smoothed using a moving average within a short window (W_C), resulting in the filtered signal ($\bar{C}_{in}(t)$). The algorithm then evaluates the standard deviation ($\sigma(\bar{C}_{in}(t))$) of this filtered signal within the same window. If the standard deviation exceeds an upper threshold (th_1) it indicates ongoing dynamic behavior, and the algorithm continues to scan forward. However, once the standard deviation jumps above this initial threshold, the algorithm begins a second evaluation phase. It continues averaging and checking the standard deviation at each step until it falls below a lower threshold (th_2), indicating a sustained period of minimal signal variation. This condition is taken as the detection of the pre-freezing point, marking the moment the signal has become stable enough to likely indicate phase transition onset.

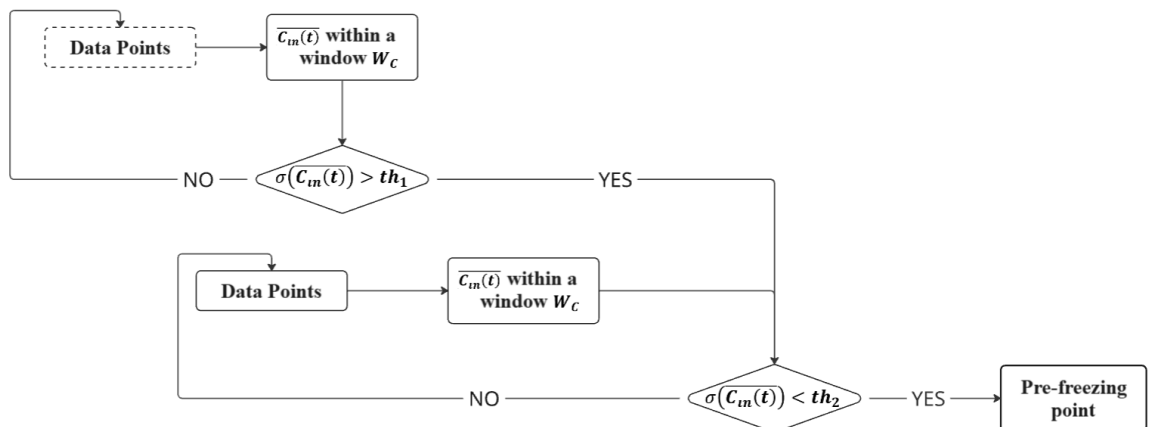


Figure 5.29. Standard deviation threshold detection algorithm schema. Author's own work.

5.2.5.4.3 Algorithms Comparative and Analysis

Figure 5.30 presents a comparative analysis of the detection performance of the two proposed algorithms, Gradient-Based Detection and Standard Deviation Thresholding, relative to the gold standard, Temperature Exothermic Peak Detection, across all experimental trials. For each method, both temperature and time detection delays are evaluated. The figure includes the mean, 95 % confidence intervals (CI), and relative uncertainty for each dataset.

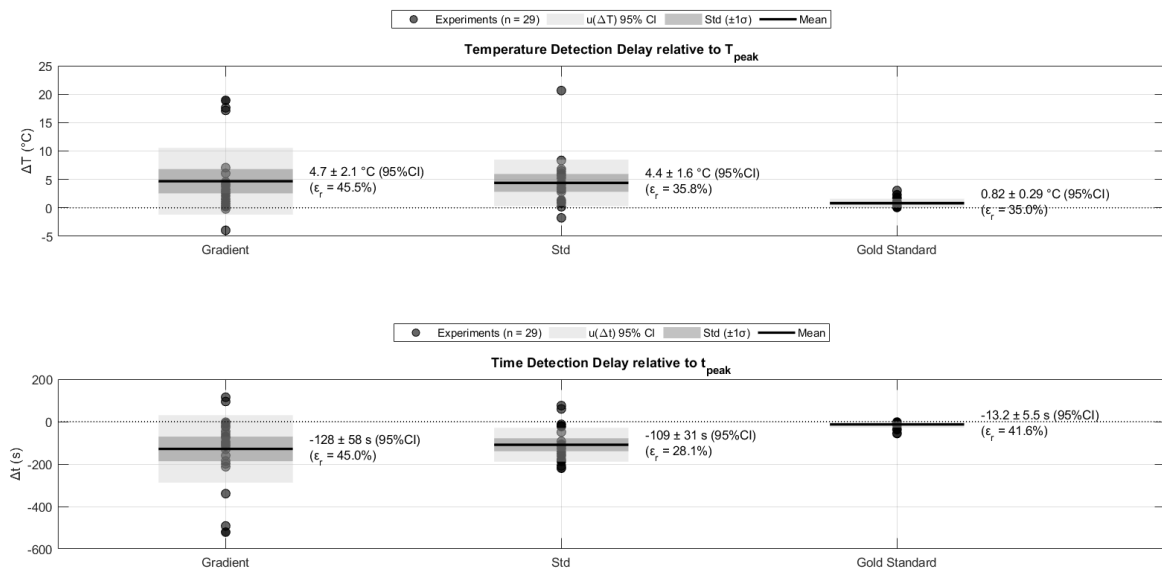


Figure 5.30. Comparison of the two proposed detection algorithms against the gold standard, based on Experiment 5 results. Each subplot presents the distribution of detection delays with mean values (solid black lines), 95 % CI (dark shaded areas), and standard deviation (light shaded areas). Scatter points represent the individual trial value. Top subplot: Temperature delay ΔT ($^{\circ}\text{C}$), defined as the difference between T_{detected} and the exothermic peak temperature T_{peak} . Bottom subplot: Time delay Δt (s), defined as the temporal offset between the detected point and the time of the exothermic peak t_{peak} . Relative uncertainty ϵ_r is also provided as a percentage of the mean value for each method. Visualization and analysis performed by the author.

The results show that both algorithms achieve comparable average detection delays. However, the Standard Deviation Threshold method demonstrates lower uncertainty, closer agreement with the gold standard, and fewer failed detections. Erroneous cases are identified by unrealistically early detections (e.g., temperature values corresponding to the experiment's starting condition) or negative detection delays, indicative of detections occurring after the exothermic peak.

Furthermore, both algorithms consistently detect events before the thermal sensor registers the exothermic peak, implying that these methods are capable of early detection of freezing onset. This is particularly relevant for applications requiring preventive measures, as the freezing front typically reaches the temperature sensor after the central and lower parts of the specimen have already frozen.

It is also observed that all methods, including the gold standard, exhibit relative uncertainties exceeding 20 %, which likely stem from human-induced variability in the experimental setup, such as differences in electrode placement, sample size, water content, and other uncontrolled parameters across trials.

In conclusion, although both detection methods produce similar average results, the Standard Deviation Thresholding algorithm is deemed more suitable for this experimental platform, due to its greater robustness, lower uncertainty, and parameter flexibility, in contrast to the Gradient method, which primarily relies on the filter window size for tuning.

5.2.5.5. Conclusions

- All samples exhibited a consistent initial drop in $\bar{C}_{in}(t)$ prior to the exothermic peak, indicating sensitivity to phase transition onset.
- The Standard Deviation Threshold method enabled robust and repeatable detection of the transition phase with minimal parameter tuning.
- The Gradient-Based method showed similar mean performance but was more sensitive to noise and filtering parameters.
- Both algorithms detected freezing events earlier than the thermal sensor, supporting their use for pre-freezing detection.
- Relative uncertainty across all methods exceeded 20 %, primarily due to experimental variability (e.g., electrode placement, sample geometry, water content).
- The standard deviation of $\bar{C}_{in}(t)$ showed a clear, repeatable peak-and-fall trend that may serve as a universal feature for freezing detection.

Based on performance, robustness, and adaptability, the Standard Deviation Threshold algorithm was selected as the preferred method for the experimental platform.

6. Detection System Proposal

Based on the experimental results, the proposed detection system prototype aims to prevent tissue damage during cryotherapy by monitoring both temperature and capacitance. The complete experimental setup, comprising the data acquisition and freezing platforms, is shown in Figure 6.1 A block diagram in Figure 6.2 further details the workflow of the prototype. Figure 6.3 presents a photograph of the prototype platform with each component clearly labeled, while Figure 6.4 provides an isometric view for a better spatial understanding of the design. Additionally, Annex 0 illustrates the electrical connections between the devices, offering a clear reference for reproducing the experiment.

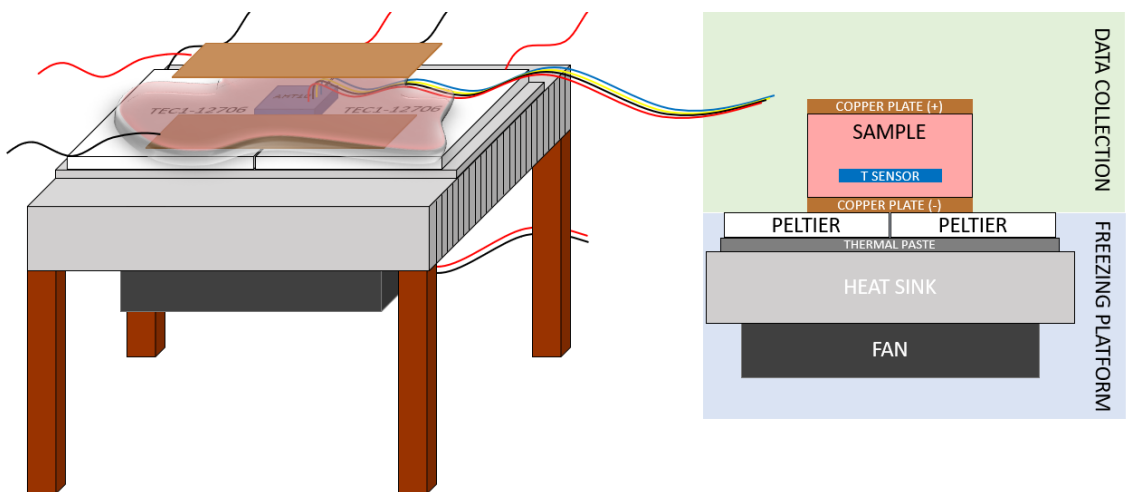


Figure 6.1. Representation of the Experimental Platform. Author's own work.

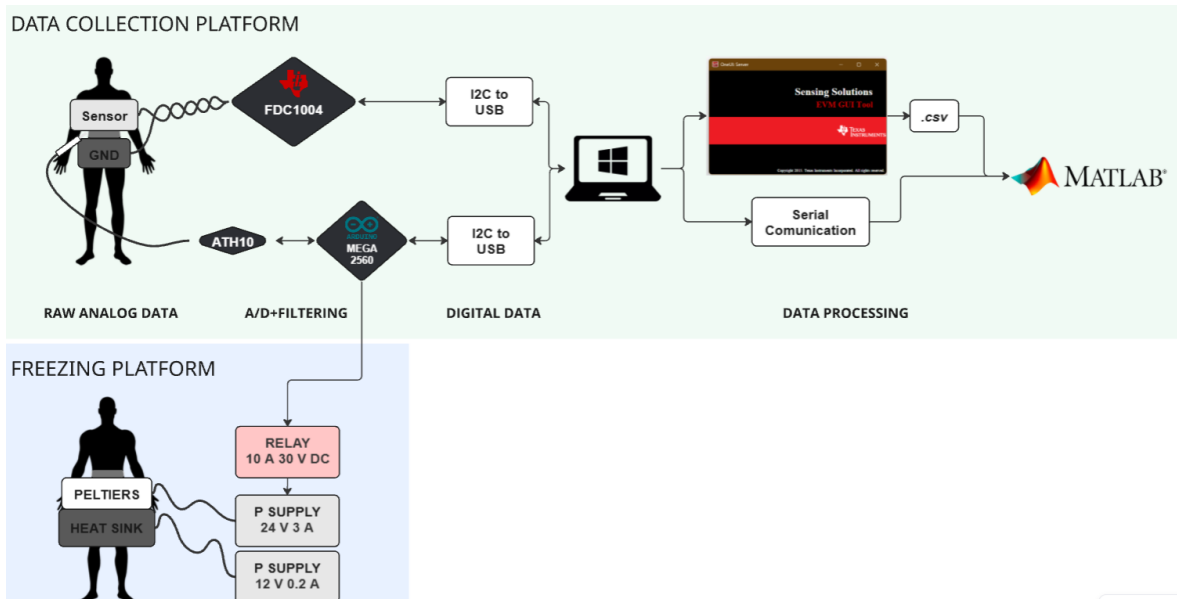


Figure 6.2. Block diagram of the proposed detection system platform, including the freezing (in blue) and the data collection (in green) platforms. Author's own work.

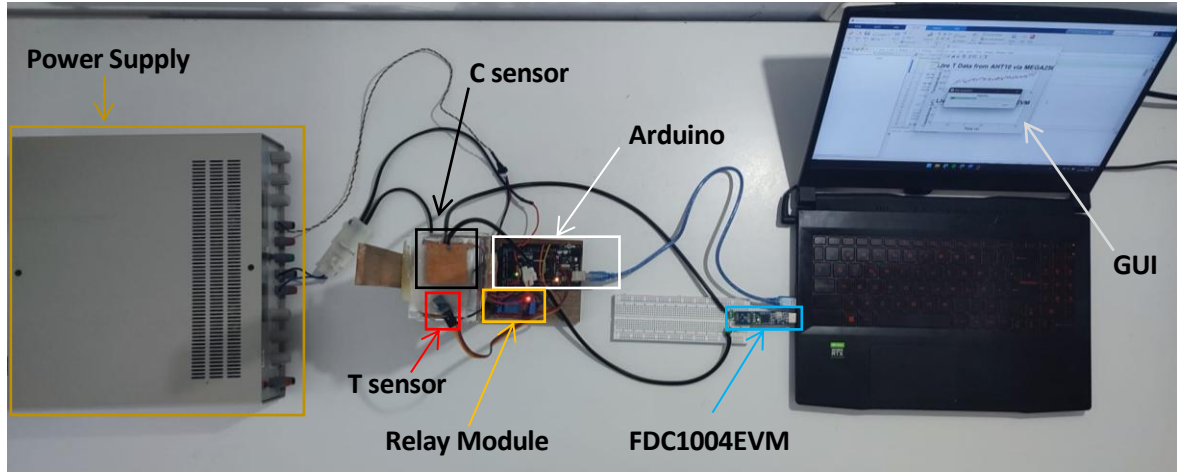


Figure 6.3. Top view of the proposed detection system platform, indicating where each element is. Author's own photograph.

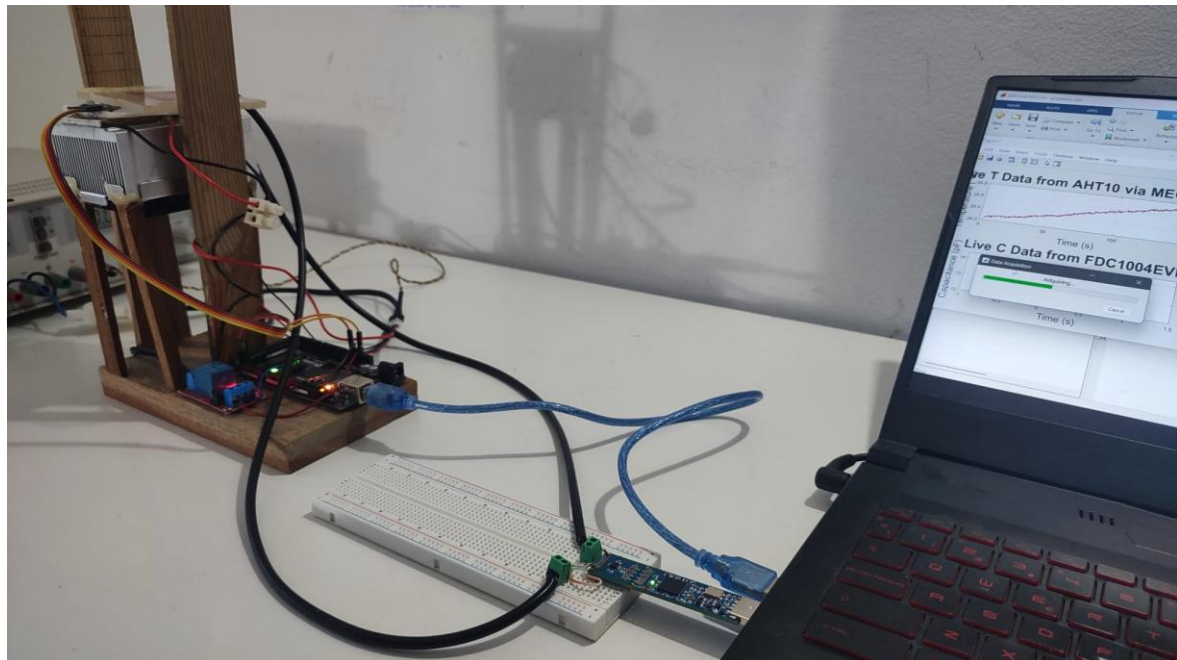


Figure 6.4. Isometric view of the proposed detection system platform built. Author's own photograph.

6.1. Freeze Detection Algorithm

As described in Section 5.2.5.4 the Standard Deviation Threshold algorithm was selected for pre-freezing detection using capacitance data. This method relies on three key parameters that must be optimized to minimize uncertainty (with 95 % confidence intervals) and reduce false detections relative to the gold standard reference point, $T_{ini,exo}$ and $t_{ini,exo}$. The optimization aims to:

- Minimize the number of detections where $\Delta T > 10 \text{ } ^\circ\text{C}$, indicating premature detection (e.g., during initial experimental conditions).
- Minimize cases where $\Delta T < 0 \text{ } ^\circ\text{C}$ or $\Delta t > 0 \text{ s}$, which would indicate detection after the exothermic peak.
- Minimize the number of trials with no detection.

These criteria will be evaluated by calculating $\Delta T \pm \varepsilon_r$ and the $\Delta t \pm \varepsilon_r$ and the difference in the number of detected points versus total trials Δn .

6.1.1. Optimization of Algorithm Parameters

To determine the optimal values of the three key parameters, window size W , upper threshold th_1 , and lower threshold th_2 , an iterative optimization procedure was implemented. The objective was to identify the parameter combination that satisfies detection requirements while minimizing the relative error and uncertainty in estimating the onset of freezing. The optimization followed a coordinate descent approach, in which two parameters were fixed while the third was varied to identify its optimal value. This process was repeated cyclically for the remaining parameters until convergence was reached, e.g. when no further improvement was observed in performance metrics.

The initial parameter values were selected heuristically, $W = 25$ samples, $th_1 = 0.02 \text{ pF}$, and $th_2 = 0.0011 \text{ pF}$, based on preliminary visual inspection of representative trials, as described in Section 5.2.5.4.2. The detection performance using this initial configuration is illustrated in Figure 5.30.

6.1.1.1. Threshold th_1 Optimization (Upper Threshold)

Preliminary analysis indicated that most freezing events could be detected using the initially proposed value of $th_1 = 0.02 \text{ pF}$. However, in some cases, especially those with greater electrode separation due to positioning inaccuracies, the drop in capacitance was less pronounced. To ensure robustness, the final value of th_1 was set to 0.017 pF , corresponding to the rounded peak of the smallest observable capacitance drop (identified in sample 6, Figure 6.5). This conservative value ensures reliable detection across all trials.



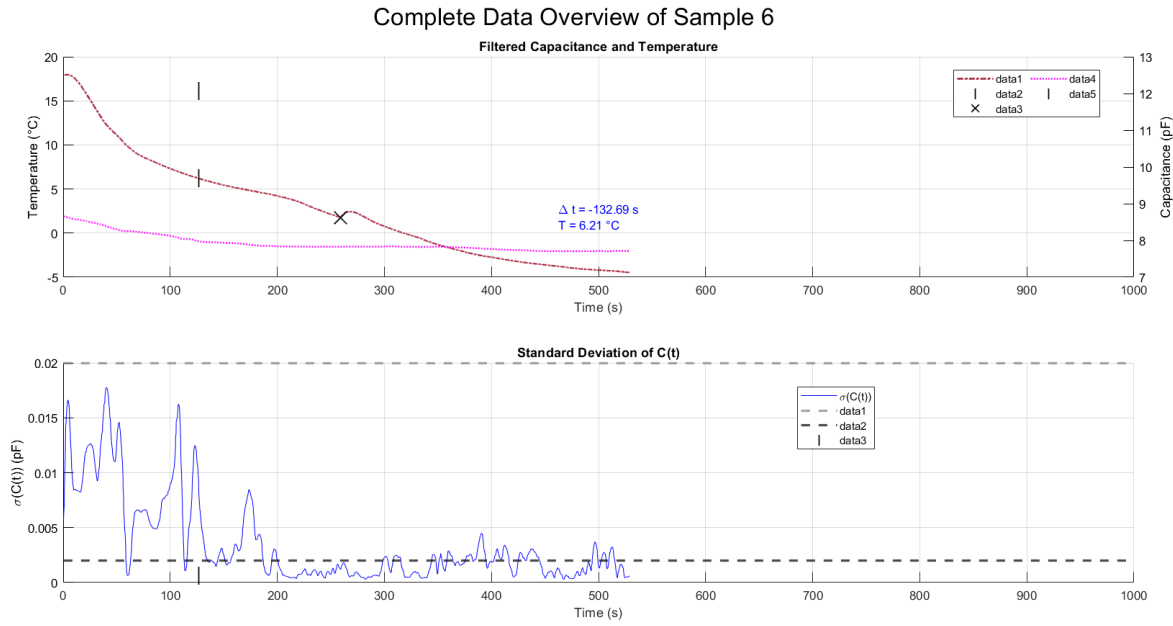


Figure 6.5. Data overview of sample 6. The temperature profile $T(t)$ (solid garnet line) and the filtered input capacitance signal $\bar{C}_{in}(t)$ (dotted magenta line, $W = 25$) are shown in the upper graph. No significant change in $\bar{C}_{in}(t)$ was detected, as the standard deviation $\sigma(\bar{C}_{in}(t))$ (solid blue line) remained below the upper threshold (solid gray line); the lower threshold (solid black line) is also shown. The x-axis indicates time (s); the left y-axis shows capacitance (pF) in the upper graph and its standard deviation (pF) in the lower graph; the right y-axis shows temperature (°C). Author's own work.

6.1.1.2. Window Size W and Lower Threshold th_2 Optimization

With th_1 fixed, an optimization of W and th_2 was performed by analysing the mean estimated ΔT (temperature difference between detection and actual freezing) and its associated 95 % confidence interval. The objective was to approach $\Delta T \approx 0$ while minimizing uncertainty, as long as the maximum number of correct detections was maintained.

Starting with $th_2 = 0.002$ pF, the optimal window size was found to be $W = 25$ samples, which maximized detection and minimized error, Figure 6.6.

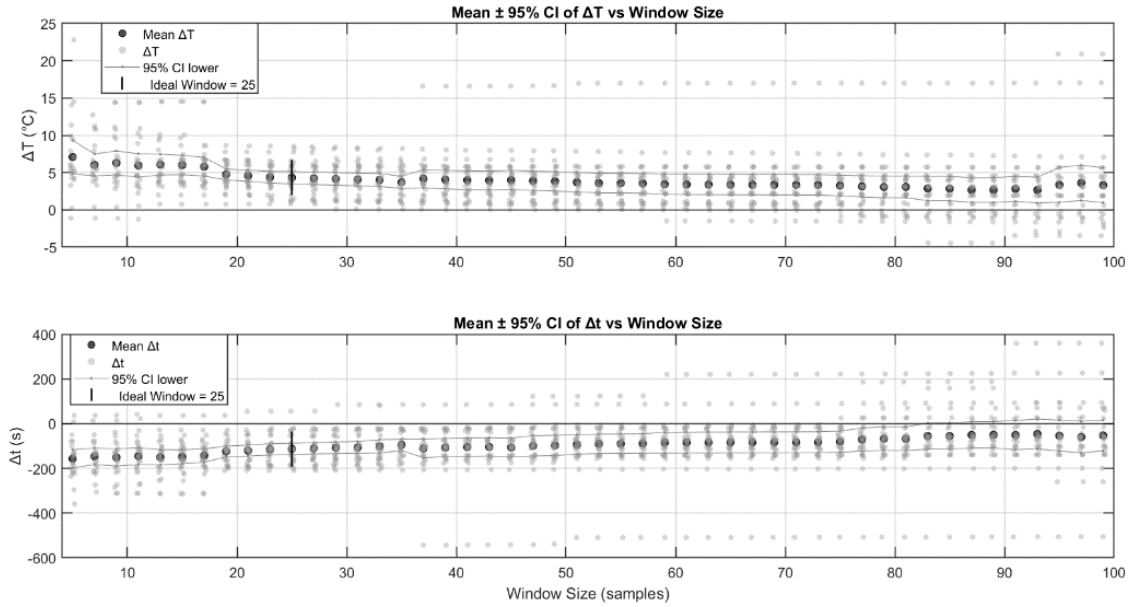


Figure 6.6. Results of the iterative parameter search. The upper plot shows the mean temperature difference $\bar{\Delta T}$ ($^{\circ}\text{C}$), and the lower plot shows the mean time delay $\bar{\Delta t}$ (s), both represented by black markers with 95 % confidence intervals (grey error bars). Individual trial values are shown as light grey points. A vertical black line indicates the selected optimal window size for a threshold $th_2 = 0.002$ pF. Author's own work.

Fixing $W = 25$, the next iteration revealed that the optimal lower threshold was $th_2 = 0.0024$ pF.

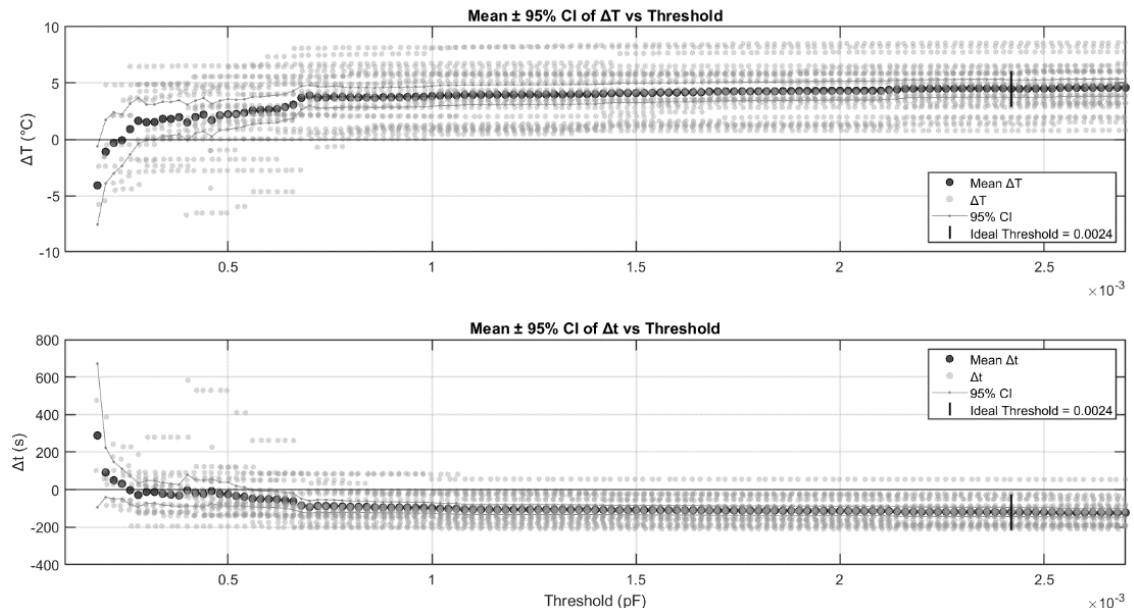


Figure 6.7. Results of the iterative parameter search. The upper plot shows the mean temperature difference $\bar{\Delta T}$ ($^{\circ}\text{C}$), and the lower plot shows the mean time delay $\bar{\Delta t}$ (s), both represented by black markers with 95 % confidence intervals (grey error bars). Individual trial values are shown as light grey points. A vertical black line indicates the selected optimal threshold th_2 for a window size of $W = 25$ samples. Author's own work.

Recalculating W for this new threshold gave an updated optimal window size of $W = 23$ samples.

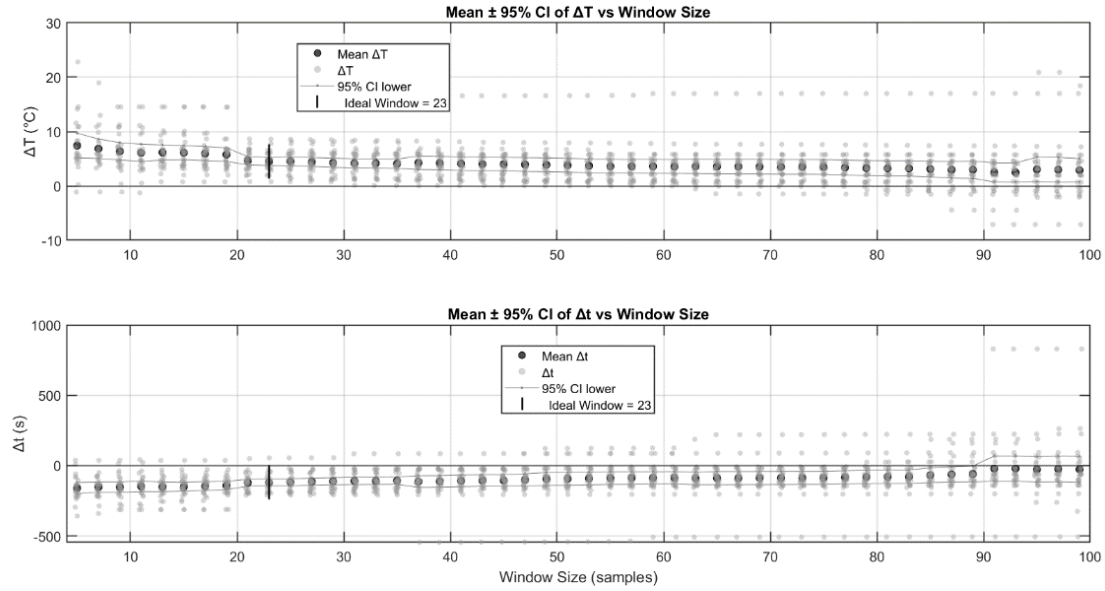


Figure 6.8. Results of the iterative parameter search. The upper plot shows the mean temperature difference $\bar{\Delta}T$ ($^{\circ}$ C), and the lower plot shows the mean time delay $\bar{\Delta}t$ (s), both represented by black markers with 95 % confidence intervals (grey error bars). Individual trial values are shown as light grey points. A vertical black line indicates the selected optimal window size for a threshold $th_2 = 0.0024$ pF. Author's own work.

A subsequent iteration for th_2 , with $W = 23$ yielded $th_2 = 0.0021$ pF, and so on.

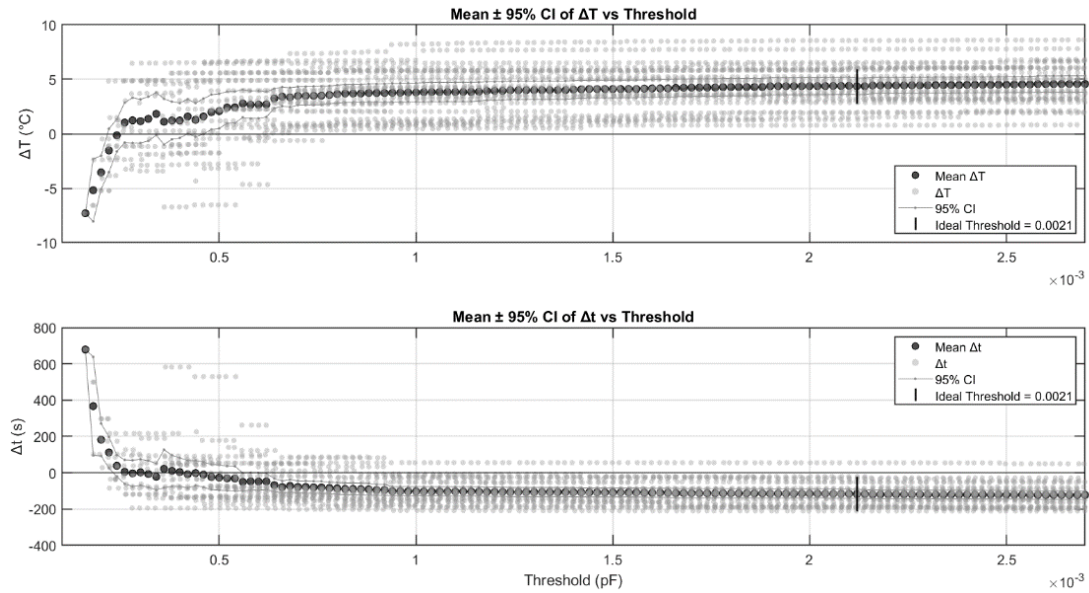


Figure 6.9. Results of the iterative parameter search. The upper plot shows the mean temperature difference $\bar{\Delta}T$ ($^{\circ}$ C), and the lower plot shows the mean time delay $\bar{\Delta}t$ (s), both represented by black markers with 95 % confidence intervals (grey error bars). Individual trial values are shown as light grey points. A vertical black line indicates the selected optimal threshold th_2 for a window size of $W = 23$ samples. Author's own work.

This iterative process revealed a loop in the parameter space: each optimization cycle would return to previously visited values, suggesting a local optimum.

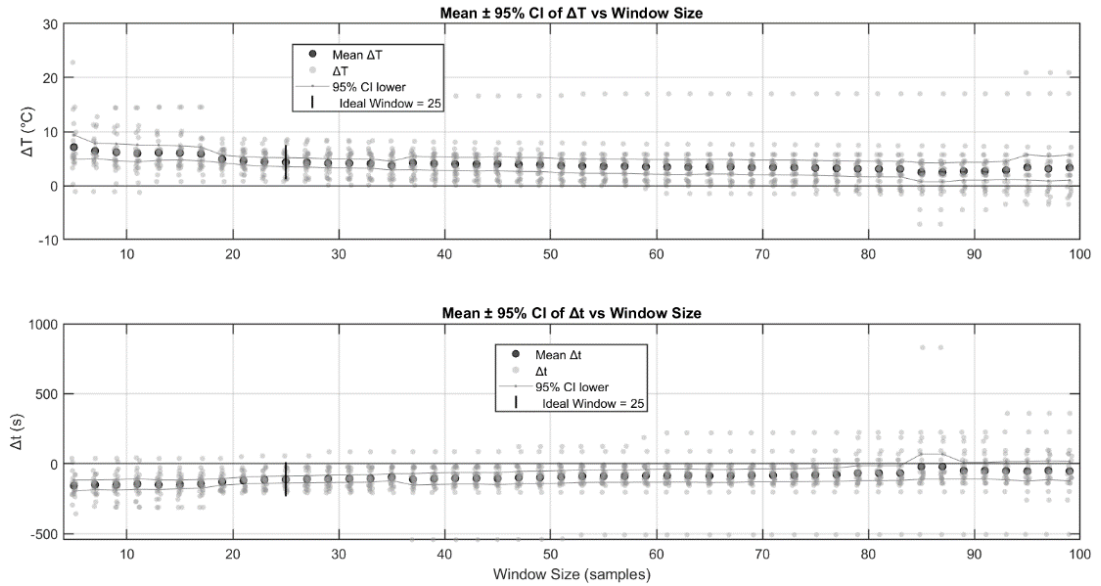


Figure 6.10. Results of the iterative parameter search. The upper plot shows the mean temperature difference $\bar{\Delta}T$ ($^{\circ}$ C), and the lower plot shows the mean time delay $\bar{\Delta}t$ (s), both represented by black markers with 95 % confidence intervals (grey error bars). Individual trial values are shown as light grey points. A vertical black line indicates the selected optimal window size for a threshold $th_2 = 0.0021$ pF. Author's own work.

To address this, a comparative plot was generated showing the performance of different parameter pairs, (th_2, W) , identified in the previous iterative analysis, Figure 6.11. While minimizing uncertainty is a key objective, the algorithm's ability to consistently detect the pre-freezing point across all trials was prioritized.

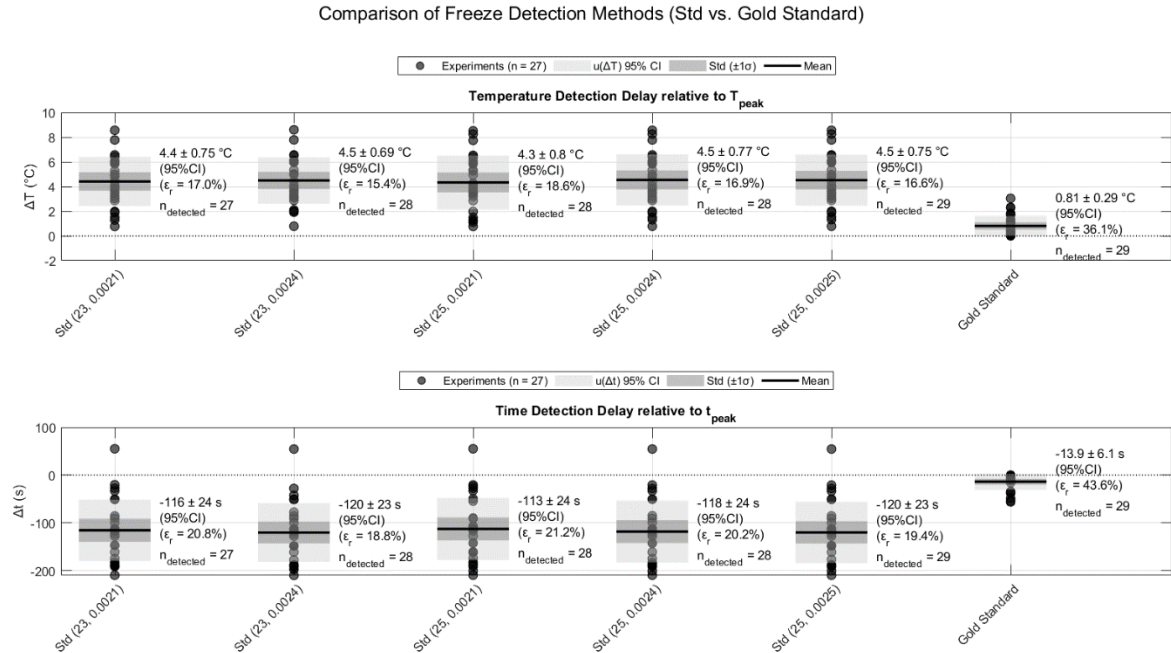


Figure 6.11. Detection delay results for different (W, th_2) parameter pairs from the optimization process, compared to the temperature-based gold standard. Each subplot shows trial delays as scatter points, with mean (black line), 95 % confidence interval (dark shade), and standard deviation (light shade). ΔT ($^{\circ}$ C), is shown above, Δt (s) below. Each pair includes relative uncertainty ϵ_r and the number of successful detections n .

Analysis by the author.



Although the configuration with a window size of $W = 23$ samples and a lower threshold $th_2 = 0.0024$ pF yielded the lowest relative error $\varepsilon_r(\Delta T) = 15.4\%$ with a $\varepsilon_r(\Delta t) = 18.7\%$, an alternative configuration with $W = 25$ samples and a lower threshold $th_2 = 0.0025$ pF was ultimately selected. Despite presenting a slightly higher relative error $\varepsilon_r(\Delta T) = 16.6\%$ with a $\varepsilon_r(\Delta t) = 19.4\%$, this configuration successfully identified a pre-freezing point in all samples (29 out of 29), whereas the uncertainty-optimized setting yielded detections in only 26 out of 29 trials.

6.1.1.3. Conclusions

The final optimized detection algorithm, applied to $n = 30$ experimental samples, yields a mean freezing detection temperature of $T = 4.5\text{ }^\circ\text{C} \pm 0.8\text{ }^\circ\text{C}$, corresponding to a relative error of $\varepsilon_r(\Delta T) = 16.6\%$ (95 % CI). The events were detected at $t = 120\text{ s} \pm 23\text{ s}$ in advance of the exothermic peak, resulting in a relative temporal error of $\varepsilon_r(\Delta t) = 19.4\%$. Only 1 out of 30 samples was not detected correctly due to the stabilization of capacitance after the exothermic peak, instead of before. This outlier can reasonably be attributed to atypical behaviour, reinforcing the potential of the method as a robust and promising approach for freezing onset detection.

6.2. Validation of the Detection System

To assess the performance of the proposed pre-freezing detection system, a statistical classification experiment was designed and conducted. This experiment utilized both positive and negative control trials to enable the construction of a confusion matrix and the calculation of key performance metrics, including sensitivity, specificity, precision, repeatability, and uncertainty.

6.2.1. Design of the Validation Experiment

6.2.1.1. Procedure

A total of $n = 45$ trials were conducted, divided as follows:

- 15 Negative Trials (*AN* – Actual Negative): In these trials, freezing was not expected. The Peltier modules were supplied with a reduced voltage ($V = 5\text{ V}$, resulting in thermal stabilization around $15\text{ }^{\circ}\text{C}$, which is safely above the freezing threshold).
- 30 Positive Trials (*AP* – Actual Positive): In these trials, freezing was intentionally induced. The Peltier modules operated at full voltage ($V = 24\text{ V}$), driving the system temperature below the freezing point to initiate the phase change.

The exothermic peak detected by the AHT10 temperature sensor served as the ground truth (or gold standard) for determining the actual onset of freezing. The general procedure for each trial was the following:

1. Assemble the system as illustrated in Figure 5.6.
2. Prepare the sample: an 8-layer, water-saturated, cellulose-based paper stack sealed in plastic.
3. Deposit the sample onto the ground electrode, ensuring good contact with it.
4. Position the top sensing electrode at the $d = 1\text{ cm}$ height mark on the column structure.
5. Apply 24 V or 5 V , depending on if it is an *AP* or *AN* trial, to each thermoelectric coolers (TECs) using the DC power supply.
6. Connect the FDC1004EVM to the computer via USB and launch the “Sensing Solutions EVM GUI” software and wait for device recognition.
7. Navigate to the Data Streaming tab and specify the data saving location
8. Start the capacitance data acquisition and connect the Arduino to a separate USB port.
9. Open the MATLAB GUI and initialize the freezing detection platform.
10. Record the data until the exothermic peak in the $T(t)$ can be detected.
11. Terminate the MATLAB GUI and save the recorded data using the “*save.m*” script.
12. Repeat the complete procedure for each trial.



6.2.1.2. Detection and Classification Criteria

Each trial was analyzed using the capacitance-based detection algorithm described in Section 6.1. The detection outcomes were compared with the ground truth to classify each trial according to the following criteria:

- Actual Negatives (*AN*) Trials:
 - o If the algorithm detects a point before the exothermic peak (*PP*), the result was labeled as a False Positive (*FP*).
 - o If no point was detected, or if detection occurred after the exothermic peak (*PN*), the result was labeled as a True Negative (*TN*).
- For Actual Positives (*AP*) Trials:
 - o If the algorithm detects a point before the exothermic peak (*PP*), the result was labeled as a True Positive (*TP*).
 - o If no detection occurred, or detection occurred after the exothermic peak (*PN*), the result was labeled as a False Negative (*FN*).

6.2.1.3. Performance Metrics

A confusion matrix was then filled with the results of the experiment and the sensitivity or recall (Eq. 5.5), accuracy (Eq. 5.6), F1 score (Eq. 5.7), precision (Eq. 5.4) were calculated. These metrics provide a quantitative evaluation of the system's ability to detect freezing onset reliably and with minimal false detections.

6.2.2. Results

6.2.2.1. Confusion Matrix and Performance Matrix

The classification results of the 45 experimental trials using the designed freezing detection system are summarized in the confusion matrix shown in Table 6.1. Each trial was categorized based on the presence or absence of an exothermic event (indicative of freezing onset) and whether the detection system correctly identified this event, following the classification criteria outlined in Section 6.2.1.2.¹

Table 6.1 Confusion matrix summarizing classification results for 45 trials.

$n = 30 + 15 = 45$	Predicted Positive (PP)	Predicted Negative (PN)
Actual Positive (AP)	$TP = 28$	$FN = 2$
Actual Negative (AN)	$FP = 2$	$TN = 13$

Using the formulas described in Chapter 5.2, the following key performance metrics were calculated:

- Precision (Positive Predictive Value): 0.9333 (Eq. 5.4), indicating that 93.33 % of detected events corresponded to true freezing-related exothermic events. This metric reflects the system's reliability in minimizing false alarms.
- Recall or Sensitivity (True Positive Rate): 0.9333 (Eq. 5.5), demonstrating that the system successfully identified 93.33 % of actual freezing events. High recall is critical in medical applications, as undetected freezing events could cause uncontrolled tissue damage due to unmonitored phase change exothermic reactions.
- Specificity (True Negative Rate): 0.8667 (Eq. 6.1), indicating that 86.67 % of non-freezing trials were correctly identified as negative. High specificity helps reduce false alarms, improving system usability.

$$\text{Specificity} = \frac{TN}{TN + FP} \quad (\text{Eq. 6.1})$$

- Accuracy (Overall Classification Rate): 0.9111 (Eq. 5.6), representing the proportion of correctly classified trials overall, indicating strong classifier coherence and performance.
- F1 Score (Harmonic Mean of Precision and Recall): 0.9333, (Eq. 5.7), confirming balanced performance, effectively minimizing false positives while maximizing true positive detections.

¹ For the full MATLAB code for classification, detection of exothermic peaks and analysis, visit Annex B7.

The results demonstrate the system's robust ability to detect freezing-related exothermic events with high precision and recall. However, the presence of two false negatives (*FN*) raises concerns in biomedical contexts. In critical applications such as criolipolysis, failing to detect a freezing event may result in uncontrolled tissue damage due to unmonitored exothermic reactions. Approximately 7 % of freezing events could potentially go undetected, posing a significant clinical risk. On the other hand, the two false positives (*FP*) might trigger unnecessary alarms or interventions, which, while less dangerous, can reduce confidence in the system and increase operational costs.

6.2.2.1.1 Statistical Significance and Confidence Intervals

To provide statistical robustness and assess reproducibility, 95 % confidence intervals (CIs) for these metrics were computed using the Wilson score interval method (Eq. 6.2). The confidence intervals indicate the range within which the true metric values are likely to lie if the experiment is repeated under similar conditions, accounting for sample variability:

$$\text{Wilson CI} = \frac{\hat{p} + \frac{z^2}{2n} \pm \sqrt{\frac{\hat{p}(1 - \hat{p})}{n} + \frac{z^2}{4n^2}}}{1 + \frac{z^2}{n}} \quad (\text{Eq. 6.2})$$

where:

- n is the sample size of the metric,
- \hat{p} is the observed proportion (e.g., precision, recall, etc.),
- $z \approx 1.96$ is the critical value from the standard normal distribution corresponding to a 95 % CI.

The confidence intervals, summarized in Table 6.2, reveal reasonably narrow ranges, indicating that the observed performance metrics are consistent and potentially reproducible under similar experimental conditions.

Table 6.2. Confidence intervals for classification metrics (Wilson score method).

Metric	Value	95 % CI Interval
Precision	0.933	[0.78, 0.98]
Recall	0.933	[0.78, 0.98]
Specificity	0.867	[0.62, 0.97]
Accuracy	0.911	[0.79, 0.96]

6.2.2.1.2 Statistical Significance: p-Value

To determine whether the system's accuracy is significantly better than random guessing, a one-sided binomial test was performed. The null hypothesis (H_0) assumes that the classifier's accuracy is no better than random chance, which corresponds to a success probability $p_0 = 0.5$ in binary classification. The alternative hypothesis (H_a) posits that the system's accuracy is greater than 50 %.

The p-value is calculated as the probability of observing at least k correct classifications out of n trials under the null hypothesis:

$$p = P(X \geq k | n, p_0) = \sum_{i=k}^n \binom{n}{i} p_0^i (1 - p_0)^{n-i} \quad (\text{Eq. 6.3})$$

where:

- p is the p-value,
- n is the total number of trials,
- k is the number of observed successes,
- p_0 is the probability of success under the null hypothesis,
- $\binom{n}{i}$ is the binomial coefficient.

Based on the confusion matrix in Table 6.1, the system correctly classified $k = 41$ out of $n = 45$ trials, yielding an observed accuracy of 91.1 %. Applying the binomial test the resulting p-value is $p < 0.0001$. This extremely low p-value strongly rejects the null hypothesis, confirming that the detection system's accuracy is statistically significantly better than random chance. These results provide robust evidence supporting the system's effective performance in detecting freezing onset.

6.2.2.2. Temporal and Thermal Characterization of Detection Events

Beyond classification accuracy, temporal and thermal analyses of detection events offer valuable insights into the consistency and reliability of the proposed system. This analysis evaluates not only whether freezing events are correctly detected but also whether detections occur consistently in time and temperature relative to the actual freezing process.¹

Figure 6.12 and Figure 6.13 illustrate representative cases: a true positive (TP) trial where freezing was correctly detected, and a true negative (TN) trial where no freezing event occurred and no false detection was triggered. The graphs display temperature $T(t)$ and filtered capacitance signal $\overline{C_{in}}(t)$, alongside detection points and exothermic peaks. The absence of detection in the TN trial confirms the system's specificity.

¹ To see all the output figures, visit the GitHub repository of this thesis.

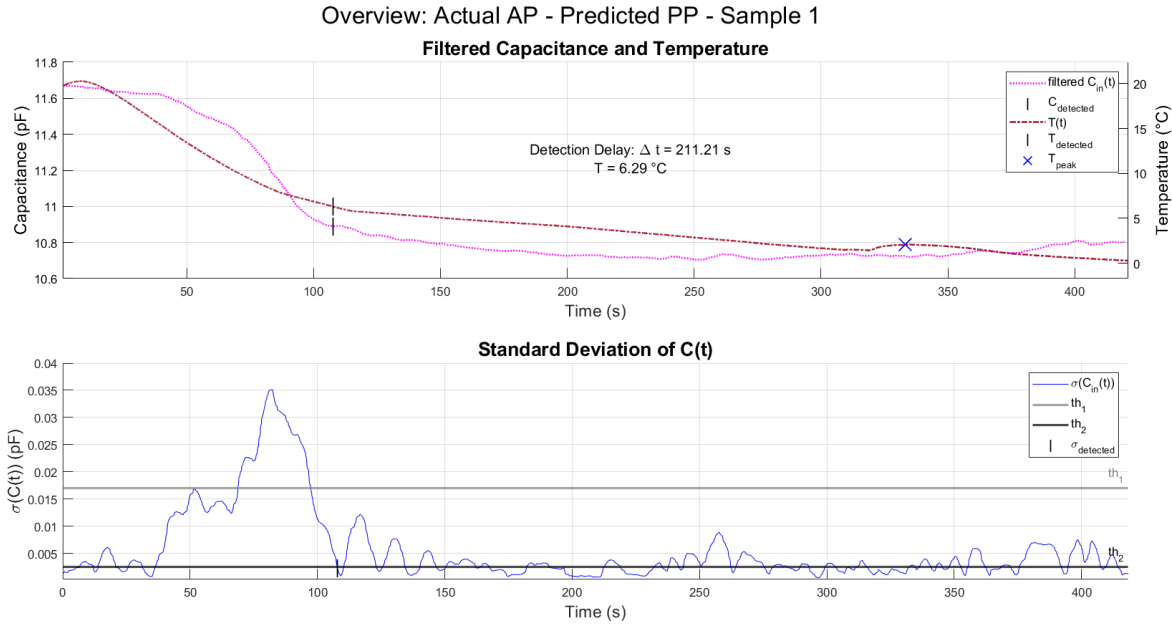


Figure 6.12. Data overview of TP sample 1: Temperature $T(t)$ (dashed garnet line, $^{\circ}\text{C}$) and filtered capacitance signal $\overline{C_{in}(t)}$ (dotted magenta line, pF; window size $W = 25$ samples). Detected points $T_{detected}$ and $C_{detected}$ and exothermic peak T_{peak} are marked. The lower graph shows standard deviation $\sigma(C_{in}(t))$ crossing upper th_1 (gray) and lower th_2 (black) thresholds. Author's own work.

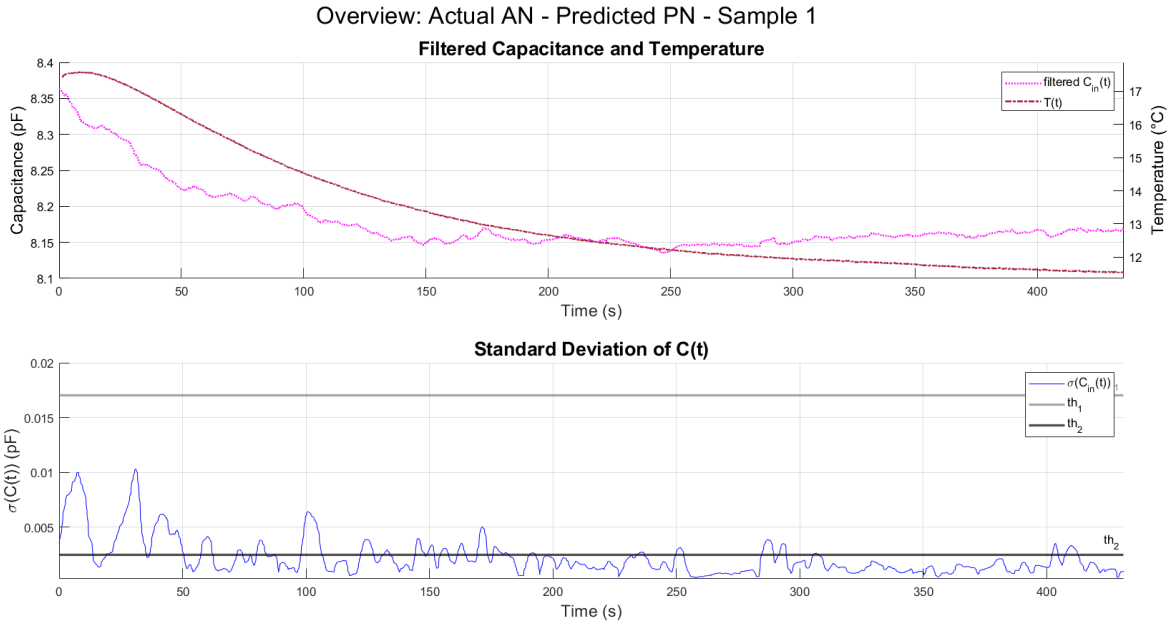


Figure 6.13. Data overview of TP sample 1: Temperature $T(t)$ (dashed garnet line, $^{\circ}\text{C}$) and filtered capacitance signal $\overline{C_{in}(t)}$, with no detection triggered. Author's own work.

To quantitatively assess detection repeatability in true positives, Figure 6.14 presents box plots of four key parameters extracted from the dataset:

- Δt : the time delay between the actual freezing onset and the detected point (s),
- ΔT : the temperature difference between the gold standard peak and the detected point ($^{\circ}$ C),
- $T_{detected}$: the temperature at the moment of detection ($^{\circ}$ C),
- $t_{detected}$: the time at which the algorithm detected the event (s).

Each subplot in 6.12. displays the full distribution of sample values (gray dots), the mean (black solid line), the standard deviation (dark gray shaded area), and the 95 % confidence interval (light gray shading). These parameters were calculated from the processed dataset using the MATLAB code provided in Annex B7, and the results are numerically summarized in Table 0.23 from Annex C6.

The analysis reveals high temporal and thermal consistency across true positive trials. Specifically, 95 % of the samples show a detection delay within the interval $\Delta t = [128, 148]$ s, with a mean value of $\bar{\Delta t} = 143$ s and an uncertainty of $u(\Delta t)_{95\%} = 11\%$. The mean temperature at which detection occurred was $\bar{T}_{detected} = 5.5 \pm 0.6$ $^{\circ}$ C (95 % CI). Furthermore, the mean temperature offset between the detected point and the exothermic peak was $\bar{\Delta T} = 4.0$ $^{\circ}$ C with $u(\Delta T)_{95\%} = 13.9\%$.

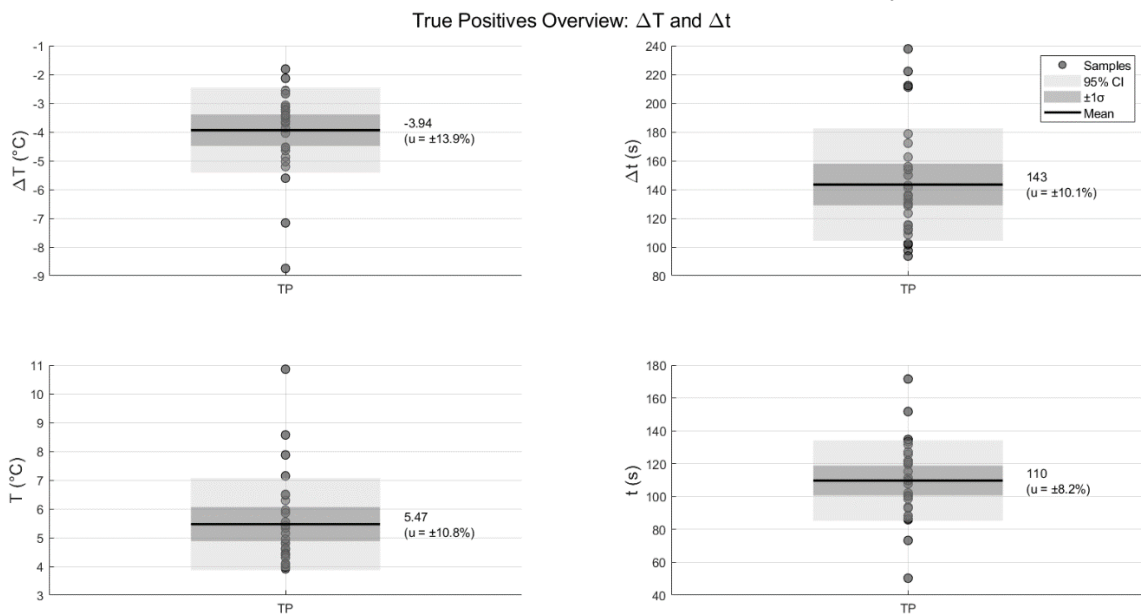


Figure 6.14. Box-and-whisker plots for TP detection parameters: ΔT (upper left, $^{\circ}$ C), Δt (upper right, s), $T_{detected}$ (lower left, $^{\circ}$ C), $t_{detected}$ (lower right, s). Each plot shows the individual sample values (gray dots), the mean (black solid line), the standard deviation (dark gray shaded area), and the 95 % CI (light gray shaded area).
Author's own work.

These findings confirm that the detection system is not only accurate but also temporally and thermally consistent, with narrow parameter spreads and tight confidence intervals, key qualities for clinical applications such as cryolipolysis.

6.2.2.2.1 Gold Standard Comparation

Although the detection algorithm shows a systematic offset relative to the gold standard, this shift should not be interpreted as a flaw but rather as a valuable anticipatory characteristic of the system. Specifically, the mean temperature at which the algorithm identified the freezing transition (T_{change}) was 5.47 °C, with a 95 % confidence interval (CI) of ± 0.59 °C, compared to 1.95 °C ± 0.34 °C for the gold standard. This 3.52 °C mean offset is clearly visible in the bottom-left panel of Figure 6.15, where the box plot reveals that algorithmic detections consistently occur at significantly higher temperatures. This apparent “early” detection is rooted in the differing nature of the two methods: while the gold standard sensor is positioned locally on the top surface of the sample, the threshold-based algorithm evaluates a broader spatial region, integrating signals indicative of bulk freezing activity. Given the vertical temperature gradient from the thermoelectric cooler (TEC) at the bottom to the sensor at the top, the algorithm’s earlier response reflects subsurface phase change activity that the surface-level sensor registers only after a delay. Furthermore, the relatively narrow distribution and tight confidence interval (as shown by the compressed interquartile range and shaded CI bands in the figure) confirm that the algorithm’s response is both consistent and statistically robust across trials. Consequently, this temporal and thermal lead time offered by the algorithm is clinically advantageous, it acts as an early warning mechanism, detecting the onset of freezing before it reaches the measurement point of the traditional sensor. This capability is particularly critical in safety-sensitive applications like cryolipolysis, where uncontrolled exothermic events must be preempted, not merely detected.

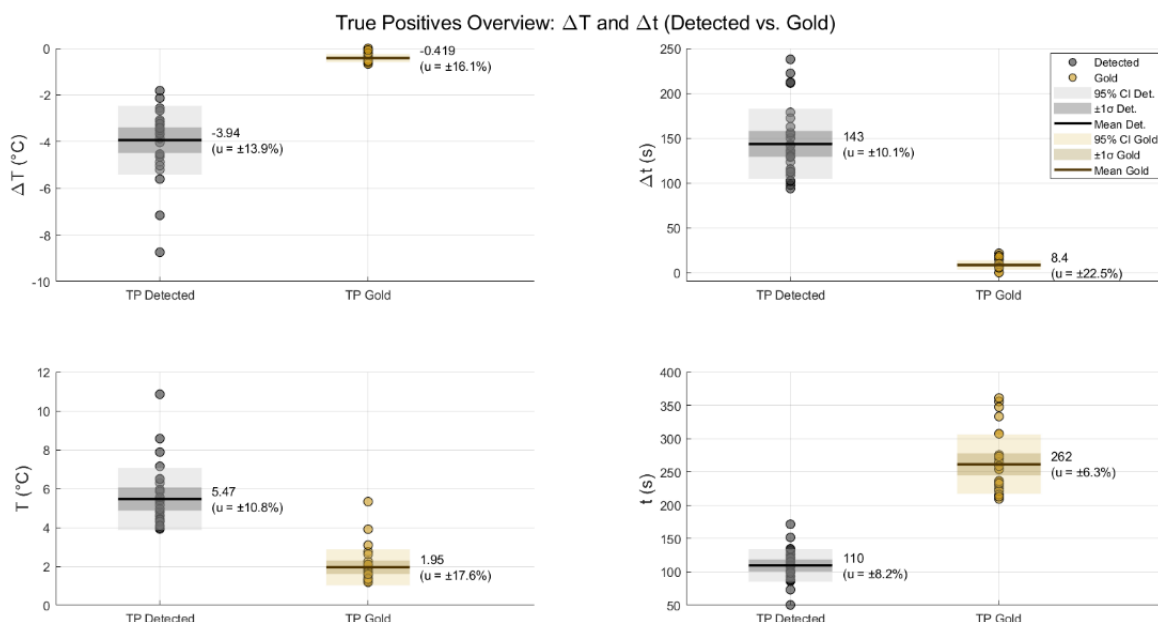


Figure 6.15. Box plots comparing freezing detection parameters for true positives between the threshold algorithm (gray) and the gold standard (yellow). Top left: ΔT (°C); Top right: Δt (s); Bottom left: T_{change} (°C); Bottom right: t_{change} (s). Each plot shows individual samples (dots), mean (solid line), standard deviation (dark band), and 95 % confidence interval (light band). The algorithm detects events earlier (lower t_{change} , higher T_{change}) with consistent uncertainty. Author’s own work.

6.2.3. Conclusions

The developed freezing detection system exhibits robust classification capabilities, achieving a high overall accuracy of 91.11 % and precision of 93.33 %. These results highlight the system's potential as a reliable, low-cost, and non-invasive tool for detecting freezing events in biomedical applications such as cryolipolysis. Statistical validation via a binomial hypothesis test produced a highly significant p-value ($p<0.0001$), confirming that the system's accuracy is substantially better than random chance. Furthermore, narrow confidence intervals for key metrics such as precision, recall, specificity, and accuracy underscore the system's reproducibility and consistency.

Temporal and thermal analyses demonstrate that the system not only accurately detects freezing events but does so with consistent timing and temperature parameters. Notably, the algorithm detects phase changes earlier than the gold standard sensor, offering a valuable early warning advantage critical for preventing uncontrolled tissue damage during cryolipolysis.

Despite these promising outcomes, the presence of false negatives underscores the necessity for improved detection reliability. Future developments should explore sensor fusion approaches, incorporating additional modalities like bioimpedance, alongside advanced data analytics to further reduce the risk of undetected freezing events and enhance clinical safety.



7. Applicable Standards

7.1. Scope of Standards Application

The present work focuses on the design and experimental validation of a laboratory-scale prototype intended for use in controlled research settings, rather than a fully certified medical device for clinical deployment. As such, full compliance with regulatory medical device standards is not formally required at this development stage. Nevertheless, to support future clinical translation and to ensure patient safety from the outset, the design process has been carried out with close reference to relevant international standards for medical electrical equipment.

By proactively considering standards such as UNE-EN 60601-1, this work establishes a foundation for subsequent iterations that may require formal certification. This approach not only enhances the safety profile of the prototype but also fosters a risk-aware engineering process that is essential for any technology intended to interact with the human body.

7.2. Applicable Standards and Electrical Safety Requirements

Biocapacitive measurement techniques generate low-intensity electric fields near the body, enabling signal detection without direct contact. While no current flows through the tissue, the electric field must remain within safe limits to avoid potential effects such as discomfort or unintended stimulation, including microshock or macroshock [114], [115].

To mitigate these risks, the project refers primarily to the UNE-EN 60601-1:2008 standard: “*Medical Electrical Equipment – Part 1: General Requirements for Basic Safety and Essential Performance*”. Particular attention has been paid to Chapter 8, “*Protection against Electrical Hazards from Medical Electrical Equipment*”, and more specifically Section 8.7, “*Leakage Currents and Patient Auxiliary Currents*”. Subclause 8.7.3 – “*Allowable Values*” outlines allowable current values under normal and single-fault conditions [115].

7.2.1. Device Classification and Risk Category

The system is classified as a BF-type applied part, electrically isolated and suitable for patient contact. According to Regulation (EU) 2017/745, it falls under Class IIb for diagnostic and monitoring use. While not certified, this classification informs the prototype’s safety and risk design.

7.2.2. Permissible Current Limits

The UNE-EN 60601-1 standard establishes the maximum contact and leakage current levels allowed under both standard operation and fault conditions. These limits are summarized in Table 7.1:

Table 7.1. Maximum permissible current values under normal and single-fault conditions according to UNE-EN 60601-1:2008 [115].

	<i>Normal Condition</i>	<i>Single-Fault Condition</i>
<i>Patient contact current</i>	100 µA	500 µA
<i>Earth leakage current</i>	5 mA	10 mA
<i>Earth leakage current (regardless of waveform or frequency)</i>	10 mA rms	10 mA rms

While the operational currents in this prototype are significantly lower than these limits, it is important to note that the biological impact of current depends on waveform, frequency, and application duration. As such, understanding human perception thresholds for both direct and alternating currents remains a vital safety consideration.

7.2.2.1. Human Perception Thresholds for DC and AC Currents

According to [114], the human body's sensitivity varies significantly with current type and frequency:

- DC (Direct Current): Perception threshold in adults starts at approximately 4 mA.
- AC (Alternating Current, 50–60 Hz): Perception threshold lowers to around 1 mA.

Physiological effects vary depending on intensity and exposure in [115]:

- DC can cause electrolytic skin effects and prolonged tingling after current cessation.
- Low-frequency AC (50–60 Hz) strongly stimulates nerves and muscles, potentially causing pain or involuntary contractions.
- However, at higher frequencies, biological tissues behave increasingly like capacitors, which raises the current perception threshold. Empirical data suggests [114]:
 - o At 10 Hz, thresholds start at *ca.* 100 µA.
 - o At 1 kHz, thresholds increase to *ca.* 2 mA.
 - o At 10 kHz, perception requires more than 10 mA.

These data support the use of AC signals in the microampere range and frequencies >1 kHz, ensuring safety and imperceptibility in biocapacitive applications.

7.3. Patient Safety and Exclusion Criteria

Despite the use of ultra-low and safe signal levels, certain populations are excluded from participation due to theoretical or uncharacterized risks:

- Patients with cardiac pacemakers or implantable cardioverter defibrillators (ICDs): Although no direct interference is expected, exclusion is precautionary.
- Individuals with metallic implants (e.g., bone plates, screws, artificial joints): These can distort electric fields and affect both measurement integrity and safety.
- Patients with fluid-filled catheters reaching the heart: Pose a potential path for internal current conduction.
- Pregnant women: Due to the absence of specific safety data, exclusion is standard practice.

These criteria are consistent with the NHANES (2000) Body Composition Procedures Manual [116], which outlines similar exclusion criteria for bioelectrical measurement procedures.

7.4. Additional Relevant Standards

To support a broader understanding of the system's safety and usability profile, several collateral standards derived from UNE-EN 60601-1 are also referenced:

7.4.1. Electromagnetic Compatibility (EMC)

UNE-EN 60601-1-2:2015/A1:2021: "*Medical Electrical Equipment – Electromagnetic Disturbances – Requirements and Tests*" ensures that devices function correctly within their electromagnetic environments without causing harmful interference. Given that this project utilizes I2C to USB communication, rather than wireless transmission, compliance with this standard is not strictly necessary, though consideration of general EMC best practices remains advisable.

7.4.2. Usability Engineering

- UNE-EN 60601-1-6:2010/A1:2015: "*Medical Electrical Equipment – General Requirements for Usability*" establishes processes for analyzing, designing, and validating usability aspects to mitigate risks associated with user interaction.
- UNE-EN 62366-1:2015/A1:2020: "*Application of Usability Engineering to Medical Devices*" provides guidelines for designing user-friendly medical devices and minimizing usability-related risks. While not mandatory for this prototype stage, incorporating these principles improves user interaction and reduces potential for error.



7.4.3. Risk Management

UNE-EN ISO 14971:2020: “*Application of Risk Management to Medical Devices*” This standard outlines systematic risk management throughout the device lifecycle. Although full compliance is not required for prototypes, applying its core concepts supports early hazard identification and safer design practices.

7.5. Summary

This prototype, while not subject to formal medical device certification, has been developed with proactive alignment to UNE-EN 60601-1 and related standards, ensuring that key safety and usability considerations are addressed from the beginning. This standards-informed approach lays a robust foundation for future iterations and eventual clinical translation, emphasizing both user safety and regulatory foresight.

8. Future Work

Although this thesis represents a significant step forward, it also marks the beginning of further development. With the simulations and electronic designs completed, the next logical phase is the creation of a compact, functional prototype capable of detecting pre-freezing conditions in biological tissues. Initial testing should be conducted on animal meat to simulate physiological behavior, followed by trials on human skin under controlled conditions. To move toward clinical use, the system will require extensive validation and must comply with medical device regulations relevant to cryolipolysis applications.

Several technical improvements can be made to enhance the current system. Integrating additional sensing modalities, such as bioimpedance, could provide complementary data and increase detection accuracy. The detection algorithm itself could also benefit from further refinement. A second, more advanced version, possibly incorporating adaptive thresholds or machine learning techniques, may improve performance under variable conditions and reduce false detections. Additionally, using faster and more sensitive temperature sensors, or improving their placement within the sample, could reduce thermal delays and better align temperature-based and capacitance-based detection.

On the hardware side, enhancing the precision of the capacitance measurement circuitry and optimizing sensor geometry may lead to more stable signals, reducing the need for heavy filtering and post-processing. Broader testing across different tissue types, sample geometries, and cooling profiles will be essential for validating the system's versatility and real-world applicability.

Furthermore, developing a PC-based real-time interface could enable immediate freezing detection and trigger automatic cessation of the cooling process upon detection. Alongside this, implementing a control system, ranging from a simple ON/OFF controller to a more sophisticated PID controller, could be explored to integrate this module into a real cryolipolysis device, improving safety and precision during treatment.

Lastly, to evaluate the system's true performance, it will be necessary to compare its behavior with that of established commercial solutions, such as those discussed in Chapter 3. A statistical comparison with these reference devices will help assess the reliability, sensitivity, and clinical potential of the proposed system. This benchmarking step will be critical in positioning the prototype as a competitive, medically relevant tool for future cryotherapy applications.

9. Sustainability Analysis

The development and implementation of this project have taken into account the environmental implications associated with the use of electronic components and materials. The manufacturing of electronic devices often involves hazardous substances such as mercury, lead, and cyanide, which pose significant risks to ecosystems and human health. Furthermore, the growing volume of electronic waste generated globally has intensified the need for sustainable design and end-of-life management.

To address these challenges, this project has adhered to key environmental directives established by the European Union, including:

- Directive 2012/19/EU (WEEE), concerning the management of waste electrical and electronic equipment (WEEE), [117].
- Directive 2011/65/EU (RoHS), which restricts the use of hazardous substances in electrical and electronic components, [118].

In the regional context of Catalonia, recycling and disposal of electronic components are managed through *Sistemes Integrats de Gestió* (SIG), which operate in compliance with the aforementioned directives. Accordingly, the design and material selection within this project have prioritized RoHS-compliant components and avoided substances restricted under current legislation.

Additionally, a waste management strategy was implemented during the prototyping and experimental phases to ensure proper disposal and minimization of environmental impact. This approach not only aligns with the applicable regulatory framework but also reflects a broader commitment to sustainability and responsible engineering practices throughout the project lifecycle.



10. Economic Analysis

This section presents a detailed breakdown of the economic costs associated with the development and execution of this thesis. For clarity, expenditures have been categorized into three main areas: hardware and software resources, consumables and laboratory procedures, and labor costs.

10.1. Materials and Software

This subsection encompasses the costs related to physical components, prototyping tools, consumables, and software licenses necessary for system development, experimental procedures, and data analysis.

10.1.1. Experimental Platform

As described in Section 4, the experimental platform includes all electronic and mechanical components required to construct the measurement system and validate its functionality. These elements are summarized in Table 10.1.

Table 10.1. Experimental Platform Building Costs.

<i>Item Description</i>	<i>Item Denomination</i>	<i>Cost (€/unit)</i>	<i>Units</i>	<i>IVA (%)</i>	<i>Total (€)</i>
<i>Arduino MEGA 2560</i>	<i>Arduino Mega 2560 Rev3</i>	€ 52.80	1	21	€ 63.89
<i>Peltier Cell</i>	<i>TEC1-12706</i>	€ 12.50	4	Included	€ 50.00
<i>Relay Module</i>	<i>JQC-3FF-S-Z</i>	€ 4.99	1	Included	€ 4.99
<i>Heatsink 1</i>	<i>FAN478</i>	€ 16.00	1	Included	€ 16.00
<i>Temperature Sensor</i>	<i>ATH10</i>	€ 14.16	2	Included	€ 28.32
<i>Copper Tape</i>	<i>RS PRO, 25mm x 33m 176-7501</i>	€ 65.70	1	21	€ 79.50
<i>Thermal Paste</i>	<i>SYY-157 silicon based thermal paste</i>	€ 8.88	1	Included	€ 8.88
<i>A/D Capacitor Board</i>	<i>FDC1004EVM, Digikey 296-38941-ND</i>	€ 209.14	1	21	€ 253.06
<i>Methacrylate Plates</i>	<i>Methacrylate 2 Piezas 20 x 20 cm</i>	€ 17.00	1	Included	€ 17.00
<i>Wire, soldering paste, connexions</i>	<i>Electronic Material</i>	€ 25.00	1	Included	€ 25.00
<i>Silicone Bars Glue</i>	<i>92886380 Leroy Merlin Silicon Bars</i>	€ 5.39	1	Included	€ 5.39
<i>Total Cost:</i>					€ 552.02



10.1.2. Experimental Procedures and Consumables

To support the experiments detailed in Section 5, additional single-use items and laboratory equipment were required. These are presented in Table 10.2.

Table 10.2. Experimental Consumable Costs.

<i>Item Description</i>	<i>Item Denomination</i>	<i>Cost (€/unit)</i>	<i>Units</i>	<i>IVA (%)</i>	<i>Total (€)</i>
Celulose Paper	Paper rolls	€ 5.99	1	Included	€ 5.99
Fuses	250 V 4 A	€ 0.29	6	Included	€ 1.74
<i>Total Cost:</i>					€ 7.73

10.2. Software and Licensing Costs

Software tools required for data analysis and documentation have a financial impact due to licensing fees. The primary tools used in this project were:

- MATLAB R2023b: Academic institutional license, provided by UPC. Personal cost: €938/year.
- Microsoft Office 365: Personal version, subscription cost: €9.99/month.

The other softwares utilized to conduct this thesis contain a free licence of use.

10.3. Engineering Costs and Labour

10.3.1. Student Research and Development Time

The total workload, equivalent to 48 ECTS credits, represents approximately 1200 hours. Using the standard UPC internship compensation rate of €8/hour, this results in €9,600.00.

10.3.2. Supervision and Collaboration Costs

The project also benefited from academic supervision, including project planning, technical validation, and feedback. This included:

- 3 in-person meetings and 6 on-line meetings.
- Review of deliverables and documentation.
- Over 120 email interactions.

An estimated total of 60 hours was attributed to supervisory effort. At a standard UPC academic rate of €17/hour, the supervisory cost is 1020€.

10.3.3. Final Summup

By systematically evaluating these costs, this analysis provides a clear understanding of the financial resources required for the successful execution of the thesis, with a final economical value of €12,177.69¹, with a 21 % of IVA included².

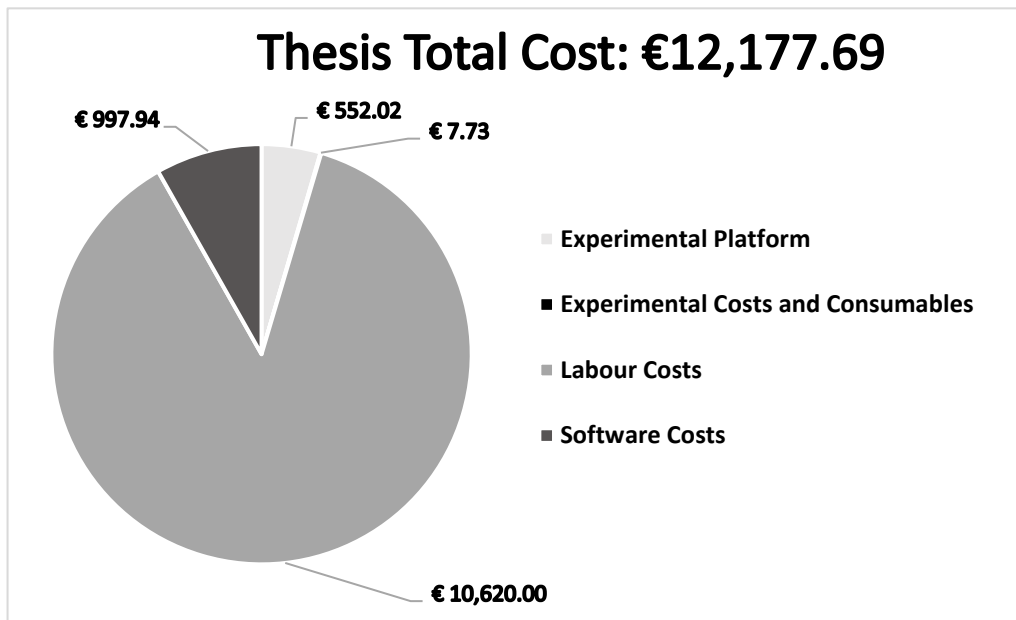


Figure 10.1. Thesis Cost Breakdown Pie Chart. Author's own work.

¹ For a detailed explanation of the economic calculations, please refer to Annex D2: Thesis Economic Study.

² The IVA break down can be seen in Annex D2: Thesis Economic Study.

Conclusions

This thesis successfully achieved its main objective: the design and validation of a laboratory-scale prototype capable of detecting pre-freezing conditions in tissue through capacitive sensing. The proposed freezing detection system demonstrates strong classification performance and reliable temporal-thermal behavior. With a classification accuracy of 91.11 % and a precision of 93.33 %, the system shows promise as a low-cost, non-invasive solution for freezing detection in biomedical applications, particularly in cryolipolysis. Furthermore, the statistical validation supports the robustness of the results: the system passed the hypothesis test with a highly significant p-value ($p < 0.0001$), and the calculated confidence intervals were tight, indicating consistent and repeatable behavior.

By monitoring the capacitive response, which precedes the thermal signature, the system offers significant safety and reliability advantages over commercially temperature-only detection systems. First, capacitive variation is not strictly localized, unlike temperature measurements, making it a more comprehensive indicator of freezing across a wider area. Second, because the capacitance-based detection occurs before a significant temperature drop, it eliminates the need to wait for a thermal injury threshold to be reached, allowing for earlier and safer intervention. These two factors make the proposed system inherently more robust and safer than conventional methods. In future designs, a hybrid approach leveraging both modalities could enhance detection reliability even further.

Beyond the experimental phase, this system could be adapted for real-time clinical use. For example, a PC-based interface could be developed to visualize detection status live and automatically halt the freezing process if freezing onset is identified. Additionally, control strategies, ranging from simple ON/OFF logic to more advanced PID regulation, could be implemented, allowing this module to be integrated into commercial cryolipolysis systems for enhanced safety and efficacy.

Bibliography

- [1] D. B. Newell and E. Tiesinga, "The International System of Units (SI), 2019 Edition," 2019, doi: 10.6028/NIST.SP.330-2019.
- [2] P. Jain, P. Agarwal, D. Mathur, P. Singh, and A. Sharma, "Evolution of cryogenics - A review on applications of cryogenics in medicine," *Mater Today Proc*, vol. 47, pp. 3059–3063, 2021, doi: 10.1016/J.MATPR.2021.05.642.
- [3] S. M. Cooper, M. Mrcgp, and R. P. R. Dawber, "The history of cryosurgery," *J R Soc Med*, vol. 94, pp. 196–201, 2001.
- [4] L. Ahmed, M. B. B. Ch, A. M. B. Shwan, B. Ch, and J. Davies Mrcs, "Epochs in Endourology History of Cryosurgery," *J Endourol*, vol. 20, no. 7, 2006, Accessed: Feb. 04, 2025. [Online]. Available: www.liebertpub.com
- [5] N. B. BSc and A. C. Freiman, "History of cryotherapy," *Dermatol Online J*, vol. 11, no. 2, 2005, doi: 10.5070/D34F62H9VT.
- [6] "A man self-administering hydrotherapy, sitting outside in a barrel. Coloured lithograph. | Wellcome Collection." Accessed: Feb. 04, 2025. [Online]. Available: <https://wellcomecollection.org/works/c3e9jt4h/images?id=k6bgkpdm>
- [7] N. K. Rho, "Revisiting the Role of Local Cryotherapy for Acne Treatment: A Review and Update," *J Clin Med*, vol. 12, no. 1, Jan. 2023, doi: 10.3390/JCM12010026.
- [8] M. H. A. Davidson, "The evolution of anaesthesia," *Br J Anaesth*, vol. 31, no. 9, pp. 417–422, 1959, doi: 10.1093/BJA/31.9.417.
- [9] A. A. Gage, "History of cryosurgery," *Semin Surg Oncol*, vol. 14, no. 2, pp. 99–109, 1998, doi: [https://doi.org/10.1002/\(SICI\)1098-2388\(199803\)14:2<99::AID-SSU2>3.0.CO;2-1](https://doi.org/10.1002/(SICI)1098-2388(199803)14:2<99::AID-SSU2>3.0.CO;2-1).
- [10] A. White, "Liquid Air: Its Application in Medicine and Surgery," *Medication Reconciliation*, vol. 56, pp. 109–112, 1899.
- [11] W. A. Pusey, "THE USE OF CARBON DIOXID SNOW IN THE TREATMENT OF NEVI AND OTHER LESIONS OF THE SKIN.A PRELIMINARY REPORT.," *J Am Med Assoc*, vol. XLIX, no. 16, pp. 1354–1356, Oct. 1907, doi: 10.1001/JAMA.1907.25320160032001H.

- [12] T. Fay and G.C. Henny, "Correlation of body segmental temperature and its relation to the location of carcinomatous metastasis: Clinical observations and response to methods of refrigeration," *Surg Gynecol Obstet*, vol. 66, pp. 512–524, 1938.
- [13] H. V Allington and O. Summary, "Liquid Nitrogen in the Treatment of Skin Diseases," 1950.
- [14] G. F. Rowbotham, A. L. Haigh, and W. G. Leslie, "Cooling cannula for use in the treatment of cerebral neoplasms," *Lancet*, vol. 1, no. 7062, pp. 12–15, Jan. 1959, doi: 10.1016/S0140-6736(59)90976-6.
- [15] Tytus J. S., "Further observations on rapid freezing and its possible application to neurosurgical techniques," *Bull Mason Clin*, vol. 15, pp. 51–61, 1961.
- [16] J. P. Shepherd and R. P. R. Dawber, "Wound healing and scarring after cryosurgery," *Cryobiology*, vol. 21, no. 2, pp. 157–169, 1984, doi: 10.1016/0011-2240(84)90207-4.
- [17] R. DAWBER, "Cold kills!," *Clin Exp Dermatol*, vol. 13, no. 3, pp. 137–150, 1988, doi: 10.1111/J.1365-2230.1988.TB01958.X.
- [18] R. P. R. Dawber, G. B. Colver, and A. J. Jackson, "Cutaneous Cryosurgery: Principles and Clinical Practice," 1992. [Online]. Available: <https://api.semanticscholar.org/CorpusID:70587843>
- [19] G. B. Bartley, J. D. Bullock, T. G. Olsen, and P. D. Lutz, "An experimental study to compare methods of eyelash ablation," *Ophthalmology*, vol. 94, no. 10, pp. 1286–1289, 1987, doi: 10.1016/S0161-6420(87)80013-1.
- [20] C. Andersen and D. Phelps, "Peripheral retinal ablation for threshold retinopathy of prematurity in preterm infants," *Cochrane Database Syst Rev*, vol. 1999, no. 2, Jul. 2000, doi: 10.1002/14651858.CD001693.
- [21] J. G. Bellows, *Cryotherapy of Ocular Disease*. Philadelphia: J.B. Lippincott Co., 1966.
- [22] I. S. Gill and A. C. Novick, "Renal cryosurgery," *Urology*, vol. 54, no. 2, pp. 215–219, 1999, doi: 10.1016/S0090-4295(99)00160-0.
- [23] R. A. Badalament, D. K. Bahn, H. Kim, A. Kumar, J. M. Bahn, and F. Lee, "Patient-reported complications after cryoablation therapy for prostate cancer," *Urology*, vol. 54, no. 2, pp. 295–300, Aug. 1999, doi: 10.1016/S0090-4295(99)00102-8.

- [24] Z. al A. Medlej *et al.*, "Cryoablation and Immunotherapy: An Enthralling Synergy for Cancer Treatment," *Curr Oncol*, vol. 30, no. 5, pp. 4844–4860, May 2023, doi: 10.3390/CURRONCOL30050365.
- [25] G. Mucciardi, C. Magno, A. Inferrera, and F. Lugnani, "Cryosurgery and Irreversible Electroporation: The State of the Art, Advantages, and Limitations," *Handbook of Electroporation*, pp. 1–16, 2016, doi: 10.1007/978-3-319-26779-1_110-1.
- [26] B. Kania and D. J. Goldberg, "Cryolipolysis: A promising nonsurgical technique for localized fat reduction," *J Cosmet Dermatol*, vol. 22, no. S3, pp. 1–7, Nov. 2023, doi: 10.1111/JOCD.16039.
- [27] C. D. Derrick, S. M. Shridharani, and J. M. Broyles, "The Safety and Efficacy of Cryolipolysis: A Systematic Review of Available Literature," *Aesthet Surg J*, vol. 35, no. 7, pp. 830–836, Sep. 2015, doi: 10.1093/ASJ/SJV039.
- [28] P. K. Donski, J. D. Franklin, J. V. Hurley, and B. M. C. O'Brien, "The effects of cooling on experimental free flap survival," *Br J Plast Surg*, vol. 33, no. 3, pp. 353–360, 1980, doi: 10.1016/S0007-1226(80)90082-X.
- [29] S. Natori, H. Higuchi, P. Contreras, and G. J. Gores, "The caspase inhibitor IDN-6556 prevents caspase activation and apoptosis in sinusoidal endothelial cells during liver preservation injury," *Liver Transplantation*, vol. 9, no. 3, pp. 278–284, Mar. 2003, doi: 10.1053/jlt.2003.50019.
- [30] H. R. Jalian and M. M. Avram, "Cryolipolysis: A Historical Perspective and Current Clinical Practice," 2013.
- [31] M. M. Avram and R. S. Harry, "Cryolipolysis for subcutaneous fat layer reduction," *Lasers Surg Med*, vol. 41, no. 10, pp. 703–708, Dec. 2009, doi: 10.1002/LSM.20864.
- [32] ASDS, "American Society for Dermatologic Surgery Survey on Dermatologic Procedures," 2019, Accessed: Feb. 04, 2025. [Online]. Available: <https://www.asds.net/portals/0/PDF/procedures-survey-results-presentation-2019.pdf>
- [33] C. Hochsinger, *Ueber eine akute kongelative Zellgewebsverhärtung in der Submentalregion bei Kindern*, Separatabdruck. Wien: Druck von Bruno Bartelt, 1902. Accessed: Feb. 04, 2025. [Online]. Available: <https://repository.meduniwien.ac.at/urn/urn:nbn:at:at-ubmw:3-109990>
- [34] H. HAXTHAUSEN, "ADIPONECROSIS E FRIGORE.," *British Journal of Dermatology*, vol. 53, no. 3, pp. 83–89, 1941, doi: 10.1111/J.1365-2133.1941.TB10506.X.

- [35] H. A. COLLINS, M. STAHLMAN, and H. W. SCOTT, "The Occurrence of Subcutaneous Fat Necrosis in an Infant Following Induced Hypothermia Used as an Adjuvant in Cardiac Surgery," *Ann Surg*, vol. 138, no. 6, p. 880, Dec. 1953, doi: 10.1097/00000658-195312000-00010.
- [36] R. Arora, T. Nandhagopal, and S. Raza, "Popsicle panniculitis," *N Engl J Med*, vol. 282, no. 17, p. 168, Feb. 1970, doi: 10.1056/NEJM197004232821709.
- [37] L. M. Solomon and H. Beerman, "COLD PANNICULITIS," *Arch Dermatol*, vol. 88, no. 6, pp. 897–900, 1963, doi: 10.1001/ARCHDERM.1963.01590240221036.
- [38] E. Hultcrantz, "Haxthausen's disease. Cold panniculitis in children," *Journal of Laryngology and Otology*, vol. 100, no. 11, pp. 1329–1332, 1986, doi: 10.1017/S0022215100101070.
- [39] Adams JE, Foster JH, and Faulk WH, "Experimental production of subcutaneous fat necrosis by general hypothermia; relation to the chemical composition of fat," *Surg Forum*, vol. 5, pp. 556–563, 1955.
- [40] A. Quesada-Cortés, L. Campos-Muñoz, R. M. Díaz-Díaz, and M. Casado-Jiménez, "Cold Panniculitis," *Dermatol Clin*, vol. 26, no. 4, pp. 485–489, Oct. 2008, doi: 10.1016/J.DET.2008.05.015.
- [41] D. Manstein, H. Laubach, K. Watanabe, W. Farinelli, D. Zurakowski, and R. R. Anderson, "Selective cryolysis: a novel method of non-invasive fat removal," *Lasers Surg Med*, vol. 40, no. 9, pp. 595–604, Nov. 2008, doi: 10.1002/LSM.20719.
- [42] B. Zelickson *et al.*, "Cryolipolysis for noninvasive fat cell destruction: initial results from a pig model," *Dermatol Surg*, vol. 35, no. 10, pp. 1462–1470, Oct. 2009, doi: 10.1111/J.1524-4725.2009.01259.X.
- [43] J. A. Preciado and J. W. Allison, "59. The effect of cold exposure on adipocytes: Examining a novel method for the non-invasive removal of fat," *Cryobiology*, vol. 57, no. 3, p. 327, Dec. 2008, doi: 10.1016/J.CRYOBIO.2008.10.060.
- [44] D. Manstein, H. Laubach, K. Watanabe, W. Farinelli, D. Zurakowski, and R. R. Anderson, "Selective cryolysis: a novel method of non-invasive fat removal," *Lasers Surg Med*, vol. 40, no. 9, pp. 595–604, Nov. 2008, doi: 10.1002/LSM.20719.
- [45] S. Jayakumar, "ZELTIQ CoolSculpting System 510(k)", Accessed: Feb. 04, 2025. [Online]. Available: <http://www.fda.gov/MedicalDevices/ResourcesforYou/Industry/default.htm>.

- [46] D. P. Friedmann, J. Kommera, P. Durga, A. Shashidhar, and K. K. Verma, "Evaluating Real-World Use and Adverse Events from 3262 Patients Treated with 18,203 Cycles of Cryolipolysis for Localized Fat Reduction: A Multi-Location Practice Retrospective Chart Review," *Aesthet Surg J*, Jan. 2025, doi: 10.1093/ASJ/SJAF007.
- [47] K. B. Klein, E. P. Bachelor, E. V. Becker, and L. E. Bowes, "Multiple same day cryolipolysis treatments for the reduction of subcutaneous fat are safe and do not affect serum lipid levels or liver function tests," *Lasers Surg Med*, vol. 49, no. 7, pp. 640–644, Sep. 2017, doi: 10.1002/lsm.22674.
- [48] K. B. Klein *et al.*, "Non-invasive cryolipolysis for subcutaneous fat reduction does not affect serum lipid levels or liver function tests," *Lasers Surg Med*, vol. 41, no. 10, pp. 785–790, Dec. 2009, doi: 10.1002/LSM.20850.
- [49] B. Hedayati, M. Juhász, S. Chu, and N. A. Mesinkovska, "Adverse Events Associated With Cryolipolysis: A Systematic Review of the Literature," *Dermatol Surg*, vol. 46, pp. S8–S13, Oct. 2020, doi: 10.1097/DSS.0000000000002524.
- [50] N. P. Barry, S. R. Jackson, A. D'Jamirze, R. J. Gates, P. K. M. Maitz, and A. Issler-Fisher, "Cold burns as a result of cosmetic cryolipolysis: An emerging concern from the NSW Statewide Burn Injury Service," *J Plast Reconstr Aesthet Surg*, vol. 76, pp. 289–291, Jan. 2023, doi: 10.1016/J.BJPS.2022.10.053.
- [51] B. Hedayati, M. Juhász, S. Chu, and N. A. Mesinkovska, "Adverse Events Associated With Cryolipolysis: A Systematic Review of the Literature," *Dermatol Surg*, vol. 46 Suppl 1, pp. S8–S13, Oct. 2020, doi: 10.1097/DSS.0000000000002524.
- [52] C. Benoit and A. Modarressi, "Severe frostbite complication after cryolipolysis: A case report," *JPRAS Open*, vol. 25, p. 46, Sep. 2020, doi: 10.1016/J.JPRA.2020.05.004.
- [53] "Contribution to the Prediction of Thermal Incidents for Cryolipolysis Equipments connected to Digital Infrastructure. | FUTUR." Accessed: Feb. 26, 2025. [Online]. Available: <https://futur.upc.edu/34324478>
- [54] S. Abboud, M. M. Radai, and S. Zlochiver, "Electrical Impedance Technique for Cryosurgery Monitoring," *Wiley Encyclopedia of Biomedical Engineering*, Apr. 2006, doi: 10.1002/9780471740360.EBS0327.
- [55] E. Dubyanskaya *et al.*, "A concept of cryoapplicator based on sapphire shaped crystal enabling control of the ice ball formation using spatially resolved elastic backscattering of light,"

- <https://doi.org/10.1117/12.2306946>, vol. 10685, pp. 294–299, May 2018, doi: 10.1117/12.2306946.
- [56] M. C. Homola, P. J. Nicklasson, and P. A. Sundsbø, “Ice sensors for wind turbines,” *Cold Reg Sci Technol*, vol. 46, no. 2, pp. 125–131, Nov. 2006, doi: 10.1016/J.COLDREGIONS.2006.06.005.
- [57] R. Felsberger, B. Schweighofer, M. Flatscher, M. Rath, M. Grubmuller, and H. Wegleiter, “Low Power Ice Detection with Capacitive and Impedance Spectroscopy-Based Measurements,” *IEEE International Symposium on Industrial Electronics*, vol. 2018-June, pp. 809–813, Aug. 2018, doi: 10.1109/ISIE.2018.8433765.
- [58] B. Rubinsky, “Cryosurgery,” *Annu Rev Biomed Eng*, vol. 2, no. 2000, pp. 157–187, 2000, doi: 10.1146/ANNUREV.BIOENG.2.1.157.
- [59] S. A. Zacarian, “How accurate is temperature monitoring in cryosurgery and is there an alternative?,” *J Dermatol Surg Oncol*, vol. 6, no. 8, pp. 627–632, 1980, doi: 10.1111/J.1524-4725.1980.TB00937.X.
- [60] A. A. Gage, S. Augustynowicz, M. Montes, J. A. Caruana, and D. A. Whalen, “Tissue impedance and temperature measurements in relation to necrosis in experimental cryosurgery,” *Cryobiology*, vol. 22, no. 3, pp. 282–288, 1985, doi: 10.1016/0011-2240(85)90148-8.
- [61] J. Liu and Y. X. Zhou, “Freezing curve-based monitoring to quickly evaluate the viability of biological materials subject to freezing or thermal injury,” *Anal Bioanal Chem*, vol. 377, no. 1, pp. 173–181, Sep. 2003, doi: 10.1007/S00216-003-2077-9.
- [62] T. H. Yu, J. Liu, and Y. X. Zhou, “Using electrical impedance detection to evaluate the viability of biomaterials subject to freezing or thermal injury,” *Anal Bioanal Chem*, vol. 378, no. 7, pp. 1793–1800, Apr. 2004, doi: 10.1007/S00216-004-2508-2.
- [63] Leonard DeBenedictis, Geroge Drangineas, Kristine Tatsutani, and Linda Pham, “Patent Application Publication,” US20240197382A1.
- [64] E. V. Petrova, H. P. Brecht, M. Motamed, A. A. Oraevsky, and S. A. Ermilov, “In vivo optoacoustic temperature imaging for image-guided cryotherapy of prostate cancer,” *Phys Med Biol*, vol. 63, no. 6, p. 064002, Mar. 2018, doi: 10.1088/1361-6560/AAB241.
- [65] H. Zheng *et al.*, “Core-multishell lanthanide-doped nanocomposite by one-pot synthesis for NIR-II emissions-based temperature sensing,” *J Alloys Compd*, vol. 911, p. 164926, Aug. 2022, doi: 10.1016/J.JALLOCOM.2022.164926.

- [66] I. N. Dolganova, A. K. Zotov, I. A. Shikunova, K. I. Zaytsev, and V. N. Kurlov, "Optically-controlled measurements of cryodestruction of biological tissues using sapphire shaped crystals," *Proceedings - International Conference Laser Optics 2020, ICLO 2020*, Nov. 2020, doi: 10.1109/ICLO48556.2020.9285697.
- [67] A. A. Gage, "Correlation of electrical impedance and temperature in tissue during freezing," *Cryobiology*, vol. 16, no. 1, pp. 56–62, 1979, doi: 10.1016/0011-2240(79)90010-5.
- [68] S. M. Abie *et al.*, "Feasibility of using electrical impedance spectroscopy for assessing biological cell damage during freezing and thawing," *Sensors*, vol. 21, no. 12, p. 4129, Jun. 2021, doi: 10.3390/S21124129/S1.
- [69] E. PRICE and L. BIRO, "Use of thermocouples in cryosurgery," *J Dermatol Surg Oncol*, vol. 9, no. 3, pp. 215–218, 1983, doi: 10.1111/J.1524-4725.1983.TB00790.X.
- [70] S. M and Z. SA, "A new impedance-based method for controlled cryosurgery of malignant tumors," *J Dermatol Surg Oncol*, vol. 3, no. 6, pp. 592–593, 1977, doi: 10.1111/J.1524-4725.1977.TB00363.X.
- [71] "CRISTAL® Cryolipolysis | 360° Bodycontouring with CRISTAL®." Accessed: Apr. 08, 2025. [Online]. Available: <https://www.cristal-bodycontouring.com/en/cristal-cryolipolysis/>
- [72] "Cooltech Define® | 360° Body Contouring - Cryolipolysis - Cooltech Define." Accessed: Apr. 08, 2025. [Online]. Available: <https://cooltechdefine.com/>
- [73] J. Happel, J. Döring, K.-L. Krieger, J. Deitschun, and D. Godlinski, "P3.2 - Printed Capacitive Sensors for Contactless Ice Detection in Automotive Liquid Conveyor Pipes," pp. 621–626, Dec. 2020, doi: 10.5162/SENSOR2017/P3.2.
- [74] M. J. Moser, T. Bretterklieber, H. Zangl, and G. Brasseur, "Strong and weak electric field interfering: Capacitive icing detection and capacitive energy harvesting on a 220-kV high-voltage overhead power line," *IEEE Transactions on Industrial Electronics*, vol. 58, no. 7, pp. 2597–2604, Jul. 2011, doi: 10.1109/TIE.2010.2098362.
- [75] T. Bretterklieber, H. Zangl, M. Motz, T. Werth, and D. Hammerschmidt, "Versatile sensor front end for low-depth modulation capacitive sensors," *Conference Record - IEEE Instrumentation and Measurement Technology Conference*, pp. 830–835, 2008, doi: 10.1109/IMTC.2008.4547152.
- [76] C. Baby K. and B. George, "A capacitive ice layer detection system suitable for autonomous inspection of runways using an ROV," *2012 IEEE International Symposium on Robotic and*

- Sensors Environments, ROSE 2012 - Proceedings, pp. 127–132, 2012, doi: 10.1109/ROSE.2012.6402627.*
- [77] “Capacitive Sensors: Design and Applications | IEEE eBooks | IEEE Xplore.” Accessed: Feb. 24, 2025. [Online]. Available: <https://ieeexplore.ieee.org/book/5264832>
- [78] J. Happel, J. Döring, K.-L. Krieger, J. Deitschun, and D. Godlinski, “P3.2 - Printed Capacitive Sensors for Contactless Ice Detection in Automotive Liquid Conveyor Pipes,” *Proceedings Sensor 2017*, pp. 621–626, May 2017, doi: 10.5162/SENSOR2017/P3.2.
- [79] M. Flatscher, M. Neumayer, T. Bretterklieber, and B. Schweighofer, “Measurement of complex dielectric material properties of ice using electrical impedance spectroscopy,” *Proceedings of IEEE Sensors*, vol. 0, Jan. 2016, doi: 10.1109/ICSENS.2016.7808533.
- [80] A. Troiano, E. Pasero, and L. Mesin, “New system for detecting road ice formation,” *IEEE Trans Instrum Meas*, vol. 60, no. 3, pp. 1091–1101, Mar. 2011, doi: 10.1109/TIM.2010.2064910.
- [81] T. Fen-Chong and A. Fabbri, “Freezing and thawing porous media: Experimental study with a dielectric capacitive method,” *Comptes Rendus - Mecanique*, vol. 333, no. 5, pp. 425–430, May 2005, doi: 10.1016/j.crme.2005.01.007.
- [82] X. Zhi, H. C. Cho, B. Wang, C. H. Ahn, H. S. Moon, and J. S. Go, “Development of a Capacitive Ice Sensor to Measure Ice Growth in Real Time,” *Sensors 2015, Vol. 15, Pages 6688-6698*, vol. 15, no. 3, pp. 6688–6698, Mar. 2015, doi: 10.3390/S150306688.
- [83] J. Krebs, “Application Report Ice Buildup Detection Using TI’s Capacitive Sensor Technology,” 2015, Accessed: May 21, 2025. [Online]. Available: www.ti.com
- [84] “Fuente de Alimentación FA-665 Fuente-Al Promax; Barcelona | Radiomuseum.org.” Accessed: May 22, 2025. [Online]. Available: https://www.radiomuseum.org/r/promax_fuente_de_alimentacion_fa_665.html
- [85] HB, “Performance Specifications”, Accessed: Mar. 31, 2025. [Online]. Available: www.hebeiltd.com.cn
- [86] “Thermoelectric”, Accessed: Apr. 09, 2025. [Online]. Available: www.lairdthermal.com
- [87] “DollaTek 5V módulo de relé de 1 Canal Escudo de Tarjeta con optoacoplador Soporte de Disparo de y bajo : Amazon.es: Industria, empresas y ciencia.” Accessed: Apr. 08, 2025. [Online]. Available: https://www.amazon.es/DollaTek-Tarjeta-optoacoplador-Soporte-Disparo/dp/B07DJ4NRC1/ref=asc_df_B07DJ4NRC1?mcid=b1ff1ea3eaf43f57b561f2d6892a9fc



- 9&tag=googshope-
- 21&linkCode=df0&hvadid=699799208119&hvpos=&hvnetw=g&hvrand=87830222651983385
10&hvpone=&hvptwo=&hvqmt=&hvdev=c&hvdvcmdl=&hvlocint=&hvlocphy=9215598&hvta
rgid=pla-1485959920035&psc=1&gad_source=1
- [88] “85x70x50mm Socket 478 CPU Cooler Fan with Heatsink & TX3 Connector.” Accessed: Mar. 31, 2025. [Online]. Available: <https://www.startech.com/en-eu/computer-parts/fan478>
- [89] “AHT10 Technical Manual”.
- [90] “Handson Technology User Guide AHT10 High-Precision Digital Temperature & Humidity Sensor Module”, Accessed: Mar. 31, 2025. [Online]. Available: <https://handsontec.com>
- [91] “Capacitive Frost or Ice Detection Reference Design-Resolution of < 1 mm, Temperature Drift < 0.25 %,” 2017, Accessed: Feb. 25, 2025. [Online]. Available: www.ti.com.
- [92] “CAP1298-1-SL Microchip Technology | Mouser España.” Accessed: Feb. 26, 2025. [Online]. Available: https://www.mouser.es/ProductDetail/Microchip-Technology/CAP1298-1-SL?qs=ZEMkBHnybRHQpta5qvC7Xg%3D%3D&srsltid=AfmBOozy_JtRSY1NQtHRrZ975dM7r5Atk7pDAru00B14rtUD4iGHMF8
- [93] “TIDA-01465 REV E1 Bill of Materials,” 2017, Accessed: Feb. 26, 2025. [Online]. Available: <http://www.ti.com/sc/docs/samptermis.htm>
- [94] “TIDA-01465 reference design | TI.com.” Accessed: Feb. 26, 2025. [Online]. Available: <https://www.ti.com/tool/TIDA-01465>
- [95] “Módulo de evaluación táctil capacitivo Texas Instruments 4 Channel USB - FDC1004EVM | RS.” Accessed: Feb. 26, 2025. [Online]. Available: <https://es.rs-online.com/web/p/kits-de-desarrollo-de-interfaz-de-usuario-hmi/8427377>
- [96] “FDC1004 data sheet, product information and support | TI.com.” Accessed: Feb. 26, 2025. [Online]. Available: <https://www.ti.com/product/FDC1004>
- [97] “FDC2214EVM | Módulo de evaluación Sensor táctil capacitivo Texas Instruments FDC2214 With Two Capacitive Sensors Evaluation Module - | RS.” Accessed: Feb. 26, 2025. [Online]. Available: <https://es.rs-online.com/web/p/kits-de-desarrollo-de-sensores/2355146>
- [98] “FDC2214 data sheet, product information and support | TI.com.” Accessed: Feb. 26, 2025. [Online]. Available: <https://www.ti.com/product/FDC2214>

- [99] “FDC2114EVM Texas Instruments | Placas de desarrollo, kits, programadores | DigiKey.” Accessed: Feb. 26, 2025. [Online]. Available: <https://www.digikey.es/es/products/detail/texas-instruments/FDC2114EVM/5452012?srsltid=AfmB0ooayo2varwJ-If8ZAIRuAsKzBkPt5EgolbkL5dVYPWjlxT8wBYT>
- [100] “FDC2114EVM Evaluation board | TI.com.” Accessed: Feb. 26, 2025. [Online]. Available: <https://www.ti.com/tool/FDC2114EVM>
- [101] “EVAL-AD7746EBZ Analog Devices | Mouser España.” Accessed: Feb. 26, 2025. [Online]. Available: https://www.mouser.es/ProductDetail/Analog-Devices/EVAL-AD7746EBZ?qs=WlvQP4zGangZD%2FWMFCTPkA%3D%3D&mgh=1&vip=1&utm_id=19105062713&utm_source=google&utm_medium=cpc&utm_marketing_tactic=emeacorp&gad_source=1&gclid=CjwKCAiAlPu9BhAjEiwA5NDSA6DHBrugnUDklmq-_LjNOpq0ApHPlknG8eJ8qLzTm3CpjTtC3TYVxoCITsQAvD_BwE
- [102] “EVAL-AD7746 Evaluation Board | Analog Devices.” Accessed: Feb. 26, 2025. [Online]. Available: <https://www.analog.com/en/resources/evaluation-hardware-and-software/evaluation-boards-kits/eval-ad7746.html#eb-overview>
- [103] “FDC1004EVM User’s Guide User’s Guide FDC1004EVM User’s Guide,” 2014, Accessed: Feb. 25, 2025. [Online]. Available: www.ti.com
- [104] S. Boutros and A. A. Hanna, “DIELECTRIC PROPERTIES OF MOIST CELLULOSE.,” *J Polym Sci Polym Chem Ed*, vol. 16, no. 1, pp. 89–94, Jan. 1978, doi: 10.1002/POL.1978.170160109;CTYPE:STRING:JOURNAL.
- [105] R. Pethig, “Dielectric properties of body tissues,” *Clinical Physics and Physiological Measurement*, vol. 8, no. 4A, pp. 5–12, 1987, doi: 10.1088/0143-0815/8/4A/002,.
- [106] M. Kombolias, J. Obrzut, K. Montgomery, M. T. Postek, D. L. Poster, and Y. S. Obeng, “Dielectric spectroscopic studies of biological material evolution and application to paper,” *Tappi J*, vol. 17, no. 9, pp. 501–506, Sep. 2018, doi: 10.32964/TJ17.09.501,.
- [107] “Capacitive Frost or Ice Detection Reference Design-Resolution of < 1 mm, Temperature Drift < 0.25 %,” 2017, Accessed: May 26, 2025. [Online]. Available: www.ti.com.
- [108] “SSZT777 Technical article | TI.com.” Accessed: May 26, 2025. [Online]. Available: <https://www.ti.com/document-viewer/lit/html/SSZT777>
- [109] R. Wang, “Accurate Frost or Ice Detection Based on Capacitive Sensing,” 2023, Accessed: May 26, 2025. [Online]. Available: www.ti.com

- [110] D. Wang, "Application Report Capacitive Sensing: Ins and Outs of Active Shielding," 2015, Accessed: May 26, 2025. [Online]. Available: www.ti.com
- [111] "Design Considerations for TIDA-00506," 2015.
- [112] "FDC1004EVM User's Guide User's Guide FDC1004EVM User's Guide," 2014, Accessed: May 26, 2025. [Online]. Available: www.ti.com
- [113] J. Krebs, "Application Report Ice Buildup Detection Using TI's Capacitive Sensor Technology," 2015, Accessed: May 26, 2025. [Online]. Available: www.ti.com
- [114] J. D. . Bronzino and D. R. . Peterson, "The biomedical engineering handbook : medical devices and human engineering edited by Joseph D. Bronzino, Donald R. Peterson," 2015.
- [115] "UNE-EN 60601-1:2008 Equipos electromédicos. Part 1: Requisito..." Accessed: Apr. 04, 2025. [Online]. Available: <https://www.en.une.org/encuentra-tu-norma/busca-tu-norma/norma?c=N0041083>
- [116] "NHANES 1999-2000 Procedure Manuals." Accessed: Apr. 04, 2025. [Online]. Available: <https://wwwn.cdc.gov/nchs/nhanes/continuousnhanes/manuals.aspx?BeginYear=1999>
- [117] "Directive - 2012/19 - EN - EUR-Lex." Accessed: Apr. 04, 2025. [Online]. Available: <https://eur-lex.europa.eu/eli/dir/2012/19/oj/eng>
- [118] "Directive - 2011/65 - EN - rohs 2 - EUR-Lex." Accessed: Apr. 04, 2025. [Online]. Available: <https://eur-lex.europa.eu/eli/dir/2011/65/oj/eng>

Annex

This annex includes only the most relevant data necessary to support and understand this thesis.

For access to all figures, plots, output statistics, and source code (MATLAB, Arduino, etc.), please refer to the GitHub repository created to publicly share all project materials:

<https://github.com/NicolauSoleCoves/Pre-Freeze-Capacitance-Detection-System>

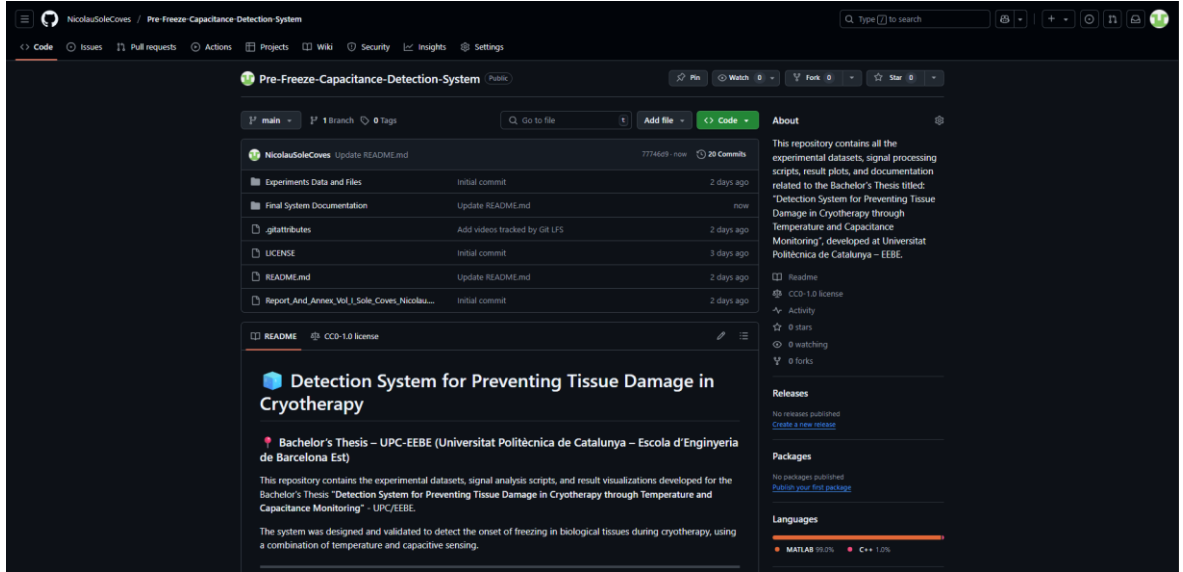
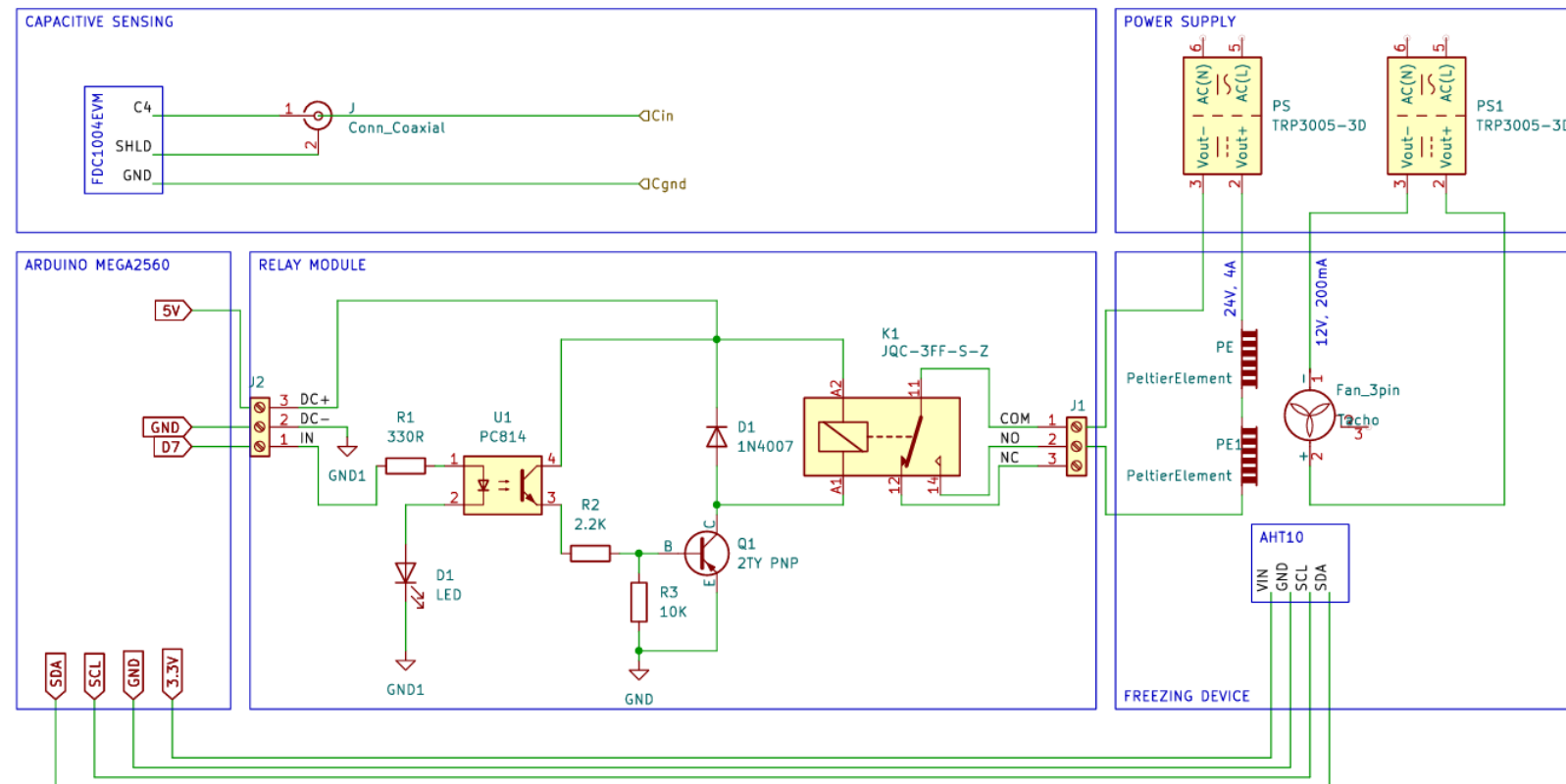


Figure 0.1. Screenshot of the GitHub repository containing the materials generated during the development of this thesis. Author's own work.

Annex A: Technical Documentation

A1. Experimental Platform Electric Schematic



A2. Bill of Materials (BOM)

Table 0.1. Bill of Materials in order to build this TFE.

<i>Item Description</i>	<i>Item Denomination</i>	<i>Cost (€/unit)</i>	<i>Units</i>	<i>IVA (%)</i>	<i>Total (€)</i>
Arduino MEGA 2560	<i>Arduino Mega 2560 Rev3</i>	€ 52.80	1	21	€ 63.89
Peltier Cell	<i>TEC1-12706</i>	€ 12.50	4	Included	€ 50.00
Relay Module	<i>JQC-3FF-S-Z</i>	€ 4.99	1	Included	€ 4.99
Heatsink	<i>FAN478</i>	€ 16.00	1	Included	€ 16.00
Temperature Sensor	<i>ATH10</i>	€ 14.16	1	Included	€ 14.16
Copper Tape	<i>RS PRO, 25mm x 33m 176-7501</i>	€ 65.70	1	21	€ 79.50
Thermal Paste	<i>SYY-157 silicon based thermal paste</i>	€ 8.88	1	Included	€ 8.88
A/D Capacitor Board	<i>FDC1004EVM, Digikey 296-38941-ND</i>	€ 209.14	1	21	€ 253.06
Methacrylate Plates	<i>Methacrylate 2 Piezas 20 x 20 cm</i>	€ 17.00	1	Included	€ 17.00
Wire, soldering paste, connexions	<i>Electronic Material</i>	€ 25.00	1	Included	€ 25.00
Silicone Bars Glue	<i>92886380 Leroy Merlin Silicon Bars</i>	€ 5.39	1	Included	€ 5.39
Total Cost:					€ 552.02

The prices listed in this table are based on the offers available through the links provided in Annex D3, as of 15/05/2025, and are intended as reference values. If no link is provided, the price is based on an estimated market value.

Annex B: Code

More programs can be found at <https://github.com/NicolauSoleCoves/Pre-Freeze-Capacitance-Detection-System>

B1. Arduino Data Collection: “PELTIER_TEMP_HUM_TIMESTAMP.ino”

```

//-----LIBRARIES-----
#include <Adafruit_AHT10.h>
// INITIAL VARIABLES
int relayPin = 7;                                     // Relay module IN pin
bool relayState = false; // Relay state (OFF initially)
Adafruit_AHT10 aht;
//-----SETUP-----
void setup() {
    pinMode(relayPin, OUTPUT);
    digitalWrite(relayPin, LOW);                         // Ensure relay starts
OFF
    Serial.begin(115200);
    delay(1000);
    Serial.println("Timestamp,Temperature,Humidity");    // CSV header

    // Error catching
    if (!aht.begin()) {
        Serial.println("Could not find AHT10? Check wiring");
        while (1) delay(10);
    }
}
//-----MAIN LOOP-----
void loop() {
    unsigned long timestamp = millis();                  // Get current time in ms

    // Check for serial input to toggle relay
    if (Serial.available()) {
        char input = Serial.read();
        if (input == '\n') {                            // Detect Enter key
            relayState = !relayState;                  // Toggle relay state
            digitalWrite(relayPin, relayState ? LOW : HIGH); // Relay is active LOW
            //Serial.println(relayState ? "Relay ON" : "Relay OFF"); // To debug
        }
    }
    // Read temperature and humidity
    sensors_event_t humidity, temp;
    aht.getEvent(&humidity, &temp);
    // Print timestamp, sensor data
    Serial.print(timestamp);
    Serial.print(",");
    Serial.print(temp.temperature);
    Serial.print(",");
    Serial.println(humidity.relative_humidity);
    //Serial.print(",");
    //Serial.println(relayState ? "ON" : "OFF");           // To debug
    // To debug
}

```



```

    delay(500); //delay for stable
readings
}

```

B2. MATLAB GUI Data Collection: “*GUI_T_C_Time.m*”

```

%% -----INITIALIZATION-----

%% PREPARE IDLE
clear all; clc; close all;

%% INITIAL CONSTANTS:
numSamples = 64;
%% SERIAL PORT SETUP:
serialPort = "COM5"; %check the port where the ARDUINO is connected.
baudRate = 115200; % check that the arduino is configured to this badurate

% Check and close old serial open communications
if exist('s', 'var')

    clear s;
end

% Create a new serial communication:
s = serialport(serialPort, baudRate);
pause(1);
flush(s);
disp("Serial connection established!");

%% ACTIVATE RELAY
write(s, [ 'T', 13, 10], "uint8")
write(s, [ 'T', 13, 10], "uint8")

%% GRAPH INITIALIZATION
temperature = [];
timeStamp_T = [];
timeStamp_CSV = [];

%% PREPARE THE CSV DATA
csvFilePath = 'C:\ti\Sensing Solutions EVM GUI-1.10.0\PC GUI\data.csv';
initialFileSize = dir(csvFilePath).bytes;
dataCSV = readtable(csvFilePath);
sample_zero = height(dataCSV);

%% -----MAIN LOOP-----
figure(1);
% Open window with cancel button:
hWaitbar = waitbar(0, 'Running...', 'Name', 'Data Acquisition', ...
    'CreateCancelBtn', 'delete(gcf);');
% Loop:
while true
    %% Exit if user closes waitbar
    if ~ishandle(hWaitbar)
        disp("Stopped by user");
        break;
    end

    %% Read and Parse Arduino Data
    while s.NumBytesAvailable > 0

```



```

    rawData = readline(s);
end

values = str2double(split(strtrim(rawData), ','));

if numel(values) == 2 && all(~isnan(values))
    timestamp_arduino = values(1) / 1000; % Convert ms to seconds
    temp = values(2);

    % Fetch the new data to the vectors
    temperature(end+1) = temp;
    timeStamp_T(end+1) = timestamp_arduino;

    %% Plot Temperature
    subplot(2,1,1);
    plot(timeStamp_T, temperature, ...
        'Color', "#A2142F", ...
        'LineStyle', '--', ...
        'LineWidth',1);
    ylabel('Temperature (°C)', 'FontSize',16);
    xlabel('Time (s)', 'FontSize',16);
    title('Live T Data from AHT10 via MEGA2560', 'FontSize',24);
    grid on;

    % View window:
    if max(timeStamp_T) > numSamples
        xlim([max(timeStamp_T) - numSamples, max(timeStamp_T)]);
    end
end

%% Plot Capacitance from CSV (unchanged)
subplot(2,1,2);
dataCSV = readtable(csvFilePath);
dataCSV = dataCSV(sample_zero:end,:);

% Fetch the new data into the vectors
evmTimestamps = cumsum(dataCSV{:, 'logDeltaMs'}) / 1000;
C4 = dataCSV{:, 'MEAS4_pF'};

plot(evmTimestamps, C4, ...
    'Color', "#000000", ...
    'LineStyle', '-', ...
    'LineWidth',1);
xlabel('Time (s)', 'FontSize',16);
ylabel('Capacitance (pF)', 'FontSize',16);
title('Live C Data from FDC1004EVM', 'FontSize',24);
grid on;

% View window
if max(evmTimestamps) > numSamples
    xlim([max(evmTimestamps) - numSamples, max(evmTimestamps)]);
end

%% Dummy update for the waiting window
if ishandle(hWaitbar)
    waitbar(rand, hWaitbar, 'Adquiring...');
end

pause(0.001); % Keep it low for near real-time
end

```



```
% If the process is terminated, close the waiting window
if ishandle(hWaitbar)
    close(hWaitbar);
end

%% -----FINAL PLOT-----
figure(2);
clf;
hold on;

yyaxis right
plot(timeStamp_T, temperature, ...
    'Color', "#A2142F", ...
    'DisplayName', 'Temperature')
ylabel('Temperature (°C)', 'FontSize', 16);
ax = gca;
ax.YColor = "#000000";
%ylim([-3, 8])

% Filter the capacitance data noise with a moving average filter:
windowSize = 10;
C4_filtered = movmean(C4, windowSize);

% Plot the data, with noise and filtered
yyaxis left
plot(evmTimestamps, C4, ...
    'Color', "#000000", ...
    'DisplayName', 'Capacitance')
plot(evmTimestamps, C4_filtered, ...
    'Color', "#EDB120", ...
    'LineStyle', '-', ...
    'DisplayName', 'Filtered Capacitance');
ylabel('Capacitance (pF)', 'FontSize', 16);
ax.YColor = "k";

xlabel('Time (s)', 'FontSize', 16);
title('Complete Data Overview', 'FontSize', 24);
legend("Location", "northeast", 'FontSize', 12, "NumColumns", 4);
grid on;
hold off;

%% -----Clean Up-----
% Turn off the relay
write(s, ['T', 13, 10], "uint8")
% Close the serial communication with the arduino
clear s;
```

B3. Ploting and saving the samples from Experiment 5, were the C curve was filtered.

```

clear; clc; close all

% Source folder containing .mat files
sourceFolder = 'C:\Users\nicol\Desktop\TFG\muntatge\MATLAB\Experiments\C\ANALISIS';

% Destination folder for figures
outputFolder = fullfile(sourceFolder, 'EXPERIMENT 5');

% Create output folder if it doesn't exist
if ~exist(outputFolder, 'dir')
    mkdir(outputFolder);
end

% Load all .mat files in the folder
files = dir(fullfile(sourceFolder, '*.mat'));
windowSize = 25;

% Iterate over all files -----
for k = 1:length(files)
    fileName = files(k).name;
    filePath = fullfile(sourceFolder, fileName);
    data = load(filePath);

    % Skip if required fields are missing
    if ~all(isfield(data, {'C4', 'temperature', 'timeStamp_T', 'evmTimestamps'}))
        fprintf('Skipping file: %s (missing required data)\n', fileName);
        continue;
    end

    % Extract sample ID from filename
    parts = regexp(fileName, '\d+', 'match');
    if isempty(parts)
        sampleID = sprintf('File_%d', k);
    else
        sampleID = sprintf('Sample_%s', parts{end});
    end

    % Remove outliers from C4
    for i = 2:length(data.C4)
        if data.C4(i) < 2 || data.C4(i) > 15.6
            data.C4(i) = data.C4(i-1);
        end
    end

    % Filter C4
    C4_filtered = movmean(data.C4, windowSize);

    % Create full-screen visible figure BEFORE plotting
    fig = figure('Visible', 'on', 'Units', 'normalized', 'OuterPosition', [0 0 1 1]);
    clf; hold on;

    % Plot temperature (yyaxis right)
    yyaxis right
    plot(data.timeStamp_T, data.temperature, ...
        'Color', "#A2142F", ...
        'LineStyle', "-.", ...

```



```
'LineWidth', 1.5, ...
'DisplayName', 'Temperature');
ylabel('Temperature (°C)', 'FontSize', 16);
ax = gca;
ax.YColor = "#000000";

% Plot capacitance (yyaxis left)
yyaxis left
plot(data.evmTimestamps, C4_filtered, ...
    'Color', "magenta", ...
    'LineStyle', ':', ...
    'LineWidth', 1.5, ...
    'DisplayName', 'Filtered Capacitance');
ylabel('Capacitance (pF)', 'FontSize', 16);
ax.YColor = "k";

% Common settings
xlabel('Time (s)', 'FontSize', 16);
title(['Complete Data Overview of ' strrep(sampleID, '_', ' ')], 'FontSize', 20);
legend("Location", "northeast", 'FontSize', 10, "NumColumns", 2);
xlim([0 1000]);
grid on;

% Force layout update
drawnow;

% Save figure as .png
savePath = fullfile(outputFolder, [sampleID '.png']);
exportgraphics(fig, savePath, 'Resolution', 300); % High resolution
close(fig); % Close to free memory

fprintf('Saved figure: %s\n', savePath);
end
```

B4. Plotting the derivative of the C sample, and detecting valleys and peaks with an average filter to the gradient.

```

clear all; clc; close all

%% -----CONSTANTS-----
-----
FolderPath = 'C:\Users\nicol\Desktop\TFG\muntatge\MATLAB\Experiments\C\ANALISIS';
fileName = '24V_celulose_film_8_layers_Ac_4_1_cm_11';
WindowSize_C = 25; % Window size for averaging C
WindowSize_dC = 99; % Window size for smoothing derivative

xlimit = [0 700];

%% ----- Load data -----
cd(folderPath);
load(fileName); % loads: timeStamp_T, temperature, evmTimestamps, C4

% Clean C4 data from outliers
for i = 2:length(C4)
    if C4(i) < 2 || C4(i) > 15.6
        C4(i) = C4(i-1);
    end
end

t_C = evmTimestamps;
t_T = timeStamp_T;

%% -----SIGNAL PROCESSING-----
%%
% Moving average filter on C4
C4_filtered = movmean(C4, WindowSize_C);

% Derivative
dt = mean(diff(t_C));
dCdt = gradient(C4_filtered, dt);

% Smooth the derivative
dCdt_smoothed = movmean(dCdt, WindowSize_dC);

% Zero-crossing detection from smoothed derivative
sign_dCdt = sign(dCdt_smoothed);
zeroCrossings = diff(sign_dCdt);

% Peaks (from + to -): -2
peakIndices = find(zeroCrossings == -2) + 1;

% Valleys (from - to +): +2
valleyIndices = find(zeroCrossings == 2) + 1;

% Extract sample ID from filename
parts = regexp(fileName, '\d+', 'match');
if isempty(parts)
    sampleID = 'Unknown Sample';
else
    sampleID = sprintf('Sample %s', parts{end});
end

%% -----PLOT-----

```



```

figure(1); clf

% First subplot: C(t) + T(t) + peaks/valleys
subplot(2,1,1);
hold on
yyaxis right
plot(t_C, C4_filtered, ...
    'Color', "magenta", ...
    'LineStyle', ':', ...
    'LineWidth', 1.5, ...
    'DisplayName', 'Filtered Capacitance');
plot(t_C(peakIndices), C4_filtered(peakIndices), 'r|', 'MarkerSize', 25,
'DisplayName', 'Peaks');
plot(t_C(valleyIndices), C4_filtered(valleyIndices), 'g|', 'MarkerSize', 25,
'DisplayName', 'Valleys');
ylabel('Capacitance (pF)', 'FontSize', 12);
ax = gca; ax.YColor = "k";

yyaxis left
plot(t_T, temperature, ...
    'Color', "#A2142F", ...
    'LineStyle', "-.", ...
    'LineWidth', 1.5, ...
    'DisplayName', 'Temperature');
ylabel('Temperature (°C)', 'FontSize', 12);
ax.YColor = "k";

xlim(xlimit);
xlabel('Time (s)');
title('Reference Data \it{C(t)} and \it{T(t)}');
legend('Location', 'best', 'NumColumns', 2);
grid on;
hold off

% Second subplot: Smoothed derivative and zero line
subplot(2,1,2);
hold on
plot(t_C, dCdt_smoothed, '-', 'Color', "k", 'LineWidth', 1.5, 'DisplayName',
sprintf('Smoothed dC/dt, W = %d', WindowSize_dC));
yline(0, '--b', 'LineWidth', 1.5, 'DisplayName', 'x = 0');
ylabel('dC/dt (nF/s)', 'FontSize', 12);
xlabel('Time (s)');
xlim(xlimit);
title('Smoothed Derivative of Filtered C');
legend('Location', 'best');
grid on;
hold off

% Super title
sgtitle(['Complete Data Overview of ' sampleID], 'FontSize', 20);

```

B5. Auxiliar Function: “*exopeak_choose.m*”

```

function [t_f_exo, T_peak, t_C_at_freeze, C_at_freeze, T_ini_exo, t_exo_ini] =
exopeak_choose(t_T, temperature, C4_filtered, t_C, trialFileName)

% === Generate unique ID for cache file based on trial file name ===
[~, trialName, ~] = fileparts(trialFileName);
trialID = regexp替換(trialName, '[^w]', '_');
datasetID = sprintf('exo_cache_%s.mat', trialID);

if isfile(datasetID)
    % === Load cached results ===
    load(datasetID, 't_f_exo', 'T_peak', 't_C_at_freeze', 'C_at_freeze', 'T_ini_exo',
't_exo_ini');
    fprintf('[INFO] Loaded cached exothermic peak data from %s\n', datasetID);
    return;
end

% === User input: Select exothermic window ===
figure;
plot(t_T, temperature);
 ylim([-5,7])
 title(sprintf('Select window around exothermic peak for %s', trialFileName),
'Interpreter', 'none');
 xlabel('Time (s)'); ylabel('Temperature (°C)');
 [t_start, ~] = ginput(1);
 xline(t_start, '--k', 'Start');
 [t_end, ~] = ginput(1);
 xline(t_end, '--r', 'End');
 if t_start > t_end
    [t_start, t_end] = deal(t_end, t_start);
end

% Indices in window
idx_window = find(t_T >= t_start & t_T <= t_end);
t_window = t_T(idx_window);
T_window = temperature(idx_window);
% Find exothermic peak
[~, idx_local_max] = max(T_window);
idx_f_exo_T = idx_window(idx_local_max);
t_f_exo = t_T(idx_f_exo_T);
T_peak = temperature(idx_f_exo_T);
% Find initial rise (minimum T before peak)
idx_ini_to_peak = idx_window(1:idx_local_max);
[~, idx_min_T_rel] = min(temperature(idx_ini_to_peak));
idx_min_T_abs = idx_ini_to_peak(idx_min_T_rel);
t_exo_ini = t_T(idx_min_T_abs);
T_ini_exo = temperature(idx_min_T_abs);
xline(t_exo_ini, 'g--', 'Min T before peak');
% Find C(t_f_exo)
[~, idx_f_exo_C] = min(abs(t_C - t_f_exo));
C_at_freeze = C4_filtered(idx_f_exo_C);
t_C_at_freeze = t_C(idx_f_exo_C);
% Cache result
save(datasetID, 't_f_exo', 'T_peak', 't_C_at_freeze', 'C_at_freeze', 'T_ini_exo',
't_exo_ini');
fprintf('[INFO] Saved exothermic peak data to %s\n', datasetID);

close;
end

```



B6. Data processing Algorithm with GUI

```

clear all;clc;close all;

%% Initial Constants:
numSamples = 60*5; % 5 minutes of data
prefrozen_detected = false;

% === Filter (moving average) for the capacitance data ===
windowSize = 25;
window_std = windowSize;

% Pre-frozen detection logic
threshold_high = 0.017;
threshold_low = 0.0025;

%% SERIAL PORT SETUP

serialPort = "COM5";
baudRate = 115200;

if exist('s', 'var')
    clear s;
end

s = serialport(serialPort, baudRate);
pause(1);
flush(s);
disp("Serial connection established!");

%% GRAPH INITIALIZATION
temperature = [];
timeStamp_T = [];
timeStamp_CSV = [];

%% Activate Relay
write(s, ['T', 13, 10], "uint8")
write(s, ['T', 13, 10], "uint8")

%% Prepare CSV data
csvFilePath = 'C:\ti\Sensing Solutions EVM GUI-1.10.0\PC GUI\data.csv';
initialFileSize = dir(csvFilePath).bytes;
dataCSV = readtable(csvFilePath);
sample_zero = height(dataCSV);

%% ----- Main Loop -----
figure(1);
hWaitbar = waitbar(0, 'Running...', 'Name', 'Data Acquisition', ...
    'CreateCancelBtn', 'delete(gcf);');
while true
    %% Exit if user closes waitbar
    if ~ishandle(hWaitbar)
        disp("Stopped by user");
        break;
    end

    % Read and Parse Arduino Data
    while s.NumBytesAvailable > 0
        rawData = readline(s);
    end

```



```

values = str2double(split(strtrim(rawData), ','));

if numel(values) == 2 && all(~isnan(values))
    timestamp_arduino = values(1) / 1000; % Convert ms to seconds
    temp = values(2);

    temperature(end+1) = temp;
    timeStamp_T(end+1) = timestamp_arduino;

    % Plot Temperature
    subplot(2,1,1);
    plot(timeStamp_T, temperature, 'Color', "#A2142F", 'LineStyle', '--',
        'LineWidth', 1);
    ylabel('Temperature (°C)', 'FontSize', 16);
    xlabel('Time (s)', 'FontSize', 16);
    title('Live T Data from AHT10 via MEGA2560', 'FontSize', 24);
    grid on;

    if max(timeStamp_T) > numSamples
        xlim([max(timeStamp_T) - numSamples, max(timeStamp_T)]);
    end
    ylim([min(temperature)-1 min(temperature)+7])
end

% Plot Capacitance from CSV (updated)
subplot(2,1,2);
hold on
dataCSV = readtable(csvFilePath);
dataCSV = dataCSV(sample_zero:end,:);

evmTimestamps = cumsum(dataCSV{:, 'logDeltaMs'}) / 1000;

C4 = dataCSV{:, 'MEAS4_pF'};
% Clean up C4 from outliers
if C4(end) < 2 || C4(end) > 15.6
    C4(end) = C4(end-1);
end
C4_filtered = movmean(C4, windowSize); % smoothing window

plot(evmTimestamps, C4, 'Color', "#000000", 'LineStyle', '-', 'LineWidth', 1);
if evmTimestamps(end) > windowSize*2
    plot(evmTimestamps, C4_filtered, 'Color', "#EDB120", 'LineStyle', '-',
        'DisplayName', 'Filtered Capacitance');
end

xlabel('Time (s)', 'FontSize', 16);
ylabel('Capacitance (pF)', 'FontSize', 16);
title('Live C Data from FDC1004EVM', 'FontSize', 24);
grid on;
hold off

if max(evmTimestamps) > numSamples
    xlim([max(evmTimestamps) - numSamples, max(evmTimestamps)]);
end

%% === Pre-frozen Detection ===
if ~prefrozen_detected && timeStamp_T(end) > 30
    % Compute rolling std
    std_C = movstd(C4_filtered, window_std);

    % Start analyzing only after 30s
    start_idx = find(evmTimestamps > 30, 1);

```



```

prefrozen_idx = NaN;
for i = start_idx:length(std_C)
    if std_C(i) > threshold_high
        for j = i+1:length(std_C)
            if std_C(j) < threshold_low
                prefrozen_idx = j;
                break;
            end
        end
        break;
    end
end

if ~isnan(prefrozen_idx)
    t_prefrozen = evmTimestamps(prefrozen_idx);
    C_prefrozen = C4_filtered(prefrozen_idx);
    fprintf('[PREFROZEN DETECTED] t = %.2f s | C = %.4f pF\n', t_prefrozen,
C_prefrozen);

    % Mark on current plot
    subplot(2,1,2);
    hold on;
    plot(t_prefrozen, C_prefrozen, 'kx', 'MarkerSize', 10, ...
        'MarkerFaceColor', 'c', 'DisplayName', 'Detected Pre-Frozen Point');
    hold off;

    % Lock detection
    prefrozen_detected = true;
end
end

%% Dummy update
if ishandle(hWaitbar)
    waitbar(rand, hWaitbar, 'Acquiring...');
end

pause(0.001); % Keep low for near real-time
end

if ishandle(hWaitbar)
    close(hWaitbar);
end

%% ----- FINAL PLOT -----
figure(2);
clf;
hold on;

yyaxis right
plot(timeStamp_T, temperature, 'Color', "#A2142F",'DisplayName', 'Temperature')
ylabel('Temperature (°C)', 'FontSize', 16);
ax = gca;
ax.YColor = "#000000";

yyaxis left
plot(evmTimestamps, C4, 'Color', "#000000", 'DisplayName', 'Capacitance')
if evmTimestamps(end) > windowHeight*2
    plot(evmTimestamps, C4_filtered, 'Color', "#EDB120",'LineStyle', '- ', 'DisplayName',
'Filtered Capacitance');
end
if exist('t_prefrozen', 'var') && exist('C_prefrozen', 'var')
    plot(t_prefrozen, C_prefrozen, 'bx', ...

```



```
'MarkerSize', 20, ...
'LineWidth',2, ...
'DisplayName', 'Detected Pre-Frozen Point');
end
ylabel('Capacitance (pF)', 'FontSize', 16);
ax.YColor = "k";

xlabel('Time (s)', 'FontSize', 16);
title('Complete Data Overview', 'FontSize', 24);
legend("Location", "northeast", 'FontSize', 12, "NumColumns", 4);
grid on;
hold off;

%% Clean Up
write(s, ['T', 13, 10], "uint8")
clear s;
```



B7. Data Validation and Figures Code

```

clear all; clc; close all;

%% ----- CONSTANTS -----
FolderPath =
'C:\Users\nicol\Desktop\TFG\muntatge\MATLAB\Experiments\FINAL_DETECTION_ALGORITHM\DATA_C
LASSIFIED';
WindowSize_C = 25;
WindowSize_S = 25;
th1 = 0.017;
th2 = 0.0025;
xlimit = [0 600];

%% ----- GET FILES -----
cd(FolderPath);
files = dir('*.*mat');

% Initialize results table
results = [];
labels = [];
%% ----- PROCESS EACH FILE -----
for k = 1:length(files)
    fileName = files(k).name;
    load(fileName); % Loads: timeStamp_T, temperature, evmTimestamps, C4

    % Skip cache files
    if startsWith(fileName, 'exo_cache')
        continue;
    end

    % Parse classification metadata from filename
    tokens = regexp(fileName, '_AP|AN|PP|PN|_(\d+).mat$', 'tokens');

    if ~isempty(tokens)
        actualClass = tokens{1}{1}; % 'AP' or 'AN'
        predictedClass = tokens{1}{2}; % 'PP' or 'PN'
        sampleNumber = tokens{1}{3}; %
        overviewTitle = sprintf('Overview: Actual %s - Predicted %s - Sample %s', ...
            actualClass, predictedClass, sampleNumber);
    else
        overviewTitle = 'Overview: Unknown Classification';
    end

    % Clean up C4 from outliers
    for i = 2:length(C4)
        if C4(i) < 2 || C4(i) > 15.6
            C4(i) = C4(i-1);
        end
    end

    % Rename variables
    t_C = evmTimestamps;
    t_T = timeStamp_T;

    % Parse file name
    isAP = contains(fileName, '_AP');
    isAN = contains(fileName, '_AN');
    isPP = contains(fileName, '_PP');
    isPN = contains(fileName, '_PN');

```



```

% Sample name
sampleID = fileName;

% Moving average and std
C4_filtered = movmean(C4, WindowSize_C);
std_C = movstd(C4_filtered, WindowSize_S);

% Initialize values
detected = false;
t_change = NaN; C_change = NaN; T_change = NaN;
T_ini_exo = NaN; t_ini_exo = NaN; T_peak_exo = NaN; t_peak_exo = NaN;
DT = NaN; Dt = NaN;

% Only call exopeak_choose if AP
if isAP
    [t_peak_exo, T_peak_exo, ~, ~, T_ini_exo, t_ini_exo] = ...
        exopeak_choose(t_T, temperature, C4_filtered, t_C, fileName);
end

% Detection via std(C)
idx_th1 = 0;
for i = 1:length(std_C)
    if std_C(i) > th1
        idx_th1 = i;
        for j = i+1:length(std_C)
            if std_C(j) < th2
                idx_th2 = j;
                t_change = t_C(j);
                C_change = C4_filtered(j);
                detected = true;
                break;
            end
        end
        break;
    end
end

% Interpolate temperature at t_change
if detected
    [t_T_unique, uniqueIdx] = unique(t_T, 'stable');
    temperature_unique = temperature(uniqueIdx);
    T_change = interp1(t_T_unique, temperature_unique, t_change);
end

% Compute DT, Dt
if isAP && detected && ~isnan(T_ini_exo)
    DT = T_ini_exo - T_change;
    Dt = t_ini_exo - t_change;
end

%% ----- PLOT -----
figure(k); clf

% Subplot 1: C(t) and T(t)
subplot(2,1,1); hold on
yyaxis left
plot(t_C, C4_filtered, 'Color', "magenta", 'LineStyle', ':', 'LineWidth', 1.5);
if detected
    plot(t_change, C_change, 'k|', 'MarkerSize', 15, 'LineWidth', 1);
end
ylabel('Capacitance (pF)', 'FontSize', 14);
ax = gca; ax.YColor = 'k';

```



```

yyaxis right
plot(t_T, temperature, 'Color', "#A2142F", 'LineStyle', "-.", 'LineWidth', 1.5);
if detected
    plot(t_change, T_change, 'k|', 'MarkerSize', 15, 'LineWidth', 1);
end
if isAP && ~isnan(T_peak_exo)
    plot(t_peak_exo, T_peak_exo, 'bx', 'MarkerSize', 15, 'LineWidth', 1);
end
ylabel('Temperature (°C)', 'FontSize', 14);
ax = gca; ax.YColor = 'k';

if isAP && detected
    text(mean(xlim()), max(C4_filtered), ...
        sprintf(['Detection Delay: \Delta t = %.2f s\nT = %.2f °C'], Dt,
T_change), ...
        'FontSize', 12, 'Color', 'k', 'HorizontalAlignment', 'center');
end
xlim(xlimit);
xlabel('Time (s)', 'FontSize', 14);
title('Filtered Capacitance and Temperature', 'FontSize', 16);
grid on;
legend({'filtered C_{in}(t)', 'C_{detected}', 'T(t)', 'T_{detected}',
'T_{peak}'}, 'Location', 'northeast', 'FontSize', 10)

% Subplot 2: std(C)
subplot(2,1,2); hold on
plot(t_C, std_C, 'b-', 'DisplayName', '\sigma(C(t))');
yline(th1, "Color", [0.5, 0.5, 0.5], "LineWidth", 2, 'Label', 'th_1');
yline(th2, 'k', "LineWidth", 2, 'Label', 'th_2');
if detected
    plot(t_change, std_C(idx_th2), 'k|', 'MarkerSize', 15, 'LineWidth', 1);
end
ylabel('\sigma(C(t)) (pF)', 'FontSize', 14);
xlabel('Time (s)', 'FontSize', 14);
xlim(xlimit);
title('Standard Deviation of C(t)', 'FontSize', 16);
grid on;
legend({'\sigma(C_{in}(t))', 'th_1', 'th_2', '\sigma_{detected}'}, 'Location',
'northeast', 'FontSize', 10)

sgtitle(overviewTitle, 'FontSize', 20);

g = gcf;
g.WindowState = 'maximized';

pngFile = fullfile(folderPath, sprintf('%s.png', fileName)); % Optional: Save as PNG
saveas(k, pngFile);
%% ----- SAVE RESULTS -----
results = [results; {
    fileName, isAP, isAN, isPP, isPN, detected, ...
    T_ini_exo, t_ini_exo, T_change, t_change, DT, Dt
}];

% Map actual and predicted labels to binary classes
% Actual: AP=1, AN=0
% Predicted: PP=1, PN=0
actual = double(strcmp(actualClass, 'AP'));
predicted = double(strcmp(predictedClass, 'PP'));

% Append to label matrix

```

```

    labels = [labels; actual, predicted];

end

%% ----- DISPLAY TABLE -----
T = cell2table(results, 'VariableNames', ...
{'FileName', 'AP', 'AN','PP','PN', 'Detected', ...
'T_ini_exo', 't_ini_exo', 'T_change', 't_change', 'DT', 'Dt'}); 

disp(T);

%%
% CONFUSION MATRIX:
% Extract actual and predicted labels
actualLabels = labels(:,1);
predictedLabels = labels(:,2);

% True Positive (TP): actual 1, predicted 1
TP = sum(actualLabels == 1 & predictedLabels == 1);

% True Negative (TN): actual 0, predicted 0
TN = sum(actualLabels == 0 & predictedLabels == 0);

% False Positive (FP): actual 0, predicted 1
FP = sum(actualLabels == 0 & predictedLabels == 1);

% False Negative (FN): actual 1, predicted 0
FN = sum(actualLabels == 1 & predictedLabels == 0);

% Manual confusion matrix
confMat = [TP, FN; FP, TN]; % [row1 = actual 1; row2 = actual 0]

disp('Confusion Matrix (manual):');
disp(array2table(confMat, ...
'VariableNames', {'Pred_Pos', 'Pred_Neg'}, ...
'RowNames', {'Actual_Pos', 'Actual_Neg'}));

% Accuracy
accuracy = (TP + TN) / (TP + TN + FP + FN);

% Precision (Positive Predictive Value)
precision = TP / (TP + FP);

% Recall / Sensitivity / True Positive Rate
recall = TP / (TP + FN);

% Specificity (True Negative Rate)
specificity = TN / (TN + FP);

% F1 Score
f1 = 2 * (precision * recall) / (precision + recall);

% Display
fprintf('Accuracy : %.2f %%\n', accuracy * 100);
fprintf('Precision : %.2f %%\n', precision * 100);
fprintf('Recall : %.2f %%\n', recall * 100);
fprintf('Specificity : %.2f %%\n', specificity * 100);
fprintf('F1 Score : %.2f %%\n', f1 * 100);

%%

```



```
% Save table in excel for future formatting
writetable(T, 'results_table.xlsx');

%% ----- SCATTER PLOTS FOR AP-PP: DT and Dt -----
isAPPP = T.AP & T.PP;
DTs_APPP = T.DT(isAPPP);
Dts_APPP = T.Dt(isAPPP);
Tchanges_APPP = T.T_change(isAPPP);
tchanges_APPP = T.t_change(isAPPP);

groupLabels = {'TP'}; % GS can be later added if needed
colors = [0.2 0.2 0.2]; % Consistent color for both plots

figure;
sgtitle('True Positives Overview: \DeltaT and \Delta t', 'FontSize', 16);

for subplot_idx = 1:4
    subplot(2,2,subplot_idx); hold on; grid on;

    xticks(1:numel(groupLabels));
    xticklabels(groupLabels);
    xlim([0.5, numel(groupLabels) + 0.5]);

    % Choose variable to plot
    if subplot_idx == 1
        y = DTs_APPP;
        ylabel('\DeltaT (\textdegree C)', 'FontSize', 14);
    end
    if subplot_idx == 2
        y = Dts_APPP;
        ylabel('\Delta t (s)', 'FontSize', 14);
    end
    if subplot_idx == 3
        y = Tchanges_APPP;
        ylabel('T (\textdegree C)', 'FontSize', 14);
    end
    if subplot_idx == 4
        ylabel('t (s)', 'FontSize', 14);
        y = tchanges_APPP;
    end
    x = ones(size(y)); % only one group

    % Scatter (Datapoints)
    scatter(x, y, 50, 'filled', ...
        'MarkerFaceColor', colors, 'MarkerEdgeColor', 'k', 'MarkerFaceAlpha', 0.6);

    % Mean & STD
    m = mean(y, 'omitnan');
    s = std(y, 'omitnan');
    n = sum(~isnan(y));
    z = 1.96; % for 95 % CI
    ci_half = z * s / sqrt(n); % confidence interval

    % Shaded std (\pm 1\sigma)
    y_patch_std = [m-s, m-s, m+s, m+s];
    fill([1-0.2 1+0.2 1+0.2 1-0.2], y_patch_std, ...
        [0.8 0.8 0.8], 'EdgeColor', 'none', 'FaceAlpha', 0.4);

    % Shaded CI
    y_patch_ci = [m - ci_half, m - ci_half, m + ci_half, m + ci_half];
    fill([1-0.2 1+0.2 1+0.2 1-0.2], y_patch_ci, [0.4 0.4 0.4], ...

```

```
'EdgeColor', 'none', 'FaceAlpha', 0.4);

% Mean line
plot([1-0.2 1+0.2], [m m], 'k-', 'LineWidth', 2);

% Legend
if subplot_idx == 2 % Only add legend once (on right subplot)
    legend({'Samples', '95 % CI', '±1σ', 'Mean'}, ...
        'Location', 'northeast', 'FontSize', 10);
end

% Label
if m ~= 0
    unc_pct = 100 * ci_half / abs(m);
    label_str = sprintf('%3g\n(u = ±%.1f%%)', m, unc_pct);
else
    label_str = sprintf('%3g\n(u = ±N/A)', m);
end
text(1 + 0.25, m, label_str, 'VerticalAlignment', 'middle', 'FontSize', 10);
end
```



Annex C: Adquired Data

To see all figures, plots and output statistics, visit:

<https://github.com/NicolauSoleCoves/Pre-Freeze-Capacitance-Detection-System>

C1. Experiment 1: Freezing Point Detection

Table 0.2. Results of Experiment 1, where $V = 11$ V.

Trial Number	$t_{i,exo}$ (s)	$T_{i,exo}$ (°C)	$t_{f,exo}$ (s)	$T_{f,exo}$ (°C)	T_f (°C)	Δt_{exo} (s)	ΔT_{exo} (°C)
1	72.51	-4.26	72.776	-4.22	-9.47	0.266	0.04
2	76.109	-4.06	76.377	-4.04	-10.32	0.268	0.02
3	68.24	-4.35	68.773	-4.31	-10	0.533	0.04
4	65.71	-4.65	66.242	-4.58	-9.73	0.532	0.07
5	61.443	-4.64	61.843	-4.58	-10.17	0.4	0.06
Average	68.802	-4.392	69.202	-4.346	-9.938	0.400	0.046
Std. Dev.	4.676	0.207	4.607	0.192	0.279	0.108	0.016
Coeff. Var. (%)	7 %	5 %	7 %	4 %	3 %	27 %	35 %

Table 0.3. Results of exerperiment 1, where $V = 12$ V.

Trial Number	$t_{i,exo}$ (s)	$T_{i,exo}$ (°C)	$t_{f,exo}$ (s)	$T_{f,exo}$ (°C)	T_f (°C)	Δt_{exo} (s)	ΔT_{exo} (°C)
1	59.71	-4.54	59.843	-4.5	-9.41	0.133	0.04
2	64.508	-4.51	64.643	-4.47	-8.35	0.135	0.04
3	82.777	-4.23	82.91	-4.21	-9.03	0.133	0.02
4	77.842	-4.74	78.642	-4.62	-8.79	0.8	0.12
5	77.576	-4.63	78.375	-4.57	-9.35	0.799	0.06
Average	72.483	-4.530	72.883	-4.474	-8.986	0.400	0.056
Std. Dev.	8.035	0.155	8.183	0.130	0.355	0.298	0.031
Coeff. Var. (%)	11 %	3 %	11 %	3 %	4 %	74 %	56 %



C2. Experiment 2: Optimal Sample Size

Table 0.4. Summary of measurements from Experiment 2 with 1 layer.

Trial Number	$t_{i,exo}$ (s)	$T_{i,exo}$ (°C)	$t_{f,exo}$ (s)	$T_{f,exo}$ (°C)	Δt_{exo} (s)	ΔT_{exo} (°C)
1	234.284	-1.95	278.746	-1.58	44.462	0.37
2	255.135	-6.15	262.5	-6.06	7.365	0.09
3	-	-	-	-	-	-
4	-	-	-	-	-	-
5	-	-	-	-	-	-
Average	244.710	-4.050	270.623	-3.820	25.914	0.230
Std. Dev.	10.426	2.100	8.123	2.240	18.549	0.140
Coeff. Var. (%)	4 %	52 %	3 %	59 %	72 %	61 %

Table 0.5. Summary of measurements from Experiment 2 with 2 layers.

Trial Number	$t_{i,exo}$ (s)	$T_{i,exo}$ (°C)	$t_{f,exo}$ (s)	$T_{f,exo}$ (°C)	Δt_{exo} (s)	ΔT_{exo} (°C)
1	-	-	-	-	-	-
2	160.86	-3.03	164.382	-2.98	3.522	0.05
3	198.343	-4.04	208.431	-3.99	10.088	0.05
4	-	-	-	-	-	-
5	-	-	-	-	-	-
Average	179.602	-3.535	186.407	-3.485	6.805	0.050
Std. Dev.	15.302	0.412	17.983	0.412	2.681	0.000
Coeff. Var. (%)	9 %	12 %	10 %	12 %	39 %	0 %

Table 0.6. Summary of measurements from Experiment 2 with 4 layers.

Trial Number	$t_{i,exo}$ (s)	$T_{i,exo}$ (°C)	$t_{f,exo}$ (s)	$T_{f,exo}$ (°C)	Δt_{exo} (s)	ΔT_{exo} (°C)
1	-	-	-	-	-	-
2	132.195	-0.2	136.09	0.5	3.895	0.7
3	98.003	2.25	101.524	2.65	3.521	0.4
4	98.703	3.81	102.01	4.02	3.307	0.21
5	-	-	-	-	-	-
Average	109.634	1.953	113.208	2.390	3.574	0.437
Std. Dev.	13.818	1.429	14.013	1.255	0.210	0.175
Coeff. Var. (%)	13 %	73 %	12 %	52 %	6 %	40 %

Table 0.7. Summary of measurements from Experiment 2 with 8 layers.

Trial Number	$t_{i,exo}$ (s)	$T_{i,exo}$ (°C)	$t_{f,exo}$ (s)	$T_{f,exo}$ (°C)	Δt_{exo} (s)	ΔT_{exo} (°C)
1	315.124	-1.11	318.221	-0.2	3.097	0.91
2	192.153	0.97	201.546	1.77	9.393	0.8
3	201.496	1.03	208.167	1.87	6.671	0.84
4	172.903	4.06	176.906	4.11	4.003	0.05
5	147.939	1.93	151.354	2.08	3.415	0.15
Average	205.923	1.376	211.239	1.926	5.316	0.550
Std. Dev.	52.578	1.526	52.143	1.248	2.188	0.338
Coeff. Var. (%)	26 %	111 %	25 %	65 %	41 %	61 %

Table 0.8. Summary of measurements from Experiment 2 with 16 layers.

Trial Number	$t_{i,exo}$ (s)	$T_{i,exo}$ (°C)	$t_{f,exo}$ (s)	$T_{f,exo}$ (°C)	Δt_{exo} (s)	ΔT_{exo} (°C)
1	547.436	-1.59	561.473	-0.04	14.037	1.55
2	488.979	-1.27	497.946	-0.05	8.967	1.22
3	463.253	1.82	469.604	2.44	6.351	0.62
4	368.097	-0.02	371.298	0.49	3.201	0.51
5	352.344	0.98	366.54	1.81	14.196	0.83
Average	444.022	-0.016	453.372	0.930	9.350	0.946
Std. Dev.	67.398	1.184	68.571	0.926	3.924	0.353
Coeff. Var. (%)	15 %	7401 %	15 %	100 %	42 %	37 %



Table 0.9. Summary of measurements from Experiment 2, validation of measurements with 8-layer samples.

Trial Number	$t_{i,exo}$ (s)	$T_{i,exo}$ (°C)	$t_{f,exo}$ (s)	$T_{f,exo}$ (°C)	Δt_{exo} (s)	ΔT_{exo} (°C)	<i>FP</i>	<i>FN</i>	<i>TP</i>	<i>TN</i>
1	180.827	0.07	183.281	0.51	2.454	0.44	1	-	-	-
2	316.281	-2.29	319.752	-1.55	3.471	0.74	-	-	1	-
3	228.958	0.91	234.455	1.59	5.497	0.68	-	-	1	-
4	141.305	4.16	144.293	4.28	2.988	0.12	1	-	-	-
5	398.986	-0.79	402.348	-0.21	3.362	0.58	-	-	1	-
6	136.288	1.78	141.198	2.19	4.91	0.41	1	-	-	-
7	189.116	3.28	193.172	3.43	4.056	0.15	1	-	-	-
8	279.116	-1.24	285.468	-0.01	6.352	1.23	-	-	1	-
9	289.725	0.04	304.327	0.92	14.602	0.88	-	-	1	-
10	268.24	-1.77	277.367	-0.37	9.127	1.4	-	-	1	-
11	121.864	2.27	125.867	2.58	4.003	0.31	1	-	-	-
12	208.279	-0.08	211.215	0.49	2.936	0.57	-	-	1	-
13	306.553	-2.08	309.969	-1.28	3.416	0.8	-	-	1	-
14	258.094	-1.15	262.843	0.09	4.749	1.24	-	-	1	-
15	274.995	-1.42	290.79	0.16	15.795	1.58	-	-	1	-
16	124.335	1.16	129.831	1.82	5.496	0.66	-	-	1	-
17	212.741	-1.16	225.443	-0.01	12.702	1.15	-	-	1	-
18	196.385	1.86	204.177	2.61	7.792	0.75	-	-	1	-
19	257.797	-1.73	261.213	-0.67	3.416	1.06	-	-	1	-
20	113.206	3.1	116.727	3.3	3.521	0.2	1	-	-	-
21	176.293	-1.22	185.526	0.36	9.233	1.58	-	-	1	-
22	-	-	-	-	-	-	-	-	1	-
23	171.474	-0.55	176.278	0.54	4.804	1.09	-	-	1	-
24	188.112	0.17	193.608	0.94	5.496	0.77	-	-	1	-
25	228.189	-1.39	240.621	0.34	12.432	1.73	-	-	1	-
26	236.194	-1.79	249.75	-0.18	13.556	1.61	-	-	1	-
27	204.467	-0.9	209.537	0.19	5.07	1.09	-	-	1	-
28	181.014	-1.36	189.394	-0.07	8.38	1.29	-	-	1	-
29	136.892	0.69	142.709	1.41	5.817	0.72	-	-	1	-
30	153.584	-1.31	162.335	0.15	8.751	1.46	-	-	1	-
Average	213.080	-0.094	219.776	0.812	6.696	0.907	<i>n</i> = 30 + 0		<i>PP</i>	<i>PN</i>
	66.796	1.719	67.521	1.384	3.776	0.459	<i>AP</i>		23	1
Std. Dev, with 96 % CI	31 %	1820 %	31 %	170 %	56 %	51 %	<i>AN</i>		6	-



C3. Experiment 3: Plate Separation Distance Optimization

Table 0.10. Summary of measurements from Experiment 3 with 1 cm of separation between plates.

Trial Number	\bar{C}_{base} (pF)	$\sigma(C_{base})$ (pF)	\bar{C}_{peak} (pF)	$\sigma(C_{peak})$ (pF)	ΔC (pF)
1	234.284	-1.95	278.746	-1.58	44.462
2	255.135	-6.15	262.5	-6.06	7.365
3	-	-	-	-	-
4	-	-	-	-	-
5	-	-	-	-	-

Table 0.11. Summary of measurements from Experiment 3 with 2 cm of separation between plates.

Trial Number	\bar{C}_{base} (pF)	$\sigma(C_{base})$ (pF)	\bar{C}_{peak} (pF)	$\sigma(C_{peak})$ (pF)	ΔC (pF)
1	234.284	-1.95	278.746	-1.58	44.462
2	255.135	-6.15	262.5	-6.06	7.365
3	-	-	-	-	-
4	-	-	-	-	-
5	-	-	-	-	-

Table 0.12. Summary of measurements from Experiment 3 with 3 cm of separation between plates.

Trial Number	\bar{C}_{base} (pF)	$\sigma(C_{base})$ (pF)	\bar{C}_{peak} (pF)	$\sigma(C_{peak})$ (pF)	ΔC (pF)
1	234.284	-1.95	278.746	-1.58	44.462
2	255.135	-6.15	262.5	-6.06	7.365
3	-	-	-	-	-
4	-	-	-	-	-
5	-	-	-	-	-

Table 0.13. Summary of measurements from Experiment 3 with 4 cm of separation between plates.

Trial Number	\bar{C}_{base} (pF)	$\sigma(C_{base})$ (pF)	\bar{C}_{peak} (pF)	$\sigma(C_{peak})$ (pF)	ΔC (pF)
1	234.284	-1.95	278.746	-1.58	44.462
2	255.135	-6.15	262.5	-6.06	7.365
3	-	-	-	-	-
4	-	-	-	-	-
5	-	-	-	-	-

Table 0.14. Summary of measurements from Experiment 3 with 5 cm of separation between plates.

Trial Number	\bar{C}_{base} (pF)	$\sigma(C_{base})$ (pF)	\bar{C}_{peak} (pF)	$\sigma(C_{peak})$ (pF)	ΔC (pF)
1	234.284	-1.95	278.746	-1.58	44.462
2	255.135	-6.15	262.5	-6.06	7.365
3	-	-	-	-	-
4	-	-	-	-	-
5	-	-	-	-	-

Table 0.15. Statistics of Experiment 3 results.

d (cm)	\bar{C}_{base} (pF)	$\sigma(C_{base})$ (pF)	$CV(C_{base})$ (%)	\bar{C}_{peak} (pF)	$\sigma(C_{peak})$ (pF)	$CV(C_{peak})$ (%)	$\bar{\Delta}C$ (pF)	$\sigma(\Delta C)$ (pF)	$CV(\Delta C)$ (%)
1	2.678	0.036	1.34	3.178	0.141	4.45	0.5	0.154	30.79
2	2.377	0.003	0.14	2.44	0.017	0.69	0.064	0.018	28.06
3	2.25	0.003	0.13	2.286	0.017	0.73	0.036	0.015	42.56
4	2.188	0.002	0.1	2.216	0.005	0.24	0.028	0.004	15.15
5	2.146	0.002	0.12	2.166	0.005	0.25	0.02	0.007	32.29

$$\text{Linear fit equation: } y = -0.100x + 0.429 \quad R^2 = 0.516$$

$$\text{Exponential fit equation: } y = 3.404e^{-1.919x} \quad R^2 = 0.889$$



C4. Experiment 4: Effect of Increasing Electrode Area

Table 0.16. Summary of measurements from Experiment 3 with 1 cm of separation between plates.

Trial Number	\bar{C}_{base} (pF)	$\sigma(C_{base})$ (pF)	\bar{C}_{peak} (pF)	$\sigma(C_{peak})$ (pF)	ΔC (pF)
1	7.047	0.01	5.62	0.026	1.427
2	7.099	0.013	5.593	0.011	1.506
3	7.059	0.006	5.591	0.048	1.468
4	7.169	0.005	5.725	0.024	1.443
5	7.042	0.005	5.618	0.022	1.425

Table 0.17. Summary of measurements from Experiment 3 with 2 cm of separation between plates.

Trial Number	\bar{C}_{base} (pF)	$\sigma(C_{base})$ (pF)	\bar{C}_{peak} (pF)	$\sigma(C_{peak})$ (pF)	ΔC (pF)
1	4.29	0.006	4.022	0.007	0.268
2	4.26	0.007	4.033	0.015	0.227
3	4.303	0.017	4.017	0.015	0.286
4	4.279	0.01	4.006	0.011	0.273
5	4.267	0.01	4.003	0.01	0.264

Table 0.18. Summary of measurements from Experiment 3 with 3 cm of separation between plates.

Trial Number	\bar{C}_{base} (pF)	$\sigma(C_{base})$ (pF)	\bar{C}_{peak} (pF)	$\sigma(C_{peak})$ (pF)	ΔC (pF)
1	3.664	0.01	3.532	0.008	0.132
2	3.651	0.01	3.537	0.006	0.114
3	3.652	0.006	3.539	0.004	0.113
4	3.62	0.005	3.498	0.009	0.122
5	3.588	0.008	3.423	0.004	0.165

Table 0.19. Summary of measurements from Experiment 3 with 4 cm of separation between plates.

Trial Number	\bar{C}_{base} (pF)	$\sigma(C_{base})$ (pF)	\bar{C}_{peak} (pF)	$\sigma(C_{peak})$ (pF)	ΔC (pF)
1	3.34	0.009	3.229	0.005	0.111
2	3.315	0.009	3.222	0.004	0.094
3	3.313	0.008	3.224	0.007	0.088
4	3.307	0.007	3.222	0.007	0.086
5	3.309	0.008	3.217	0.007	0.092

Table 0.20. Summary of measurements from Experiment 3 with 5 cm of separation between plates.

Trial Number	\bar{C}_{base} (pF)	$\sigma(C_{base})$ (pF)	\bar{C}_{peak} (pF)	$\sigma(C_{peak})$ (pF)	ΔC (pF)
1	3.176	0.005	3.112	0.005	0.064
2	3.179	0.004	3.113	0.008	0.066
3	3.181	0.01	3.124	0.005	0.057
4	3.183	0.01	3.118	0.008	0.065
5	3.199	0.013	3.128	0.004	0.071

Table 0.21. Statistics of Experiment 4 results.

d (cm)	\bar{C}_{base} (pF)	$\sigma(C_{base})$ (pF)	$CV(C_{base})$ (%)	\bar{C}_{peak} (pF)	$\sigma(C_{peak})$ (pF)	$CV(C_{peak})$ (%)	$\bar{\Delta C}$ (pF)	$\sigma(\Delta C)$ (pF)	$CV(\Delta C)$ (%)
1	7.083	0.053	0.74	5.629	0.055	0.98	1.454	0.034	2.33
2	4.28	0.017	0.4	4.016	0.012	0.3	0.264	0.022	8.4
3	3.635	0.031	0.85	3.506	0.049	1.4	0.129	0.021	16.4
4	3.317	0.013	0.4	3.223	0.004	0.13	0.094	0.01	10.6
5	3.183	0.009	0.29	3.119	0.007	0.23	0.065	0.005	7.64

$$\text{Linear fit equation: } y = -0.295x + 1.285$$

$$R^2 = 0.616$$

$$\text{Exponential fit equation: } y = 6.907e^{-1.562x}$$

$$R^2 = 0.988$$



C5. Experiment 5: Input Capacitance Behaviour Correlated to Freeze

Table 0.22. Different tried Correlation Parameters Statistics Results.

Experiment Name	<i>t</i> ₁	<i>t</i> ₂	<i>C</i> ₁	<i>C</i> ₂	<i>T</i> _i	<i>T</i> _f	Δt	ΔC	$\Delta Temp$	<i>m(t,C)</i>	$\Delta C/\Delta T$
24V_celulose_film_8_layers_Ac_4_1_cm_1	214.93	258.81	7.83	7.83	1.78	2.42	4.39E+01	-4.38E-03	6.40E-01	-9.98E-05	-6.84E-03
24V_celulose_film_8_layers_Ac_4_1_cm_2	137.70	280.46	12.77	12.88	1.84	2.80	1.43E+02	1.14E-01	9.60E-01	7.99E-04	1.19E-01
24V_celulose_film_8_layers_Ac_4_1_cm_3	149.83	269.87	9.55	9.62	2.22	2.61	1.20E+02	7.15E-02	3.90E-01	5.95E-04	1.83E-01
24V_celulose_film_8_layers_Ac_4_1_cm_4	69.33	224.76	9.99	10.20	4.42	4.47	1.55E+02	2.10E-01	5.00E-02	1.35E-03	4.20E+00
24V_celulose_film_8_layers_Ac_4_1_cm_5	637.31	718.06	9.45	9.44	4.74	4.75	8.08E+01	-2.42E-03	1.00E-02	-3.00E-05	-2.42E-01
24V_celulose_film_8_layers_Ac_4_1_cm_6	575.42	594.32	11.97	11.97	3.33	3.39	1.89E+01	-1.00E-03	6.00E-02	-5.29E-05	-1.67E-02
24V_celulose_film_8_layers_Ac_4_1_cm_7	508.53	639.00	9.32	9.34	3.36	3.39	1.30E+02	1.60E-02	3.00E-02	1.23E-04	5.35E-01
24V_celulose_film_8_layers_Ac_4_1_cm_8	279.23	371.68	8.00	8.04	-0.18	1.50	9.25E+01	3.63E-02	1.68E+00	3.93E-04	2.16E-02
24V_celulose_film_8_layers_Ac_4_1_cm_9	239.39	295.85	8.93	9.07	-0.81	2.17	5.65E+01	1.40E-01	2.98E+00	2.48E-03	4.70E-02
24V_celulose_film_8_layers_Ac_4_1_cm_10	147.28	228.17	9.58	9.61	0.99	1.33	8.09E+01	3.10E-02	3.40E-01	3.83E-04	9.11E-02
24V_celulose_film_8_layers_Ac_4_1_cm_11	230.51	418.20	11.76	12.07	-1.81	-0.45	1.88E+02	3.14E-01	1.36E+00	1.67E-03	2.31E-01
24V_celulose_film_8_layers_Ac_4_1_cm_12	267.80	344.98	8.84	8.86	2.00	2.45	7.72E+01	1.79E-02	4.50E-01	2.32E-04	3.99E-02
24V_celulose_film_8_layers_Ac_4_1_cm_13	145.29	254.14	11.84	12.39	-1.72	-0.01	1.09E+02	5.54E-01	1.71E+00	5.09E-03	3.24E-01
24V_celulose_film_8_layers_Ac_4_1_cm_14	120.74	183.74	10.79	11.13	0.78	2.57	6.30E+01	3.39E-01	1.79E+00	5.38E-03	1.89E-01
24V_celulose_film_8_layers_Ac_4_1_cm_15	131.11	237.65	9.68	10.04	0.17	2.44	1.07E+02	3.63E-01	2.27E+00	3.41E-03	1.60E-01
24V_celulose_film_8_layers_Ac_4_1_cm_16	138.57	266.28	12.68	13.09	1.32	1.49	1.28E+02	4.18E-01	1.70E-01	3.27E-03	2.46E+00
24V_celulose_film_8_layers_Ac_4_1_cm_17	241.69	366.60	8.75	8.76	-0.88	0.19	1.25E+02	1.43E-02	1.07E+00	1.14E-04	1.33E-02
24V_celulose_film_8_layers_Ac_4_1_cm_18	111.35	295.61	12.70	13.19	-0.85	1.42	1.84E+02	4.99E-01	2.27E+00	2.71E-03	2.20E-01
24V_celulose_film_8_layers_Ac_4_1_cm_19	128.58	370.20	10.49	11.20	1.97	2.87	2.42E+02	7.06E-01	9.00E-01	2.92E-03	7.85E-01
24V_celulose_film_8_layers_Ac_4_1_cm_20	1076.58	1215.02	11.95	12.10	2.07	2.55	1.38E+02	1.56E-01	4.80E-01	1.13E-03	3.25E-01
24V_celulose_film_8_layers_Ac_4_1_cm_21	1711.02	1856.37	12.02	12.23	2.00	2.45	1.45E+02	2.04E-01	4.50E-01	1.41E-03	4.54E-01
24V_celulose_film_8_layers_Ac_4_1_cm_22	114.03	315.54	12.25	13.38	0.51	1.54	2.02E+02	1.14E+00	1.03E+00	5.65E-03	1.11E+00
24V_celulose_film_8_layers_Ac_4_1_cm_23	1020.28	1201.04	15.33	15.75	-0.51	0.94	1.81E+02	4.20E-01	1.45E+00	2.32E-03	2.90E-01
24V_celulose_film_8_layers_Ac_4_1_cm_24	601.13	829.86	12.43	12.77	-1.89	-0.19	2.29E+02	3.46E-01	1.70E+00	1.51E-03	2.03E-01
24V_celulose_film_8_layers_Ac_4_1_cm_25	1399.16	1620.21	12.76	13.00	-1.76	0.01	2.21E+02	2.36E-01	1.77E+00	1.07E-03	1.34E-01
24V_celulose_film_8_layers_Ac_4_1_cm_26	2095.59	2315.41	12.92	13.16	-1.51	0.17	2.20E+02	2.44E-01	1.68E+00	1.11E-03	1.45E-01
24V_celulose_film_8_layers_Ac_4_1_cm_27	216.17	326.33	7.84	7.89	1.66	2.30	1.10E+02	5.36E-02	6.40E-01	4.87E-04	8.38E-02
24V_celulose_film_8_layers_Ac_4_1_cm_28	1159.02	1236.12	8.09	8.64	1.41	1.98	7.71E+01	5.48E-01	5.70E-01	7.11E-03	9.61E-01
24V_celulose_film_8_layers_Ac_4_1_cm_29	2051.61	2147.32	8.29	8.34	1.62	2.10	9.57E+01	4.94E-02	4.80E-01	5.16E-04	1.03E-01
<i>Mean (avg)</i>		1.30E+02	2.49E-01	1.01E+00	0.00183	4.54E-01					
<i>Standard Deviation (sd)</i>		5.81E+01	2.58E-01	7.75E-01	1.90E-03	8.64E-01					
<i>Coefficient of variation (CV)</i>		45 %	104 %	77 %	104 %	190 %					



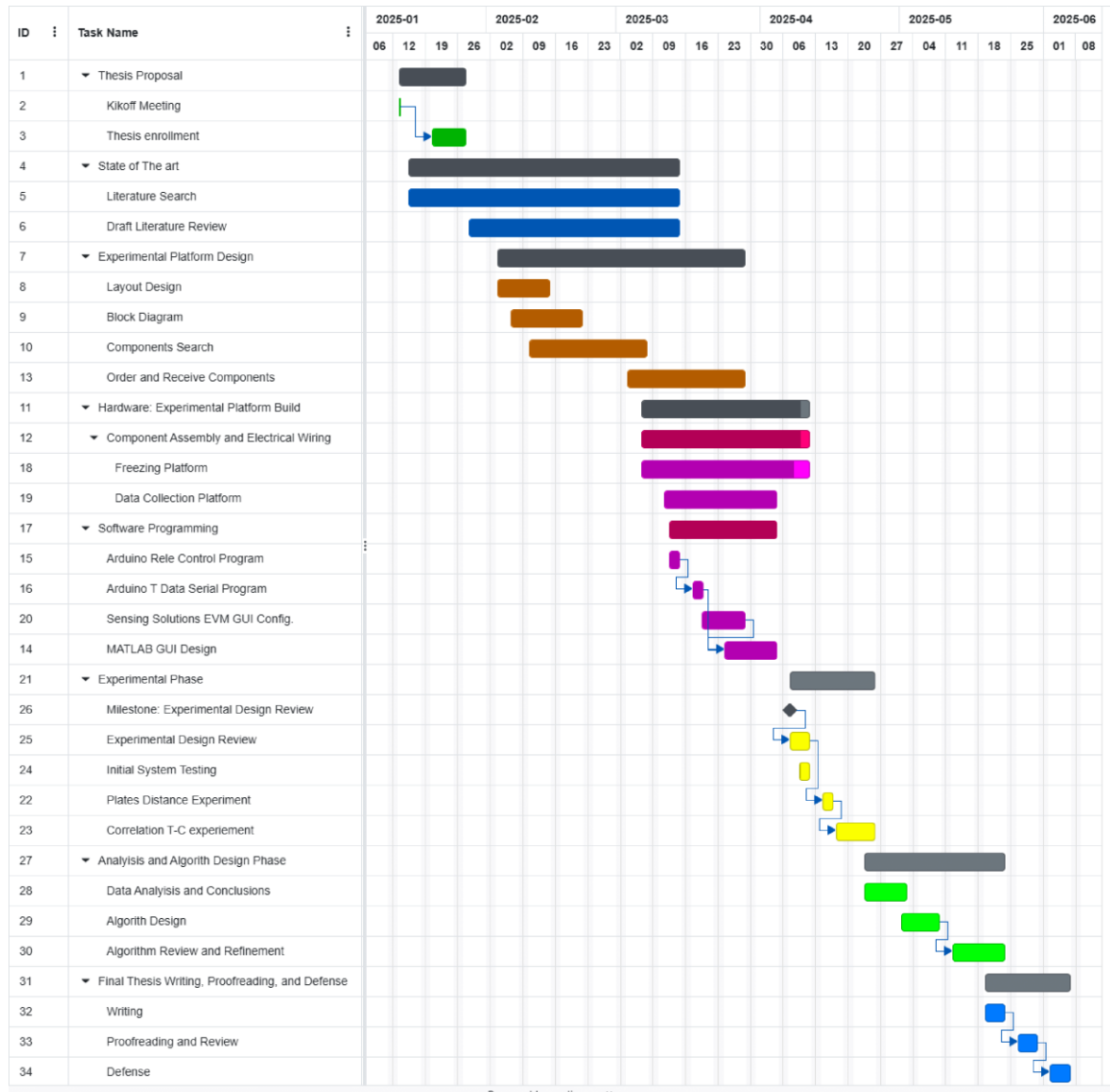
C6. Statistic Analysis of the Proposed Algorithm

Table 0.23. Results of the Threshold Algorithm Validation.

FileName	AP	AN	PP	PN	ICE?
24V_celulose_film_8_layers_Ac_4_1_cm_AN_PN_1.mat	FALSE	TRUE	FALSE	TRUE	FALSE
24V_celulose_film_8_layers_Ac_4_1_cm_AN_PN_10.mat	FALSE	TRUE	FALSE	TRUE	FALSE
24V_celulose_film_8_layers_Ac_4_1_cm_AN_PN_11.mat	FALSE	TRUE	FALSE	TRUE	FALSE
24V_celulose_film_8_layers_Ac_4_1_cm_AN_PN_12.mat	FALSE	TRUE	FALSE	TRUE	FALSE
24V_celulose_film_8_layers_Ac_4_1_cm_AN_PN_13.mat	FALSE	TRUE	FALSE	TRUE	FALSE
24V_celulose_film_8_layers_Ac_4_1_cm_AN_PN_2.mat	FALSE	TRUE	FALSE	TRUE	FALSE
24V_celulose_film_8_layers_Ac_4_1_cm_AN_PN_3.mat	FALSE	TRUE	FALSE	TRUE	FALSE
24V_celulose_film_8_layers_Ac_4_1_cm_AN_PN_4.mat	FALSE	TRUE	FALSE	TRUE	FALSE
24V_celulose_film_8_layers_Ac_4_1_cm_AN_PN_5.mat	FALSE	TRUE	FALSE	TRUE	FALSE
24V_celulose_film_8_layers_Ac_4_1_cm_AN_PN_6.mat	FALSE	TRUE	FALSE	TRUE	FALSE
24V_celulose_film_8_layers_Ac_4_1_cm_AN_PN_7.mat	FALSE	TRUE	FALSE	TRUE	FALSE
24V_celulose_film_8_layers_Ac_4_1_cm_AN_PN_8.mat	FALSE	TRUE	FALSE	TRUE	FALSE
24V_celulose_film_8_layers_Ac_4_1_cm_AN_PN_9.mat	FALSE	TRUE	FALSE	TRUE	FALSE
24V_celulose_film_8_layers_Ac_4_1_cm_AN_PP_1.mat	FALSE	TRUE	TRUE	FALSE	TRUE
24V_celulose_film_8_layers_Ac_4_1_cm_AN_PP_2.mat	FALSE	TRUE	TRUE	FALSE	TRUE
24V_celulose_film_8_layers_Ac_4_1_cm_AP_PN_1.mat	TRUE	FALSE	FALSE	TRUE	FALSE
24V_celulose_film_8_layers_Ac_4_1_cm_AP_PN_2.mat	TRUE	FALSE	FALSE	TRUE	FALSE
24V_celulose_film_8_layers_Ac_4_1_cm_AP_PP_1.mat	TRUE	FALSE	TRUE	FALSE	TRUE
24V_celulose_film_8_layers_Ac_4_1_cm_AP_PP_10.mat	TRUE	FALSE	TRUE	FALSE	TRUE
24V_celulose_film_8_layers_Ac_4_1_cm_AP_PP_11.mat	TRUE	FALSE	TRUE	FALSE	TRUE
24V_celulose_film_8_layers_Ac_4_1_cm_AP_PP_12.mat	TRUE	FALSE	TRUE	FALSE	TRUE
24V_celulose_film_8_layers_Ac_4_1_cm_AP_PP_13.mat	TRUE	FALSE	TRUE	FALSE	TRUE
24V_celulose_film_8_layers_Ac_4_1_cm_AP_PP_14.mat	TRUE	FALSE	TRUE	FALSE	TRUE
24V_celulose_film_8_layers_Ac_4_1_cm_AP_PP_15.mat	TRUE	FALSE	TRUE	FALSE	TRUE
24V_celulose_film_8_layers_Ac_4_1_cm_AP_PP_16.mat	TRUE	FALSE	TRUE	FALSE	TRUE
24V_celulose_film_8_layers_Ac_4_1_cm_AP_PP_17.mat	TRUE	FALSE	TRUE	FALSE	TRUE
24V_celulose_film_8_layers_Ac_4_1_cm_AP_PP_18.mat	TRUE	FALSE	TRUE	FALSE	TRUE
24V_celulose_film_8_layers_Ac_4_1_cm_AP_PP_19.mat	TRUE	FALSE	TRUE	FALSE	TRUE
24V_celulose_film_8_layers_Ac_4_1_cm_AP_PP_2.mat	TRUE	FALSE	TRUE	FALSE	TRUE
24V_celulose_film_8_layers_Ac_4_1_cm_AP_PP_20.mat	TRUE	FALSE	TRUE	FALSE	TRUE
24V_celulose_film_8_layers_Ac_4_1_cm_AP_PP_21.mat	TRUE	FALSE	TRUE	FALSE	TRUE
24V_celulose_film_8_layers_Ac_4_1_cm_AP_PP_22.mat	TRUE	FALSE	TRUE	FALSE	TRUE
24V_celulose_film_8_layers_Ac_4_1_cm_AP_PP_23.mat	TRUE	FALSE	TRUE	FALSE	TRUE
24V_celulose_film_8_layers_Ac_4_1_cm_AP_PP_24.mat	TRUE	FALSE	TRUE	FALSE	TRUE
24V_celulose_film_8_layers_Ac_4_1_cm_AP_PP_25.mat	TRUE	FALSE	TRUE	FALSE	TRUE
24V_celulose_film_8_layers_Ac_4_1_cm_AP_PP_26.mat	TRUE	FALSE	TRUE	FALSE	TRUE
24V_celulose_film_8_layers_Ac_4_1_cm_AP_PP_27.mat	TRUE	FALSE	TRUE	FALSE	TRUE
24V_celulose_film_8_layers_Ac_4_1_cm_AP_PP_28.mat	TRUE	FALSE	TRUE	FALSE	TRUE
24V_celulose_film_8_layers_Ac_4_1_cm_AP_PP_3.mat	TRUE	FALSE	TRUE	FALSE	TRUE
24V_celulose_film_8_layers_Ac_4_1_cm_AP_PP_4.mat	TRUE	FALSE	TRUE	FALSE	TRUE
24V_celulose_film_8_layers_Ac_4_1_cm_AP_PP_5.mat	TRUE	FALSE	TRUE	FALSE	TRUE
24V_celulose_film_8_layers_Ac_4_1_cm_AP_PP_6.mat	TRUE	FALSE	TRUE	FALSE	TRUE
24V_celulose_film_8_layers_Ac_4_1_cm_AP_PP_7.mat	TRUE	FALSE	TRUE	FALSE	TRUE
24V_celulose_film_8_layers_Ac_4_1_cm_AP_PP_8.mat	TRUE	FALSE	TRUE	FALSE	TRUE
24V_celulose_film_8_layers_Ac_4_1_cm_AP_PP_9.mat	TRUE	FALSE	TRUE	FALSE	TRUE

Annex D: Project Management

D1. GANTT Diagram



D2. Thesis Economic Study

Experimental Platform

Item Description	Item Denomination	Cost (€/unit)	Units	IVA (%)	Total (€)
Arduino MEGA 2560	<i>Arduino Mega 2560 Rev3</i>	€ 52.80	1	21	€ 63.89
Peltier Cell	<i>TEC1-12706</i>	€ 12.50	4	Included	€ 50.00
Relay Module	<i>JQC-3FF-S-Z</i>	€ 4.99	1	Included	€ 4.99
Heatsink 1	<i>FAN478</i>	€ 16.00	1	Included	€ 16.00
Temperature Sensor	<i>ATH10</i>	€ 14.16	2	Included	€ 28.32
Copper Tape	<i>RS PRO, 25mm x 33m 176-7501</i>	€ 65.70	1	21	€ 79.50
Thermal Paste	<i>SYY-157 silicon based thermal paste</i>	€ 8.88	1	Included	€ 8.88
A/D Capacitor Board	<i>FDC1004EVM, Digikey 296-38941-ND</i>	€ 209.14	1	21	€ 253.06
Methacrylate Plates	<i>Methacrylate 2 Piezas 20 x 20 cm</i>	€ 17.00	1	Included	€ 17.00
Wire, soldering paste, connexions	<i>Electronic Material</i>	€ 25.00	1	Included	€ 25.00
Silicone Bars Glue	<i>92886380 Leroy Merlin Silicon Bars</i>	€ 5.39	1	Included	€ 5.39
Total Cost:					€ 552.02

Experimental Costs and Consumables

Item Description	Item Denomination	Cost (€/unit)	Units	IVA (%)	Total (€)
Celulose Paper	<i>Paper rolls</i>	€ 5.99	1	Included	€ 5.99
Fuses	<i>250 V 4 A</i>	€ 0.29	6	Included	€ 1.74
Total Cost:					€ 7.73

Labour Costs

Item Description	Item Denomination	Cost (€/unit)	Hours	Total (€)	
Research and Development	<i>Minimum wage intership UPC</i>	€ 8.00	840	€ 6,720.00	
Documentation and final review	<i>Minimum wage intership UPC</i>	€ 8.00	360	€ 2,880.00	
Supervision	<i>Lecturer average wage (UPC, Spain)</i>	€ 17.00	60	€ 1,020.00	
Total Cost:					€ 10,620.00

Software Costs

Item Description	Item Denomination	Cost (€/unit)	Units	Total (€)	
OFICE 365	<i>Word, Excel, Outlook 2018 (monthly)</i>	€ 9.99	6	€ 59.94	
MATLAB	<i>MATLAB 2023b Licence</i>	€ 938.00	1	€ 938.00	
Total Cost:					€ 997.94

Total Thesis IVA (21%): € 2,557.32

Total Thesis Cost: € 12,177.69



D3. Thesis Economic Study – Price Links

Materials

Arduino MEGA 2560:

<https://www.amazon.es/Arduino-Mega-2560-R3-Microcontrolador/dp/B0046AMGW0>

Peltier Cell:

<https://www.digikey.es/es/products/detail/mikroelektronika/MIKROE-3828/10712655>

Relay Module:

<https://www.amazon.es/DollaTek-Tarjeta-optoacoplador-Soporte-Disparo/dp/B07DJ4NRC1>

Heatsink 1:

<https://www.amazon.es/Startech-com-FAN478-Ventilador-CPU-socket/dp/B00006B8EX>

Temperature Sensor:

<https://www.amazon.es/TECNOIOT-Temperatura-Humedad-Digital-Reemplazar/dp/B08XG1W72J>

Copper Tape:

<https://es.rs-online.com/web/p/cintas-metalicas/1767501>

Thermal Paste:

<https://www.amazon.es/SYY-Herramientas-actualizaci%C3%A1n-Procesador-Enfriadores/dp/B09XV2JTWL>

A/D Capacitor Board (FDC1004EVM):

<https://www.digikey.es/es/products/detail/texas-instruments/FDC1004EVM/5066968>

Methacrylate Plates:

<https://www.amazon.es/Metacrilato-transparente-mm-100-cm/dp/B0895ZN4QT>

Silicone Glue Bars:

<https://www.leroymerlin.es/productos/bolsa-6-barras-de-silicona-transparente-11-gsc-001401330-92886380.html>

Services and Software

Research and Development (Salary Reference):

<https://www.glassdoor.es/Salaries/barcelona-spain-junior-research-engineer-salary>

Supervision (Salary Reference):

<https://www.glassdoor.com/Salary/Universitat-Politecnica-de-Catalunya-Lecturer-Barcelona-Spain-Salaries>

Documentation and Final Review (Salary Reference):

<https://www.glassdoor.es/Salaries/barcelona-spain-junior-research-engineer-salary>

Office 365:

<https://www.microsoft.com/en-us/microsoft-365/buy/compare-all-microsoft-365-products>

MATLAB:

<https://de.mathworks.com/pricing-licensing.html>

